STABILITY AND ELECTROCHEMICAL REGENERATION OF ACTIVATED CARBON ELECTRODES FOR CAPACITIVE DEIONIZATION

by

Adrian Serrano Mora

MASc., The University of British Columbia, 2016

A THESIS SUBMITTED IN PARTIAL FULFILLMENT OF

THE REQUIREMENTS FOR THE DEGREE OF

DOCTOR OF PHILOSOPHY

in

THE FACULTY OF GRADUATE AND POSTDOCTORAL STUDIES

(Chemical and Biological Engineering)

THE UNIVERSITY OF BRITISH COLUMBIA

(Vancouver)

August 2020

The following individuals certify that they have read, and recommend to the Faculty of Graduate and Postdoctoral Studies for acceptance, the dissertation entitled:

STABILITY AND ELECTROCHEMICAL REGENERATION OF ACTIVATED CARBON ELECTRODES FOR CAPACITIVE DEIONIZATION

submitted by Adrian Serrano Mora in partial fulfillment of the requirements for

the degree of Doctor of Philosophy

in Chemical and Biological Engineering

Examining Committee:

Dr. Madjid Mohseni, Chemical and Biological Engineering
Co-supervisor

Dr. David P. Wilkinson, Chemical and Biological Engineering
Co-supervisor

Dr. Heather Trajano, Chemical and Biological Engineering
University Examiner

Dr. Edouard Asselin, Materials Engineering
University Examiner

Additional Supervisory Committee Members:

Dr. Naoko Ellis, Chemical and Biological Engineering
Supervisory Committee Member

Dr. Dan Bizzotto, Chemistry
Supervisory Committee Member

Abstract

The stability and electrochemical regeneration of activated carbon electrodes used for Capacitive Deionization have been investigated. To assess the electrode state, electrochemical properties such as capacitance and potential at the point of zero charge (E_{PZC}) were monitored and complemented by elemental composition, wettability and bulk porosity analysis.

Long-term cycling was performed with electrolytes containing dissolved organic matter (DOM) and iron (II) under anaerobic and aerobic conditions. It was found that DOM, at concentrations of up to 40 mg L^{-1}, had a marginal impact on capacitance loss and relocation of the E_{PZC}. On the other hand, the scaling nature of iron was apparent from early cycling stages, in waters containing as little as 0.2 mg Fe^{2+} L^{-1}. In all cases performed, elemental composition analysis demonstrated that incorporation of oxygen to the surface occurred predominantly during the first 15 to 20 cycles. Specifically, the oxygen content increased by a factor of four. Over this time frame, the contact angle decreased from approx. 130° to 34°, on average; which indicated an increase in electrode wettability. In addition, cycling experiments with simple electrolytes revealed improved electrode stability as cycling time increased and as pH decreased. Degradation tests conducted using a two-electrode cell demonstrated the effect of reaction coupling between the processes of carbon corrosion and oxygen reduction. As a result, electrode decay occurred at an accelerated rate.

Electrochemical regeneration was proven successful at recovering the electrode capacitance but not at regressing the E_{PZC}. Their corresponding response surfaces were mapped through a 3^2-factorial design of experiments and revealed a significant potential dependence. Further tests revealed a point of maximum recovery near a potential of -1.68 V vs RHE and 50 s

of holding time. Furthermore, the contribution of a regenerative step to the long-term electrode stability was assessed. In general, an improved retention of capacitance was observed during the first 25 cycles. However, it was noted that most of the capacitance recovered was lost in the subsequent degradation cycles. Consequently, the apparent initial improvement did not translate to an extension of the electrode lifetime, deeming this approach inadequate to mitigate the effect of carbon corrosion.

Lay Summary

Desalination of brackish water can be used to supply the increasing global freshwater demand. Among the available desalination technologies, capacitive deionization is a low energy, electrostatic approach that can be implemented as part of household water treatment devices. This is particularly useful in locations where the water provided, has been inadequately treated by the supplying utility. In this research, special attention was given to the degradation process occurring during continuous operation and its relation to electrode performance decay. This was studied under a variety of conditions, with focus on the contribution made by organic and inorganic species, naturally present in groundwater. Furthermore, a non-chemical method to restore and delay performance decay was explored. Insights gained from this study emphasize the importance of adequate pre-treatment and careful selection of cycling parameters to extend and balance unit lifetime and desalination performance.

Preface

This dissertation is original, unpublished, independent work by the author, Adrian Serrano Mora.

The cross-sectional SEM imaging used to estimate bulk porosity, presented in Chapter 6 and 7, were performed by Amir Peyman Soleymani and Dr. Jasna Jankovic at the University of Connecticut.

Two manuscripts are in preparation for submission to peer-reviewed journals:

- Adrian Serrano Mora, David P. Wilkinson & Madjid Mohseni. "Influence of dissolved organic matter and iron on the electrochemical, morphological and physical properties of activated carbon electrodes used in capacitive deionization".
- Adrian Serrano Mora, David P. Wilkinson & Madjid Mohseni. "Effect of reductive potentials on the recovery of key electrochemical parameters and cyclability of activated carbon electrodes used in capacitive deionization (CDI)".

The results of this study have been presented in the following conferences:

- Adrian Serrano Mora, David P. Wilkinson & Madjid Mohseni. "Capacitive Deionization of Brackish Water: Influence of Water Matrix on the Stability of Activated Carbon Electrodes". Poster Presentation at the Water Quality and Technology Conference, November 3rd – 6th 2019, Dallas, TX.

- Adrian Serrano Mora, David P. Wilkinson & Madjid Mohseni. "Desalination of Brackish Waters Using Capacitive Deionization". Poster Presentation at the 8th Annual Young Electrochemists Symposium, July 2019, Vancouver, BC.
- Adrian Serrano Mora, David P. Wilkinson & Madjid Mohseni. "Stability and Electrochemical Regeneration of Activated Carbon Electrodes for Long-term Capacitive Deionization of Brackish Water in Presence of Fouling and Scaling Agents". Oral Presentation at the International Young Water Professionals Conference, June 23rd – 27th 2019, Toronto, ON.
- Adrian Serrano Mora, David P. Wilkinson & Madjid Mohseni. "Desalination of Brackish Waters Using Capacitive Deionization". Poster Presentation at the IC-IMPACTS Annual General Meeting, March 2018, Vancouver, BC.
- Adrian Serrano Mora, David P. Wilkinson & Madjid Mohseni. "Desalination of Brackish Water through Capacitive Deionization". Poster Presentation at the Canadian Water Summit, June 20th – 22nd 2018, Vancouver, BC.
- Adrian Serrano Mora, David P. Wilkinson & Madjid Mohseni. "Long-term Evaluation of Modified Activated Carbon Electrodes for Capacitive Deionization". Oral Presentation at the 233rd Electrochemical Society Meeting, May 13th – 17th 2018, Seattle, WA.
- Adrian Serrano Mora, David P. Wilkinson & Madjid Mohseni. "The Challenge of Long-term Stability for the Capacitive Deionization (CDI) of Brackish Water". Poster Presentation at the IC-IMPACTS Annual General Meeting, March 2018, Vancouver, BC.

- Adrian Serrano Mora, David P. Wilkinson & Madjid Mohseni. "Desalination of Brackish Water by Capacitive Deionization (CDI): The Effect of Continuous Operation on the Performance of Activated Carbon Electrodes (ACEs)". Oral Presentation at the 67th Canadian Chemical Engineering Conference, October 22nd – 25th 2017, Edmonton, AB.
- Adrian Serrano Mora, David P. Wilkinson & Madjid Mohseni. "Long-term Stability, Fouling and Scaling of Activated Carbon Electrodes used in Capacitive Deionization (CDI) of Brackish Water". Poster Presentation at the IC-IMPACTS Annual General Meeting, March 2017, Vancouver, BC.

Table of Contents

Abstract ..... **iii**

Lay Summary ..... **v**

Preface ..... **vi**

Table of Contents ..... **ix**

List of Tables ..... **xiii**

List of Figures ..... **xviii**

List of Symbols ..... **xli**

List of Abbreviations ..... **xlii**

Acknowledgements ..... **xliv**

Dedication ..... **xlvi**

Chapter 1: Introduction **1**

1.1 Motivation 1

1.2 Research Scope 3

1.3 Thesis Layout 4

1.4 Literature Review 6

1.4.1 Application of Capacitive Deionization (CDI) 6

1.4.2 Carbon Oxidation in Electrochemical Systems 8

1.4.3 Evidence of Faradaic Reactions in CDI 12

1.4.3.1 Inversion Effect & Reduction of Surface Area 13

1.4.3.2 Relocation of the Electrode E_{PZC} 15

1.4.3.3 Asymmetrical Charge Flow 17

1.4.3.4 Solution pH 18
1.4.4 Fouling and Scaling in CDI 22
1.4.5 Strategies to Mitigate Faradaic Reactions 26
1.4.5.1 Membrane Capacitive Deionization 26
1.4.5.2 Electrodes Doped with Metal Oxides 27
1.4.6 Electrochemical Regeneration 29
1.5 Knowledge Gaps 30
1.6 Thesis Objectives 32
1.7 Significance & Novelty 33
Chapter 2: Experimental Procedure 35
2.1 Electrode Fabrication 35
2.2 Electrochemical Characterization 35
2.2.1 Cyclic Voltammetry 36
2.2.2 Electrochemical Impedance Spectroscopy (EIS) 38
2.3 Degradation Experiments 38
2.3.1 Three-Electrode Cell 38
2.3.2 Two-Electrode Cell Experiments 41
2.4 Electrochemical Regeneration Experiments 43
2.4.1 Factorial Design of Experiments 44
2.4.2 Extended Surface Response Study 44
2.4.3 Effect of Electrochemical Regeneration on Electrode Cyclability 45
2.5 Ex-situ Analysis 45

2.6 Quality Control & Assurance 47

Chapter 3: Stability of Activated Carbon Electrodes 50

3.1 Beginning-of-Life (BOL) Electrode Characteristics 50

3.2 Baseline Degradation: Effect of Dissolved Oxygen 55

3.3 Degradation in the Presence of Scaling and Fouling Solutes 69

3.3.1 Effect of Iron (Fe^{2+}) 69

3.3.2 Effect of Organic Matter 83

3.4 Effect of Cycling Time and Solution pH 92

3.5 Electrode Stability using a Two-Electrode Flow Cell 104

3.6 Conclusions 118

Chapter 4: Electrochemical Regeneration 121

4.1 Investigating the Recovery of Capacitance and E_{PZC} Regression 122

4.2 Further Probing along the Potential Domain 131

4.3 Influence on Electrode Stability 133

4.4 Conclusions 145

Chapter 5: Conclusions and Recommendations for Future Work 148

5.1 Conclusions 148

5.2 Recommendations for future work 153

Bibliography 157

Appendices 172

Appendix A 172

A.1 Degradation in Presence of Scaling and Fouling Solutes 172

A.2 Effect of Cycling Time and Solution pH 176
A.3 Electrode Stability using a Two-Electrode Flow Cell 177
A.4 Raw and Normalized FTIR Spectra 179
A.5 Bulk Porosity Analysis 185
A.6 Discharging Potentials of Degradation Experiments 197
Appendix B 203
B.1 Investigating the Recovery of Capacitance and E_{PZC} regression 203
B.2 Further Probing along the Potential Domain 207
B.3 Raw and Normalized FTIR Spectra 209
B.4 Porosity Analysis 213
B.5 Discharging Potentials of Regeneration Experiments 216
Appendix C 219
C.1 Technical Drawings of the Electrochemical Cell 219

List of Tables

Table 1.1 Secondary reactions in CDI between 0 and 1.5 V vs SHE 13

Table 1.2 Secondary reactions in CDI affecting the solution pH value 20

Table 2.1 Experimental solution compositions to study the effect of organic carbon and iron on the electrode stability. All experiments were performed at room temperature with an electrolyte concentration of 1 M (NaCl), a half cycle time of 5 min and a working electrode potential of 1.2 V vs RHE 40

Table 2.2 Summary of experiments carried out to further understand the role of half cycle time and pH on the electrode degradation. All experiments were performed at room temperature with an electrolyte concentration of 1 M (NaCl) 40

Table 2.3 Summary of conditions for the experiments performed using a two-electrode electrochemical cell. All experiments were performed at room temperature with an electrolyte concentration of 17.1 mM (NaCl) 43

Table 2.4 Experimental design for screening parameter levels for electrochemical regeneration study 44

Table 2.5 Infrared absorption regions for oxygen containing functionalities 47

Table 3.1 Oxygen to carbon ratios and contact angle for electrodes at different degradation stages (i.e., C/C_0) after cycling at a working electrode potential of 1.2 V vs RHE with a half cycle time of 5 min at room temperature under anaerobic (1 M NaCl, N_2 saturated) and aerobic conditions (1 M NaCl, O_2 saturated) 69

Table 3.2 Oxygen and iron to carbon ratios for electrodes at different points of their lifetime (i.e., C/C_0) after cycling at a working electrode potential of 1.2 V vs RHE with a half cycle time of 5 min, at room temperature and different Fe^{2+} concentrations (3.58, 35.8 & 358 μM $FeCl_2$ L^{-1}). Uncertainty represents the propagation of error attributed to the averages and standard deviations obtained from three EDS elemental composition analyses.....81

Table 3.3 Contact angle for electrodes at different points of their lifetime (i.e., C/C_0) after cycling at a working electrode potential of 1.2 V vs RHE with a half cycle time of 5 min, at room temperature and different Fe^{2+} concentrations (3.58, 35.8 & 358 μM $FeCl_2$ L^{-1}). Uncertainty represents the standard error 81

Table 3.4 Oxygen to carbon ratios and contact angle for electrodes at different degradation stages (i.e., C/C_0) after cycling at a working electrode potential of 1.2 V vs RHE with a half cycle time of 5 min and at room temperature under 20 mg SRNOM L^{-1} 91

Table 4.1 ANOVA results summary for the recovery of capacitance after the application of potential-holding time treatments 126

Table 4.2 Oxygen to carbon ratios of electrodes regenerated under different potential-holding time treatments after degradation at a working electrode potential of 1.2 V vs RHE and a half cycle time of 5 min under baseline conditions (1 M NaCl, O_2 saturated) until a C/C_0 value ≈ 0.85. Uncertainty represents the propagation of error attributed to the averages and standard deviations obtained from three EDS elemental composition analyses..... 129

Table 4.3 Comparison of the oxygen to carbon ratios and contact angle of electrodes at the end-of-life (EOL), cycled with and without an electrochemical regeneration step. The electrode was cycled at a working electrode potential of 1.2 V vs RHE with a 5 min half cycle time under baseline conditions (1 M NaCl, O_2 saturated) and under presence of 20 mg SRNOM L^{-1} (1 M NaCl, O_2 saturated) or 0.2 mg Fe^{2+} L^{-1} (1 M NaCl, O_2 saturated). The electrode was regenerated at a working electrode potential of -1.68 V vs RHE and 10 s of holding time under baseline conditions (1 M NaCl, O_2 saturated)..... 144

Table A.1 Discharging potential (V vs RHE) for experiments conducted under N_2 or O_2 saturation with a working electrode potential of 1.2 V vs RHE and a half cycle time of 5 min. The discharge potential equals the open circuit potential measured at the beginning of each set of cycles..... 197

Table A.2 Discharging potential (V vs RHE) for experiments conducted under O_2 saturation with a working electrode potential of 1.2 V vs RHE and a half cycle time of 5 min in presence of 0.2 and 2.0 mg Fe^{2+} L^{-1}. The discharge potential equals the open circuit potential measured at the beginning of each set of cycles 197

Table A.3 Discharging potential (V vs RHE) for experiments conducted under N_2 or O_2 saturation with a working electrode potential of 1.2 V vs RHE and a half cycle time of 5 min in presence of 20 mg Fe^{2+} L^{-1}. The discharge potential equals the open circuit potential measured at the beginning of each set of cycles..... 198

Table A.4 Discharging potential (V vs RHE) for experiments conducted under N_2 or O_2 saturation with a working electrode potential of 1.2 V vs RHE and a half cycle time of 5 min in presence of 20 and 40 mg SRNOM L^{-1}. The discharge potential equals the open circuit potential measured at the beginning of each set of cycles..... 198

Table A.5 Discharging potential (V vs RHE) for experiments conducted under O_2 saturation with a half cycle time of 5 min under acidic (pH = 1) and alkaline (pH = 13) conditions. The working electrode potential for the experiments conducted at a pH of 1 was 1.2 V vs RHE. On the other hand, the working electrode potential for experiments conducted at a pH of 13 was 0.49 V vs RHE. The discharge potential equals the open circuit potential measured at the beginning of each cycle..... 199

Table A.6 Discharging potential (V vs RHE) for experiments conducted under O_2 saturation with a working electrode potential of 1.2 V vs RHE, a half cycle time of 5 min with and without pH adjustment after every cycle. The discharge potential equals the open circuit potential measured at the beginning of each cycle..... 200

Table B.1 Discharging potential (V vs RHE) for regeneration experiments of the 3^2-factorial design of experiments conducted under O_2 saturation and 1 M NaCl with different working electrode potentials and holding times. The discharge potential equals the open circuit potential measured at the beginning of each experiment..... 216

Table B.2 Discharging potential (V vs RHE) for regeneration experiments conducted along the potential domain conducted under O_2 saturation and 1 M NaCl with a holding time of 50 s. The discharge potential equals the open circuit potential measured at the beginning of each experiment 217

Table B.3 Discharging potential (V vs RHE) for degradation experiments performed with a working electrode potential of 1.2 V and a half cycle time of 5 min under O_2 saturation and regeneration experiments performed with a working electrode potential of -1.68 V vs RHE and a holding time of 10 s. The electrolyte concentration was 1 M NaCl. The discharge potential equals the open circuit potential measured at the beginning of each experiment..... 217

Table B.4 Discharging potential (V vs RHE) for degradation experiments performed with a working electrode potential of 1.2 V and a half cycle time of 5 min under O_2 saturation and 0.2 mg Fe^{2+} L^{-1} and regeneration experiments performed with a working electrode potential of -1.68 V vs RHE and a holding time of 10 s. The electrolyte concentration was 1 M NaCl. The discharge potential equals the open circuit potential measured at the beginning of each experiment..... 218

Table B.5 Discharging potential (V vs RHE) for degradation experiments performed with a working electrode potential of 1.2 V and a half cycle time of 5 min under O_2 saturation and 20 mg SRNOM L^{-1} and regeneration experiments performed with a working electrode potential of -1.68 V vs RHE and a holding time of 10 s. The electrolyte concentration was 1 M NaCl. The discharge potential equals the open circuit potential measured at the beginning of each experiment..... 218

List of Figures

Figure 1.1 Thesis infographic showing the general research problem, thesis objectives, key findings and the big picture implications of this study.....6

Figure 1.2 (a & b) Schematic of the production of a diluted stream by flow-by capacitive deionization of a concentrated stream upon the application of a driving force which can be (c) a constant potential or (d) a constant current.....8

Figure 1.3 Structures of different oxygen-based functionalities evolved during carbon oxidation 10

Figure 1.4 Schematic of the effluent conductivity as a function of time for a pristine and cycled electrode exhibiting an inversion peak.....14

Figure 1.5 Schematic diagrams showing the role of electrode potential at the point of zero charge in the electrosorption of ions under different applied potentials. (a) The surface negative groups impart an overall negative charge to the electrode surface and, when in solution, will spontaneously adsorb cations; (b) upon the application of a potential below the E_{PZC}, a fraction of the surface charge is balanced but overall, the net charge is negative and some cations are released; (c) when the applied potential is equal to the E_{PZC}, the net charge is zero and the double layer is at the point of minimum capacitance; and (d) when the potential applied is larger than the $E_{PZC,}$ the net charge is positive and some anions are adsorbed 17

Figure 1.6 Iron Pourbaix diagram (modified with permission from ELSEVIER from Moreno-Casillas et al. (2007) [57]) 25

Figure 2.1 (a) Compartmentalized three-electrode cell setup separated by a Nafion™ membrane; (b) Activated carbon working electrode, and (c) Teflon enclosure for the Nafion™ membrane 37

Figure 2.2 Two-electrode flow-cell assembly and ancillary equipment (pH probe, peristaltic pump, power supply, relay & multimeter) 42

Figure 2.3 Process flow diagram for the two-electrode flow-cell assembly 43

Figure 3.1 Pristine electrode cyclic voltammogram obtained at a scan rate of 1 mV s^{-1} in 17.1 mM deaerated NaCl at room temperature. Shaded area indicates integration boundaries for capacitance calculation and minimum and maximum currents used to estimate the electrode E_{PZC} 52

Figure 3.2 Pristine electrode complex impedance plane plot obtained at 0.5 V vs RHE between 350 kHz – 5 mHz in 17.1 mM deaerated NaCl at room temperature with a sine amplitude of 5 mV (3.54 mV_{RMS}) 53

Figure 3.3 SEM image of an electrode at beginning-of-life conditions showing (a) the electrode morphology (acquired with an electron accelerating voltage of 15 kV, using a spot size of 4) and (b) the electrode cross section containing the active material (i.e., activated carbon) and the carbon fiber paper used as a support (i.e., Toray® TGP-H-120) 54

Figure 3.4 Selected cyclic voltammograms obtained at 1 mV s^{-1} and 17.1 mM deaerated NaCl at room temperature for electrodes cycled under anaerobic conditions at a working electrode potential of 1.2 V vs RHE and a half cycle time of 5 min 57

Figure 3.5 Selected cyclic voltammograms obtained at 1 mV s^{-1} and 17.1 mM deaerated NaCl at room temperature for electrodes cycled under aerobic conditions at a working electrode potential of 1.2 V vs RHE and a half cycle time of 5 min 58

Figure 3.6 Normalized capacitance as a function of the number of cycles performed under N_2 or O_2 saturation at a working electrode potential of 1.2 V vs RHE with a half cycle time of 5 min and at room temperature. Error bars represent the range between two replicates.....60
Figure 3.7 E_{PZC} profiles as a function of the number of cycles performed under N_2 or O_2 saturation at a working electrode potential of 1.2 V vs RHE with a half cycle time of 5 min and at room temperature. Error bars represent the range between two replicates 61
Figure 3.8 Cumulative charge passed as a function of cycling time for the first 5 cycles performed under aerobic conditions, a working electrode potential of 1.2 V vs RHE and a half cycle time of 5 min. The red dotted line represents the potentiostatic cycling protocol used. The insert shows the data for cycle number 3 and the charge accumulated is graphically represented by the green line.....62
Figure 3.9 Charge accumulated per set of cycles performed as a function of the number of cycles performed under N_2 or O_2 saturation at a working electrode potential of 1.2 V vs RHE with a half cycle time of 5 min and at room temperature. Error bars represent the range between two replicates. Insert shows the power law relationship between the charge accumulated and cycles performed up until the 50^{th} cycle.....65
Figure 3.10 H^+ produced per set of cycles performed and final pH profiles as a function of the number of cycles performed under N_2 or O_2 saturation at a working electrode potential of 1.2 V vs RHE with a half cycle time of 5 min and at room temperature. Each set of cycles performed began with fresh, unbuffered electrolyte with a pH of 7.06 ± 0.06. Error bars represent the range between two replicates.....66

Figure 3.11 Schematic of the carbon corrosion process and its impact on the electrode surface. The two reactions occur simultaneously and independent of one another. The formation of an oxide layer reduces the amount of available active sites and the evolution of CO_2 reduces the electrode surface area 67

Figure 3.12 Normalized capacitance as a function of the number of cycles performed under O_2 saturation at a working electrode potential of 1.2 V vs RHE with a half cycle time of 5 min and different Fe^{2+} concentrations (from $FeCl_2$) at room temperature. Gray markers provided as a reference for baseline results. Error bars represent the range between two replicates 72

Figure 3.13 (a) Cyclic voltammograms obtained at 1 mV s^{-1} in 17.1 mM deaerated NaCl and (b) complex impedance plane plots obtained at 0.5 V vs RHE between 350 kHz – 5 mHz in 17.1 mM deaerated NaCl for the electrode at the beginning-of-life (BOL) and after 5 cycles at 1.2 V vs RHE with a half cycle time of 5 min in the presence of 20 mg Fe^{2+} L^{-1} (358 μM $FeCl_2$ L^{-1}) 73

Figure 3.14 E_{PZC} profiles as a function of the number of cycles performed under O_2 saturation at a working electrode potential of 1.2 V vs RHE with a half cycle time of 5 min and different Fe^{2+} concentrations (from $FeCl_2$) at room temperature. Gray markers provided as a reference for baseline results. Error bars represent the range between two replicates 74

Figure 3.15 Charge accumulated per set of cycles performed as a function of the number of cycles performed under O_2 saturation at a working electrode potential of 1.2 V vs RHE with a half cycle time of 5 min and different Fe^{2+} concentrations (from $FeCl_2$) at room temperature. Gray markers provided as a reference for baseline results. Error bars represent the range between two replicates. Insert shows the power law relationship between the charge accumulated and cycles performed 75

Figure 3.16 H^+ produced per set of cycles performed and final pH profiles as functions of the number of cycles performed under O_2 saturation at a working electrode potential of 1.2 V vs RHE with a half cycle time of 5 min and different Fe^{2+} concentrations (from $FeCl_2$) at room temperature. Each set of cycles performed began with fresh, unbuffered electrolyte with a pH of 6.47 ± 0.10, 5.63 ± 0.08 and 5.45 ± 0.14, for the solutions containing 2.0, 2.0 and 20 mg Fe^{2+} L^{-1}, respectively. Gray markers provided as a reference for baseline results. Error bars represent the range between two replicates 76

Figure 3.17 SEM image (acquired with an electron accelerating voltage of 15 kV, using a spot size of 4) of an electrode at end-of-life conditions showing the electrode morphology after cycling under aerobic conditions in presence of 0.2 mg Fe^{2+} L^{-1}, at a working electrode potential of 1.2 V vs RHE and a half cycle time of 5 min.....78

Figure 3.18 SEM image (acquired with an electron accelerating voltage of 15 kV, using a spot size of 4) of an electrode at end-of-life conditions showing the electrode morphology after cycling under aerobic conditions in presence of 2.0 mg Fe^{2+} L^{-1}, at a working electrode potential of 1.2 V vs RHE and a half cycle time of 5 min.....79

Figure 3.19 SEM image (acquired with an electron accelerating voltage of 15 kV, using a spot size of 4) of an electrode at end-of-life conditions showing the electrode morphology after cycling under aerobic conditions in presence of 20 mg Fe^{2+} L^{-1}, at a working electrode potential of 1.2 V vs RHE and a half cycle time of 5 min.....80

Figure 3.20 Change in transmittance of for the O – H and C – O absorption bands for electrodes cycled with a working electrode potential of 1.2 V vs RHE, a half cycle time of 5 min under aerobic conditions and 0.2 mg Fe^{2+} L^{-1} (3.58 μM $FeCl_2$ L^{-1}) at different degradation stages relative to that exhibited by an electrode at EOL conditions. The dotted lines represent the actual change in transmittance. The solid lines are given to facilitate the visualization of the trend of the data 82
Figure 3.21 Change in transmittance of for the O – H and C – O absorption bands for electrodes cycled with a working electrode potential of 1.2 V vs RHE, a half cycle time of 5 min under aerobic conditions and 2.0 mg Fe^{2+} L^{-1} (35.8 μM $FeCl_2$ L^{-1}) at different degradation stages relative to that exhibited by an electrode at EOL conditions. The dotted lines represent the actual change in transmittance. The solid lines are given to facilitate the visualization of the trend of the data 83
Figure 3.22 Normalized capacitance as a function of the number of cycles performed under O_2 saturation at a working electrode potential of 1.2 V vs RHE with a half cycle time of 5 min, at room temperature and different SRNOM concentrations. Gray markers provided as a reference for baseline results. Error bars represent the range between two replicates.....86
Figure 3.23 E_{PZC} profiles as a function of the number of cycles performed under O_2 saturation at a working electrode potential of 1.2 V vs RHE with a half cycle time of 5 min, at room temperature and different SRNOM concentrations. Gray markers provided as a reference for baseline results. Error bars represent the range between two replicates.....87

Figure 3.24 Charge accumulated per set of cycles performed as a function of the number of cycles performed under O_2 saturation at a working electrode potential of 1.2 V vs RHE with a half cycle time of 5 min, at room temperature and different SRNOM concentrations. Gray markers provided as a reference for baseline results. Error bars represent the range between two replicates. Insert shows the power law relationship between the charge accumulated and cycles performed 89

Figure 3.25 H^+ produced per set of cycles performed and final pH profiles as functions of the number of cycles performed under O_2 saturation at a working electrode potential of 1.2 V vs RHE with a half cycle time of 5 min and at room temperature. Each set of cycles performed began with fresh, unbuffered electrolyte with a pH of 4.19 ± 0.02 and 3.85 ± 0.01 for the solutions containing 20 and 40 mg SRNOM L^{-1}, respectively. Gray markers provided as a reference for baseline results. Error bars represent the range between two replicates.....90

Figure 3.26 Change in transmittance of for the O – H and C – O absorption bands for electrodes cycled with a working electrode potential of 1.2 V vs RHE, a half cycle time of 5 min under aerobic conditions and 20 mg SRNOM L^{-1} at different degradation stages relative to that exhibited by an electrode at EOL conditions. The dotted lines represent the actual change in transmittance. The solid lines are given to facilitate the visualization of the trend of the data 91

Figure 3.27 Normalized capacitance as a function of the number of cycles performed under O_2 saturation with a half cycle time of 5 min, at room temperature and different electrolyte pH conditions. The working electrode potential for the experiments conducted at a pH of 1 and with and without pH adjustment was 1.2 V vs RHE. On the other hand, the working electrode potential for experiments conducted at a pH of 13 was 0.49 V vs RHE. In all cases, the discharge potential was equal to the open circuit potential measured at the beginning of each set of cycles (see Appendix A). The initial electrolyte pH of the experiments with and without pH adjustment was 7. Error bars represent the range between two replicates 97

Figure 3.28 E_{PZC} profiles as a function of the number of cycles performed under O_2 saturation with a half cycle time 5 min, at room temperature, an electrolyte concentration of 1 M (NaCl) and different electrolyte pH conditions. The working electrode potential for the experiments conducted at a pH of 1 and with and without pH adjustment was 1.2 V vs RHE. On the other hand, the working electrode potential for experiments conducted at a pH of 13 was 0.49 V vs RHE. In all cases, the discharge potential was equal to the open circuit potential measured at the beginning of each set of cycles (see Appendix A). The initial electrolyte pH of the experiments with and without pH adjustment was 7. Error bars represent the range between two replicates 98

Figure 3.29 Normalized capacitance as a function of time the working electrode was held at a potential of 1.2 V vs RHE for different half cycle times. Cycles performed under O_2 saturation, an electrolyte concentration of 1 M (NaCl) and at room temperature. Error bars represent the range between two replicates 100

Figure 3.30 E_{PZC} profile as a function of time at a working electrode potential of 1.2 V vs RHE for different half cycle times. Cycles performed under O_2 saturation, an electrolyte concentration of 1 M (NaCl) and at room temperature. Error bars represent the range between two replicates 101

Figure 3.31 Schematic of the development of the oxide layer as a result of the carbon corrosion process. Evolution of CO_2 occurs simultaneously and over time becomes the main Faradaic reaction. The formation of an oxide layer reduces the amount of available active sites and the evolution of CO_2 reduces the electrode surface area..... 102

Figure 3.32 (a) Final pH and (b) final H^+ concentration at the end of every set of cycles performed with a working electrode potential of 1.2 V vs RHE for different half cycle times. Cycles performed under O_2 saturation, an electrolyte concentration of 1 M (NaCl) and at room temperature. Error bars represent the range between two replicates 104

Figure 3.33 Equivalent circuit of the two-electrode cell setup..... 106

Figure 3.34 (a) Normalized capacitance, and (b) E_{PZC} profiles as functions of the number of cycles performed under N_2 saturation at a cell potential of 1.3 V and 1.8 V with a half cycle time of 5 min, an electrolyte concentration of 17.1 mM (1000 mg NaCl L^{-1}) and at room temperature. The electrodes were discharged at zero voltage (i.e., $V_{cell} = 0$). Error bars represent the range between two replicates..... 107

Figure 3.35 Electrode potential distribution throughout cycling (1^{st}-30^{th} cycle) with a cell potential of 1.3 V and a half cycle time of 5 min performed under N_2 saturation using an electrolyte concentration of 17.1 mM (1000 mg NaCl L^{-1}) at room temperature. The electrodes were discharged at zero voltage (i.e., $V_{cell} = 0$)..... 108

Figure 3.36 Electrode potential distribution throughout cycling (31st-65th cycle) with a cell potential of 1.3 V and 1.8 V and a half cycle time of 5 min performed under N_2 saturation using an electrolyte concentration of 17.1 mM (1000 mg NaCl L^{-1}) at room temperature. The electrodes were discharged at zero voltage (i.e., $V_{cell} = 0$) 109

Figure 3.37 (a) Normalized capacitance, and (b) E_{PZC} profiles as a function of the number of cycles performed under O_2 saturation at a cell potential of 1.3 V with a half cycle time of 5 min, an electrolyte concentration of 17.1 mM (1000 mg NaCl L^{-1}) and at room temperature. The electrodes were discharged at zero voltage (i.e., $V_{cell} = 0$). Error bars represent the range between two replicates 111

Figure 3.38 Electrode potential distribution throughout cycling (1st-20th cycle) with a cell potential of 1.3 V with a half cycle time of 5 min performed under O_2 saturation using an electrolyte concentration of 17.1 mM (1000 mg NaCl L^{-1}) at room temperature. The electrodes were discharged at zero voltage (i.e., $V_{cell} = 0$) 112

Figure 3.39 Electrode potential distribution throughout cycling (21st-40th cycle) with a cell potential of 1.3 V with a half cycle time of 5 min performed under O_2 saturation using an electrolyte concentration of 17.1 mM (1000 mg NaCl L^{-1}) at room temperature. The electrodes were discharged at zero voltage (i.e., $V_{cell} = 0$) 113

Figure 3.40 (a) Normalized capacitance and (b) E_{PZC} profiles as functions of the number of cycles performed under O_2 saturation at a cell potential of 1.0 V with a half cycle time of 5 min, an electrolyte concentration of 17.1 mM (1000 mg NaCl L^{-1}) and at room temperature. The electrodes were discharged at zero voltage (i.e., $V_{cell} = 0$). Error bars represent the range between two replicates 115

Figure 3.41 Electrode potential distribution throughout cycling (1^{st}-50^{th} cycle) with a cell potential of 1.0 V with a half cycle time of 5 min performed under O_2 saturation using an electrolyte concentration of 17.1 mM (1000 mg NaCl L^{-1}) at room temperature. The electrodes were discharged at zero voltage (i.e., $V_{cell} = 0$) 116

Figure 3.42 Electrode potential distribution throughout cycling (51^{st}-100^{th} cycle) with a cell potential of 1.0 V with a half cycle time of 5 min performed under O_2 saturation using an electrolyte concentration of 17.1 mM (1000 mg NaCl L^{-1}) at room temperature. The electrodes were discharged at zero voltage (i.e., $V_{cell} = 0$) 117

Figure 4.1 Schematic showing the potential profile of the cycling and electrochemical regeneration protocol. The electrode was degraded at a potential of 1.2 V vs RHE with a half cycle time of 5 min until a value of $C/C_0 \approx 0.85$. The electrochemical regeneration consisted of a reductive potential, between -0.4 and -2.1 V vs RHE for holding times of 10, 50 and 90 s under baseline conditions (1 M NaCl, O_2 saturated). Electrode discharge was conducted with a working electrode potential equal to the open circuit potential measured at the beginning of the experiment which was, on average, 0.560 ± 0.001 V vs RHE..... 123

Figure 4.2 Capacitance recovered as a function of holding time and applied potential. Error bars indicate the range between two replicates..... 124

Figure 4.3 E_{PZC} recovery as a function of holding time and applied potential. Error bars indicate the range between two replicates..... 125

Figure 4.4 Cyclic voltammograms obtained in deaerated 17.1 mM NaCl at room temperature and 1 mV s^{-1} for the pristine (BOL), cycled (degraded to $C/C_0 \approx 0.85$) and regenerated electrodes under selected potential-holding time treatments. Diagrams are enlarged to exhibit the change in the capacitive response and shift of the E_{PZC} 127

Figure 4.5 Complex impedance plane plots obtained at 0.5 V vs RHE between 350 kHz – 5 mHz in 17.1 mM deaerated NaCl at room temperature with a sine amplitude of 5 mV (3.54 mV_{RMS}) for the pristine (BOL), cycled (degraded to $C/C_0 \approx 0.85$) and regenerated electrodes under selected potential-holding time treatments 127

Figure 4.6 Change in transmittance of for the O – H and C – O absorption bands for electrodes regenerated at -2.1 and -0.4 V vs RHE and a holding time of 10 s relative to that exhibited by a degraded electrode to a C/C_0 value $\approx$ 0.85. The dotted lines represent the actual change in transmittance. The solid lines are given to facilitate the visualization of the trend of the data . 130

Figure 4.7 Change in transmittance of for the O – H and C – O absorption bands for electrodes regenerated at -2.1 and -0.4 V vs RHE and a holding time of 90 s relative to that exhibited by a degraded electrode to a C/C_0 value $\approx$ 0.85. The dotted lines represent the actual change in transmittance. The solid lines are given to facilitate the visualization of the trend of the data . 130

Figure 4.8 (a) Capacitance and (b) E_{PZC} recovered as a function of applied potential for different potential-holding time treatments. Additional 50 s holding time points along the potential domain. Results from the 3^2-factorial DOE provided as reference as a way of contrast. The electrodes were degraded at a potential of 1.2 V vs RHE with a half cycle time of 5 min under baseline conditions (1 M NaCl, O_2 saturated) until a value of $C/C_0 \approx 0.85$. Error bars indicate the range between two replicates..... 132

Figure 4.9 (a) Cyclic voltammograms obtained in deaerated 17.1 mM NaCl at room temperature and 1 mV s^{-1} for the pristine (BOL), cycled (degraded to $C/C_0 \approx 0.85$) and regenerated electrodes cycled under an applied potential of -1.68 V vs RHE and 50 s of holding time under baseline conditions (1 M NaCl, O_2 saturated) and (b) Complex impedance plane plots obtained at 0.5 V vs RHE between 350 kHz – 5 mHz in 17.1 mM deaerated NaCl at room temperature with a sine amplitude of 5 mV (3.54 mV_{RMS}) for the pristine (BOL), cycled (degraded to $C/C_0 \approx 0.85$) and regenerated electrodes under an applied potential of -1.68 V vs RHE and 50 s of holding time under baseline conditions (1 M NaCl, O_2 saturated) 133

Figure 4.10 Normalized capacitance as a function of the number of cycles performed after degradation at a working electrode potential of 1.2 V vs RHE under baseline conditions (1 M NaCl, O_2 saturated) with a half cycle time of 5 min and after a regeneration step at a working electrode potential of -1.68 V vs RHE and 10 s of holding time under baseline conditions (1 M NaCl, O_2 saturated). Results are contrasted against cycling experiments without the use of a regeneration step. Error bars represent the range between two replicates 135

Figure 4.11 E_{PZC} profile as a function of the number of cycles performed after degradation at a working electrode potential of 1.2 V vs RHE under baseline conditions (1 M NaCl, O_2 saturated) with a half cycle time of 5 min and after a regeneration step at a working electrode potential of -1.68 V vs RHE and 10 s of holding time under baseline conditions (1 M NaCl, O_2 saturated). Results are contrasted against cycling experiments without the use of a regeneration step. Error bars represent the range between two replicates 136

Figure 4.12 Normalized capacitance as a function of the number of cycles performed after degradation at a working electrode potential of 1.2 V vs RHE under presence of 0.2 mg Fe^{2+} L^{-1} (1 M NaCl, O_2 saturated) with a half cycle time of 5 min and after a regeneration step at a working electrode potential of -1.68 V vs RHE and 10 s of holding time under baseline conditions (1 M NaCl, O_2 saturated). Results are contrasted against cycling experiments without the use of a regeneration step. Error bars represent the range between two replicates 137
Figure 4.13 E_{PZC} profile as a function of the number of cycles performed after degradation at a working electrode potential of 1.2 V vs RHE under baseline conditions under presence of 0.2 mg Fe^{2+} L^{-1} (1 M NaCl, O_2 saturated) with a half cycle time of 5 min and after a regeneration step at a working electrode potential of -1.68 V vs RHE and 10 s of holding time under baseline conditions (1 M NaCl, O_2 saturated). Results are contrasted against cycling experiments without the use of a regeneration step. Error bars represent the range between two replicates..... 138
Figure 4.14 Normalized capacitance as a function of the number of cycles performed after degradation at a working electrode potential of 1.2 V vs RHE under presence of 20 mg SRNOM L^{-1} (1 M NaCl, O_2 saturated) with a half cycle time of 5 min and after a regeneration step at a working electrode potential of -1.68 V vs RHE and 10 s of holding time under baseline conditions (1 M NaCl, O_2 saturated). Results are contrasted against cycling experiments without the use of a regeneration step. Error bars represent the range between two replicates 139

Figure 4.15 E_{PZC} profile as a function of the number of cycles performed after degradation at a working electrode potential of 1.2 V vs RHE under presence of 20 mg SRNOM L^{-1} (1 M NaCl, O_2 saturated) with a half cycle time of 5 min and after a regeneration step at a working electrode potential of -1.68 V vs RHE and 10 s of holding time under baseline conditions (1 M NaCl, O_2 saturated). Results are contrasted against cycling experiments without the use of a regeneration step. Error bars represent the range between two replicates 140

Figure 4.16 Complex impedance plane plots obtained at 0.5 V vs RHE between 350 kHz – 5 mHz in 17.1 mM deaerated NaCl at room temperature with a sine amplitude of 5 mV (3.54 mV_{RMS}) for consecutive degradation and regeneration steps. The electrode was degraded under baseline conditions (1 M NaCl, O_2 saturated) at a working electrode potential of 1.2 V vs RHE with a 5 min half cycle time and regenerated at a working electrode potential of -1.68 V vs RHE and 10 s of holding time under baseline conditions (1 M NaCl, O_2 saturated)..... 141

Figure 4.17 Complex impedance plane plots obtained at 0.5 V vs RHE between 350 kHz – 5 mHz in 17.1 mM deaerated NaCl at room temperature with a sine amplitude of 5 mV (3.54 mV_{RMS}) for consecutive degradation and regeneration steps. The electrode was degraded under presence of 20 mg SRNOM L^{-1} (1 M NaCl, O_2 saturated) at a working electrode potential of 1.2 V vs RHE with a 5 min half cycle time and regenerated at a working electrode potential of -1.68 V vs RHE and 10 s of holding time under baseline conditions (1 M NaCl, O_2 saturated)..... 142

Figure 4.18 Complex impedance plane plots obtained at 0.5 V vs RHE between 350 kHz – 5 mHz in 17.1 mM deaerated NaCl at room temperature with a sine amplitude of 5 mV (3.54 mV_{RMS}) for consecutive degradation and regeneration steps. The electrode was degraded under presence of 0.2 mg Fe^{2+} L^{-1} (1 M NaCl, O_2 saturated) at a working electrode potential of 1.2 V vs RHE with a 5 min half cycle time and regenerated at a working electrode potential of -1.68 V vs RHE and 10 s of holding time under baseline conditions (1 M NaCl, O_2 saturated) 143

Figure 4.19 Change in transmittance of for the O – H and C – O absorption bands for electrodes at EOL conditions cycled with a working electrode potential of 1.2 V vs RHE and a half cycle time of 5 min with a regeneration step at -1.68 V vs RHE and a holding time of 50 s relative to that exhibited by the corresponding electrode at EOL conditions cycled with a working electrode potential of 1.2 V vs RHE and a half cycle time of 5 min without a regeneration step. The dotted lines represent the actual change in transmittance. The solid lines are given to facilitate the visualization of the trend of the data 145

Figure A.1 Normalized capacitance as a function of the number of cycles performed under N_2 or O_2 saturation at a working electrode potential of 1.2 V vs RHE, a half cycle time of 5 min and 20 mg Fe^{2+} L^{-1}. Gray markers provided as a reference for aerobic results. Error bars represent the range between two replicates 172

Figure A.2 E_{PZC} profiles as a function of the number of cycles performed under N_2 or O_2 saturation at a working electrode potential of 1.2 V vs RHE, a half cycle time of 5 min and 20 mg Fe^{2+} L^{-1}. Gray markers provided as a reference for aerobic results. Error bars represent the range between two replicates 173

Figure A.3 Normalized capacitance as a function of the number of cycles performed under N_2 or O_2 saturation at a working electrode potential of 1.2 V vs RHE, a half cycle time of 5 min and 20 mg SRNOM L^{-1}. Error bars represent the range between two replicates 174
Figure A.4 E_{PZC} profiles as a function of the number of cycles performed under N_2 or O_2 saturation at a working electrode potential of 1.2 V vs RHE, a half cycle time of 5 min and 20 mg SRNOM L^{-1}. Error bars represent the range between two replicates 175
Figure A.5 Normalized capacitance and E_{PZC} as functions of time at a working electrode potential of 1.2 V vs RHE for a half cycle time of 250 min. Cycles performed under O_2 saturation and an electrolyte strength of 1 M (NaCl). Error bars represent the range between two replicates 176
Figure A.6 (a) Normalized capacitance and (b) E_{PZC} profiles as functions of the number of cycles performed under O_2 saturation and 0.2 mg Fe^{2+} L^{-1} at a cell potential of 1.3 V and a half cycle time of 5 min. Error bars represent the range between two replicates 177
Figure A.7 Electrode potential distribution throughout cycling (1^{st}-35^{th} cycle) with a cell potential of 1.3 V and a half cycle time of 5 min performed under O_2 saturation and 0.2 mg Fe^{2+} L^{-1} using an electrolyte concentration of 17.1 mM (1000 mg NaCl L^{-1}) at room temperature. The electrodes were discharged at zero voltage (i.e., $V_{cell} = 0$) 178
Figure A.8 FTIR spectra of electrodes at different degradation stages after cycling under anaerobic conditions at a working electrode potential of 1.2 V vs RHE and a half cycle time of 5 min ... 179
Figure A.9 FTIR spectra of electrodes at different degradation stages after cycling under aerobic conditions at a working electrode potential of 1.2 V vs RHE and a half cycle time of 5 min ... 179

Figure A.10 FTIR spectra of electrodes at different degradation stages after cycling under aerobic conditions and 0.2 mg Fe^{2+} L^{-1} at a working electrode potential of 1.2 V vs RHE and a half cycle time of 5 min 180
Figure A.11 FTIR spectra of electrodes at different degradation stages after cycling under aerobic conditions and 2.0 mg Fe^{2+} L^{-1} at a working electrode potential of 1.2 V vs RHE and a half cycle time of 5 min 181
Figure A.12 FTIR spectra of electrodes at different degradation stages after cycling under aerobic conditions and 20 mg Fe^{2+} L^{-1} at a working electrode potential of 1.2 V vs RHE and a half cycle time of 5 min 181
Figure A.13 FTIR spectra of electrodes at different degradation stages after cycling under aerobic conditions and 20 mg SRNOM L^{-1} at a working electrode potential of 1.2 V vs RHE and a half cycle time of 5 min 182
Figure A.14 Normalized FTIR spectra of electrodes at different degradation stages after cycling under anaerobic conditions at a working electrode potential of 1.2 V vs RHE and a half cycle time of 5 min. Electrode at end-of-life used as the reference for normalization 182
Figure A.15 Normalized FTIR spectra of electrodes at different degradation stages after cycling under aerobic conditions at a working electrode potential of 1.2 V vs RHE and a half cycle time of 5 min. Electrode at end-of-life used as the reference for normalization 183
Figure A.16 Normalized FTIR spectra of electrodes at different degradation stages after cycling under aerobic conditions and 0.2 mg Fe^{2+} L^{-1} at a working electrode potential of 1.2 V vs RHE and a half cycle time of 5 min. Electrode at end-of-life used as the reference for normalization 183

Figure A.17 Normalized FTIR spectra of electrodes at different degradation stages after cycling under aerobic conditions and 2.0 mg Fe^{2+} L^{-1} at a working electrode potential of 1.2 V vs RHE and a half cycle time of 5 min. Electrode at end-of-life used as the reference for normalization 184

Figure A.18 Normalized FTIR spectra of electrodes at different degradation stages after cycling under aerobic conditions and 20 mg Fe^{2+} L^{-1} at a working electrode potential of 1.2 V vs RHE and a half cycle time of 5 min. Electrode at end-of-life used as the reference for normalization 184

Figure A.19 Normalized FTIR spectra of electrodes at different degradation stages after cycling under aerobic conditions and 20 mg SRNOM L^{-1} at a working electrode potential of 1.2 V vs RHE and a half cycle time of 5 min. Electrode at end-of-life used as the reference for normalization 185

Figure A.20 Raw and processed images used to estimate the bulk porosity of a pristine electrode 185

Figure A.21 Raw and processed images used to estimate the bulk porosity of an electrode at EOL conditions after cycling under aerobic conditions with a working electrode potential of 1.2 V vs RHE and a half cycle time of 5 min..... 188

Figure A.22 Raw and processed images used to estimate the bulk porosity of an electrode at EOL conditions after cycling under aerobic conditions and 0.2 mg Fe^{2+} L^{-1} with a working electrode potential of 1.2 V vs RHE and a half cycle time of 5 min..... 190

Figure A.23 Raw and processed images used to estimate the bulk porosity of an electrode at EOL conditions after cycling under aerobic conditions and 20 mg Fe^{2+} L^{-1} with a working electrode potential of 1.2 V vs RHE and a half cycle time of 5 min..... 192
Figure A.24 Raw and processed images used to estimate the bulk porosity of an electrode at EOL conditions after cycling under aerobic conditions and 20 mg SRNOM L^{-1} with a working electrode potential of 1.2 V vs RHE and a half cycle time of 5 min..... 195
Figure B.1 Cyclic voltammograms obtained in deaerated 17.1 mM NaCl at room temperature and 1 mV s^{-1} for the pristine (BOL), cycled (degraded to $C/C_0 \approx 0.85$) and regenerated electrodes under different potential-holding time treatments. Diagrams are enlarged to exhibit the change in the capacitive response and shift of the E_{PZC} 203
Figure B.2 Complex impedance plane plots obtained at 0.5 V vs RHE between 350 kHz – 5 mHz in 17.1 mM deaerated NaCl at room temperature with a sine amplitude of 5 mV (3.54 mV_{RMS}) for the pristine (BOL), cycled (degraded to $C/C_0 \approx 0.85$) and regenerated electrodes under different potential-holding time treatments 205
Figure B.3 Cyclic voltammograms obtained in deaerated 17.1 mM NaCl at room temperature and 1 mV s^{-1} for the pristine (BOL), cycled (degraded to $C/C_0 \approx 0.85$) and regenerated electrodes under different reductive potentials and a holding time of 50 s. Diagrams are enlarged to exhibit the change in the capacitive response and shift of the E_{PZC}..... 207
Figure B.4 Complex impedance plane plots obtained at 0.5 V vs RHE between 350 kHz – 5 mHz in 17.1 mM deaerated NaCl at room temperature with a sine amplitude of 5 mV (3.54 mV_{RMS}) for the pristine (BOL), cycled (degraded to $C/C_0 \approx 0.85$) and regenerated electrodes under different reductive potentials and a holding time of 50 s..... 208

Figure B.5 FTIR spectra of electrodes regenerated at -2.1, -1.25 and -0.4 V vs RHE and a holding time of 10 s after cycling at a working electrode potential of 1.2 V vs RHE and a half cycle time of 5 min 209
Figure B.6 FTIR spectra of electrodes regenerated at -2.1, -1.25 and -0.4 V vs RHE and a holding time of 50 s after cycling at a working electrode potential of 1.2 V vs RHE and a half cycle time of 5 min 209
Figure B.7 FTIR spectra of electrodes regenerated at -2.1, -1.25 and -0.4 V vs RHE and a holding time of 90 s after cycling at a working electrode potential of 1.2 V vs RHE and a half cycle time of 5 min 210
Figure B.8 FTIR spectra at the end-of-life of electrodes cycled with a working electrode potential of 1.2 V vs RHE and a half cycle time of 5 min and an added regenerative step with working electrode potential of -1.68 V vs RHE and a holding time of 10 s 210
Figure B.9 Normalized FTIR spectra of regenerated electrodes with different reductive potentials and a holding time of 10 s after cycling to a C/C_0 value ≈ 0.85 at a working electrode potential of 1.2 V vs RHE and a half cycle time of 5 min. Electrode at a C/C_0 value ≈ 0.85 used as the reference for normalization 211
Figure B.10 Normalized FTIR spectra of regenerated electrodes with different reductive potentials and a holding time of 50 s after cycling to a C/C_0 value ≈ 0.85 at a working electrode potential of 1.2 V vs RHE and a half cycle time of 5 min. Electrode at a C/C_0 value ≈ 0.85 used as the reference for normalization 211

Figure B.11 Normalized FTIR spectra of regenerated electrodes with different reductive potentials and a holding time of 90 s after cycling to a C/C_0 value ≈ 0.85 at a working electrode potential of 1.2 V vs RHE and a half cycle time of 5 min. Electrode at a C/C_0 value ≈ 0.85 used as the reference for normalization 212

Figure B.12 Normalized FTIR spectra of electrodes at the end-of-life of electrodes cycled with a working electrode potential of 1.2 V vs RHE and a half cycle time of 5 min with a regeneration step at -1.68 V vs RHE and a holding time of 50 s Electrode at the end-of-life cycled with a working electrode potential of 1.2 V vs RHE and a half cycle time of 5 min used as the reference for normalization 212

Figure B.13 Raw and processed images used to estimate the bulk porosity of an electrode degraded to a C/C_0 value ≈ 0.85 213

Figure B.14 Raw and processed images used to estimate the bulk porosity of an electrode regenerated at a potential of -1.68 V vs RHE and a holding time of 50 s after cycling under aerobic conditions with a working electrode potential of 1.2 V vs RHE and a half cycle time of 5 min until a C/C_0 value ≈ 0.85 215

Figure C.1 Isometric view and dimensions in centimeters (top view) of the lid of the working electrode side of the electrochemical cell 219

Figure C.2 Isometric view and dimensions in centimeters (top view) of the lid of the two-electrode flow-cell 219

Figure C.3 Isometric view and dimensions in centimeters (top view) of the lid of the counter electrode side of the electrochemical cell 220

Figure C.4 Isometric view and dimensions in centimeters (top view) of the electrode holder .. 220

Figure C.5 Schematic and dimensions in centimeters of the compartments of the electrochemical cell 221

List of Symbols

Symbol	Description	Units
Latin Letters		
C	Specific Capacitance	$F\ g^{-1}$
E	Potential	V
E_{PZC}	Potential at the Point of Zero Charge	V
i	Current	A
m	Mass of Active Material	g
R_{ct}	Charge Transfer Resistance	Ω
t	Time	s
Greek Letters		
α	Significance Level	
γ	Activity Coefficient	
ν	Scan Rate	$mV\ s^{-1}$
Superscript		
0	Standard Condition	
Subscript		
0	Initial State	
1	Integration Lower Limit	
2	Integration Upper Limit	

List of Abbreviations

Abbreviation	Description
ACC	Activated Carbon Cloth
ANOVA	Analysis of Variance
BET	Brunauer-Emmett-Teller
BOL	Beginning of Life
BSA	Bovine Serum Albumin
CDI	Capacitive Deionization
CE	Counter Electrode
CPE	Constant Phase Element
CV	Cyclic Voltammogram
DC	Direct Current
DMA	Dimethylacetamide
DOM	Dissolved Organic Matter
ED	Electrodialysis
EDL	Electrical Double Layer
EDLCs	Electrical Double Layer Capacitors
EDS	Energy Dispersive Spectra
EOL	End of Life
FTIR	Fourier Transform Infrared Spectroscopy
GO	Graphene Oxide
HCT	Half Cycle Time
HER	Hydrogen Evolution Reaction
IHSS	International Humic Substances Society
LOD	Limit of Detection
MCDI	Membrane Capacitive Deionization
MED	Multi-effect Distillation
MSF	Multistage Flash Distillation
NOM	Natural Organic Matter
OER	Oxygen Evolution Reaction
OMC	Ordered Mesoporous Carbon
PEMFC	Proton Exchange Membrane Fuel Cell
POU	Point of Use
PTFE	Polytetrafluoroethylene
PVDF	Polyvinylidene Fluoride
RHE	Reversible Hydrogen Electrode
RO	Reverse Osmosis

Abbreviation	Description
SAC	Salt Adsorption Capacity
SEM	Scanning Electron Microscopy
SHE	Standard Hydrogen Electrode
TDS	Total Dissolved Solids
TEM	Transmission Electron Microscopy
TOC	Total Organic Carbon
ToF-SIMS	Time of Flight Secondary Ion Mass Spectrometry
TPD	Temperature Program Desorption
WE	Working Electrode
XPS	X-Ray Photoelectron Spectroscopy

Acknowledgements

First and foremost, I would like to express my gratitude towards my supervisors, Dr. David P. Wilkinson and Dr. Madjid Mohseni, for their support and guidance throughout this project. I appreciate the opportunity to work under their supervision. I want to thank them for their patience and thoughtful feedback. As part of their groups, I was exposed to many invaluable experiences that helped me in my development as a person and research scientist.

I especially appreciate the time and feedback given by Dr. Naoko Ellis and Dr. Dan Bizzotto as part of my examining committee.

I would also like to thank IC-IMPACTS for funding this project and providing over the years of my doctoral studies, opportunities to network and learn from researchers and industry partners. As an international student and former Four-Year Fellowship holder, I am grateful for the financial support awarded by the University of British Columbia.

Many thanks to the CHBE staff: Doug Yuen, Graham Liebelt, Richard Ryoo, Sarah Jackson, Miles Garcia, Marlene Chow & Lori Tanaka. Special thanks to RES'EAU staff: Keyvan Maleki, Heidi Backous, Candace Cook & Rebecca Smith.

I appreciate the time & support given by Jenny Lai & Lan Kato from Earth & Ocean Sciences, and Benjamin Herring from the Shared Instrument Facility at the Chemistry Department.

To the group members, in Dr. Wilkinson's and Dr. Mohseni's lab that I met over the years; thanks for your mentorship, support and feedback over the different stages of my project.

I recognize also the outstanding work performed by two summer students: Nick and Mantaj. Thanks for your dedication.

To my friends: Pranav, Ruben, Saad, Sean and Sid; thanks for your support and the good times. I am extremely proud of your endeavors and achievements. I know you will succeed, no matter what you do.

My most sincere appreciation to Universidad de Costa Rica for sponsoring my doctoral studies. It is an honour to be joining my alma mater. Special thanks to Esteban Durán and Adolfo Ulate, for their mentorship and willingness to help. I also recognize and appreciate the continuous and vital assistance given by the Office of International Affairs staff of Universidad de Costa Rica, in particular Vivian Madrigal.

I am filled with gratitude towards my Mom, Dad and Sister. Your support was crucial to get over the lows, which were many and sometimes lengthy as I struggled, learned and grew up over the past 7 years. Thanks for your patience, for listening and mostly, for always believing in me.

With love to my parents and sister

For your endless love and support

Chapter 1: Introduction

1.1 Motivation

Utilization of non-traditional water resources, such as saline water reservoirs, can be used to aid the supply of fresh water for human consumption. In the upcoming decades, exploitation of these resources will be fundamental to address the impact of climate change and increased human activity on water demand. A substantial amount of water, containing relatively low concentration of Total Dissolved Solids (TDS), can be found in groundwater reservoirs. These reserves, classified as brackish waters, contain between 1 000 to 15 000 mg TDS L^{-1} [1], [2] (as a reference, seawater contains TDS levels above 35 000 mg L^{-1} [3]). Before human consumption, saline waters must be treated to TDS concentration levels under 500 mg L^{-1} (i.e., aesthetical objective below taste threshold) [4]. Among different desalination technologies, reverse osmosis (RO) is the most common and widely applied process throughout the world. Other common technologies include multistage flash distillation (MSF), multi-effect distillation (MED) and electrodialysis (ED) [5], [6]. However, considering that in RO, MSF and MED water is removed from the solutes, justifying their application in low salinity solutions becomes somewhat of a challenge from an energy and economic standpoint. This has served as a driver to find less energy intensive processes to deionize brackish waters. Closely related to ED, Capacitive Deionization (CDI) has recently received a great deal of attention, in light of the advances and cost reduction in highly-porous carbonaceous materials [6].

In CDI, water is deionized by momentarily storing ions (i.e., by electrosorption) in the electrical double layer (EDL) formed at the surface of a porous electrode when there is excess of charge on its surface. The charge (i.e., negative at the cathode and positive at the anode) induced at the electrode surface is counterbalanced by ions in a diffuse layer of charge, as described by the

Gouy-Chapman-Stern model [7]. In this way, CDI cyclically operates between charging-discharging steps in which, by the application or absence of an external driving force (i.e., potential or current), a diluted or concentrated stream can be produced, respectively. However, despite its entirely electrostatic operational principle, the occurrence of Faradaic or secondary processes cannot be neglected under typical operational conditions. Common parasitic reactions include oxygen reduction and carbon oxidation (i.e., carbon corrosion). Other plausible processes such as oxygen and chlorine evolution are prevented by working below the thermodynamic potential for water oxidation (E^0 = 1.23 V vs SHE).

Of the secondary processes that occur in CDI, carbon corrosion is, perhaps, the one that affects the electrodes lifetime the most [8]–[14]. As carbon oxidation proceeds with continuous cycling, adverse changes occur to electrochemical properties such as capacitance and potential at the point of zero charge (E_{PZC}) and to morphological features of the electrode such as surface functional groups and porous network. These changes, in practice, result in a continuous decrease in system performance (i.e., salt adsorption). Moreover, when natural water sources are considered, the presence of other solutes (i.e., water matrix composition) reduce the availability of active sites, thereby inducing fouling or scaling on the electrode surface. Substances that have been found to have such influence include natural organic matter (NOM) and iron based compounds [15]–[19]. Conveniently, the impact of fouling and scaling has been shown to be, for the most part, reversible by performing a chemical rinse [15], [20], [21]. Nonetheless, the contribution of these processes to the change in the electrochemical properties and morphological features of the electrode is unknown. In contrast, the loss of performance attributed to carbon corrosion is a continuous process which seems only to be mitigated by operating the cell at lower cell potentials which, on a practical level, reduces the desalination capability of the system. An

interesting concept, yet to be discussed in the CDI literature, is to regenerate the electrode surface, by reduction of the oxygen containing functionalities formed during the cycling process. A very limited number of reports suggest that oxidized carbon can be, to some extent, reduced through electrochemical methods [22]–[25]. Despite the discrepancies found between these reports, the possibility of extending the electrodes lifetime using an *in-situ* method, makes the study of this approach valuable for the CDI community.

1.2 Research Scope

This study aims to investigate the long-term stability and electrochemical regeneration of electrodes used for CDI of brackish waters. Loss of electrode stability is primarily attributed to the occurrence of carbon oxidation. Electrode stability is related to the retention of electrode performance. Thus, this is associated with the electrode properties that contribute to the electrosorption of ions such as capacitance and electrode potential at the point of zero charge. In some cases, a performance metric such as salt adsorption capacity includes the overall contribution of many properties into one practical measurement. To a lesser extent, fouling and scaling processes also affect the electrode performance. The first part of this research examines the effect of known fouling and scaling agents on the changes that occur, throughout the electrode life, to important electrochemical and morphological properties of the electrodes used in CDI. Secondly, this study explores the utilization of electrochemical regeneration techniques to alleviate the impact of carbon oxidation. This is done firstly by investigating the recovery of electrochemical and morphological properties under different potential-time treatments. Subsequently, a regenerative step is included as part of the cycling protocol to assess its effect on the electrode long-term cyclability.

Literature has demonstrated that electrode stability is negatively affected by an increase in cycling potential. As a result, in this study, degradation experiments were conducted at a working electrode potential of 1.2 V vs RHE. By charging the electrode at this potential, the occurrence of carbon oxidation was facilitated while still maintaining conditions that did not favoured oxygen evolution from the water electrolysis reaction. More importantly, from a practical point of view, it caused the electrode decay to occur over a reasonable amount of time. Upon the baseline findings herein presented, future investigations should prioritize the study of other cycling potentials (i.e., above and below 1.2 V vs RHE) to deeper the understanding of the effect of carbon oxidation on the changes occurring to the electrode electrochemical and morphological properties under typical CDI conditions. Subsequently, the effect of complex electrolytes (i.e., with supplementary amounts of fouling or scaling agents) at different concentrations and cycling potentials relevant to CDI could be investigated. Finally, given the expected differences in electrode degradation at different cycling potentials, it would be valuable to assess the effectiveness of the application of electrochemical regeneration approaches to electrodes degraded at different cycling potentials.

1.3 Thesis Layout

This thesis manuscript consists of five chapters

- Chapter 1 provides the motivation and scope of this study. Furthermore, it presents a survey of the literature relevant to the main objectives of this research. First, the occurrence of carbon corrosion in electrochemical systems is reviewed. Subsequently, attention is given to the impact of carbon oxidation on different parameters of the CDI process. In addition, the challenge of fouling and scaling in CDI and the available strategies to mitigate the occurrence of secondary processes are discussed. The

literature review finishes with an overview of different efforts carried with the objective to electrochemically reduce and regenerate the electrode surface. Chapter 1 concludes with the presentation of the identified knowledge gaps, research objectives and the significance and novelty of this research.

- Chapter 2 presents the experimental methods utilized to fulfill the thesis objectives.
- Chapter 3 covers the study of the electrode stability under different conditions. Specifically, the influence of dissolved oxygen, fouling and scaling agents, cycling time and pH on electrochemical and morphological properties are presented and discussed. Subsequently, results obtained using a two-electrode cell configuration are presented as a way of contrast to those obtained using a three-electrode cell.
- Chapter 4 covers the investigation of electrochemical regeneration approaches for electrodes used in CDI. First, the results of a preliminary factorial design of experiments are presented and discussed. Then, the influence of a regenerative approach on the electrode stability is evaluated under different electrolyte compositions.
- Chapter 5 provides a summary of the main findings of this research and a list of recommendations to extend the work presented in this thesis.

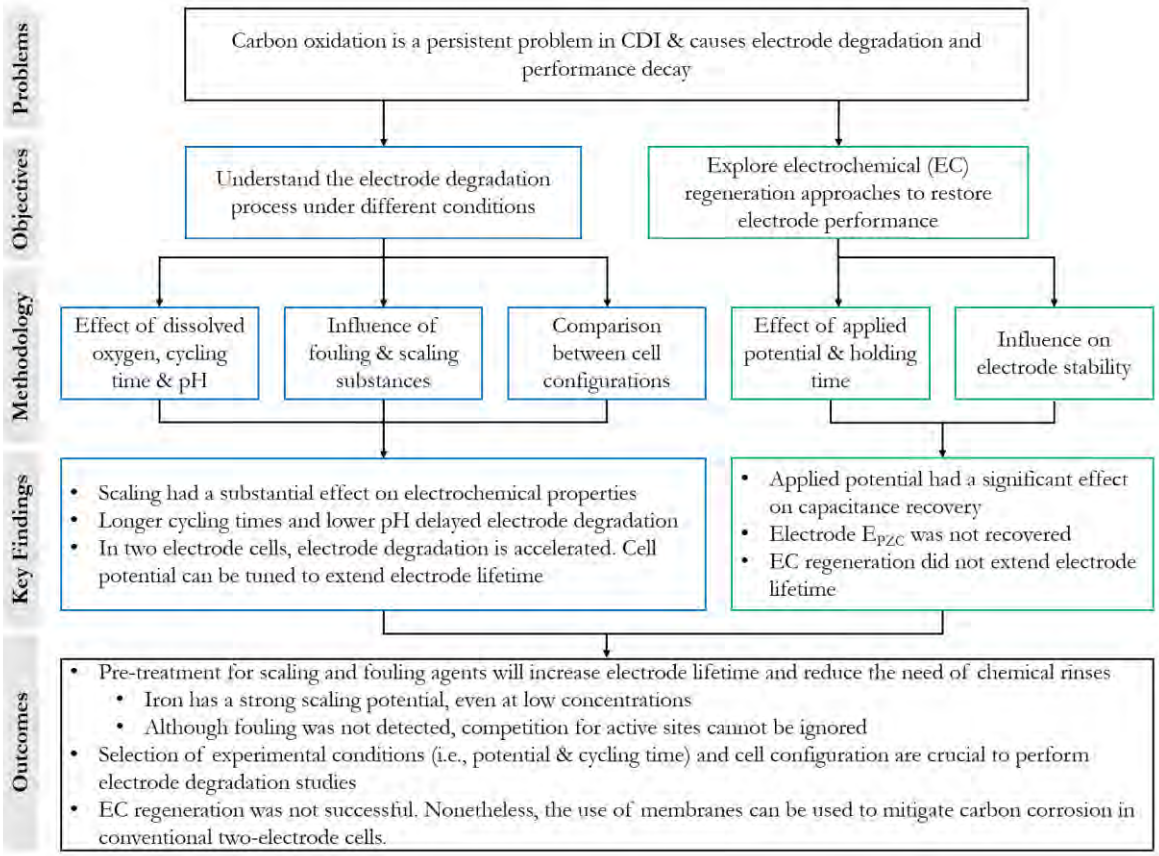

Figure 1.1 Thesis infographic showing the general research problem, thesis objectives, key findings and the big picture implications of this study

1.4 Literature Review

1.4.1 Application of Capacitive Deionization (CDI)

CDI is an electrochemical technology that is used to remove TDS from water through electrosorption. With the aid of an external power source, CDI utilizes high surface area electrodes to momentarily fix ions in the electrical double layer (EDL). The migration of ions towards the electrode surface is based on the electrostatic attraction to oppositely charged surfaces. As mentioned earlier, the ion arrangement (i.e., co-ions and counterions) near the electrode surface can be described using the Gouy-Chapman-Stern model [7]. The driving force behind the process of electrosorption can be current or potential. In practice, while a galvanostatic or potentiostatic hold is maintained, the conductivity of the process effluent decreases until all active sites, at the

electrode surface, are saturated. At this point, desalination stops, and the cell is discharged. Usual metrics of performance include salt adsorption capacity (i.e., mg TDS removed per gram of electrode mass), charge efficiency (i.e., mg TDS removed per charge passed) and energy consumption (i.e., kWh m^{-3} of freshwater produced). Depending on the type of CDI cell being used (i.e., conventional CDI or membrane CDI), the protocol for electrode discharge might change. For instance, in conventional CDI, electrodes are usually discharged at zero voltage (V_{cell} = 0 V), and the migration of the ions from the electrode surface to the bulk of the electrolyte is strictly diffusional. To expedite the process, inverted potentials or currents can be used to repel the counterions from the electrode surface. Nonetheless, in conventional CDI this option is rarely used, as there exists the possibility of electrosorption of ions once the polarity or current of the electrode is inverted. In contrast, in membrane CDI (MCDI), reverse voltage discharge or reverse current discharge can be used without considering counterion electrosorption during the discharge step. In MCDI, ion exchange membranes are placed in front of the electrodes and only allow the release of counterions.

There are several architectures for CDI application. The most studied is the flow-by architecture. In this design, water flows between the electrodes, which are separated by a non-conductive spacer to prevent short-circuiting. Another common CDI cell architecture is flow-through. In this cell, the electrolyte is pushed through the electrodes, taking advantage of their porous network. Other designs involve the use of flow electrodes and static electrode designs such as the "swiss-roll" architecture. More details about these can be found in Porada et al. (2013) [26] and Suss et al. (2015) [27].

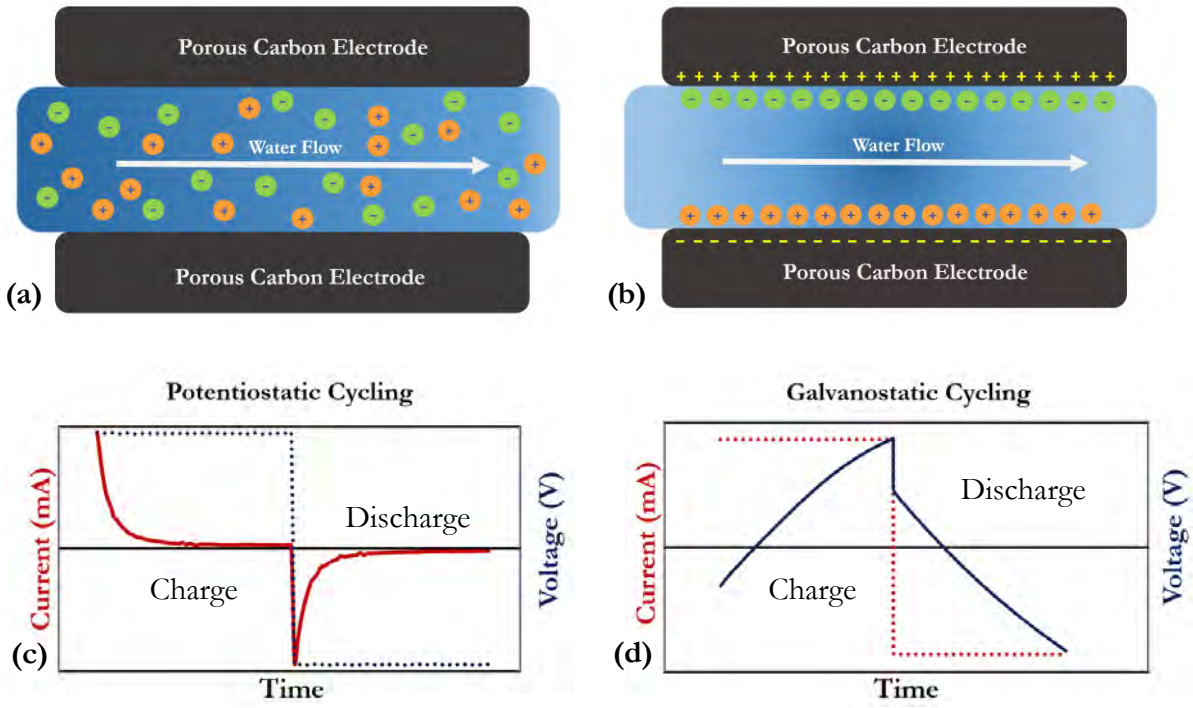

Figure 1.2 (a & b) Schematic of the production of a diluted stream by flow-by capacitive deionization of a concentrated stream upon the application of a driving force which can be (c) a constant potential or (d) a constant current

1.4.2 Carbon Oxidation in Electrochemical Systems

In CDI, carbon oxidation (E^0 = 0.207 V vs RHE [28]) is categorized as a Faradaic or secondary process. Parasitic reactions consume charge, thus reducing the efficiency of the primary process where charge is intended to be utilized. This reaction is also present in other electrochemical systems such as proton exchange membrane fuel cells (PEMFC) [29]–[38] and supercapacitor applications [39]. As is the case with CDI, the occurrence of carbon oxidation in these systems, upon continuous cycling, has a detrimental impact on performance and has been extensively studied in the PEMFC community. Despite the evident differences in applications, the experience gained in these fields can serve as a steppingstone to further understand the effect of carbon oxidation on CDI systems.

Kangasniemi et al. (2004) [31] demonstrated that a variety of surface oxygen functionalities (see Figure 1.3) can be formed during carbon oxidation. In particular, carboxylic acids, lactones, anhydrides, carbonyls, quinones, phenols and ethers were distinguished by means of thermogravimetric analysis coupled with mass spectrometry. Moreover, the electroactive quinone-hydroquinone pair was observed to increase with cycling time (in cyclic voltammetry around 0.55 V vs RHE). On the other hand, the rate of surface oxidation was observed to be faster during the first 16 hours of cycling, then gradually decreasing over the 120 hours of experimentation. During this period, the amount of surface oxygen was determined, by x-ray photoelectron spectroscopy (i.e., XPS), to increase from an initial value of 4.8% to 8.5% and 9.3% after 16 and 120 hours of testing at 1.2 V, respectively. As a result of carbon corrosion, the wettability or hydrophilic nature of the material (10% PTFE Vulcan XC-72) increased. This was determined by a decrease in the contact angle from 147 ± 3 (pristine) to 111 ± 7 degrees (after 120 h of operation at 1.2 V). Maass et al. (2008) [35] observed that, at constant potential, the corrosion rate of Ketjenblack EC300J® decreased with time following an exponential decay. This behaviour was most evident in the experiments carried out at 0.7 and 1.0 V (45 min of holding time). The semi-stable corrosion rate observed, as time progressed, was attributed to the formation and accumulation of a rather stable oxide layer. In comparison, corrosion rates under potentio-dynamic conditions were found to be larger than those observed at constant potential. Moreover, corrosion rates increased when the electrode potential window of the sweep was expanded to include lower and higher potentials. Above 1 V, unfavourable conditions prevailed due to the high overpotential for carbon corrosion. On the other hand, between 60 to 650 mV, generation of surface defects were likely to occur as a result of chemical oxidation by action of H_2O_2 (e.g., C_{surf} + n H_2O_2 → w C_{surf}=O + x $C_{surf}O_2$ + y C_{surf}OH + z C_{surf}OOH, where n, w, x, y and z are the

stoichiometric coefficients). To reduce the corrosion process, the authors explored the use of graphitized supports. Although the mechanism of oxidation still occurred through the same steps, their findings showed lower oxidation rates under potentio-dynamic conditions when compared with the baseline electrode, which were attributed to the more homogenous surface, with lower number of defects of the graphitized carbon used.

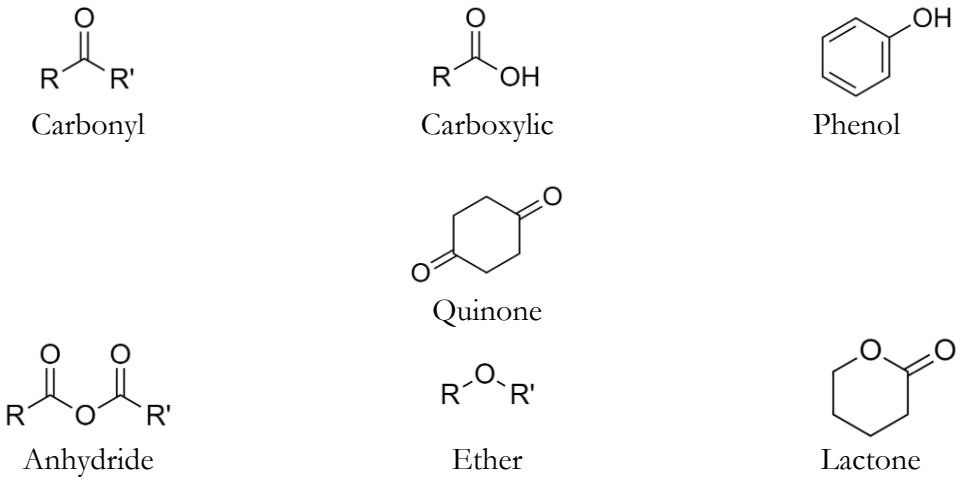

Figure 1.3 Structures of different oxygen-based functionalities evolved during carbon oxidation

Similar carbon oxidation resistance with a graphitized support was observed by Macauley et al. (2018) [38]. When compared with a high surface area support, the corrosion rate exhibited by the graphitized carbon was substantially lower, especially at cell potentials above 0.9 V. For instance, at a cell potential of 1.2 V, the corrosion rate for a high surface area support was between 5 and 6 times higher than the one of the graphitized supports. Avasarala et al. (2010) [36], in their work with Vulcan XC-72, used cyclic voltammetry and showed that the current density at 1.2 V vs RHE gradually decreased with cycling (i.e., 0 to 16 hours or 0 to 1200 cycles in 0.1 M $HClO_4$ at 50 mV s^{-1}). Through XPS analysis of pristine and cycled electrodes, the authors found a decrease in carbon content of approximately 20% and a marginal increase in oxygen content. Thus, the authors proposed that carbon was oxidized to CO_2 predominantly without the formation of

surface oxides. However, this claim could have been strengthened with evidence of the elemental content of intermediate samples (i.e., at different stages of cycling). Analysis and deconvolution of the XPS spectra indicated the presence of lactones, carboxylic, ether, hydroxyl and ketone functionalities. It was also found that C−O groups dominated over C=O and C−OO after cycling at 50 mV s^{-1} in 0.1 M $HClO_4$ for 16 hours. In contrast, when corrosion was held at a constant potential (i.e., 0.9 and 1.2 V vs RHE) coverage by C=O predominated over C−O and C−OO groups. In addition, there were differences in the amount of surface oxygen when comparing the two constant potential protocols. After treatment at 1.2 V, the amount of surface oxygen decreased (~10%) when compared to the pristine electrode but, when treated at 0.9 V an increase (~30%) in surface oxygen was noted. However, when the electrode was cycled between 0 and 1.2 V vs RHE, the oxygen content increased 3-fold. He et al. (2016) [39], in their work with carbon based electrical double layer capacitors (EDLCs) in 1 M Li_2SO_4, attributed the simultaneous evolution of CO and CO_2 (at cell voltages above 0.6 V vs SHE) to the oxidation of naturally occurring oxygen groups in Kynol (i.e., an activated carbon fabric). Through analysis of temperature program desorption (TPD) data, the formation of CO_2 was assigned to the presence of anhydrides and lactones while the formation of CO derived from the existence of quinones and carbonyl groups.

From these studies it is possible to see that carbon corrosion will proceed, to different extents, in many of the readily available carbonaceous materials typically used in electrochemical research and applications. Moreover, the potential range to which these materials were exposed to, include the operational window typically used in CDI process (i.e., below 1.23 V vs SHE). Considering the on and off nature of CDI, the applied charging potential (or cell potential), the electrolyte condition and composition; there exists the possibility of variation in the degradation

rate of the electrode, the formation of different intermediate oxides and the loss of carbon if the potential is driven high enough to desorb the surface oxides as CO_2. Altogether, these processes will translate into a progressive, likely irreversible, loss of performance and a reduced electrode lifetime.

1.4.3 Evidence of Faradaic Reactions in CDI

Although carbon oxidation is perhaps the major contributor to performance decay and charge inefficiency in CDI, there are a few other secondary reactions that exist in CDI. Traditionally, CDI systems operate below the water electrolysis potential (E^0 = 1.23 V vs SHE); thus, the formation of chlorine from chloride ions and oxygen from water are unlikely processes to occur. Below the water electrolysis potential, oxygen reduction (E^0 = 0.69 V vs SHE) (i.e., on the cathodic side of the cell) consumes charge and generates hydrogen peroxide as a product which can be also reduced to water [40]–[42]. He et al. (2016) [41] reported the formation of H_2O_2, in a 5 mM NaF solution, to peak around 60 μM at an applied potential of 1.2 V. The rate of production was observed to increase as the applied potential changed from 0.5 to 1.5 V and was, consequently, accompanied by a decrease in dissolved oxygen. At high cell potentials (i.e., 1.2 and 1.5 V), H_2O_2 concentration gradually decreased over the charging step due to reductive processes (see eqn. 1.5). It was further reduced during the discharge step at 0 V, due to adsorption processes. Noteworthy, the behaviours presented in this study correspond to those occurring during the first cycle (HCT of 30 min). It is likely, as cycling proceeds, that these profiles will exhibit different behaviour.

Table 1.1 Secondary reactions in CDI between 0 and 1.5 V vs SHE

Anodic Reactions	E^0 vs SHE	
$2Cl^- \rightarrow Cl_2 + 2e^-$	1.36	(1.1)
$2H_2O \rightarrow O_2 + 4H^+ + 4e^-$	1.23	(1.2)
$C_{surf} + 2H_2O \rightarrow CO_2 + 4H^+ + 4e^-$	0.7 - 0.9	(1.3)
$C_{surf} + H_2O \rightarrow CO_{surf} + 2H^+ + 2e^-$	0.21	(1.4)
Cathodic Reactions		
$H_2O_2 + 2H^+ + 2e^- \rightarrow 2H_2O$	1.78	(1.5)
$O_2 + 4H^+ + 4e^- \rightarrow 2H_2O$	1.23	(1.6)
$O_2 + 2H^+ + 2e^- \rightarrow H_2O_2$	0.69	(1.7)
$2H^+ + 2e^- \rightarrow H_2$	0.00	(1.8)

Carbon corrosion, on the other hand, has been shown to cause a decrease in surface area [8], [9], [11], [17], a relocation of the potential at the point of zero charge (E_{PZC}) [8]–[10], [43]–[45], and an increase in resistivity [8], [9]. Moreover, pH variations [8], [9], [14], [40], [41], [43], [46]–[49], uneven charge/discharge cycles (i.e., charge accumulation) [14], [46], [49], [50] and the evolution of oxygen-containing functional groups [11], [40], [49], [51] (i.e., C=O) at the electrode surface have been used to demonstrate the existence and extent of carbon corrosion and other Faradaic processes.

1.4.3.1 Inversion Effect & Reduction of Surface Area

Evidence of performance degradation has been observed as early as 5 days for a flow-through cell (i.e., the solution is forced to pass through the electrodes) equipped with activated carbon cloth electrodes (ACC) and operated at 0.9 V with a cycling time of 1 hour. Here, Bouhadana et al. (2011) [49] observed that the incorporation of oxygen containing surface groups was accompanied by a behaviour described as a "functionality inversion". The marker for this phenomenon was noted to be a sudden increase in conductivity at the beginning of the charging step with an increasing magnitude over time (see Figure 1.4). The manifestation of the inversion

effect was seen to be dependent on the applied potential, as noted by Cohen et al. (2013) [8]. At a potential of 0.7 V, the appearance of the inversion effect was delayed until the 14th day of operation. In addition, this study demonstrated that the positive electrodes are the ones most significantly impacted by the long-term cycling. In comparison to the cathodes, the anodes showed a greater content of surface oxygen groups, a larger reduction in their surface area (approx. 15% smaller) and an increase in resistivity (approx. two orders of magnitude) after prolonged cycling.

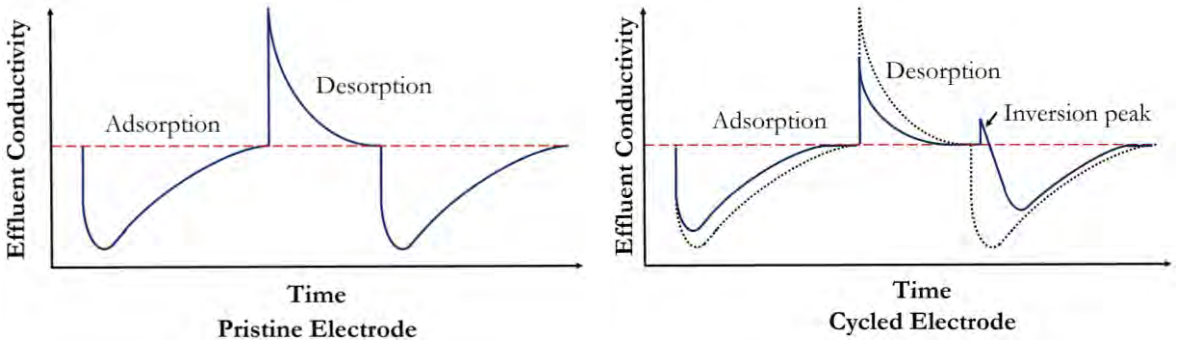

Figure 1.4 Schematic of the effluent conductivity as a function of time for a pristine and cycled electrode exhibiting an inversion peak

CDI cell architecture was also shown to have an effect on the appearance of the inversion effect. Cohen et al. (2015) [9] showed that for flow-by CDI architecture (i.e., solution flow parallel to the electrodes), the inversion point was reached after 18 days of cycling while using the same voltage window (i.e., 0 to 0.9 V) and electrode material (i.e., ACC) as in their previous study (i.e., [8]). In the flow-through design, the solution is forced to flow from one electrode to the other. Hence, it was hypothesized that the accelerated oxidation was a result of the forced interaction between alkaline and acidic species [28] formed at the cathode and anode [52], respectively.

The study by Cohen et al. (2015) [9] also demonstrated that the cycling protocol also affects the cell stability. By using the periodic interchange in the polarization of the electrodes, the salt adsorption capacity (SAC) of a flow-through cell (same as in [8]), operated between -0.9 and

0.9 V, remained almost unchanged after 34 days of operation. In comparison, the cell with no potential shifting was observed to decay after 5 days of operation [8].

Duan et al. (2015) [11] also observed the inversion effect when studying ordered mesoporous carbons (OMC) with different properties (i.e., surface area, porosity, oxygen content). After 50 cycles at a cell potential of 1.2 V (half cycle time or HCT of 30 min), BET analysis revealed a reduction in surface area of approx. 4% and 14% which was coupled with a decrease in total pore volume of approx. 6% and 22% for the cathode and anode, respectively. On the other hand, Haro et al. (2011) [17] compared the loss of surface area of three different types of carbon electrodes: carbon aerogel, activated carbon and carbon cloth. After 20 cycles at a cell potential of 1.0 V (charging time of 80 min), the surface area determined through BET analysis was reduced by approx. 6%, 22% and 25% for carbon aerogel, activated carbon and carbon cloth electrodes, respectively.

It is important to point out that these studies were carried using a two-electrode cell configuration. In this sense, although the potential difference between the anode and cathode remains constant throughout the experiment, the potential distribution among the electrodes might not be equal. More importantly, the relative position of the cell potential difference and the individual electrode potential on the thermodynamic scale cannot be controlled. However, by aid of a reference electrode, it is possible to know the relative thermodynamic position. Despite this limitation, the use of a two-electrode cell is an appropriate representation of a practical CDI cell.

1.4.3.2 Relocation of the Electrode E_{PZC}

The electrode E_{PZC} is a vital parameter in CDI (see Figure 1.5). As the applied potential is bounded by the water electrolysis potential, the difference between the anodic potential and the anode E_{PZC} indicates the usable potential window for anion electrosorption. In the same way, the

difference between the cathodic potential and the cathode E_{PZC} denotes the useful potential window for cation electrosorption. Tobias & Soffer (1983) [53] demonstrated, by modifying carbon black to different extents, that the electrode E_{PZC} became progressively positive as the carbon surface oxidizes. Gao et al. (2014) [10] observed a shift close to 440 mV for carbon xerogel electrodes cycled at a cell potential of 1.2 V (HCT of 30 min) for 248 cycles and then cycled with inversed polarity at -1.2 V for another 272 cycles. Carbon cloth, in contrast, showed a positive relocation of approx. 260 mV after 32 hours of operation at a cell potential of 1.2 V [43]. In this study, Gao et al. (2016) [43] also showed that there was a negligible shift of the cathodes E_{PZC}. In a similar way, Lu et al. (2017) [45] reported no modification of the cathode E_{PZC} and a change of about 400 mV for the anode cycled at a cell potential of 1.2 V for 121 cycles (activated carbon electrodes and a HCT of 20 min). It is noteworthy that these studies presented the changes in E_{PZC} by contrasting values at the beginning-of-life (BOL) and at a distant point in the electrode lifetime (sometimes at end-of-life). Hence, the profile change of the E_{PZC} with cycling is not resolved. Knowing this could reveal important insights regarding the incorporation of oxygen at the electrode surface.

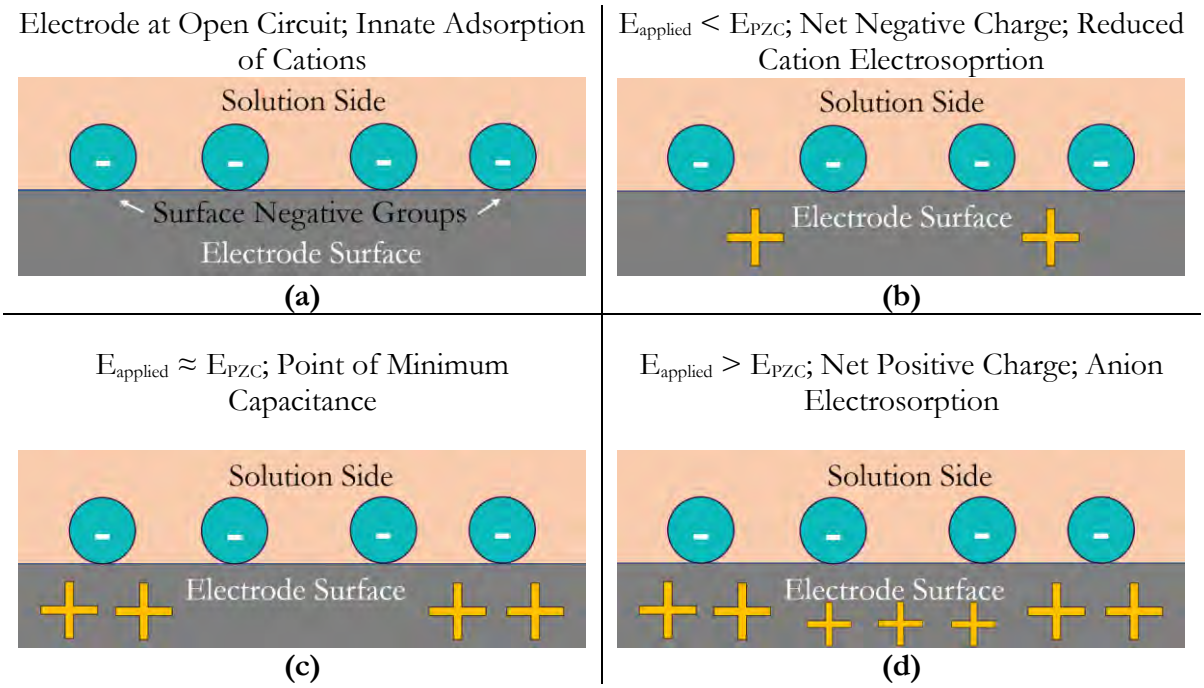

Figure 1.5 Schematic diagrams showing the role of electrode potential at the point of zero charge in the electrosorption of ions under different applied potentials. (a) The surface negative groups impart an overall negative charge to the electrode surface and, when in solution, will spontaneously adsorb cations; (b) upon the application of a potential below the E_{PZC}, a fraction of the surface charge is balanced but overall, the net charge is negative and some cations are released; (c) when the applied potential is equal to the E_{PZC}, the net charge is zero and the double layer is at the point of minimum capacitance; and (d) when the potential applied is larger than the E_{PZC}, the net charge is positive and some anions are adsorbed

1.4.3.3 Asymmetrical Charge Flow

The existence of Faradaic reactions can be demonstrated by analysis of the cumulative charge that is passed and released during the charging and discharging portions of the cycle. Since CDI is a purely electrostatic method, in the absence of secondary reactions, there should be no charge disparity between the charging and discharging step. Bouhadana et al. (2011) [14] utilized this concept to demonstrate the effect of cell potential and dissolved oxygen on the occurrence of parasitic processes. In their study, accumulation of charge became apparent at a cell potential of 0.7 V and became larger as potential increased to 0.9 and 1.1 V. In contrast, when the cell was

cycled at 0.5 V, the behaviour of charge accumulation was symmetrical. Under the same potential conditions, but under nitrogen saturation, asymmetric results were observed only at a cell potential of 1.1 V. Moreover, Lee et al. (2010) [46] reported that the amount of charge passed during the adsorption stage, with cell potentials of 0.8, 1.0, 1.2 and 1.5 V, was approx. 2.5, 2.3, 2.2 and 2.2 times larger, respectively, than that passed during the desorption stage. It is noteworthy that in this study, asymmetric charge-discharge times were used (i.e., 10/5 min), therefore the analysis of charge was, to some extent, incomplete.

1.4.3.4 Solution pH

Variations in pH during CDI operation can also be used as a marker for the occurrence of Faradaic processes. The reactions presented in Table 1.2 emphasize that H^+, depending on the applied potential, can be generated and consumed, resulting in deviations from the initial solution pH (see equations 1.3, 1.4, 1.5 & 1.7). For instance, Bouhadana et al. (2011) [14] showed that pH variations (measured inline at the outlet of the CDI cell) followed a similar behaviour as that shown by the accumulation of charge (i.e., changes in pH due to the occurrence of parasitic reactions increased with charging potential, and were larger for experiments performed under air saturation). For instance, at a cell potential of 1.1 V, the pH profiles under air and nitrogen saturation displayed a slight difference. In particular, at the end of the cycle, experiments under air saturation displayed consistently higher pH values. At the other tested potentials, variations in pH under air saturation were significantly larger than those observed under nitrogen saturation.

Although the authors did not discuss this behaviour, in air saturated systems, the process of oxygen reduction (see equation 1.7) occurs during the charging stage. Furthermore, the resulting hydrogen peroxide can be reduced following equation 1.5. These two processes consume H^+ and therefore will increase the pH of the system and may be, to some extent, responsible for the

behavior observed. On the other hand, in nitrogen saturated systems, oxygen can be generated through water electrolysis (see equation 1.2). In addition, a relatively small amount could be trapped in the electrode porous network and can be reduced to hydrogen peroxide. Given the reasonably less amount of oxygen in the system, the consumption of H^+ will be lower than that of the experiments performed under air saturation, thus explaining the lower pH observed, at the end of each cycle, in the nitrogen saturated experiments. Furthermore, during the charging stage, the pH value was more acidic for experiments conducted under air saturation. This was an indication that oxidation processes were occurring at a greater extent under air saturation. On the other hand, no data was provided about the potential distribution of the electrodes. It would have been valuable to determine the individual electrode potential (vs. a reference electrode) to elucidate whether the presence of oxygen and the occurrence of reduction processes influenced the potential attributed to the anode. In particular, a larger anodic potential will increase the production of H^+ as a result of a larger driving force for oxidation processes. The redistribution of applied potential was observed by Pillay and Newman (1996) [54], in their work with electrical double layer capacitors. This behaviour was explained to be caused by the system response to the difference in kinetics of the Faradaic processes occurring at both ends of the cell in order to increase the coulombic efficiency. Clearly, the presence of dissolved oxygen influences the oxidation processes occurring on the cell anode. However, its effect seems to be primarily indirect (i.e., because of the processes occurring at the cell cathode).

Table 1.2 Secondary reactions in CDI affecting the solution pH value

Anodic Reactions	E^0 vs SHE	
$2H_2O \rightarrow O_2 + 4H^+ + 4e^-$	1.23	(1.2)
$C_{surf} + 2H_2O \rightarrow CO_2 + 4H^+ + 4e^-$	0.7 - 0.9	(1.3)
$C_{surf} + H_2O \rightarrow CO_{surf} + 2H^+ + 2e^-$	0.21	(1.4)
Cathodic Reactions		
$H_2O_2 + 2H^+ + 2e^- \rightarrow 2H_2O$	1.78	(1.5)
$O_2 + 2H^+ + 2e^- \rightarrow H_2O_2$	0.69	(1.7)

In addition, Cohen et al. (2013) [8] observed that cycling at a charging potential of 0.7 V had a negligible impact on the pH (measured inline at the outlet of the CDI cell) amplitude change over 13 days of cycling. In addition, the final pH after every cycle stayed close to a value of 6.5. In contrast, when the cell was cycled at a potential of 0.9 V, not only did the final pH decreased gradually, but also the extent of change increased over time. The latter seemed to stabilize around the 6th to 7th day of operation. The potential dependence of the outlet pH stream was also studied by Tang et al. (2017) [40]. After a 15-minute charging step, at cell potentials of 0.9, 1.2 and 1.5 V the pH varied from an initial pH close to 6.5 to values of ~5, ~4.5 and ~4, respectively. After the discharge step of 15 min at 0 V, the outlet stream returned to its initial value only for the case at 0.9 V and remained slightly acidic for the cases at 1.2 and 1.5 V. Different results were reported by He et al. (2016) [41]. In this study, at potentials of 0.5 and 0.9 V, the pH (measured in the recycling reservoir) progressively increased during the charging stage from an initial value of ~6.5 to final values of ~7.5 and ~9.8, respectively. For tests at potentials of 1.2 and 1.5 V, an initial increase in pH was then followed by a slight and rapid decrease, respectively. The authors attributed this behaviour to the dominant role of oxygen and hydrogen peroxide reduction at the cathode at low cell potentials (i.e., 0.5 and 0.9 V). Conversely, depletion of dissolved oxygen and exacerbation of the carbon corrosion process, generated an abundance of protons thus leading to

the decrease in pH at higher cell potentials (1.2 and 1.5 V). In a similar manner Lee et al. (2010) [46] noted that at cell potentials of 0.8 and 1.0 V, the pH (measured inline at the outlet of the CDI cell) of the outflow gradually increased from an initial value of 8 and leveled at a value of ~10. In contrast, at cell potentials of 1.2 and 1.5 V, after a relatively short period of pH increase, the resulting solution exhibited values close to 8 and 4, respectively, at the end of the charging step and the decay profile resembled the one reported by He et al. (2016) [41].

As mentioned previously, studies performed using a two-electrode cell provide results which are representative of the behaviour of practical cells. However, addressing fundamental questions requires of careful potential control to maintain, as much as possible, a constant driving force for the electrosorption and secondary processes. The contrasting results reported by the different studies surveyed, suggest that more effort is required to clarify the change and, if any, the role of pH during the CDI process.

On the whole, the effect of carbon corrosion can be observed and monitored through practical and fundamental measurements. The discovery and investigation of the inversion effect through conductivity measurements revealed the importance of applied potential, the cycling protocol (i.e., zero voltage discharge vs reverse polarization), and cell architecture (i.e., flow-by vs flow-through) on the long-term stability of the CDI process. On the other hand, the investigation of changes in surface area and relocation of the electrode E_{PZC} highlighted that some carbonaceous materials, such as carbon aerogels, exhibit a relatively stronger oxidation resistance (i.e., either lower shift in E_{PZC} or higher retention of surface area as cycling progresses, or both). Analysis of the cumulative charge and pH underlined the role of applied potential and dissolved oxygen. In this study, given the limitation arising from the electrode dimensions (refer to section 2.1) and, consequently the small amount of active material in each electrode (i.e., very low SAC), tracking

the inversion effect was not possible. Nonetheless, other degradation markers, such as the change in oxygen content, evolution of oxygen containing surface groups and the corresponding shift in the electrode E_{PZC} were used to monitor electrode degradation (refer to sections 2.2 and 2.5). Moreover, analysis of cumulative charge allowed one to further understand the process of carbon corrosion.

1.4.4 Fouling and Scaling in CDI

The unwanted deposition of compounds (either dissolved or suspended, organic or inorganic) present in natural waters is one of the many challenges associated with the application of CDI for water treatment. With time, the effectiveness of the operation will be hindered, requiring corrective measurements to continue operation.

In conventional CDI, lack of an ion selective membrane allows different charged species to migrate into the charged porous structure of the electrodes. As a result, competition for active sites is unavoidable and due to the properties of the species such as size and charge, they can interact with the surface and can be also influenced by the local environment in the pores (i.e., pH). For instance, Mossad & Zou (2013) [15] observed that iron as Fe^{3+} and humic acid salt, usually used as a NOM surrogate, affected the TDS removal efficiency and freshwater production rate. Over a period of 30 hours, the presence of 1.8 mg Fe^{3+} L^{-1} reduced the former by approx. 8% and the latter by around 200 mL min^{-1}. Moreover, it was determined that approx. 30% of the inflowing iron was accumulated on the electrode surface, presumably in the form of iron hydroxide, thus explaining the loss of performance. On the other hand, humic salt at a concentration of 10 mg L^{-1} (~3.1 mg Total Organic Carbon or TOC L^{-1}) had a substantially larger effect than Fe^{3+}. Over the same operational time, the removal efficiency decreased by 15% and the freshwater outflow was reduced from 2 L min^{-1} to a value close to 1.25 L min^{-1}. The authors

hypothesized that humic acid, due to its weak charge, could be retained on the electrodes due to chemical adsorption and/or hydrophobic interactions. Similarly, Wang et al. (2015) [21] proposed that once adsorbed, dissolved organic matter (DOM) might obstruct the porous network due to its size and molecular weight. In addition, Gabelich et al. (2002) [55] found that an increase in NOM concentration, from 2.6 to 9.8 mg TOC L^{-1}, reduced to different extents, the removal efficiency of Ca^{2+}, Mg^{2+}, K^{+}, Na^{+}, SO_4^{2-}, Cl^{-}, NO_3^{-} and F^{-}. In addition, at both TOC levels, DOM was not completely released back into the solution during the regeneration step, thus indicating the fouling potential of this particular type of organic material. This was attributed to the entanglement between the DOM and the carbon structure. Mitigation of fouling (i.e., organics) and scaling (i.e., inorganics) has been shown to be possible by the use of a chemical aid such as alkaline (e.g., NaOH) or acid solutions (e.g., citric acid), respectively [15], [20], [21]. In contrast, for ions such as Ca^{2+}, Mg^{+} and Na^{+}, although competition for active sites still exists, their desorption during the regeneration step has been reported to be 100% efficient [15], [20].

Recently, Wang et al. (2020) [19] reported on the scaling nature of iron containing waters when treated by CDI. The authors also explored the effect arising from the combination of iron with surrogates for NOM such as humic acid and bovine serum albumin (BSA). Using a batch CDI cell, with a cell potential of 1.4 V and an HCT of 20 min, they observed a decrease in SAC with an increase in iron concentration (i.e., 1, 2.5, 5 and 10 mg Fe L^{-1}). Moreover, at a constant iron concentration of 1 mg L^{-1}, the gradual increase of humic acid and BSA (i.e., 1, 2.5, 5 and 10 mg L^{-1}) resulted in a further decrease in SAC. In contrast with the study by Mossad & Zou (2013), the electrode scaling was determined to be Fe_2O_3 instead of $Fe(OH)_3$, and was a phenomenon largely affecting the cathode, due to the electrostatic attraction to positively charged species. Analysis of the pore structure indicated that loss of performance can be attributed to a reduction

in active sites, in the micropores, as a result of pore blocking. Given the commonly applied potentials and observed pH values during CDI operation, several iron species could be present during cycling of a CDI cell. Some of these, according to stability diagrams [56], [57] (i.e., potential as a function of pH as shown in Figure 1.6) and the reactivity of iron in aqueous solutions, include Fe^{2+}, Fe^{3+}, iron oxides (e.g., α-Fe_2O_3 or Hematite, γ-Fe_2O_3 or Maghemite), iron hydroxides (e.g., $Fe(OH)_2$ and $Fe(OH)_3$ or Bernalite) and iron oxide hydroxides (e.g., α-FeOOH or Goethite, γ-FeOOH or Lepidocrocite and β-FeOOH or Akaganéite) [58]. Moreover, due to the properties of iron, complex formation with other inorganic ions (i.e., carbonate, bicarbonate, chloride, sulphate, phosphate) and some organic substances is a possibility [59]. The complexity of iron aqueous chemistry suggests that identification of the iron species formed during CDI operation is valuable from a mechanistic point of view, however it is beyond the scope of this study.

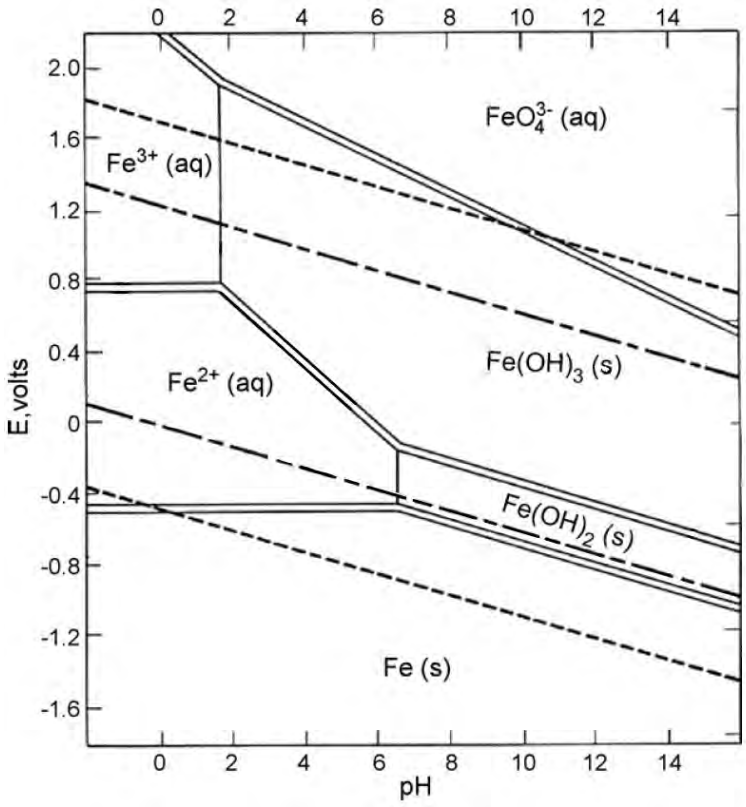

Figure 1.6 Iron Pourbaix diagram (modified with permission from ELSEVIER from Moreno-Casillas et al. (2007) [57])

The formation of fouling and scaling deposits negatively impact the removal efficiency of TDS. The effect of organic matter has been linked to the physical entrapment of large molecules in the electrode porous structure. On the other hand, insoluble iron species are formed as a result of the conditions of potential and pH near the electrode surface. As these deposits develop, access to active sites becomes restricted. By measurement of the electrode capacitance, the impact of fouling and scaling can be further investigated. At the same time, the charge of these substances could shift the electrode E_{PZC}. Although fouling and scaling deposits can be removed by the aid of a chemical rinse, in this study these effects are not alleviated in order to understand their role on the electrode electrochemical and morphological properties.

1.4.5 Strategies to Mitigate Faradaic Reactions

1.4.5.1 Membrane Capacitive Deionization

Membrane CDI (MCDI) employs ion exchange membranes to enhance desalination due to the inability of co-ions to migrate to the oppositely charged electrode. Therefore, the excess of co-ions is counterbalanced by an increased electrosorption of counter-ions. Another advantage of MCDI, arises from the low oxygen permeability exhibited by some ion exchange membranes, such as Nafion® [60], which in turn can isolate the cathode from ubiquitous dissolved oxygen, thus inhibiting the cathodic reduction of oxygen.

In this sense, Tang et al. (2017) [40] observed that the production of H_2O_2 in MCDI was below 3 μM at cell potentials of 0.9, 1.2 and 1.5 V. In contrast, H_2O_2 production peaked at around 40 μM in conventional CDI. The inhibiting nature was corroborated by a stable level of dissolved oxygen around 7.5 mg L^{-1} over the 15 min of charging time at cell potentials of 0.9, 1.2 and 1.5 V. Conversely, in conventional CDI dissolved oxygen values decreased to approx. 2, 1.5 and 1 mg L^{-1}, respectively as a result of the cathodic oxygen reduction reaction. When comparing pH profiles, the only appreciable difference is that, in conventional CDI the change in pH occurs at a relatively faster rate.

The long-term effect of the inhibition of oxygen reduction was reported by Omosebi et al. (2014) [61]. Comparison of CDI and MCDI, equipped with carbon xerogel electrodes, after 50 cycles of operation (i.e., cell potential of 1.2 V and an HCT of 30 min) revealed a stable SAC of ~4 mg NaCl L^{-1} for MCDI. In contrast, the SAC in CDI mode decreased, following a linear trend, from ~2 mg NaCl L^{-1} to ~0 mg NaCl L^{-1} over the same time frame (i.e., 50 hours). In agreement with this behaviour, analysis of the E_{PZC} indicated a substantial positive shift of 500 mV for the CDI anode, whereas the MCDI anode only shifted 200 mV. In both configurations, the cathode's

E_{PZC} displayed a shift of around 100 mV. These results indicated the detrimental effect of dissolved oxygen on the anode surface by acceleration of surface oxidation through the formation of a reaction couple [61], between the oxygen reduction reaction and the carbon oxidation reaction, that results in the progressive increase of the anodic potential (as mentioned in section 1.4.2.4). Although in this study the potential distribution to the cathode and anode was not reported, the smaller cathodic E_{PZC} shift could be explained by the relatively lower potentials to which the cathode is usually exposed to during the charging step. As cycling proceeded, it is likely that the cathode was progressively exposed to more positive potentials and, once it became larger than 0.2 V vs RHE, the surface underwent oxidation.

1.4.5.2 Electrodes Doped with Metal Oxides

The impregnation of metal oxides such as TiO_2, SnO_2, MnO_2 into activated carbon and graphene oxide has been explored with the aim of promoting the cathodic reduction of oxygen and thus limiting the reaction coupling with carbon corrosion [51], [62]–[64]. An additional outcome of this approach has been the increase of the electrode SAC. For instance, Srimuk et al. (2017) [51] reported that the addition of TiO_2 to activated carbon exhibited an initial SAC of 17.4, 16.2 and 11.4 mg g^{-1} for metal loadings of 15%, 25% and 35%, respectively and converged to ~2 mg g^{-1} after 60 hours of operation at a cell potential of 1.2 V and a HCT of 30 min. In contrast, unmodified electrodes lost their entire SAC in only 15 hours of operation.

The studies by El-Deen et al. (2014, 2014b & 2015) [62]–[64] with doped graphene oxide (GO) have also shown also improved SACs. Specifically, MnO_2 doped GO presented a SAC between 3.5 and 5.0 mg g^{-1} at a cell potential of 1.2 V and an HCT of 120 min. In comparison, untreated GO exhibited at SAC of approx. 2 mg g^{-1} [62]. Graphene oxide modified with SnO_2, showed lower SAC when compared to the ones of GO-MnO_2. At a cell potential of 1.4 V and

HCT of 90 min, a dopant level of 15% exhibited a maximum SAC of 1.49 mg g^{-1}, almost doubling the reported SAC for untreated GO [63]. For these two studies, however, the claim of improved stability is based on the retention of capacitance after 50 cyclic voltammogram (CV) sweeps between -0.4 and 0.6 V vs Ag/AgCl. By using this protocol, only 0.7% and 4.9% of the initial capacitance was lost for the GO-MnO_2 and GO-SnO_2 electrodes, respectively. Clearly, the amount of time the electrode is under adverse potential conditions is limited and does not reflect typical CDI operation. The inclusion of TiO_2 displayed, when compared to the other two modified materials, the largest improvement in SAC. At an HCT of 5 min and cell potentials of 0.8, 1.0 and 1.2 V, SACs of approx. 9, 14 and 16 mg g^{-1}, respectively, were achieved. For this material, less than 1% of the initial desalination capacity was lost after 25 cycles at a cell potential of 0.8 V [64].

The effect of carbon corrosion and oxygen reduction can be alleviated in MCDI. No signs of secondary reactions such as the production of H_2O_2, concentration of dissolved oxygen and pH profiles indicated the mitigation of these secondary processes. Nonetheless, since water acts as the oxygen donor, the process of carbon corrosion will proceed despite the utilization of membranes. This process, as described in previous section, is potential dependent. Therefore, this study utilizes a three-electrode cell to investigate the process of electrode degradation with a fix driving force (i.e., anode potential). In conventional two-electrode cells, the potential difference is maintained but there is no control over the potential distribution. This study then, provides a contrast between degradation results obtained with different cell configurations. In addition, this enables a further understanding of the apparent reaction synergy occurring between the processes of carbon corrosion and oxygen reduction.

1.4.6 Electrochemical Regeneration

Although strategies to mitigate the effect of Faradaic processes exist, the incorporation of oxygen functionalities on the electrode surface is a persistent and progressive process in carbon-based CDI applications. Nevertheless, there are not many studies investigating the feasibility of electrochemical approaches to regenerate (i.e., reduce) the electrode surface. A reason for this might be the suspected kinetic impediment and strong pH dependence of the process asserted by Jannakoudakis et al. (1990) [23]. There exist a few literature cases where, to different degrees, surface carbon oxides have been electrochemically reduced. Yang and Ling (1995) [22] observed, for glassy carbon, that the fresh oxygen containing functionalities formed after holding a 1.6 V potential for 5 min were not stable and reduced at -1.2 V after holding the potential for 1 min. Jannakoudakis et al. (1990) [23] reported that, for carbon fibres in 0.5 M H_2SO_4, after reduction at a current density of -10 mA mg^{-1} for 1 min (in 0.5 M H_2SO_4), the surface remained deeply functionalized. Nonetheless, there was a decrease of approx. 2.6 and 1.6 times in the intensity for the binding energies associated with the C – OH (-285.7 eV) and C = O (-288 eV) functions, respectively. In contrast, there was an increase of approx. 2.3 times in the intensity for the binding energies associated with the COOH function. The study by Binder et al. (1964) [24] showed that, for carbon electrodes, a fraction of the species formed at the surface were removed below the hydrogen evolution potential after galvanostatic treatment at -25 mA cm^{-2} in 20% H_2SO_4. One possible drawback of the electrochemical reduction of surface oxides, as revealed by Theodoridou et al. (1981) [25] while studying highly oriented carbon fibres, could be the acceleration of the initial oxidation process. This arises from the incomplete reduction process that occurs at potentials near the hydrogen evolution reaction potential (complete reduction requires approx.

-0.5 V vs SHE) [65] which results in a highly defective surface (i.e., with active C sites), prone to be oxidized in the subsequent cycles [25].

The application of reductive potentials to address the issue of carbon oxidation in CDI is an area of great opportunity. However, little is known about the electrochemical reduction of carbonaceous surface oxides. Among the few studies available, contrasting outcomes have been reported for different carbon materials and conditions. It is unclear whether some surface oxides are more prone to be reduced than others. In addition, the potential dependence (i.e., linear, non-linear) of the reduction process efficiency is unknown. A method to qualitatively assess the effectiveness of the reduction process is the determination of the electrode E_{PZC}. A successful trial will result in a regression of the E_{PZC}, thus increasing the effective potential window for electrosorption. In addition, the extent to which the electrode capacitance is affected by holding the electrode potential below the HER thermodynamic potential is unknown. In combination, changes in these two parameters (capacitance and E_{PZC}) will provide insights regarding the applicability of electrochemical regeneration approaches for CDI electrodes.

1.5 Knowledge Gaps

The literature survey performed is indicative of the potential detrimental effect that carbon oxidation has on the electrode stability. Moreover, it is a phenomenon that affects primarily the positive electrode (i.e., the anode). Among the repercussions of this process, reduction of surface area, increase in resistivity and a positive displacement of the electrodes E_{PZC} are quite significant. In addition, the presence of dissolved oxygen may exacerbate the corrosion process by the formation of a reaction couple between carbon oxidation at the anode and oxygen reduction at the cathode.

A number of studies pertaining to stability and secondary reactions in CDI have been conducted. However, most of these studies were performed using the more practical two-electrode cell configuration. An advantage that this type of cell offers is the possibility of obtaining performance metrics such as salt adsorption capacity, water recovery, charge efficiency and specific energy consumption. However, potential control (i.e., individual electrode potential) with this type of cell is non-existent. This setup though, can maintain a potential difference between the electrodes, but the relative electrode position cannot be controlled. However, this can be determined with the aid of a reference electrode in a three-electrode setup. In addition, information related to electrochemical properties such as capacitance and E_{PZC} requires an experimental setup designed to use working and counter electrodes that comply with recommended aspect ratios (e.g., $CE_{Area} >> WE_{Area}$); separated compartments to avoid interference from processes occurring at the CE on the WE, tuned electrolyte concentration and a potentiostat. Thus, most studies report electrochemical properties only at the beginning-of-life (BOL) and end-of-life (EOL) conditions. In addition, stability studies have been only carried out with solutions containing one electrolyte of choice (i.e, NaF, KCl or NaCl). Moreover, studies with fouling and scaling solutes have focused on the effect on operational parameters such as SAC, charge efficiency and specific power consumption.

Another interesting matter in these studies, was the selection of cycling parameters such as the applied potential and cycling time, as it did not follow a standard protocol. In fact, the only consideration was regarding the applied potential, which was aimed to be kept below the water electrolysis potential of 1.23 V vs RHE, to avoid any interference from this Faradaic reaction. The literature review indicated that the effect of secondary processes (Faradaic and non-Faradaic) on the electrode degradation and cell performance decay are dependent on the applied potential, the

use of reverse polarization and cell architecture. Therefore, comparison among studies was a challenging task. However, the development of a standardized protocol and a state-of-the-art reference material to evaluate the long-term performance of new materials would be of extreme value for the CDI field.

Strategies to mitigate the effect of Faradaic reactions have been proven effective at small scale. Nonetheless, when transferred to real life applications, their implementation can result in an increased operational complexity and cost. With this in mind, the use of an *in-situ*, electrochemical regeneration approach is an attractive, yet to be explored alternative for application in CDI devices. It is unknown, given the contradictory evidence found in the literature, if under typical CDI conditions (i.e., pH) the process is viable. If so, it is of great value to assess changes in morphology and recovery of vital electrochemical properties such as capacitance and E_{PZC}, and to assess the impact of this methodology on the electrode lifetime.

1.6 Thesis Objectives

This study aims to investigate key fundamental aspects to the operation and efficacy of electrodes used in the CDI process.

- First, it investigates the effect of natural organic matter and iron on the progressive changes that occur, during long term cycling, to the electrochemical (i.e., capacitance and E_{PZC}) and morphological properties (i.e., surface composition, contact angle and bulk porosity) of activated carbon electrodes used in CDI.
- Second, it examines the application of electrochemical regeneration approaches with the intention to mitigate the effect of carbon oxidation. The effectiveness is assessed by monitoring the change in capacitance and E_{PZC} of the electrodes, as well as analysis of the electrode morphology. Moreover, integration of a regenerative step as part of

the cycling protocol and its effect on the long-term stability of the electrodes is explored.

- Third, it investigates the influence of cycling time and pH on the electrochemical properties (i.e., capacitance and E_{PZC}) of activated carbon electrodes used in CDI during long-term operation.
- Fourth, it analyzes the stability of activated carbon electrodes using a two-electrode setup by investigating the effect of dissolved oxygen and applied potential on the electrochemical properties (i.e., capacitance and E_{PZC}) during long-term operation. Moreover, the effect of Faradaic processes on the potential distribution is discussed.

All in all, this study aims to provide useful technical insights to help develop the next generation of CDI applications, especially those meant to be used as Point-of-Use (POU) devices.

1.7 Significance & Novelty

The appeal of CDI relies on its simple operation, good water recovery, relatively low energy consumption, and easy maintenance. Despite these merits, CDI has not yet made a significant penetration in the drinking water sector, particularly as a Point-of-Use (POU) device. The development of materials with improved salt adsorption capacity and the evolution of cell architecture has created enough momentum to motivate the industry to pursue the application of this technology in the field. Nevertheless, the electrode durability is still an aspect that requires further understanding and development before the technology moves fully into the next stage.

Considering that the anode is the electrode most affected by secondary reactions, this study is based on the utilization of a three-electrode setup to isolate the positive electrode and carry experiments under carefully controlled potentiostatic conditions. This is done with the objective of understanding the change in electrochemical and morphological properties that occur

during the electrode lifetime under the presence of known fouling and scaling agents, such as NOM and iron, without the interference of the processes happening at the cathodic side of the cell. Additionally, this study presents the surface response of capacitance and E_{PZC} as a function of applied reduction potential and holding time. Furthermore, the effect of an *in-situ* electrochemical regenerative step on the electrodes operational life is also assessed.

Chapter 2: Experimental Procedure

2.1 Electrode Fabrication

A carbon ink consisting of activated carbon (YEC-8A), PVDF (Sigma) as a binder, and DMA (Sigma) as a solvent was used as a baseline for this study. Approximately 100 mg of PVDF was added to 4 mL of DMA and the mixture was stirred overnight at room temperature to ensure all binder material was dissolved. Then, 0.9 g of activated carbon was slowly added to the PVDF/DMA solution. The carbonaceous slurry was left to stir overnight at room temperature to allow homogeneous dispersion of the active material. Toray® paper (TGP-H-120, Fuel Cell Store) with a wet-proofing of 30 wt.% was used as the support for the carbon slurry. Kapton® film was used to insulate the uncoated portions of the support to prevent interferences from the support material on the electrochemical measurements. The prepared carbon ink was coated on the surface of the support with the aid of a micrometer film applicator (MTI Corporation) at an aperture of 500 μm. The prepared electrodes were left inside a fume-hood to dry overnight and were then placed inside an oven at 80 °C for an hour to evaporate any remaining solvent. To calculate the loading of active material, electrodes were weighed before and after ink coating.

2.2 Electrochemical Characterization

Electrochemical characterization was performed in deoxygenated 1000 mg L^{-1} NaCl (17.1 mM NaCl) (ACS, Fisher) unbuffered solution made with deionized water (18.2 MΩ, Milli-Q® Integral 5, Millipore Sigma). The electrolyte initial pH was 7.04 ± 0.06. The three-electrode cell used consisted of graphite foil with an approx. geometric area of 64 cm^2 as the counter electrode, a low-profile Ag/AgCl reference electrode (RRPEAGCL, Pine research) and a working carbon electrode with a geometric area of 2.84 cm^2 (approx. real surface area of 9 m^2, considering an average active material loading of 4.5 mg and a specific surface area of 2000 m^2 g^{-1}). The 3-

electrode cell, shown in Figure 2.1, consisted of two symmetric compartments (6.1 x 4.5 x 4.5 cm) (technical drawings of the different components of the electrochemical cell are presented in Appendix C), separated by a Nafion™ membrane. All characterization experiments were performed using fresh, unbuffered electrolyte (100 mL of 17.1 mM NaCl). Electrochemical techniques were performed with the aid of a Biologic VMP-3 potentiostat and data processing was done with the EC-Lab software. All potential values reported in this work are referred to the Reversible Hydrogen Electrode (RHE). Prior to characterization, the electrolyte was bubbled with nitrogen (99.998%, Praxair) for 30 minutes with the aid of a porous frit. To ensure proper electrode wetting, the electrode to be characterized was first submerged in deionized water (18.2 MΩ, Milli-Q® Integral 5, Millipore Sigma) and then in electrolyte for a period of 30 min each (pristine electrodes were submerged in deionized water for at least 12 hours). After the electrochemical characterization was performed, the electrode was submerged in deionized water for at least 1 hour.

2.2.1 Cyclic Voltammetry

The electrode capacitance was extracted from the third cyclic voltammogram scan between 0 and 1.0 V vs RHE at a scan rate of 1 mV s^{-1}. The I-E curve was integrated between 0.2 and 0.8 V vs RHE (limits displaying capacitive response) and the electrode specific capacitance was calculated using equation (2.1) [11], [21], [66]:

$$C = \frac{\int_{E_1}^{E_2} |i| dE}{2 \cdot m \cdot \upsilon \cdot (E_2 - E_1)} \tag{2.1}$$

where i is the current in mA, m the mass of active material in g, ν the scan rate in mV s^{-1} and E_2 and E_1 the upper and lower limits of the potential window, respectively, in V. The E_{PZC} was determined as the potential of the forward sweep at which the current exhibits its minimum value

within the section of the voltammogram where capacitive response (i.e., rectangular) is observed [10], [44], [67]–[70]. The electrolyte concentration was chosen to be 17.1 mM as it was the most diluted solution that exhibited a rectangular response and resolved E_{PZC} (i.e., the current minimum within the rectangular response of the forward scan). More diluted electrolytes resulted in resistive (i.e., tilted) CV response and more concentrated electrolytes resulted in progressively, more flat I-E responses between 0.2 and 0.8 V vs RHE which made the E_{PZC} of the forward potential sweep more difficult to locate as the electrolyte concentration increased.

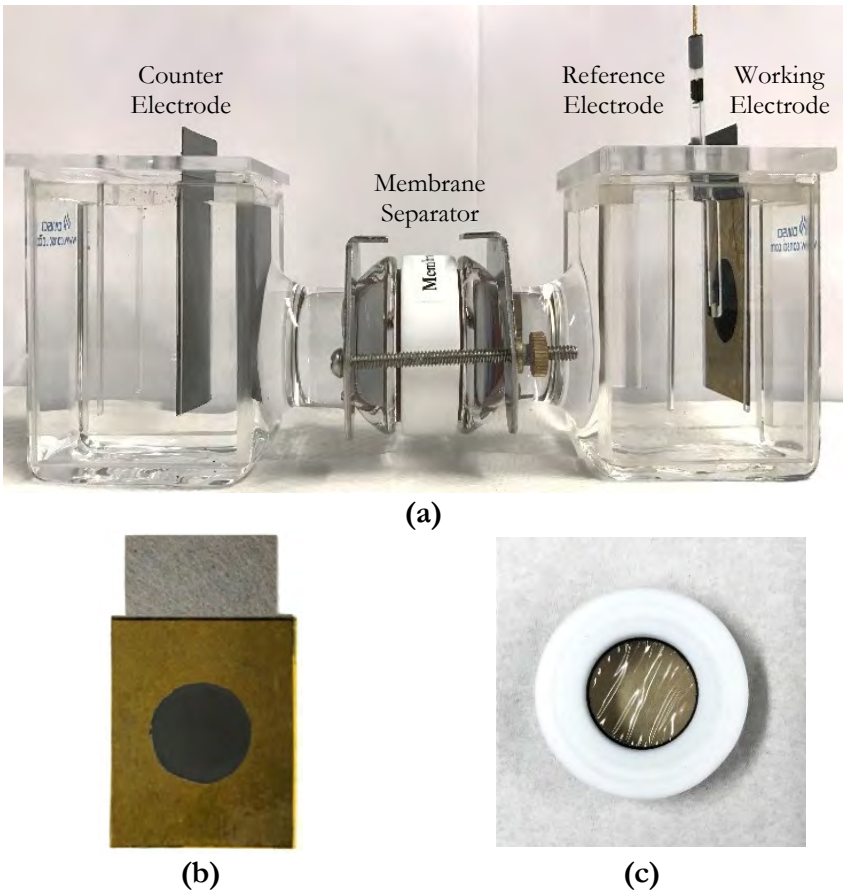

Figure 2.1 (a) Compartmentalized three-electrode cell setup separated by a Nafion™ membrane; (b) Activated carbon working electrode, and (c) Teflon enclosure for the Nafion™ membrane

2.2.2 Electrochemical Impedance Spectroscopy (EIS)

Impedance spectrum was obtained at a potential of 0.5 V vs RHE, using a sine amplitude of 5 mV (3.54 V_{RMS}) and scanning frequencies from 350 kHz to 5 mHz. The spectrum was collected using 10 points per decade with logarithmic spacing. Before data collection, the working electrode was held at 0.5 V vs RHE for 10 minutes and the resulting impedance was the average of three measurements per frequency.

2.3 Degradation Experiments

2.3.1 Three-Electrode Cell

Activated carbon electrodes were cycled using a traditional 3-electrode cell, at a potential of 1.2 V vs RHE under different water compositions, which are summarized in Table 2.1. The electrolyte concentration in all cycling experiments was 1 M (NaCl) and the pH, of the working electrode compartment, was measured before and after cycling. The initial electrolyte pH for the different experiments is presented in Tables 2.1 and 2.2. Every set of cycles was performed using fresh, unbuffered electrolyte (100 mL of 1 M NaCl), and only the working electrode compartment contained, if any, supplementary amount of a solute (i.e., Suwannee River Natural Organic Matter or Fe^{2+}). The cycling protocol consisted of a 5 min charging step followed by an isochronous discharging step at a potential equal to the open circuit potential. To measure the open circuit potential, it is required that no load (either potential or current) is applied to the circuit by the power amplifier (potentiostat). The value of the open circuit potential was measured at the beginning of each experiment. Tables included in Appendices A and B present these values for the different experiments performed and discussed herein. Electrochemical characterization was performed after 5 charge-discharge cycles (until the 50^{th} cycle). In some experiments, after the 50^{th} cycle, characterization was performed with intervals of 10 cycles. This was done having in mind

that the profile of the capacitance curve was already clear, and the normalized capacitance of the electrode was near a C/C_0 value of 0.10. To ensure saturation, the electrolyte solution was sparged with O_2 (99.993%, Praxair) or N_2 (99.998%, Praxair) for 30 min before each test and continued, at a lower flow rate, throughout the experiment. To test the influence of organic matter and iron, Suwannee River Natural Organic Matter (SRNOM) (International Humic Substances Society) was used as a surrogate at concentrations of 20 and 40 mg NOM L^{-1} while iron (II) chloride ($FeCl_2$) (ACS, Sigma) was used at concentrations that resulted in approx. 0.2, 2.0 and 20 mg Fe^{2+} L^{-1} (3.58, 35.8 & 358 μM $FeCl_2$ L^{-1}), respectively. Tests were conducted at high electrolyte concentration (i.e., 1 M NaCl) to overcome the ohmic potential drop caused by the membrane separator and inter-electrode distance between the counter and working electrode. Further experiments, under oxygen saturation, were carried out to clarify the effect of different half cycle times and pH conditions (only in the working electrode compartment) on the electrode degradation (see Table 2.2).

The selection of different half cycle times was based on using multipliers of the 5 min HCT used for the other degradation experiments. This allowed a straightforward comparison when the normalized capacitance (C/C_0) and E_{PZC} were plotted as a function of the time the working electrode was held at a potential of 1.2 V vs RHE (instead of the number of cycles performed). For instance, the time the working electrode was held at 1.2 V vs RHE after 5 cycles of the 1 min HCT protocol was equal to the time the electrode was held at 1.2 V for one cycle of the 5 min HCT. Similarly, the time the working electrode was held at 1.2 V vs RHE after 5 cycles of the 5 min HCT protocol was equal to the time the electrode was held at 1.2 V for one cycle of the 25 min HCT. pH adjustment was done with the aid of a 0.1 M NaOH solution after every set of 10 cycles. The concentration of NaOH was chosen to be 0.1 M NaOH so that the volume

added to the cell did not significantly change the volume of the solution inside the compartment (less than 1 mL). Each experiment was performed in duplicate. After the degradation experiment was performed, the electrode was submerged in deionized water for at least 1 hour.

Table 2.1 Experimental solution compositions to study the effect of organic carbon and iron on the electrode stability. All experiments were performed at room temperature with an electrolyte concentration of 1 M (NaCl), a half cycle time of 5 min and a working electrode potential of 1.2 V vs RHE

Experiment	Solution Composition & Gas Saturation	Initial Electrolyte pH
1	Baseline, N_2	7.04 ± 0.06
2	Baseline, O_2	
3	20 mg SRNOM L^{-1}, N_2	4.19 ± 0.02
4	20 mg SRNOM L^{-1}, O_2	
5	40 mg SRNOM L^{-1}, O_2	3.85 ± 0.01
6	20 mg Fe^{2+} L^{-1}, N_2	5.45 ± 0.14
7	20 mg Fe^{2+} L^{-1}, O_2	
8	2.0 mg Fe^{2+} L^{-1}, O_2	5.63 ± 0.08
9	0.2 mg Fe^{2+} L^{-1}, O_2	6.47 ± 0.10

Table 2.2 Summary of experiments carried out to further understand the role of half cycle time and pH on the electrode degradation. All experiments were performed at room temperature with an electrolyte concentration of 1 M (NaCl)

Experiment	Half Cycle Time (min)	Initial Electrolyte pH	Applied Potential (V vs RHE)
1	1	7.04 ± 0.06	1.2
2	25		
3	50		
4	250		
Experiment	**pH**		
5	1	-	1.2
6	13	-	0.49
7	Adjusted after 5 cycles	7.04 ± 0.06	1.2

2.3.2 Two-Electrode Cell Experiments

Figures 2.2 and 2.3 shows, respectively, the image and the process flow diagram of the two-electrode flow-cell assembly used to cycle activated carbon electrodes at different cell potentials and water compositions, which are summarized in Table 2.3. Each experiment was performed in duplicate and using fresh, unbuffered electrolyte. The initial electrolyte pH for different experiments is presented in Table 2.3. To resemble more practical conditions, the electrolyte concentration in all cycling experiments was 17.1 mM (NaCl). A peristaltic pump was used to maintain the electrolyte flow rate at 20 mL min^{-1}. pH was measured (HI5522, Hanna) and logged (HI92000 software, Hanna) every 10 s throughout the duration of the tests. A DC power supply (1688B, BK Precision) was used to apply a potential bias to the electrodes. The potential distribution between the anode and cathode was recorded against a Ag/AgCl reference electrode (RRPEAGCL, Pine research) using a potentiostat (VMP-3, Biologic). Given the importance of the changes occurring to the potential attributed to the anode, the reference electrode was placed closely, at a distance of 3 mm. The interelectrode distance was 1.6 cm. Thus, the distance between the cathode and the reference electrode was 1.3 cm. Current was measured by means of a multimeter (38XR-A, Amprobe) and logged (38SW-A, Amprobe) at one second intervals throughout the duration of the tests. A relay (ProXR, National Control Devices) controlled the cycling protocol, which consisted of a 5 min charging step followed by an isochronous discharging step at zero voltage discharge (i.e., $V_{cell} = 0$). Electrochemical characterization was performed after 10 charge-discharge cycles. To ensure saturation, the electrolyte solution was sparged with O_2 (99.993%, Praxair) or N_2 (99.998%, Praxair) for 30 min before each test and continued, at a lower flow rate, throughout the experiment.

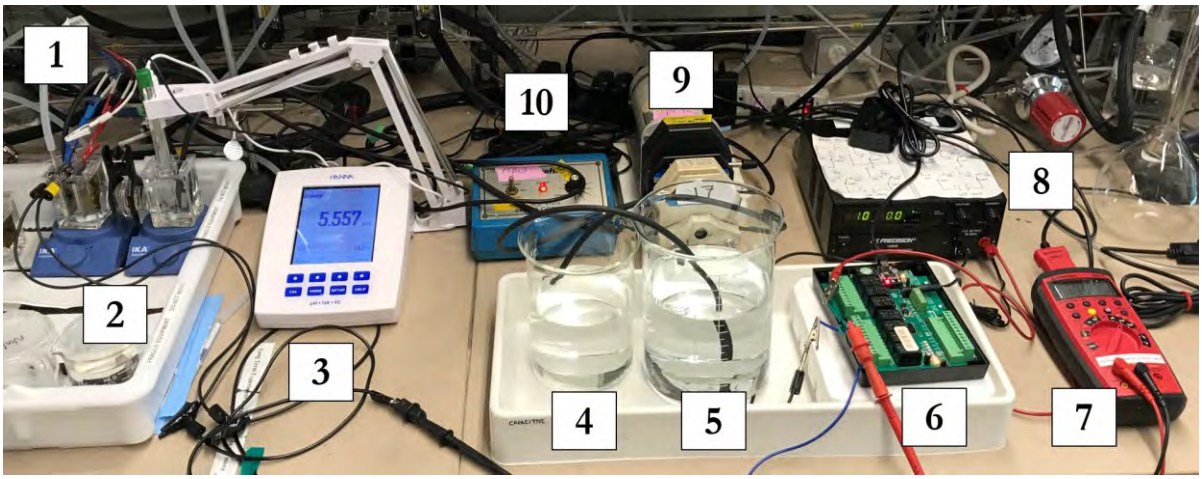

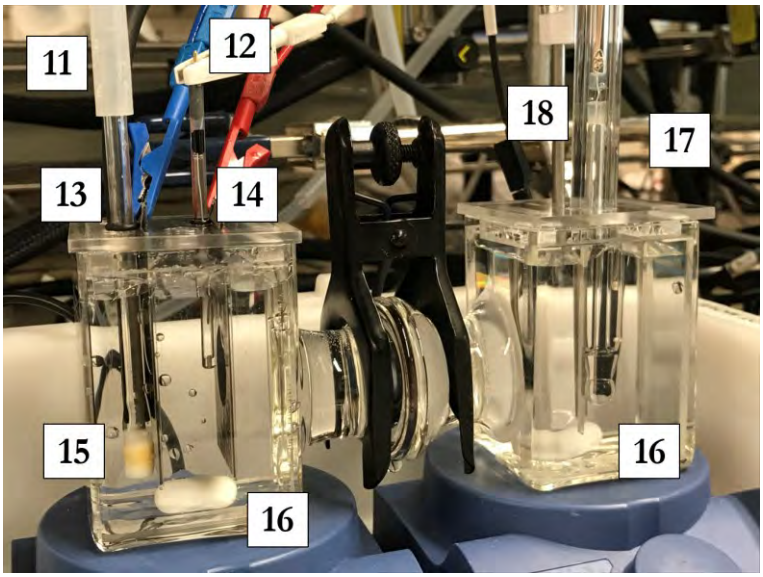

1. Connection to potentiostat
2. Electrochemical cell
3. pH data logger
4. Outlet reservoir
5. Inlet reservoir
6. Relay
7. Ammeter
8. DC power supply
9. Peristaltic pump
10. Motor drive
11. Connection to gas supply
12. Reference electrode
13. Cathode
14. Anode
15. Porous frit sparger
16. Magnetic mixer
17. pH probe
18. Temperature probe

Figure 2.2 Two-electrode flow-cell assembly and ancillary equipment (pH probe, peristaltic pump, power supply, relay & multimeter)

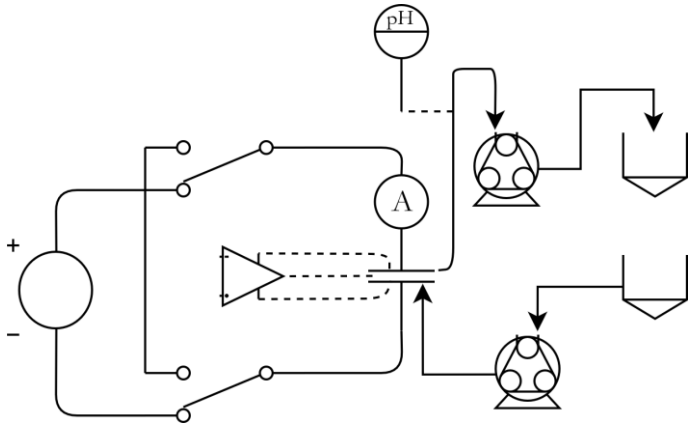

Figure 2.3 Process flow diagram for the two-electrode flow-cell assembly

Table 2.3 Summary of conditions for the experiments performed using a two-electrode electrochemical cell. All experiments were performed at room temperature with an electrolyte concentration of 17.1 mM (NaCl)

Experiment	Solution Composition & Gas Saturation	Cell Potential (V)	Initial Electrolyte pH
1	Baseline, N_2	1.3	7.04 ± 0.06
2	Baseline, N_2	1.8	
3	Baseline, O_2	1.3	
4	Baseline, O_2	1.0	
5	0.2 mg Fe^{2+} L^{-1}, O_2	1.3	6.47 ± 0.10

2.4 Electrochemical Regeneration Experiments

Tests were performed using a 3-electrode cell (shown in Figure 2.1) under the same electrolyte concentration (i.e., 1 M NaCl) and O_2 saturation conditions as the degradation experiments. The pH, of the working electrode compartment, was measured before and after the regeneration experiments. The initial electrolyte pH was 7.04 ± 0.06. A potentiostat (1470E, Solartron Analytical) was used to control the potential of the working electrode. The recovery of capacitance and E_{PZC} were calculated following equations 2.2 and 2.3:

$$Capacitance\ Recovery\ (\%) = \frac{C_{Recovered}}{C_{lost}} \cdot 100 = \frac{C_{Regeneration} - C_{Degraded}}{C_{initial} - C_{Degraded}} \cdot 100 \qquad (2.2)$$

$$E_{PZC}\ recovered\ (V) = E_{PZC\ Regeneration} - E_{PZC\ Degraded} \qquad (2.3)$$

where C refers to the specific capacitance, in F g^{-1}, and E_{PZC} refers to the potential at the point of zero charge, in V, at different electrode stages. Both parameters were obtained from cyclic voltammograms obtained following the protocol described in section 2.2.1. Equation 2.2 represents the percent capacitance recovery observed after performing a potential-holding time treatment to an electrode degraded to a C/C_0 value ~ 0.85. In other words, it represents how much of the capacitance that was lost during degradation is being recovered after the electrochemical regeneration treatment.

2.4.1 Factorial Design of Experiments

A 3^2-factorial design of experiments was used to explore the recovery response of the electrode capacitance and E_{PZC}. The experimental matrix is summarized in Table 2.4. Analysis of variance (ANOVA) was used to determine if the parameters studied had a significant (with a significance level, α, of 0.05) effect on capacitance and E_{PZC} recovery. Each potential-holding time treatment was performed in duplicate.

Table 2.4 Experimental design for screening parameter levels for electrochemical regeneration study

Parameter	Low	Center-point	High
Potential (V vs RHE)	-2.1	-1.25	-0.4
Holding time (s)	10	50	90

2.4.2 Extended Surface Response Study

The surface response obtained was further investigated by carrying out regeneration experiments along the potential domain with working electrode potentials of -1.89, -1.68, -1.46,

-0.83 and -0.61 V vs RHE with a holding time of 50 s. Each potential-holding time treatment was performed in duplicate.

2.4.3 Effect of Electrochemical Regeneration on Electrode Cyclability

An electrochemical regeneration stage, using a working electrode potential of -1.68 V vs RHE and a holding time of 10s, was conducted after every 5 degradation cycles (until the 30th cycle)[1] and after every 10 cycles (until the 50th or 70th cycle) until the normalized capacitance reached a value of $C/C_0 \approx 0.10$ to evaluate the effectiveness of preventive reductive steps on extending the electrodes operational life. Additional tests were performed using electrolytes containing SRNOM at 20 mg NOM L^{-1} and Fe^{2+} at 0.2 mg L^{-1}. The initial electrolyte pH values were 4.19 ± 0.02 and 6.47 ± 0.10 for the SRNOM and Fe^{2+} tests, respectively. Each experiment was performed in duplicate.

2.5 Ex-situ Analysis

Electrode samples, at different values of C/C_0, were prepared by performing additional experiments under the same conditions presented in Table 2.1. Other electrode samples included electrodes at beginning and end-of-life and electrodes after application of different potential-holding time treatments (as presented in Table 2.4 and section 2.4.2 and 2.4.3) under different experimental conditions. After degradation or regeneration, the electrodes were placed in deionized water for a period of 12 h. Then, the electrodes were left to dry for 48 h at room temperature inside beakers partially covered with laboratory film to prevent deposition of dust on the electrode surface. Once dry, the Kapton® film used to insulate the uncoated parts of the Toray® support was removed with the aid of tweezers. A hole puncher, with a 22 mm diameter

[1] As presented in section 4.3, after the 30th cycle capacitance was no longer being recovered

was used to carefully separate the piece of support coated with the active material. An X-ACTO precision knife was used to cut the circular piece into 4 equal pieces. The contact angle was measured using a FTA1000 system. At least three images of a 5 μL water drop deposited with a micropipette were processed by Fta32_Video software. Fourier-transform infrared (FTIR) spectrum was collected using a PerkinElmer Frontier FT-IR at a resolution of 2 cm^{-1} over a wavenumber region of 650 – 4000 cm^{-1}. The spectrum acquired was the result of 8 cumulative scans. Table 2.5 presents a summary of relevant absorption bands associated with probable oxygen functionalities at the electrode surface. Imaging (SEM) and elemental analysis using energy dispersive X-ray analysis (EDS) were performed using a Philips XL-30 SEM equipped with a Bruker Quantax 200 energy-dispersion X-ray microanalysis system. SEM images were collected at different magnifications, using a working distance in the vicinity of 10 mm, an electron accelerating voltage of 15 kV, using a spot size (i.e., the beam diameter at the sample surface) of 4 and at 60 kcps. EDS was collected from at least three different electrode sections at a magnification of 1000x, using the full window of the acquired image and a spot size of 6 during 30 s. Bulk porosity was estimated from five different cross-sectional SEM images with the aid of ImageJ software. To obtain cross-sectional samples, a rectangular portion of the electrode was filled with an epoxy resin (Epothin, Buehler) and polished (LaboPol-5, Struers) once the epoxy cured and then it was gold coated (Denton Vacuum) to produce a conductive surface that enabled the collection of SEM images. These were collected using a Thermofisher Scientific TeneoLV SEM at an electron accelerating voltage of 15 kV at different magnifications.

The thickness of the electrode (approx. 400 μm including the carbon fiber support) did not make possible the use of TEM, which requires very thin (<150 nm) samples for the electrons to transmit through. On the other hand, analysis of samples at the beginning and end-of-life with

ToF-SIMS (time of flight secondary ion mass spectrometry) did not provide information about C – O, C = O or CO_2 evolution which were of interest to complement the discussion regarding changes in surface functionalities. On the other hand, possibilities did not exist locally to perform XPS, mercury porosimetry or helium pycnometry.

Table 2.5 Infrared absorption regions for oxygen containing functionalities

Compound class	Absorption (cm^{-1})	Bond	Appearance	Reference
Alcohol	3650 – 3400	O – H	Broad & strong	[71]
	1410 - 1260		Strong	[72]
	1150 – 1050	C – O	Strong	[71]
Carbonyl	1770 – 1660	C = O	Strong	
Carboxylic acid	3300 – 2500	O – H	Broad & strong	
	1760 – 1710	C – O	Strong	
Ether	1150 – 1050	C – O	Strong	

2.6 Quality Control & Assurance

All the degradation and regeneration experiments as well as pH measurements were performed in duplicate (n = 2). Hence, the values for capacitance and E_{PZC} reported herein represent the average of the two replicates performed. As discussed in section 2.2.1, these values were extracted from the third cyclic voltammogram scan. The error bars associated with these measurements is the distance between the two replicates. The use of two replicates is justified by the following reasons:

- For degradation and regeneration experiments conducted with a 3-electrode setup the difference between normalized capacitance and E_{PZC} replicates was, on average, of 0.04 units (4%) and 26 mV, respectively. On the other hand, for degradation experiments conducted with a 2-electrode setup the difference between normalized capacitance and E_{PZC} replicates was, on average, of 0.05 units (5%) and 23 mV, respectively. From this perspective, performing a third replicate was not deemed essential. However, the use of only two replicates may raise concerns regarding reproducibility. This is an important

point to be considered, as the analysis of potential outliers cannot be conducted. This is the case for normalized capacitance and E_{PZC} replicates that differed in more than 0.1 units (10%) and 50 mV, respectively. Nonetheless, by careful inspection of the overall trend of the curve to which they belong, they do not affect the main findings that are inferred from the complete data set.

- Time consuming nature of the electrode degradation process. To study the progressive change in electrochemical properties throughout the electrode life, degradation experiments were conducted until 85 – 90 % of the initial capacitance was lost, which took from 450 min up to 600 min of cycling per electrode. Moreover, to have well resolved curves of the capacitance loss and E_{PZC} shift, the cycling domain (i.e., time) was divided in portions of 5 cycles up until the 50^{th} cycle.
- Time consuming nature of electrochemical characterization: to determine the electrode E_{PZC}, the cyclic voltammogram had to be collected at a scan rate of 1 mV s^{-1}. Cyclic voltammograms collected with faster scan rates did not exhibited the required feature. As a result, to cover three cyclic scans over a potential window of 1 V, 1 hr and 40 min were required. In addition, the impedance spectrum was collected down to frequencies as low as 5 mHz so that the AC signal could propagate into the deeper pores of the electrode and capture its capacitive response. The collection of the spectrum, as detailed in section 2.2.2 had a duration of 1 hr.
- Availability of resources: only a limited number of electrochemical cells and channels on the potentiostat were available to carry the experiments.

The elemental composition analysis and contact angle measurements were performed at least at three different points. The error bars associated with these measurements is the standard

error of the mean. When necessary, uncertainty was reported following error propagation equations. Due to sample limitations and the destructive nature of the ATR-FTIR used, these spectra were collected just once.

Chapter 3: Stability of Activated Carbon Electrodes

The progressive change in the electrode capacitance and E_{PZC} as a consequence of cycling under different water compositions is presented in this chapter. Electrochemical results are complemented by the corresponding assessment of the electrodes elemental composition, bulk porosity and wettability.

The discussion begins with a description of the raw electrode characteristics at the beginning-of-life, i.e., prior to any degradation experiments. Pristine cyclic voltammograms and complex impedance plot planes and key aspects of them are presented and used throughout the discussion of the results. Next, the role of dissolved oxygen on the electrode degradation is examined by contrasting results obtained under nitrogen and oxygen saturated conditions. Subsequently, the effect of iron at concentrations of 0.2, 2.0 and 20 mg Fe^{2+} L^{-1} and organic carbon at 20 and 40 mg SRNOM L^{-1} on electrode stability is discussed. Next, the effect of parameters such as half cycle time and electrolyte pH is presented. Finally, results obtained using a more practical two-electrode electrochemical cell operated at typical cell voltages are presented. The latter is done to compare and highlight the advantages of using either a two or a three-electrode investigative approach.

3.1 Beginning-of-Life (BOL) Electrode Characteristics

The active carbon material (YEC-8A) used for electrosorption had an average particle size of 10 μm and an approximate surface area of 2000 m^2 g^{-1}. Once in electrode form, the material exhibited a specific capacitance of 99.7 ± 1.6 F g^{-1} in an electrolyte containing 17.1 mM NaCl (1000 mg NaCl L^{-1}). As mentioned in section 2.2.1, capacitance was obtained from the third scan of a cyclic voltammogram performed with a scan rate of 1 mV s^{-1}. The electrode exhibited a traditional capacitive response (i.e., rectangular) to the potential sweep between 0.2 and 0.8 V vs

RHE (see shaded area in Figure 3.1). The electrode E_{PZC} was estimated by inspecting the forward and reverse sweeps, after respectively locating the potentials associated with the current minimum and maximum within the region of capacitive response [10], [44], [67]–[70]. The complex impedance plane plot shown in Figure 3.2 displayed a depressed semicircle in the high frequency range, which could be modelled by a constant phase element (CPE) [73]–[75] in parallel with a resistor. Wang et al. (2020) [19] attributed the presence of the semicircle to ion accumulation at the electrode-electrolyte interface. The vertically aligned tail that formed from the mid to low frequency range (i.e., to the right of the semicircle) was indicative of the capacitive behaviour of the electrode. Compositional analysis through SEM-EDS revealed that the pristine electrode consisted of approx. 94.3% ± 0.2% carbon, 4.9% ± 0.2% oxygen and 1.5% ± 0.1% fluorine. Weak peaks for oxygen functionalities were observed in the raw FTIR spectra and a high contact angle of 131° ± 2.40° indicated the initial hydrophobic nature of the electrode. Furthermore, cross-sectional SEM image analysis indicated that, at BOL, the electrode possessed a bulk porosity of 51.6% ± 3.8%. The SEM images presented in Figure 3.3 show the morphology of the electrode surface, in which larger pores and the particle size of the used active material can be identified. It was possible to see smaller binder agglomerates around larger carbon particles. In addition, the cross-sectional images provided a view of the intraparticle porosity (used to estimate bulk porosity), by contrasting darker regions (i.e., epoxy filling) and lighter regions (i.e., carbon particles) as presented in Appendix A. Furthermore, it was possible to identify the fibers of the carbon fiber paper used as the support for the active material.

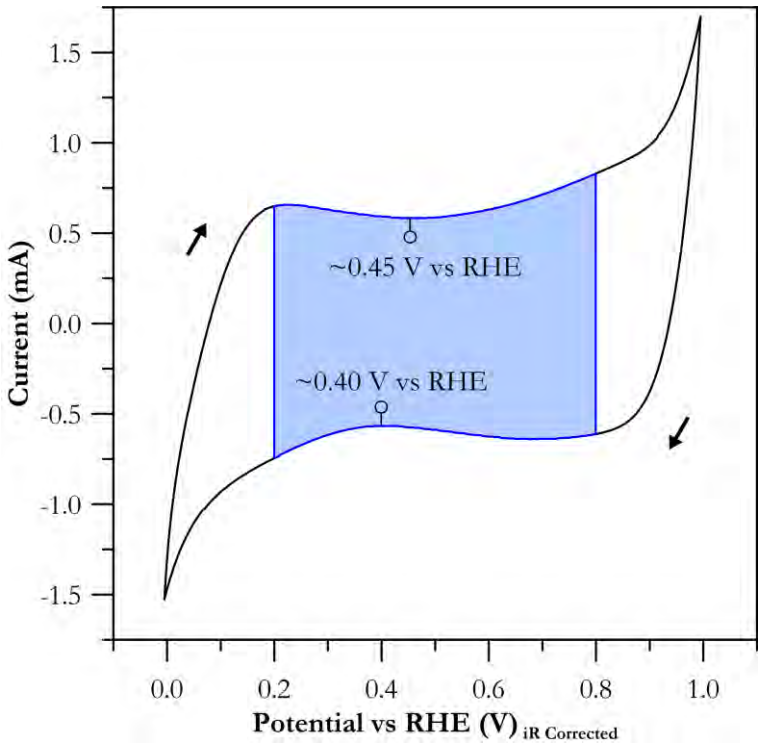

Figure 3.1 Pristine electrode cyclic voltammogram obtained at a scan rate of 1 mV s^{-1} in 17.1 mM deaerated NaCl at room temperature. Shaded area indicates integration boundaries for capacitance calculation and minimum and maximum currents used to estimate the electrode E_{PZC}

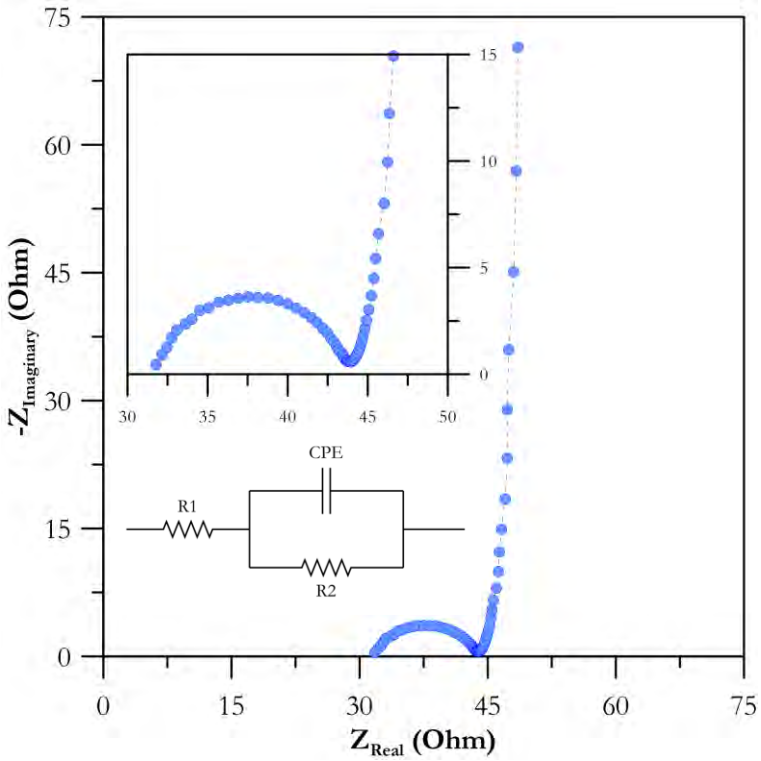

Figure 3.2 Pristine electrode complex impedance plane plot obtained at 0.5 V vs RHE between 350 kHz – 5 mHz in 17.1 mM deaerated NaCl at room temperature with a sine amplitude of 5 mV (3.54 mV_{RMS})

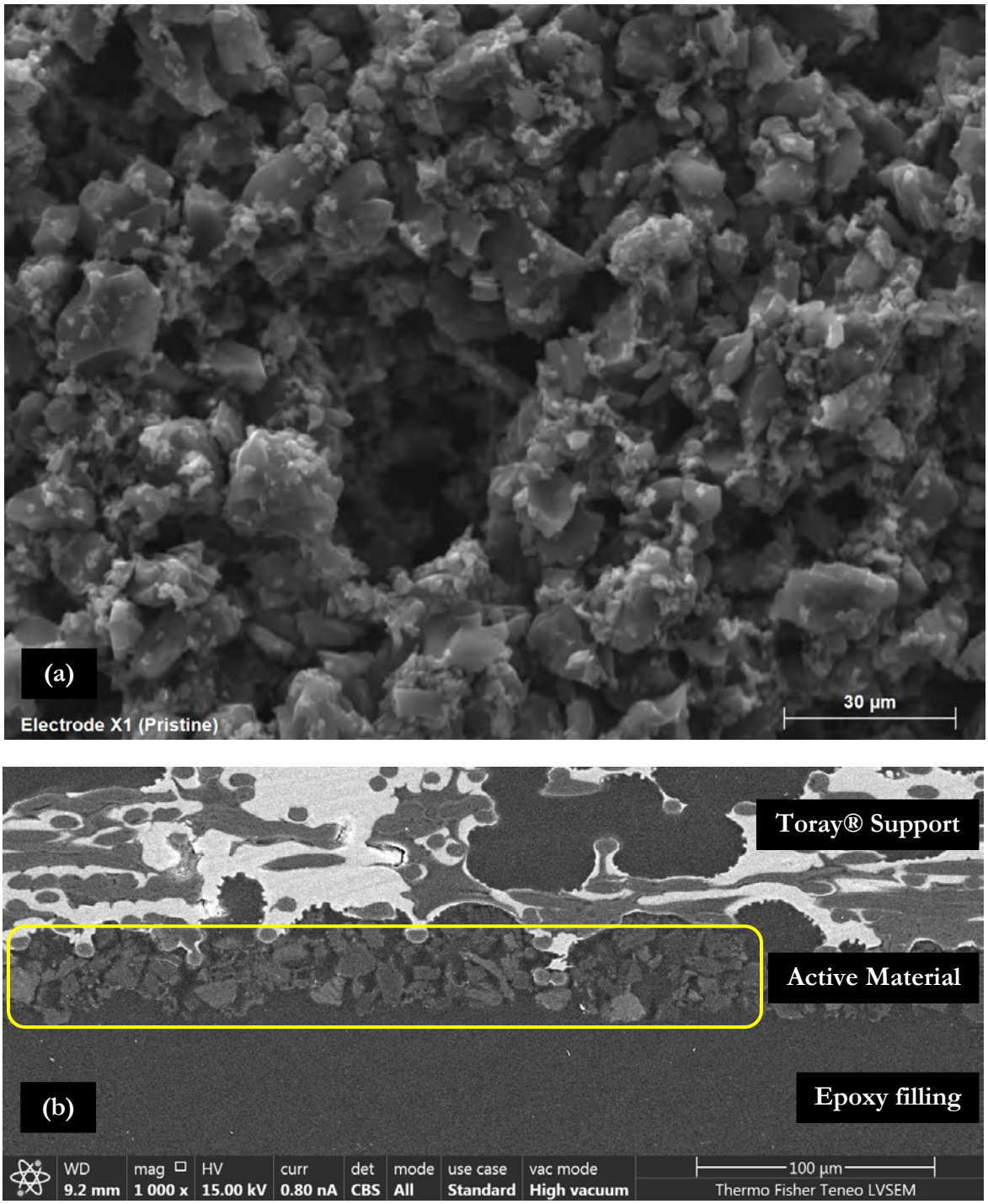

Figure 3.3 SEM image of an electrode at beginning-of-life conditions showing (a) the electrode morphology (acquired with an electron accelerating voltage of 15 kV, using a spot size of 4) and (b) the electrode cross section containing the active material (i.e., activated carbon) and the carbon fiber paper used as a support (i.e., Toray® TGP-H-120)

3.2 Baseline Degradation: Effect of Dissolved Oxygen

The effect of dissolved oxygen was studied by performing degradation experiments under anaerobic and aerobic conditions using a three-electrode electrochemical cell, a working electrode potential of 1.2 V vs RHE and a half cycle time of 5 minutes. In all cases, the discharge potential was equal to the open circuit potential measured at the beginning of each set of cycles (a detailed table has been included in Appendix A). This was done to provide further evidence that dissolved oxygen does not directly partake in the corrosion process happening at the anodic side of the cell. Moreover, these experiments served as a benchmark to compare degradation in the presence of different concentrations of SRNOM and Fe^{2+}.

Selected cyclic voltammograms at different electrode degradation stages are presented in Figures 3.4 and 3.5. For both, N_2 and O_2 saturated experiments, the capacitive or rectangular response of the electrode deteriorated over time. Specifically, the area under the current-potential curve decreased as cycling proceeded. This correlated to a reduction in the electrode capacitance, as displayed in Figure 3.6. An additional feature observed in the voltammograms is the slanted response of the reverse scan, which could be attributed to an increase in resistivity. This resulted in a loss of symmetry, which prevented the localization of the current maximum of the reverse scan associated with the E_{PZC}. Given the recurrence of this behaviour, the E_{PZC} values herein reported were referred only to the potential coupled with the current minimum of the forward scan. In accordance with the study by Tobias & Soffer (1983) [53], careful inspection of the voltammograms resulted in noting that this feature progressively shifts to more positive values as surface oxidation proceeded. These values are shown in Figure 3.7. Another interesting characteristic of the voltammograms was the sudden current change at the extremes of the potential window. Towards the upper potential limit, the increase in current after 0.8 V vs RHE

can be attributed to the occurrence of carbon oxidation and, closer to the 1.0 V vs RHE, to water electrolysis (due to the initially neutral electrolyte). It is important to consider then, that a fraction of the loss of capacitance and shift of the E_{PZC} might have been caused as a result of the cyclic voltammetry due to carbon oxidation and water electrolysis (due to shielding of active sites by oxygen). Nonetheless, one would expect most of the electrode degradation to have occurred during the cycling protocol, where a potentiostatic charge step at 1.2 V vs RHE was used. As was previously mentioned, one of the by-products of the corrosion process and water electrolysis is the generation of H^+. As a result, the initially neutral electrolyte became acidic and the water electrolysis and carbon oxidation potential shifted to higher values according to equation 3.1:

$$E = E^0 - 0.059 \cdot pH \tag{3.1}$$

where E^0 is the standard reduction potential. Therefore, as the electrolyte became acidic, the occurrence of these reactions was diminished given the reduced voltage difference applied (i.e., the difference between the applied potential and theoretical potential, E, in equation 3.1). As the number of performed cycles increased, the current peaks decreased gradually and suggested that carbon oxidation and some, unidentified, reduction processes occurring at the limits of the scan progressively slowed down upon continuous cycling. It is important to recall that each characterization started with fresh electrolyte, which was at neutral pH. Therefore, the decrease in the peaks, especially those near the upper potential window, was not the result of a reused acidic electrolyte.

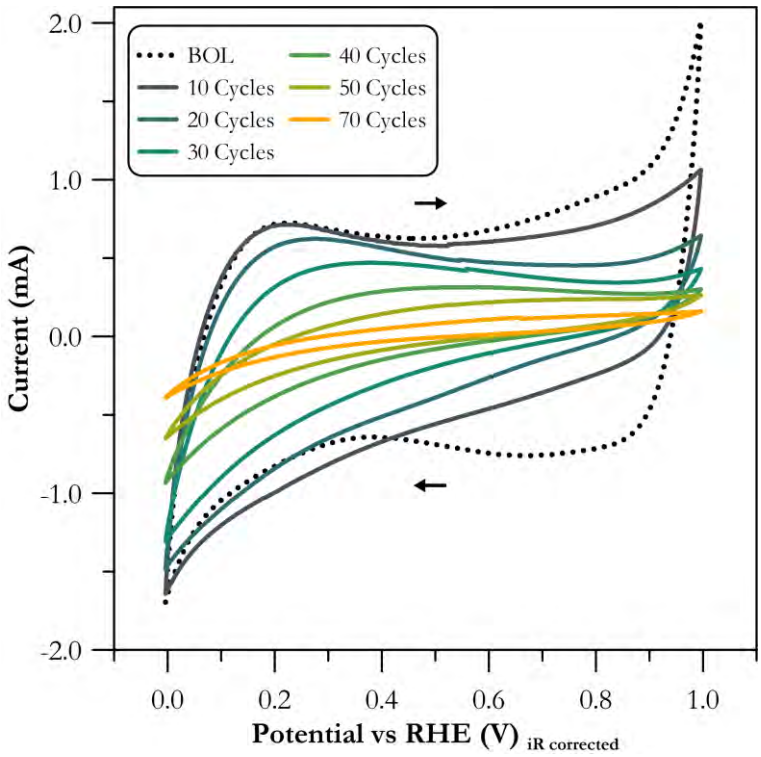

Figure 3.4 Selected cyclic voltammograms obtained at 1 mV s^{-1} and 17.1 mM deaerated NaCl at room temperature for electrodes cycled under anaerobic conditions at a working electrode potential of 1.2 V vs RHE and a half cycle time of 5 min

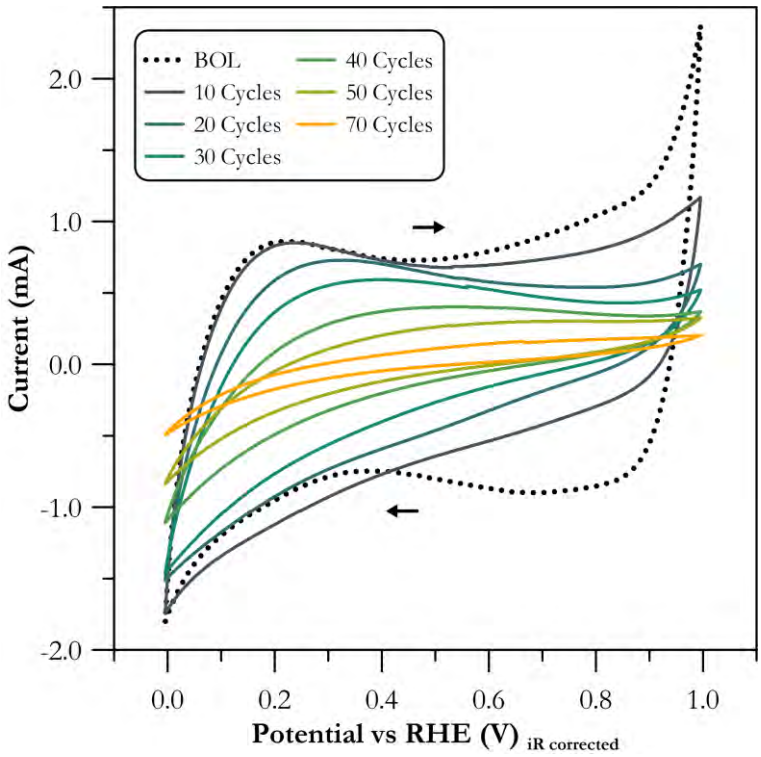

Figure 3.5 Selected cyclic voltammograms obtained at 1 mV s^{-1} and 17.1 mM deaerated NaCl at room temperature for electrodes cycled under aerobic conditions at a working electrode potential of 1.2 V vs RHE and a half cycle time of 5 min

The effect of dissolved oxygen on the loss of capacitance and shift of the E_{PZC} is presented in Figures 3.6 and 3.7, respectively. These figures show that in the absence of dissolved oxygen, both capacitance and E_{PZC} show no remarkable difference when compared to the ones obtained under oxygen saturation. However, in both cases there is a decrease in capacitance and a positive shift of the E_{PZC} with cycling. From a practical perspective, the electrodes only lasted 300 min when cycled at a potential of 1.2 V vs RHE. It is important to note that in the case of tests conducted under nitrogen saturation, oxygen, although it was purged from the solution, might have been generated as a result of the cycling potential applied. In particular, this could be significant during the first few cycles of each set of cycles performed, because of the initially neutral electrolyte (i.e., pH of 7.04 ± 0.06). At this pH, the potential for OER is 0.814 vs RHE,

meaning that a voltage difference of ~0.4 V was applied. As the system became acidic, due to the occurrence of oxidation processes, the voltage difference applied decreased but remained positive and thus, theoretically, the applied potential was large enough to drive the OER. For instance, at the end of the first 5 cycles, a final pH of ~3 was measured. At this pH, the potential for OER is 1.05 V vs RHE and the voltage difference applied was 0.15 V. As the final pH of the electrolyte increased with the set of cycles performed (see Figure 3.10), the voltage difference was always positive (i.e., the applied potential was, theoretically, large enough to drive the OER), and oxygen may have been used to oxidize the electrode, contributing also to the accumulation of charge and production of H^+ (see Figures 3.9 and 3.10). However, the small differences observed between the anaerobic and aerobic cases suggest that most of the oxidation occurred through the donation of oxygen by water to functionalize the electrode surface or evolve CO_2. The effect of dissolved oxygen is further discussed in section 3.5, where a comparison between anaerobic and aerobic environments is presented by contrasting the results obtained using a 2-electrode cell setup. Finally, it is important to note that no visual confirmation of gas evolution was observed during the experiments. On the other hand, the potential window available for electrosorption, defined by the difference between the electrode E_{PZC} and the oxygen evolution reaction (OER) potential, quickly reduced as cycling progressed. It is important to recall that the OER potential depends on the pH. Therefore, the operational window of the electrode will change according to the solution pH (and the electrode E_{PZC}).

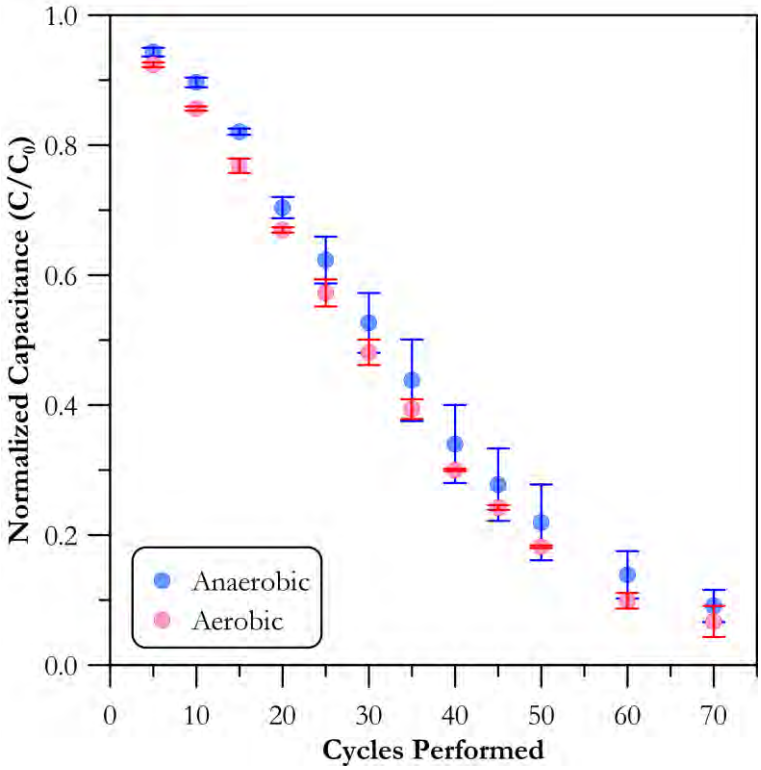

Figure 3.6 Normalized capacitance as a function of the number of cycles performed under N_2 or O_2 saturation at a working electrode potential of 1.2 V vs RHE with a half cycle time of 5 min and at room temperature. Error bars represent the range between two replicates

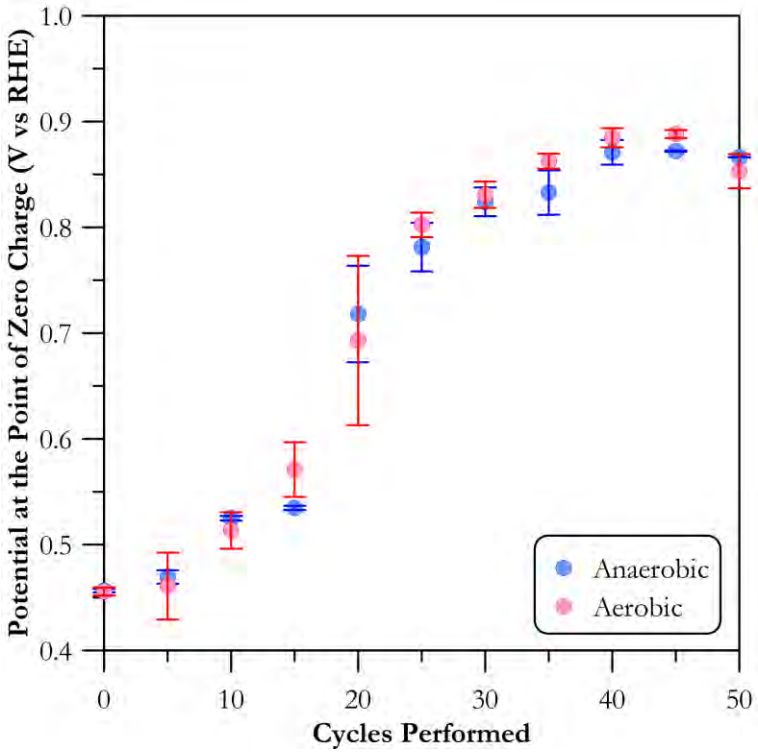

Figure 3.7 E_{PZC} profiles as a function of the number of cycles performed under N_2 or O_2 saturation at a working electrode potential of 1.2 V vs RHE with a half cycle time of 5 min and at room temperature. Error bars represent the range between two replicates

The accumulation of charge at the end of each set of cycles performed shown in Figure 3.9 followed a power-law decrease up until the 50th cycle. Charge can be calculated by integration of the current-time response with respect to time, following equation 3.2:

$$Electric\ Charge\ (coulombs) = \int_{t_1}^{t_2} i\ dt \qquad (3.2)$$

where i is the current in amperes, t_1 and t_2 the time in seconds at the beginning of the charge or discharge step and at end of the charge or discharge step, respectively. To calculate the accumulation of charge, the portions of the charge and discharge steps of the cycling protocol were treated separately. Then, the cumulative charge can be calculated for every cycle and its value

corresponds to the addition of the charging and discharging portions of the cycle. Figure 3.8 presents an equivalent, more visual form to observe the process of accumulation of charge. In this figure, with aid of the EC-LAB software (Biologic), the cumulative charge from the beginning of the experiments as a function of time is presented. As mentioned earlier, the values presented in Figure 3.9 are then the ones at the end of each set of cycles.

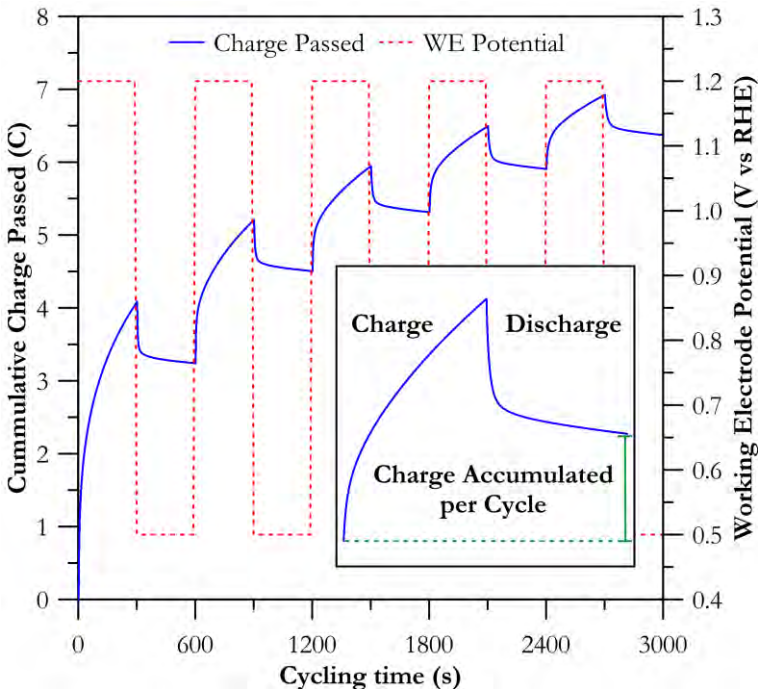

Figure 3.8 Cumulative charge passed as a function of cycling time for the first 5 cycles performed under aerobic conditions, a working electrode potential of 1.2 V vs RHE and a half cycle time of 5 min. The red dotted line represents the potentiostatic cycling protocol used. The insert shows the data for cycle number 3 and the charge accumulated is graphically represented by the green line

On the other hand, the H^+ production shown in Figure 3.10, followed an exponential decrease. pH was measured at the beginning and end of every set of cycles performed with a pH probe (Hanna Instruments). H^+ transport through the Nafion™ membrane, used to separate the two cell compartments, was not taken into account. From the value of pH recorded, the amount of H^+ in the solution was calculated using equation 3.3. The change in H^+ then was calculated

following equation 3.4. The H^+ produced was calculated by multiplying the change in $[H^+]$ by the electrolyte volume used per compartment, which was 100 mL. An important consideration to have in mind is the accuracy of the pH measurements, given that they were performed in solutions with high ionic strength (i.e., containing 1 M NaCl and in some cases, 0.1 M HCl or 0.1 M NaOH) and that the activity of H^+ could have been affected, introducing an uncertainty in the pH measurement and $[H^+]$ calculation, as per the definition of pH (see equation 3.5), where γ is the activity coefficient.

$$[H^+] = 10^{-pH} \tag{3.3}$$

$$\Delta[H^+] = [H^+]_{final} - [H^+]_{initial} \tag{3.4}$$

$$pH = -\log_{10}([H^+] \cdot \gamma_{H^+}) \tag{3.5}$$

In these two figures, the similarity observed between the anaerobic and aerobic tests strengthened the hypothesis that dissolved oxygen does not directly participate in the carbon corrosion process. On the other hand, the relatively large accumulation of charge and production of H^+ observed during the first 20 cycles could be explained by water electrolysis and also the presence of prone to be oxidized carbon-based features such as surface defects, as explained by Avasarala et al. (2010) [36] when studying Vulcan XC-72 (i.e., carbon black) for PEMFC applications. Consequently, these features had a negligible contribution to the electrode capacitance. This is supported by the relatively linear decrease in capacitance observed between the 10^{th} and 50^{th} cycle. The loss of capacitance is due to the loss active sites as a result of two phenomena: evolution of surface oxides at the electrode surface, which modify the electrode E_{PZC}, and evolution of carbon dioxide (see Figure 3.11), which could impact the porous network (i.e., coalescence of pores), thereby decreasing the electrode surface area. Kinoshita & Bett (1973) [76], while studying the oxidation of carbon black (Neo Spectra), reported that the growth of oxide

film with time followed a power law and that it was dependent, also, on the applied potential. In addition, it was observed that CO_2 was generated simultaneously and became the primary oxidation process at longer times. This was the result of a decrease in the rate of formation of surface oxides, which was the primary oxidation process at shorter times. The authors proposed that these two processes were independent of one another, and that the continuous generation of surface oxides involved the diffusion of a reactant (i.e., water) through the oxide later for its reaction with an active site. On the other hand, oxidation to CO_2 occurred at active sites located on edge planes and through gasification of surface oxides. With regards to the role of water electrolysis, as noted earlier, the process of oxygen evolution could be contributing to the accumulation of charge and H^+ production presented in Figures 3.9 and 3.10 as a result of the voltage difference applied, considering the electrolyte pH (i.e., neutral at the beginning of each set of cycles performed) and the applied potential (i.e., 1.2 V vs RHE).

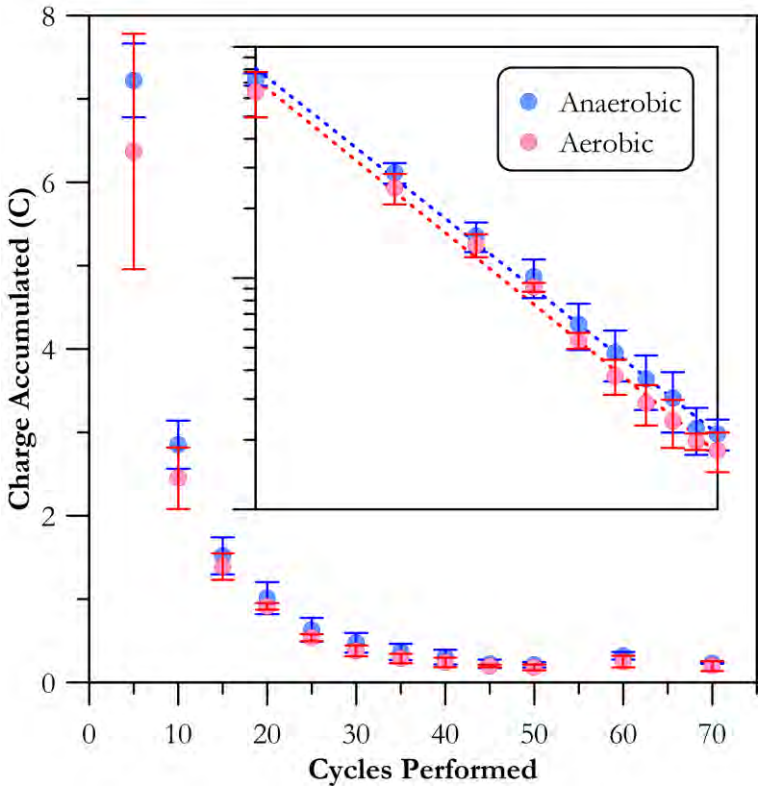

Figure 3.9 Charge accumulated per set of cycles performed as a function of the number of cycles performed under N_2 or O_2 saturation at a working electrode potential of 1.2 V vs RHE with a half cycle time of 5 min and at room temperature. Error bars represent the range between two replicates. Insert shows the power law relationship between the charge accumulated and cycles performed up until the 50th cycle

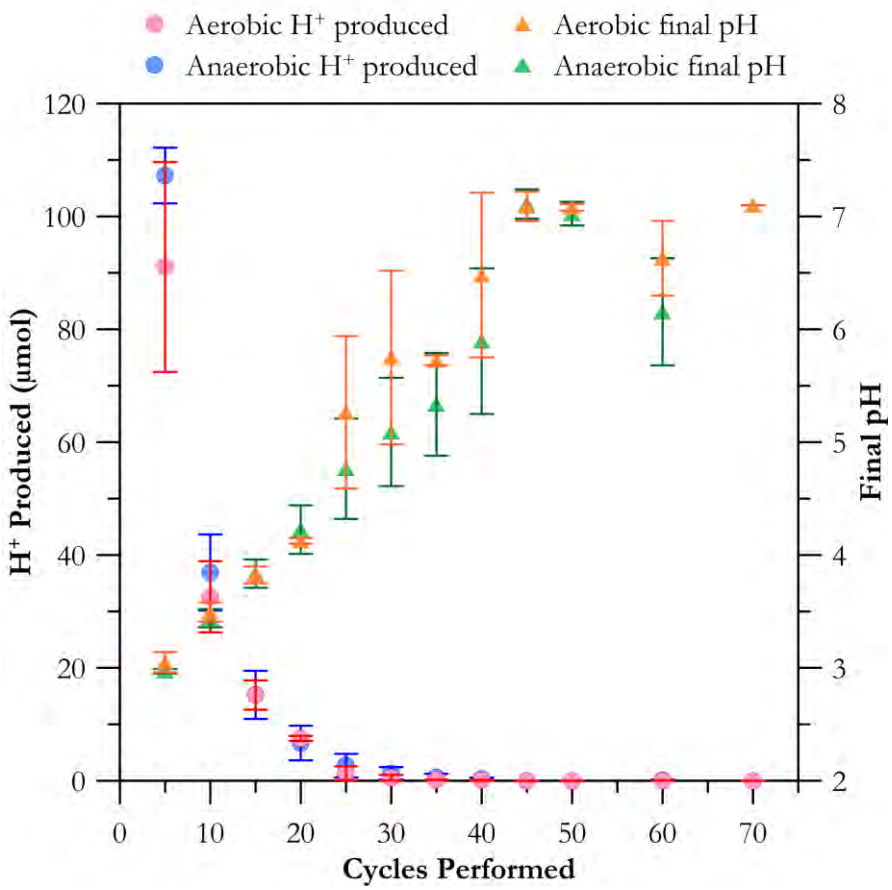

Figure 3.10 H^+ produced per set of cycles performed and final pH profiles as a function of the number of cycles performed under N_2 or O_2 saturation at a working electrode potential of 1.2 V vs RHE with a half cycle time of 5 min and at room temperature. Each set of cycles performed began with fresh, unbuffered electrolyte with a pH of 7.06 ± 0.06. Error bars represent the range between two replicates

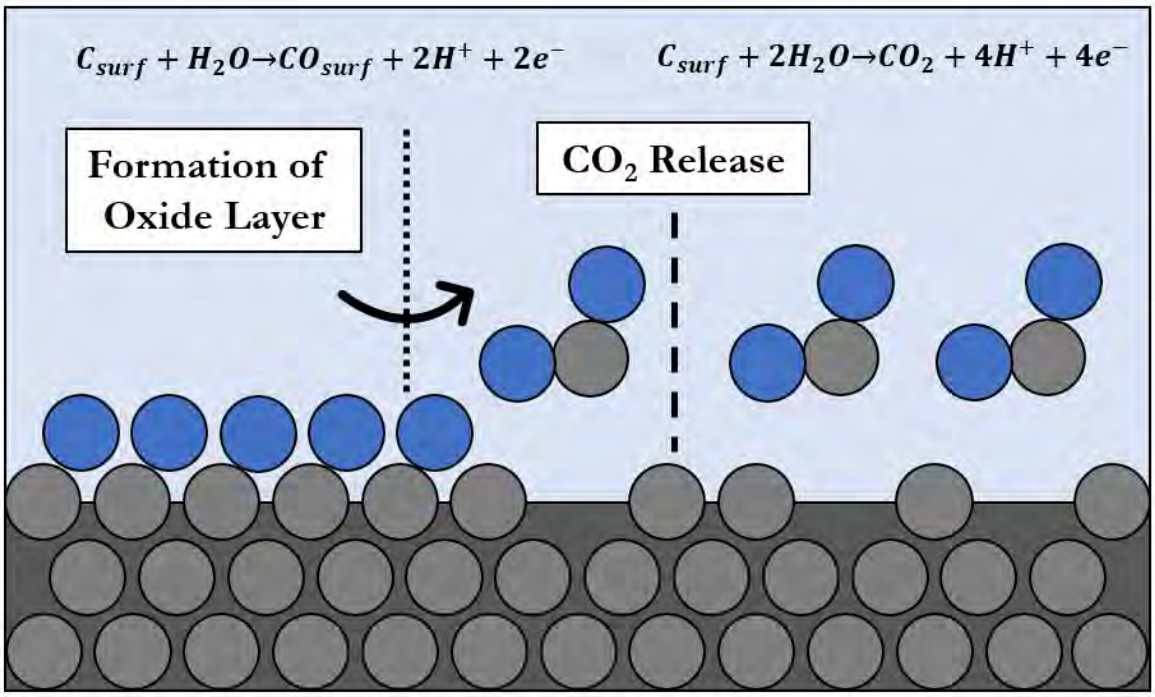

Figure 3.11 Schematic of the carbon corrosion process and its impact on the electrode surface. The two reactions occur simultaneously and independent of one another. The formation of an oxide layer reduces the amount of available active sites and the evolution of CO_2 reduces the electrode surface area

Additionally, the oxygen to carbon ratios (O/C) shown in Table 3.1 suggest that oxygen was incorporated in the electrode surface during the first 15 to 20 cycles. Specifically, the oxygen content approx. quadrupled during this time frame (see the normalized capacitance point, C/C_0, at a value of 0.8), then remained rather stable at values of C/C_0 close to 0.6 and 0.4. Interestingly, at end-of-life (EOL) the O/C ratio displayed a reduction of 4% and 5% for the aerobic and anaerobic case, respectively. This could be related to the evolution of CO_2 from the electrode surface. Changes in the electrode wettability could also be used to evaluate the extent of electrode oxidation. The values for the contact angle, also presented in Table 3.1, showed a substantial change during the first 15 to 20 cycles, hence indicating a decrease in hydrophobicity with oxygen incorporation in the electrode. FTIR analysis was challenging due to scattering and the curved

baseline response of the collected spectrum. To perform the analysis, the collected raw FTIR spectrum at different C/C_0 values was normalized relative to the corresponding spectrum (i.e., anaerobic or aerobic) at the end-of-life (EOL) and was background corrected (refer to Appendix A.4 for the raw and normalized FTIR spectra). The EOL spectrum was used as a reference, as it could be hypothesized that it possessed a fully developed surface oxide layer and electrodes with higher C/C_0 values could show qualitative differences as the oxide layer may have not covered some areas of the electrode. In the normalized and background corrected spectrum, a positive change in transmittance change can be correlated with a decrease in absorption with respect to the reference spectrum. Furthermore, the background correction was only performed to regions associated with the absorption by oxygen functionalities that showed a narrow, sharp peak. Analysis of broad peaks were avoided due to the error associated with establishing the background absorption curve.

With these considerations, there were no major differences noted between the reference and electrodes at different C/C_0 values. This observation agrees with the proposed carbon corrosion mechanism where a surface oxide layer will form, grow and extend to deeper areas of the electrode. In addition, FTIR only scans the most top layer of the material and is only a qualitative analysis technique. In this sense, the use of other techniques that offer quantitative results, such as x-ray photoelectron spectroscopy (XPS) can be helpful to elucidate the ratio of oxygen functional groups formed during the corrosion process. Finally, cross-sectional SEM image analysis (provided in Appendix A) indicated that, at EOL under aerobic conditions, the electrode bulk porosity increased slightly from an initial value of 51.6% ± 3.8% to a value of 56.9% ± 1.8%.

Table 3.1 Oxygen to carbon ratios and contact angle for electrodes at different degradation stages (i.e., C/C_0) after cycling at a working electrode potential of 1.2 V vs RHE with a half cycle time of 5 min at room temperature under anaerobic (1 M NaCl, N_2 saturated) and aerobic conditions (1 M NaCl, O_2 saturated)

C/C_0	O/C^2 x 10^2		Contact Angle (degrees)[3]	
	Anaerobic	Aerobic	Anaerobic	Aerobic
BOL[4]	5.22 ± 1.70		131± 2.4	
0.8	21.1 ± 0.52	20.5 ± 0.70	37 ± 1.7	32 ± 0.3
0.6	22.4 ± 0.52	21.9 ± 0.58	39 ± 3.1	29 ± 5.1
0.4	20.3 ± 0.70	21.5 ± 0.23	28 ± 3.4	32 ± 1.2
EOL	15.0 ± 3.62	17.8 ± 1.66	27 ± 3.1	39 ± 3.5

3.3 Degradation in the Presence of Scaling and Fouling Solutes

3.3.1 Effect of Iron (Fe^{2+})

Iron (as Fe^{2+}) is a typical constituent of groundwater and it has been reported to have an adverse effect on the desalination performance of CDI systems [15], [19]. The scaling nature of iron arises from the possible formation of insoluble species such as iron (III) hydroxide and iron (III) oxide. As noted in section 1.4.4, the speciation of iron in CDI systems is closely related to the electrolyte pH, the applied potential and dissolved oxygen. These precipitates might restrict access to active sites, and thus reduce the electrode capacitance, and modify the surface charge of the electrode, affecting the electrode E_{PZC}.

To test the effect of iron on these electrochemical properties and other morphological features such as oxygen surface functionalities and wettability, tests were conducted with solutions containing 0.2, 2.0 and 20 mg Fe^{2+} L^{-1} (3.58, 35.8 & 358 μM $FeCl_2$ L^{-1}) using a three-electrode cell setup, a working electrode potential of 1.2 V vs RHE and a half cycle time of 5 minutes. In all cases, the discharge potential was equal to the open circuit potential measured at the beginning of

[2] Uncertainty represents the propagation of error attributed to the averages and standard deviations obtained from three EDS elemental composition analyses
[3] Uncertainty represents the standard error
[4] BOL refers to a pristine, unwetted electrode

each set of cycles (a detailed table has been included in Appendix A). Solutions were prepared with Fe^{2+} to replicate the typical groundwater iron speciation. Nonetheless, as previously mentioned, once in solution, the speciation will be determined by variables such as pH and potential, as well as the presence of dissolved oxygen. The profile of capacitance loss is displayed in Figure 3.12 for different Fe^{2+} concentrations. As mentioned before, a small contribution to the loss of capacitance and E_{PZC} shift can be expected from carbon oxidation occurring as a result of the upper potential limit of the cyclic voltammetry scan (1.0 V vs RHE) and electrolyte pH. Additionally, oxygen evolved during cyclic voltammetry (upper potential limit of 1.0 V vs RHE) and cycling at 1.2 V vs RHE could be trapped in the vicinity of the pores, preventing the access to active sites. These curves revealed the scaling potential of iron, even at the lowest tested concentration of 0.2 mg Fe^{2+} L^{-1}. The loss of capacitance was more pronounced at higher levels of 2.0 and 20 mg Fe^{2+} L^{-1}, although no notable difference was observed for these two levels. In contrast with the baseline results (i.e., under aerobic conditions) where 90% of the initial capacitance was lost after 300 min of operation at 1.2 V vs RHE, the trials conducted in the presence of iron reached this value around the 45^{th} cycle (i.e., 225 min at 1.2 V vs RHE). Another interesting feature appeared during the first five cycles. As iron concentration increased, the loss of capacitance slowed down, when compared to that of the baseline. In fact, for the trial at 20 mg Fe^{2+} L^{-1}, a capacitance slightly larger than the initial value was calculated. This could be the result of the combined effect of pseudo-capacitance and an increase in resistivity arising from the initial formation of iron-based deposits. This hypothesis was based on the slight increase (~5%) of the shaded area observed in the cyclic voltammogram (see Figure 3.11). In fact, several studies have reported the pseudocapacitive properties of Fe_2O_3 [77]–[79]. The effect of resistivity was also noted in the reverse scan of the voltammogram and in the increase of the depressed semicircle

diameter (i.e., associated with ion accumulation at the electrode-electrolyte interface [19] and the development of oxygen surface functionalities [80]) of the Nyquist plot presented in Figure 3.13. Moreover, the E_{PZC} profiles, shown in Figure 3.14, displayed a decrease in voltage up to approx. 130 mV when compared to the baseline E_{PZC}. The initial effect of this occurrence was compensated by the formation of surface oxides, hence the overall positive shift of the E_{PZC}. However, over the duration of the cycling experiments, the E_{PZC} values for the iron trials were consistently lower than those of the baseline. The profiles for charge accumulation and production of H^+ presented respectively in Figures 3.15 and 3.16, showed similar behaviour to that of the baseline (i.e., power-law decrease in the accumulation of charge and exponential decrease in the production of H^+). Moreover, most obvious differences appeared during the first 15 to 20 cycles. When compared to those of the baseline case, both charge accumulation and H^+ produced are slightly lower for the experiments performed in solutions containing iron. This could be attributed to the initial pH of the electrolyte. These were 6.47 ± 0.10, 5.63 ± 0.08 and 5.45 ± 0.14 for the solutions containing 0.2, 2.0 and 20 mg Fe^{2+} L^{-1}, respectively. The slightly more acidic electrolytes will reduce the voltage difference applied (i.e., the difference between the applied potential and the theoretical potential required to drive the water electrolysis and carbon oxidation reaction is reduced as pH decreases), especially during the first cycles of each set performed. For instance, the voltage difference applied for OER at the initial pH condition was 0.35, 0.30 and 0.29 V (compared to the 0.39 V observed under baseline conditions) for the solutions containing 0.2, 2.0 and 20 mg Fe^{2+} L^{-1}, respectively. Therefore, as with the baseline case but to a slightly lesser extent, some of the charge accumulated and the produced H^+ could be ascribed to the process of oxygen evolution.

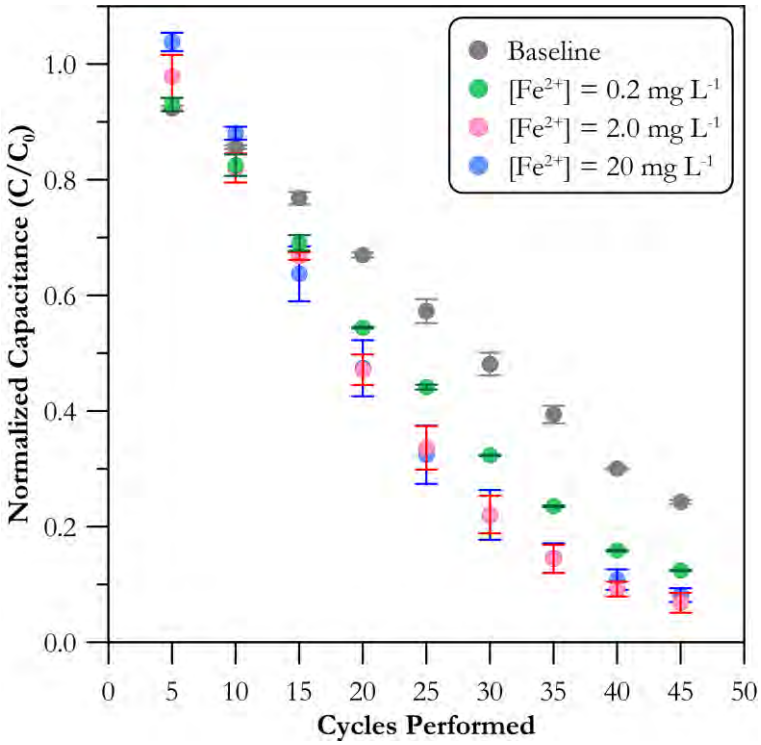

Figure 3.12 Normalized capacitance as a function of the number of cycles performed under O_2 saturation at a working electrode potential of 1.2 V vs RHE with a half cycle time of 5 min and different Fe^{2+} concentrations (from $FeCl_2$) at room temperature. Gray markers provided as a reference for baseline results. Error bars represent the range between two replicates

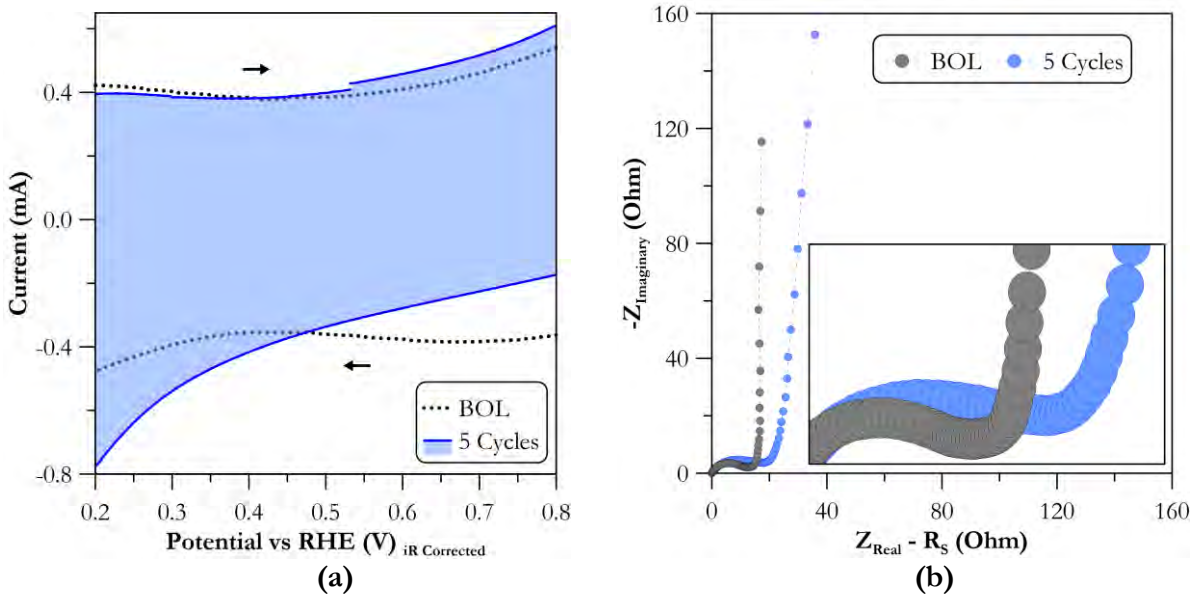

Figure 3.13 (a) Cyclic voltammograms obtained at 1 mV s^{-1} in 17.1 mM deaerated NaCl and (b) complex impedance plane plots obtained at 0.5 V vs RHE between 350 kHz – 5 mHz in 17.1 mM deaerated NaCl for the electrode at the beginning-of-life (BOL) and after 5 cycles at 1.2 V vs RHE with a half cycle time of 5 min in the presence of 20 mg Fe^{2+} L^{-1} (358 μM $FeCl_2$ L^{-1})

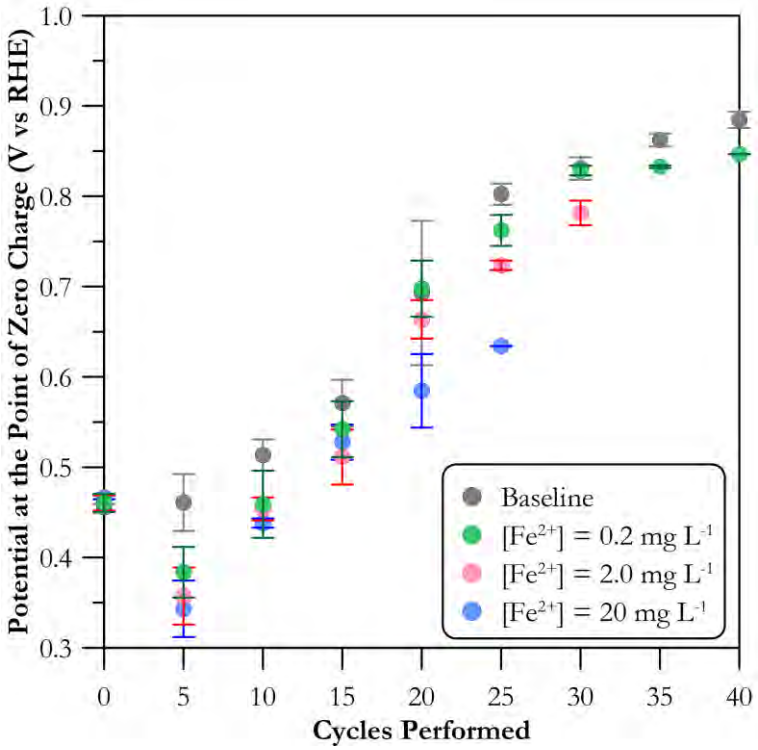

Figure 3.14 E_{PZC} profiles as a function of the number of cycles performed under O_2 saturation at a working electrode potential of 1.2 V vs RHE with a half cycle time of 5 min and different Fe^{2+} concentrations (from $FeCl_2$) at room temperature. Gray markers provided as a reference for baseline results. Error bars represent the range between two replicates

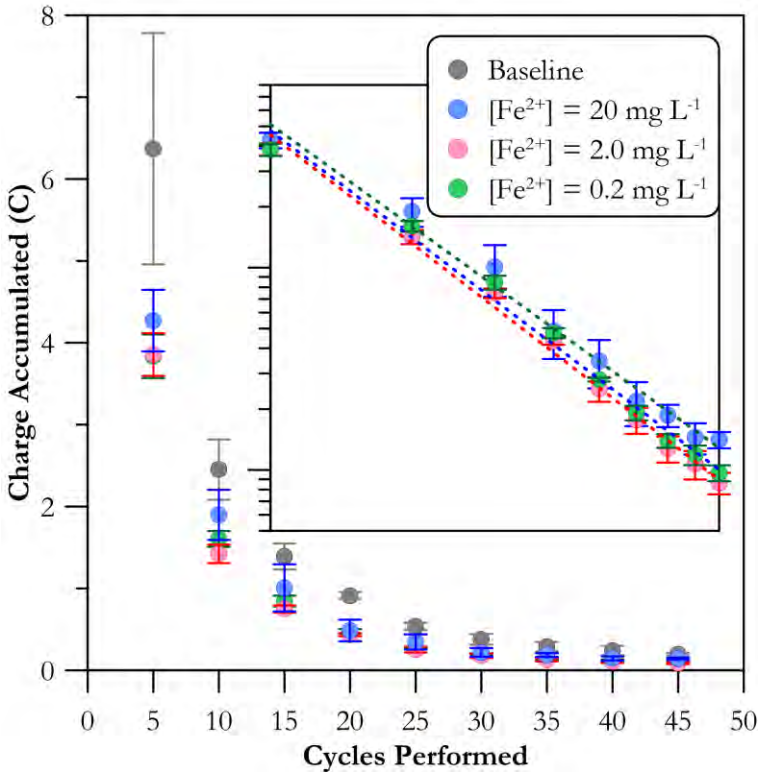

Figure 3.15 Charge accumulated per set of cycles performed as a function of the number of cycles performed under O_2 saturation at a working electrode potential of 1.2 V vs RHE with a half cycle time of 5 min and different Fe^{2+} concentrations (from $FeCl_2$) at room temperature. Gray markers provided as a reference for baseline results. Error bars represent the range between two replicates. Insert shows the power law relationship between the charge accumulated and cycles performed

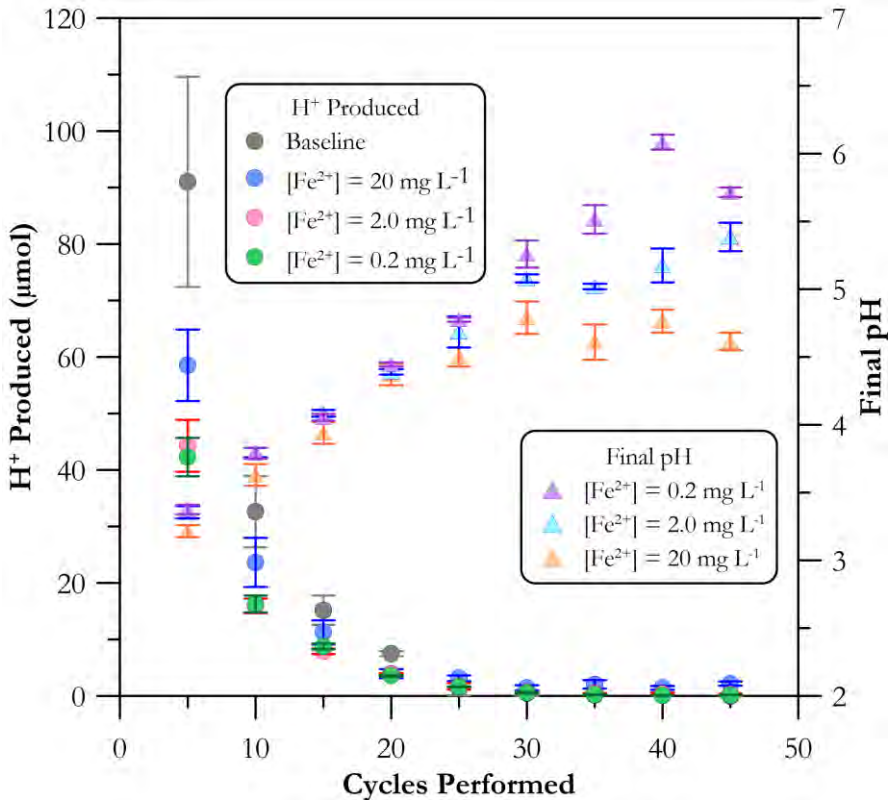

Figure 3.16 H^+ produced per set of cycles performed and final pH profiles as functions of the number of cycles performed under O_2 saturation at a working electrode potential of 1.2 V vs RHE with a half cycle time of 5 min and different Fe^{2+} concentrations (from $FeCl_2$) at room temperature. Each set of cycles performed began with fresh, unbuffered electrolyte with a pH of 6.47 ± 0.10, 5.63 ± 0.08 and 5.45 ± 0.14, for the solutions containing 2.0, 2.0 and 20 mg Fe^{2+} L^{-1}, respectively. Gray markers provided as a reference for baseline results. Error bars represent the range between two replicates

As was the case for the baseline, the O/C ratios presented in Table 3.2 show a significant increase (i.e., approx. four times) in oxygen content during the first 15 cycles performed. In addition, Table 3.2 presents the iron to carbon ratio (Fe/C) calculated from elemental analysis. For electrodes cycled under 0.2 and 2.0 mg Fe^{2+} L^{-1}, iron was only found for the last stages of degradation. In contrast, iron content increased progressively over all stages of degradation for the case at 20 mg Fe^{2+} L^{-1}. Similar trends were exhibited by the measured contact angle, as shown

in Table 3.3. A steep increase in wettability occurred during early cycling as the electrode surface became oxidized. Interestingly, the contact angle increased at the EOL conditions for the experiments at 0.2 and 2.0 mg Fe^{2+} L^{-1}. The opposite was observed for the test at 20 mg Fe^{2+} L^{-1}. Furthermore, cross-sectional SEM image analyses (provided in Appendix A) indicated that, at EOL under the presence of 0.2 and 20 mg Fe^{2+} L^{-1}, the electrode bulk porosity had values of 50.8% ± 1.7% and 46.9% ± 2.8%, respectively (at BOL, bulk porosity was 51.6% ± 3.8%). The slightly reduced porosity observed at 20 mg Fe^{2+} could be linked to the coating of larger carbon particles by insoluble iron-based substances such as Fe_2O_3 or $Fe(OH)_3$. The SEM images presented in Figures 3.17, 3.18 and 3.19 correspond to electrodes at the end-of-life cycled in the presence of 0.2, 2.0 and 20 mg Fe^{2+} L^{-1}, respectively, and show very similar morphological features. In fact, they did not show any striking difference than those presented in Figure 3.3 for the electrode at beginning-of-life. However, Figure 3.19 shows a few bright spots that did not appear in Figures 3.17 and 3.18. It is likely that these spots are iron deposits. Analysis of the FTIR spectra followed the treatment described in section 3.2. Qualitatively, the raw FTIR spectra (refer to Appendix A.4) demonstrated the evolution of the same absorption bands associated with oxygen functionalities that develop under baseline conditions. In the normalized and background corrected spectrum, a positive (negative) change in transmittance change can be correlated with a decrease (increase) in absorption with respect to the reference spectrum (i.e., electrode at end-of-life condition). Subtle changes with respect to the reference were observed for the tests performed with 0.2 and 2 mg Fe^{2+} L^{-1} for the O – H and C – O absorption bands (see Figures 3.20 and 3.21).

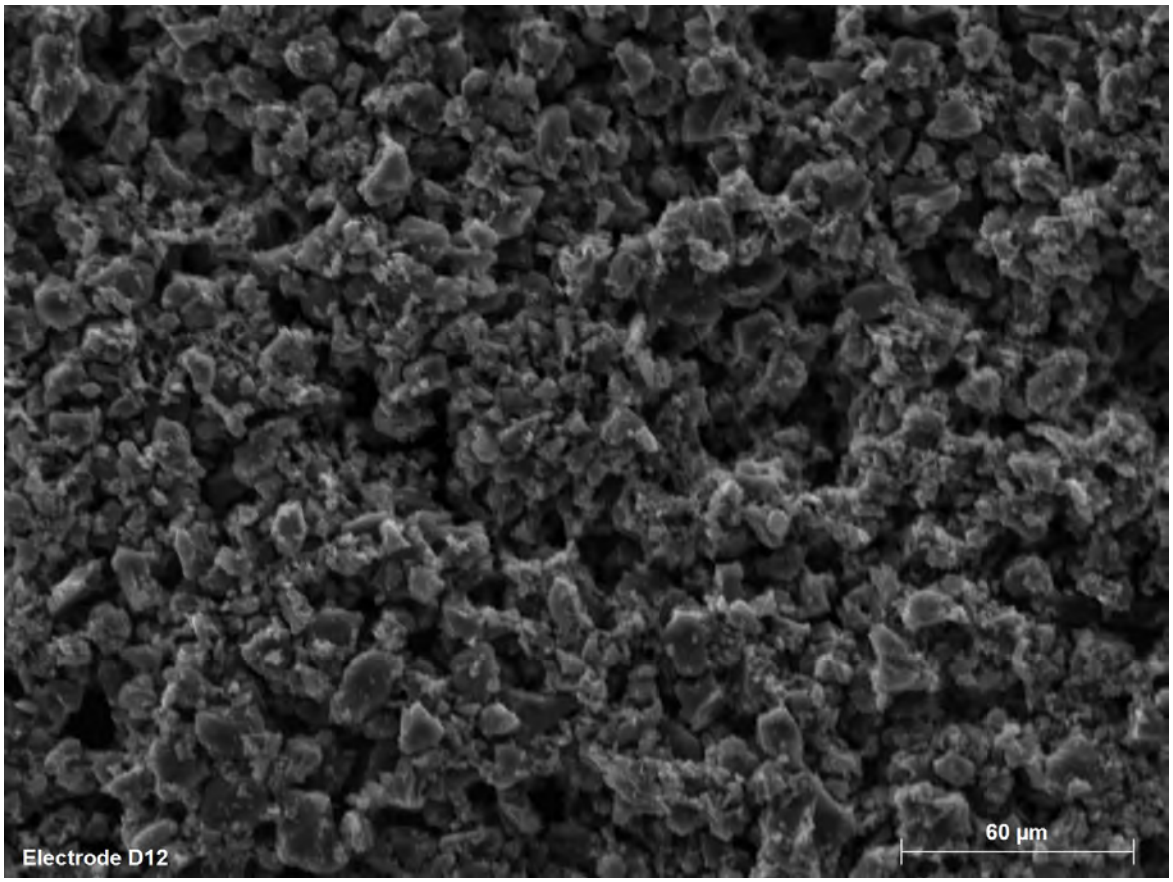

Figure 3.17 SEM image (acquired with an electron accelerating voltage of 15 kV, using a spot size of 4) of an electrode at end-of-life conditions showing the electrode morphology after cycling under aerobic conditions in presence of 0.2 mg Fe^{2+} L^{-1}, at a working electrode potential of 1.2 V vs RHE and a half cycle time of 5 min

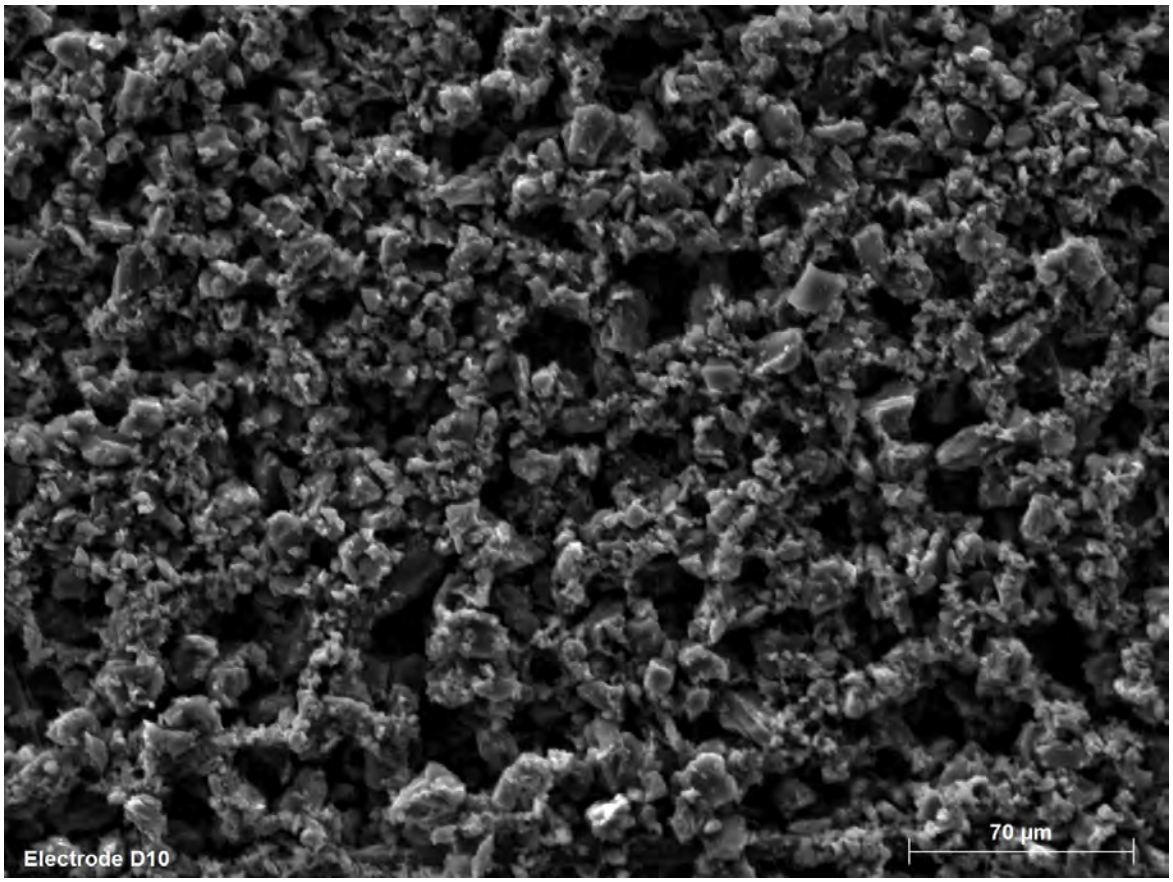

Figure 3.18 SEM image (acquired with an electron accelerating voltage of 15 kV, using a spot size of 4) of an electrode at end-of-life conditions showing the electrode morphology after cycling under aerobic conditions in presence of 2.0 mg Fe^{2+} L^{-1}, at a working electrode potential of 1.2 V vs RHE and a half cycle time of 5 min

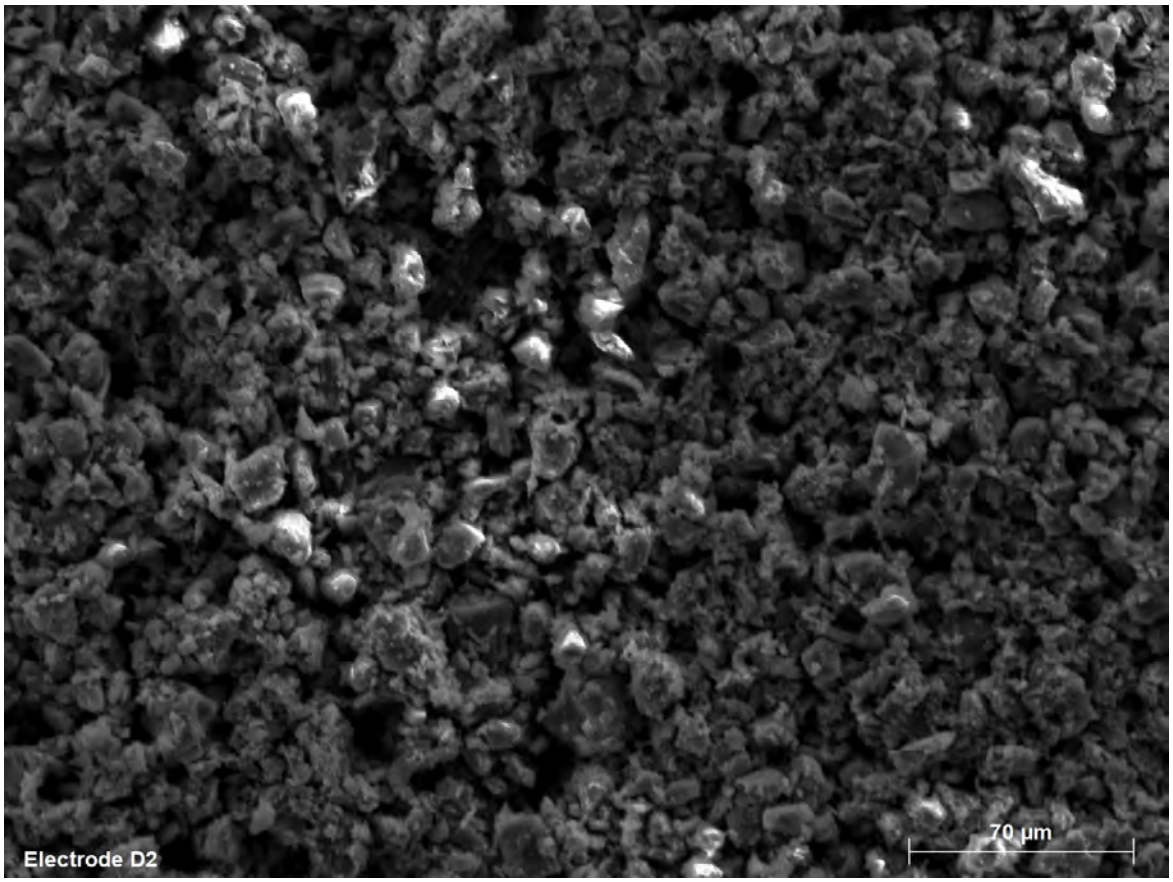

Figure 3.19 SEM image (acquired with an electron accelerating voltage of 15 kV, using a spot size of 4) of an electrode at end-of-life conditions showing the electrode morphology after cycling under aerobic conditions in presence of 20 mg Fe^{2+} L^{-1}, at a working electrode potential of 1.2 V vs RHE and a half cycle time of 5 min

Table 3.2 Oxygen and iron to carbon ratios for electrodes at different points of their lifetime (i.e., C/C_0) after cycling at a working electrode potential of 1.2 V vs RHE with a half cycle time of 5 min, at room temperature and different Fe^{2+} concentrations (3.58, 35.8 & 358 μM $FeCl_2$ L^{-1}). Uncertainty represents the propagation of error attributed to the averages and standard deviations obtained from three EDS elemental composition analyses

C/C_0	0.2 mg Fe^{2+} L^{-1}		C/C_0	2.0 mg Fe^{2+} L^{-1}		C/C_0	20 mg Fe^{2+} L^{-1}	
	O/C x 10^2	Fe/C		O/C x 10^2	Fe/C x 10^{-2}		O/C x 10^2	Fe/C
BOL	5.22 ± 1.70		BOL	5.22 ± 1.70		BOL	5.22 ± 1.70	
0.9	18.4 ± 0.61	<LOD[5]	0.8	19.1 ± 0.44	<LOD	0.7	20.4 ± 0.75	1.13 ± 0.14
0.7	20.2 ± 0.75	<LOD	0.6	19.9 ± 0.65	<LOD	0.5	20.5 ± 0.31	2.18 ± 0.43
0.4	21.1 ± 0.81	<LOD	0.3	21.5 ± 0.45	0.755 ± 0.19	0.3	23.4 ± 0.57	3.90 ± 1.23
EOL	13.9 ± 5.16	$8.32 \times 10^{-4} \pm 7.29\ 10^{-5}$	EOL	18.2 ± 3.74	1.56 ± 0.55	EOL	25.8 ± 9.45	5.38 ± 1.35

Table 3.3 Contact angle for electrodes at different points of their lifetime (i.e., C/C_0) after cycling at a working electrode potential of 1.2 V vs RHE with a half cycle time of 5 min, at room temperature and different Fe^{2+} concentrations (3.58, 35.8 & 358 μM $FeCl_2$ L^{-1}). Uncertainty represents the standard error

C/C_0	0.2 mg Fe^{2+} L^{-1}	C/C_0	2.0 mg Fe^{2+} L^{-1}	C/C_0	20 mg Fe^{2+} L^{-1}
	Contact Angle (degrees)		Contact Angle (degrees)		Contact Angle (degrees)
BOL	131± 2.4	BOL	131± 2.4	BOL	131± 2.4
0.9	41 ± 0.7	0.8	35 ± 2.4	0.7	34 ± 0.6
0.7	34 ± 2.0	0.6	38 ± 1.8	0.5	32 ± 0.9
0.4	59 ± 3.5	0.3	47 ± 2.3	0.3	29 ± 1.7
EOL	63 ± 3.7	EOL	58 ± 5.3	EOL	20 ± 1.1

[5] LOD means Limit of Detection

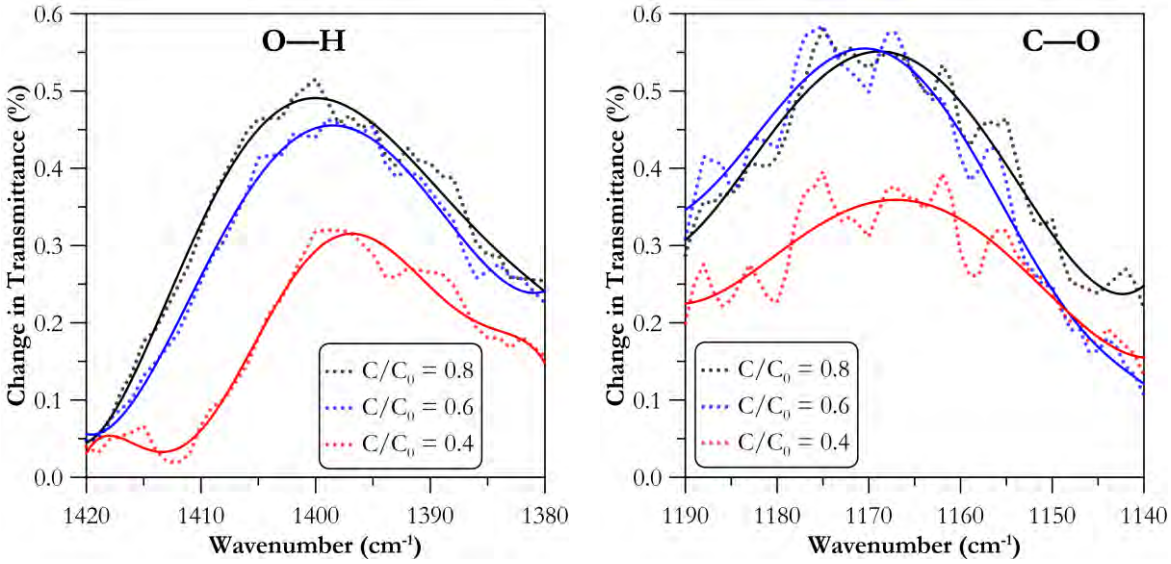

Figure 3.20 Change in transmittance of for the O – H and C – O absorption bands for electrodes cycled with a working electrode potential of 1.2 V vs RHE, a half cycle time of 5 min under aerobic conditions and 0.2 mg Fe^{2+} L^{-1} (3.58 μM $FeCl_2$ L^{-1}) at different degradation stages relative to that exhibited by an electrode at EOL conditions. The dotted lines represent the actual change in transmittance. The solid lines are given to facilitate the visualization of the trend of the data

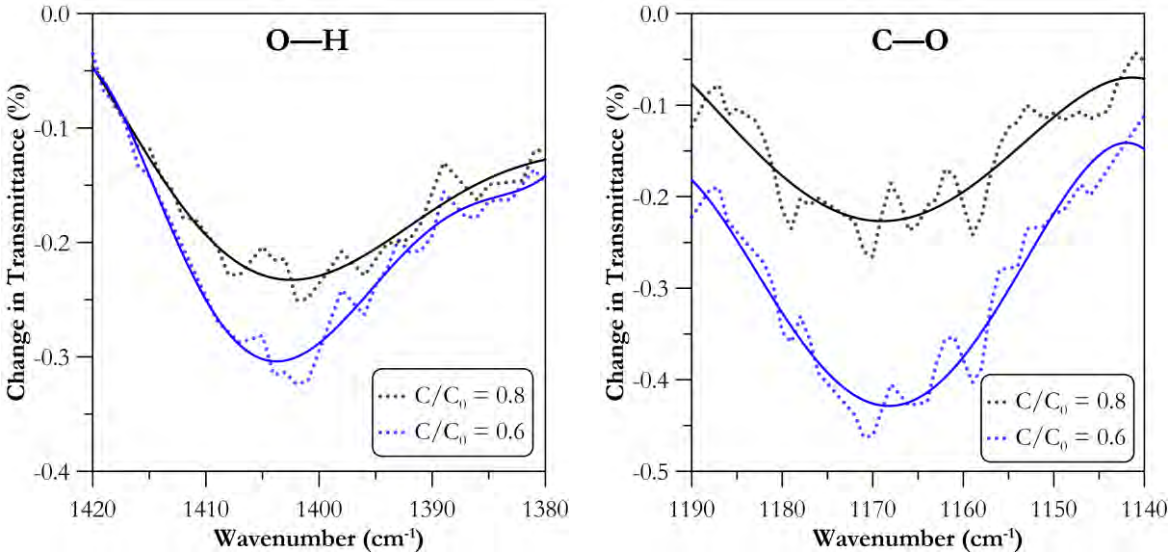

Figure 3.21 Change in transmittance of for the O – H and C – O absorption bands for electrodes cycled with a working electrode potential of 1.2 V vs RHE, a half cycle time of 5 min under aerobic conditions and 2.0 mg Fe^{2+} L^{-1} (35.8 μM $FeCl_2$ L^{-1}) at different degradation stages relative to that exhibited by an electrode at EOL conditions. The dotted lines represent the actual change in transmittance. The solid lines are given to facilitate the visualization of the trend of the data

3.3.2 Effect of Organic Matter

The presence of organic matter in water has been shown to be detrimental to CDI performance due to fouling by physical enmeshment with the porous network [15], [55]. Given its negatively charged nature, organic matter is also attracted to the anode surface and can potentially occupy active sites, thus further reducing the desalination performance. Fouling can also affect electrochemical properties such as capacitance and E_{PZC} due to the numerous functionalities present in the organic matter molecule. In this project, Suwannee River NOM isolate was used as a surrogate for organic carbon found in natural water. Experiments were conducted with electrolytes containing 20 and 40 mg SRNOM L^{-1} using a three-electrode cell setup, a working electrode potential of 1.2 V vs RHE and a half cycle time of 5 minutes. In all

cases, the discharge potential was equal to the open circuit potential measured at the beginning of each set of cycles (a detailed table has been included in Appendix A).

The electrode capacitance loss, shown normalized in Figure 3.22, and the E_{PZC} displayed in Figure 3.23 suggest that SRNOM had, if any, an inconsequential fouling impact. Regardless of the concentration of SRNOM (20 or 40 mg SRNOM L^{-1}), capacitance was lost and the E_{PZC} relocated to more positive values with no substantial difference when compared to those exhibited by electrodes cycled under baseline aerobic conditions. Nonetheless, this should not be taken as an indicative that this type of organic carbon does not affect desalination performance. In other words, although no evidence for physical enmeshment was found, the inherent negative charge of organic matter, competition for active sites cannot be ruled out. However, testing this was out of the scope of this study and has been reported elsewhere [15], [55]. The low fouling potential of SRNOM may be explained by its estimated molecular weight of 1030 Daltons (Da), as reported by Bazri and Mohseni (2016) [81] in their study about the effect of NOM on the suspended ion exchange process. When compared with Suwanee River Humic Acid (SRHA), with an estimated molecular weight of 1540 Da, lower DOC removals were observed and were attributed to the blockage of relatively larger pores by SRHA. In contrast, the relatively smaller SRNOM molecules were able to travel further inside the resin porous structure. Similar results were reported by Dixit et al. (2018) [82] when studying the competitive uptake of Microcystin-LR (MCLR) under presence of different fractions of NOM. In this study, the removal of MCLR was hindered as a result of pore blockage when larger molecular weight fractions of NOM (i.e., SRHA) were present in solution. On the other hand, they hypothesized that NOM fractions with molecular weights below 1000 Da could access smaller micropores and compete for active sites at the resin surface. The results of these studies [81], [82] support the hypothesis that SRNOM, with its relatively lower

molecular weight, did not block the electrode pores. This being said, it would be valuable to conduct experiments with other NOM fractions with higher molecular weight to elucidate the role of this parameter on the occurrence of fouling and the competition for active sites.

Another possible hypothesis for the negligible impact of SRNOM could arise from the structural modification of NOM due to electrooxidation, given the potential applied during cycling. However, this would be an unlikely hypothesis because the electrooxidation of organic matter requires the use of a high oxidation potential electrode, such as boron doped diamond, to allow the generation of OH radicals (E^0 = 2.8 V vs SHE) while inhibiting the process of water electrolysis [83].

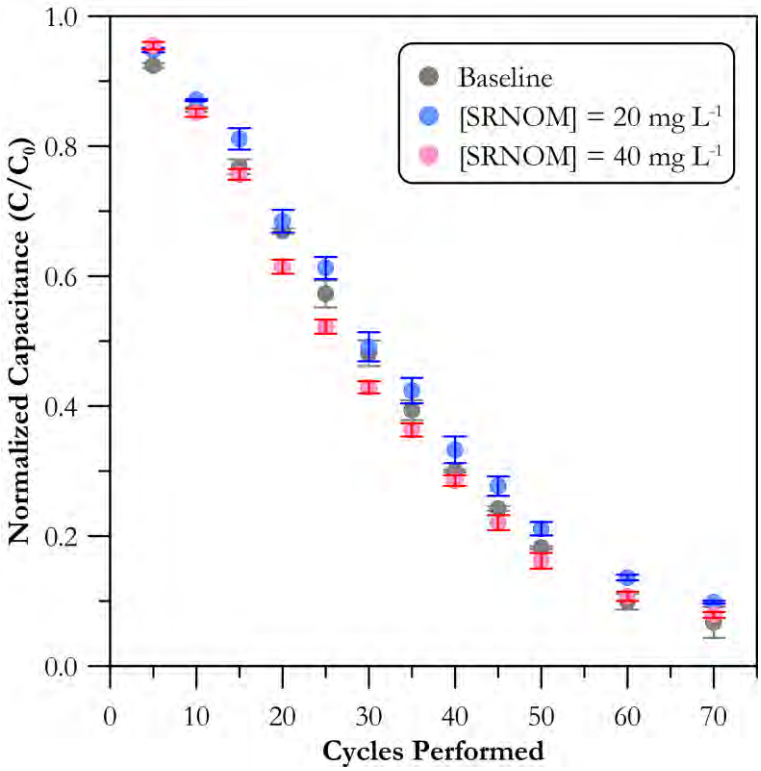

Figure 3.22 Normalized capacitance as a function of the number of cycles performed under O_2 saturation at a working electrode potential of 1.2 V vs RHE with a half cycle time of 5 min, at room temperature and different SRNOM concentrations. Gray markers provided as a reference for baseline results. Error bars represent the range between two replicates

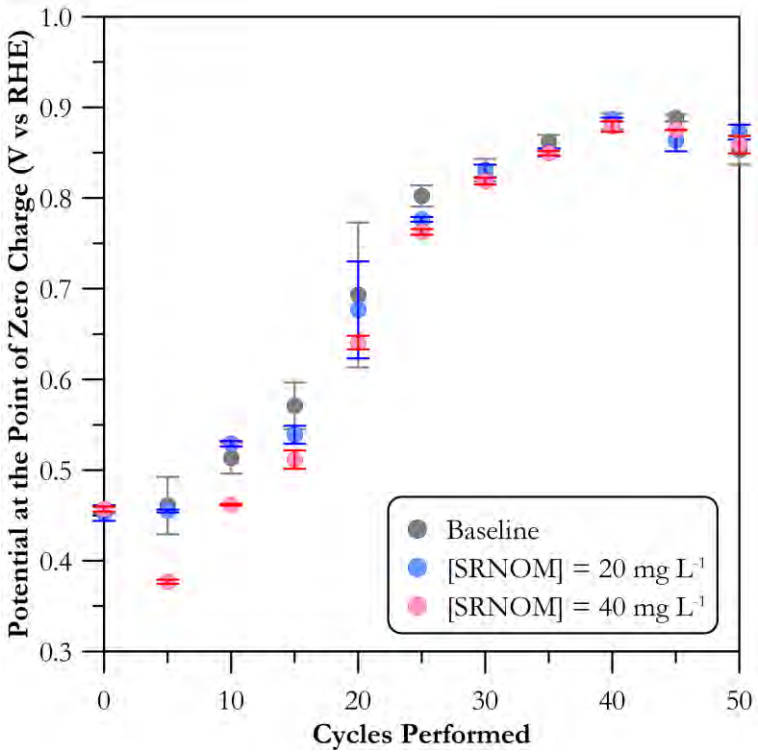

Figure 3.23 E_{PZC} profiles as a function of the number of cycles performed under O_2 saturation at a working electrode potential of 1.2 V vs RHE with a half cycle time of 5 min, at room temperature and different SRNOM concentrations. Gray markers provided as a reference for baseline results. Error bars represent the range between two replicates

The accumulation of charge and H^+ production, respectively shown in Figures 3.24 and 3.25, showed analogous profiles as those seen for the baseline and iron experiments. That was, a power-law decrease in accumulation of charge and an exponential decrease in H^+ production. Moreover, major change in these parameters occurred during the first 15 to 20 cycles. As well as with the baseline case, the significantly larger accumulation of charge and H^+ production did not correlate with an accelerated loss of capacitance or E_{PZC} shift, hence supporting the hypothesis that the easily oxidizable features had a negligible contribution to the electrode capacitance. However, when compared to the baseline, the substantial reduction in the accumulation of charge and production of H^+ could be attributed to the initial pH of the electrolyte used. As presented in

Table 2.1, the initial pH for the electrolyte containing 20 and 40 mg SRNOM L^{-1} was 4.19 ± 0.02 and 3.85 ± 0.01, respectively. As a result, especially during the first few cycles of each set of cycles performed, the voltage difference applied for OER was 0.22 and 0.20 V (compared to the 0.39 V observed under baseline conditions) for the electrolyte containing 20 and 40 mg SRNOM L^{-1}, respectively. Therefore, the applied voltage difference for oxygen evolution and carbon oxidation are much lower in comparison to those experienced under baseline conditions. Nonetheless, some of the charge accumulated and H^+ produced can be assigned to the OER. In addition, the trend observed for the O/C ratio and contact angle (see Table 3.4), for the trials conducted in the presence of 20 mg SRNOM L^{-1}, agreed with those observed for the baseline experiment. Furthermore, cross-sectional SEM image analysis indicated that, at EOL under presence of 20 mg SRNOM L^{-1}, the electrode bulk porosity increased from an initial value of 51.6% ± 3.8% to a value of 59.7% ± 4.4%. Analysis of the FTIR spectra followed the treatment described in section 3.2 and was only performed for electrode cycled in the presence of 20 mg SRNOM L^{-1}.Qualitatively, the raw FTIR spectra (refer to Appendix A.4) demonstrated the evolution of the same absorption bands associated with oxygen functionalities than those develop under baseline conditions. Following earlier discussion, in the normalized and background corrected spectrum, a positive change in transmittance change can be correlated with a decrease in absorption with respect to the reference spectrum (i.e., electrode at end-of-life condition). Figure 3.26 shows the minor changes with respect to the reference were observed for the O – H and C – O absorption bands.

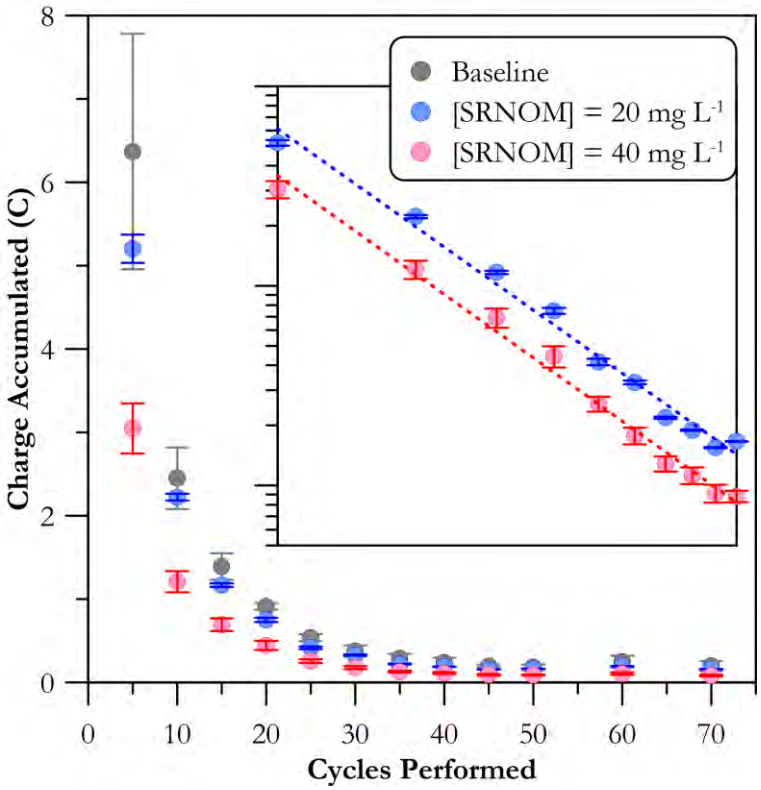

Figure 3.24 Charge accumulated per set of cycles performed as a function of the number of cycles performed under O_2 saturation at a working electrode potential of 1.2 V vs RHE with a half cycle time of 5 min, at room temperature and different SRNOM concentrations. Gray markers provided as a reference for baseline results. Error bars represent the range between two replicates. Insert shows the power law relationship between the charge accumulated and cycles performed

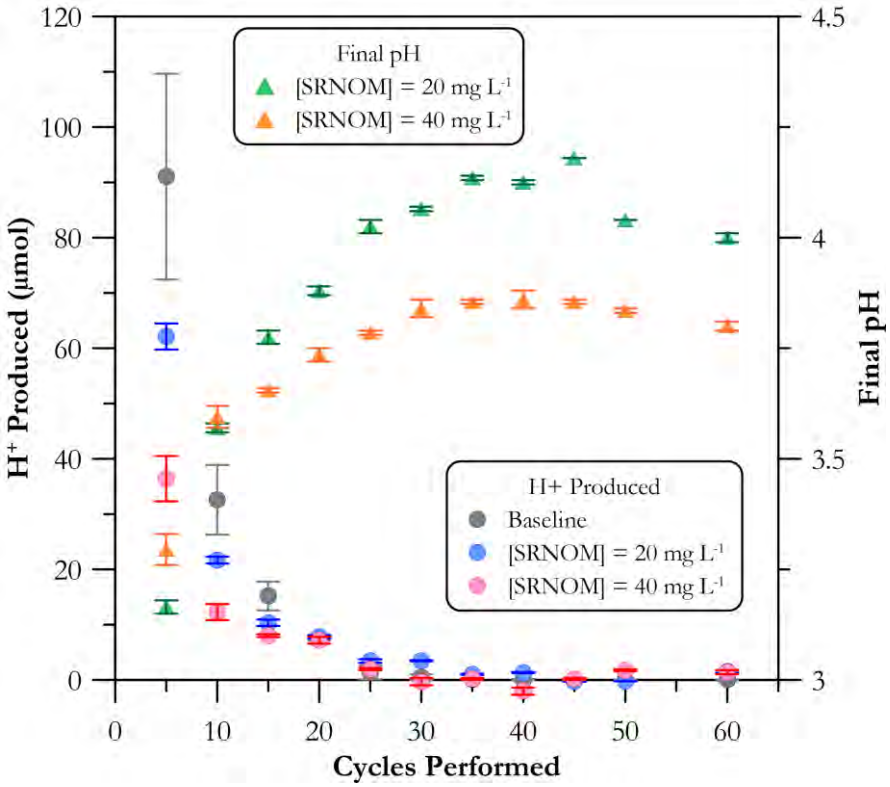

Figure 3.25 H^+ produced per set of cycles performed and final pH profiles as functions of the number of cycles performed under O_2 saturation at a working electrode potential of 1.2 V vs RHE with a half cycle time of 5 min and at room temperature. Each set of cycles performed began with fresh, unbuffered electrolyte with a pH of 4.19 ± 0.02 and 3.85 ± 0.01 for the solutions containing 20 and 40 mg SRNOM L^{-1}, respectively. Gray markers provided as a reference for baseline results. Error bars represent the range between two replicates

Table 3.4 Oxygen to carbon ratios and contact angle for electrodes at different degradation stages (i.e., C/C_0) after cycling at a working electrode potential of 1.2 V vs RHE with a half cycle time of 5 min and at room temperature under 20 mg SRNOM L^{-1}

C/C_0	$O/C^6 \times 10^2$	Contact Angle (degrees)[7]
BOL	5.22 ± 1.70	131 ± 2.4
0.8	20.7 ± 0.46	28 ± 3.1
0.6	22.1 ± 0.41	33 ± 2.5
0.4	22.2 ± 0.19	29 ± 2.3
EOL	15.3 ± 3.36	28 ± 0.9

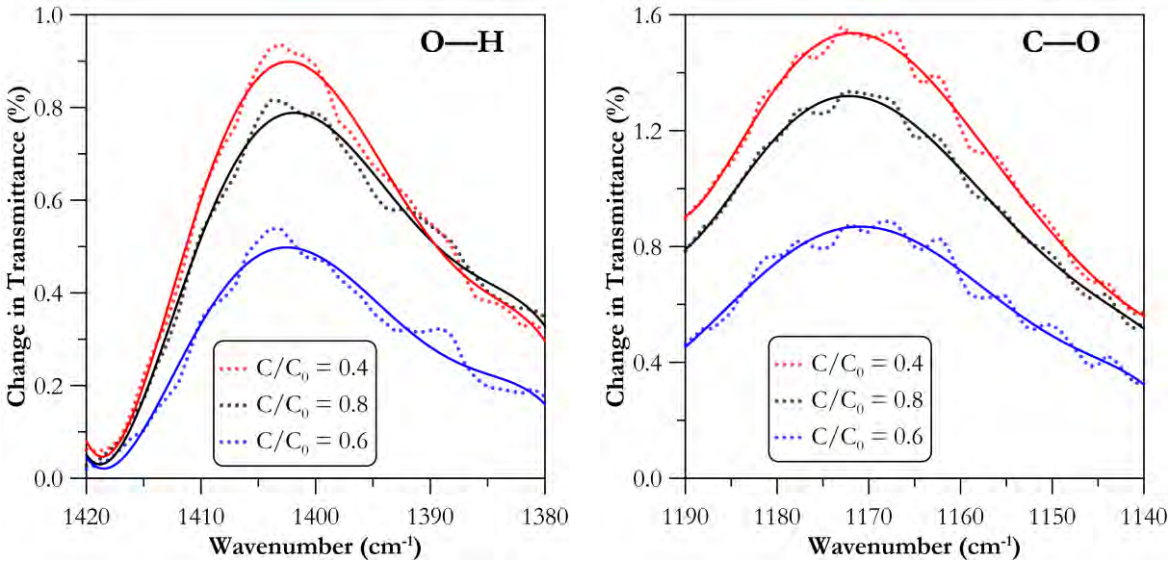

Figure 3.26 Change in transmittance of for the O – H and C – O absorption bands for electrodes cycled with a working electrode potential of 1.2 V vs RHE, a half cycle time of 5 min under aerobic conditions and 20 mg SRNOM L^{-1} at different degradation stages relative to that exhibited by an electrode at EOL conditions. The dotted lines represent the actual change in transmittance. The solid lines are given to facilitate the visualization of the trend of the data

[6] Uncertainty represents the propagation of error attributed to the averages and standard deviations obtained from three EDS elemental composition analyses
[7] Uncertainty represents the standard error

3.4 Effect of Cycling Time and Solution pH

The effect of cycling time on electrode stability is yet to be reported for CDI applications. Traditionally, the charging and discharging steps are of equal duration. Ideally, these are defined by the time it takes the system to reach equilibrium between the influent and effluent conductivity levels. This is also dependent on the applied potential, which acts as the driving force for electrosorption and secondary processes, such as carbon corrosion. The latter, as shown by equations 1.3 and 1.4, will result in the formation of surface oxides, CO_2 and H^+.

As mentioned in section 3.2, Kinoshita & Bett (1973) [76] reported that CO_2 evolution (equation 1.3) became the dominant oxidation pathway as time increased. On the other hand, the diminishing rate of oxide formation over time is indicative of the oxide layer passivating effect. Maass et al. (2008) [35] observed this when comparing the carbon corrosion rates (Ketjenblack EC300J®) between potentiodynamic and potentiostatic cycling conditions and reported lower oxidation rates for electrodes cycled with a constant potential. Under potentiodynamic conditions, the formation of the passivating layer was limited, as time the electrode spent at adverse potentials (i.e., where carbon corrosion is accelerated) was significantly reduced. Further evidence was provided by Macauley et al. (2018) [38] where a decrease in the carbon corrosion rate, at a cell potential of 0.9 V, was observed when increasing the potential holding time from 30 to 300 s. Given the absence of a standard protocol to evaluate CDI materials, it is vital to understand the role of HCT (in addition to that of applied potential) on electrode stability to fairly assess and compare different electrode materials.

In addition, as was presented in section 1.4.3.4, the occurrence of Faradaic reactions will affect the electrolyte pH. Moreover, localized pH environments are expected to be encountered at the electrode surface depending on the type of Faradaic reactions occurring. Under typical CDI

operation, little is known about the effect, if any, of the role of pH on electrode degradation. Nonetheless, corrosion studies of different carbon-based materials for PEMFC and chlor-alkali applications are available and serve as a good starting point for CDI researchers. However, most of the PEMFC studies have been carried, understandably, at low pH values but relatively closer potentials to those found in CDI applications; and chlor-alkali investigations [84]–[88] have dealt with wider pH ranges but high enough potentials to drive the brine electrolysis process. In the more applicable study by Yi et al. (2017) [89], the largest oxidation current (for glassy carbon) at a potential of 1.8 V vs RHE was observed in alkaline conditions (0.1 M KOH) followed by the one in acidic (0.5 M H_2SO_4) and neutral (0.5 M K_2SO_4) electrolytes. This study proposed a catalytic effect of H^+ on the oxidation process and an OH radical process in alkaline media. However, the latter is unlike to occur under typical CDI conditions.

To explore the influence of electrolyte pH, four different conditions were tested: acidic (pH = 1) and alkaline (pH = 13), and with and without pH adjustment. The sources of H^+ and OH^- were HCl and NaOH, respectively. These susbstances were chosen as their counterions were already present, at a concentration of 1 M, in the electrolyte. Under alkaline conditions, the cycling potential was adjusted to account for the thermodynamic changes occurring to the water electrolysis potential (i.e., following the expression $E = 1.23 - 0.059 \cdot pH$). As a reference, at a pH of 1, the thermodynamic potential for the OER is of 1.17 V vs RHE. Considering that, in this case, a potential of 1.2 V vs RHE was applied, a difference of 30 mV with the thermodynamic potential for OER exists. With this in mind, under alkaline conditions (pH = 13 and E_{OER} = 0.46 V vs RHE) the electrode was cycled at a potential of 0.49 V vs RHE. Conversely, as the pH of the solution progressively decreased during tests with and without pH adjustment, mantaining a constant voltage difference throughout the duration of each set of cycles was not possible.

Nonetheless, the role of pH on the occurrence of carbon oxidation and its implication on the results and the trends observed are discussed. With regards to pH adjustment, this was done after every cycle with the aid of NaOH (0.1 M), to restore the pH to a value close to the initial one (i.e., a pH value of 7) and mimic a constant inflow of fresh brackish water solution. After performing 10 cycles, the electrolyte was disposed and the next round of 10 degradation cycles (i.e., after the characterization protocol) was conducted with fresh electrolyte (with a pH of 7). In the experiments performed without pH adjustment, the electrolyte was used for 10 consecutive cycles (i.e., no pH adjustment between cycles) and was then discarded and replaced with fresh electrolyte (with an initial pH of 7) for the next round of 10 degradation cycles (i.e., after the characterization protocol).

Figures 3.27 and 3.28 present the effect of electrolyte pH on the loss of capacitance and relocation of the E_{PZC}, respectively. As mentioned earlier, a small contribution to the electrode loss of capacitance and shift in the E_{PZC} might be occurring as a consequence of the electrochemical characterization protocol. It was noted that adjusting the pH to 7 after every cycle had no effect on the rate of capacitance loss and E_{PZC} relocation. This result is interesting, as one would have expected a higher degree of electrode degradation as a result of adjusting the pH to 7 (i.e., the initial electrolyte pH) after every cycle. As mentioned before, a higher voltage difference for carbon oxidation was applied at a neutral pH of 7 than that applied at acidic conditions. Figure 3.27 shows, if anything, a slighlty larger electrode capacitance loss. In contrast, in the case without pH adjustment, one would have expected a lesser degree of electrode degradation because at more acidic conditions, the potential for carbon oxidation is smaller (due to the reduced voltage difference being applied). As explained earlier, the acidic nature of the electrolyte would have persisted for 10 consecutive cycles. To elucidate the role of neutral pH, it would be valuable to

conduct degradation experiments with a buffered solution, so that one can maintain a constant voltage difference and compare results with experiments performed at more acidic and alkaline conditions.

Similar capacitance loss was oberved during alkaline cycling. However, after the 20th cycle, the E_{PZC} exhibited a slower shift. This might be an indication that electrode degradation ocurred through a different mechanism (i.e., not carbon corrosion). For instance, in the study by Yi et al. (2017) [89], the electrolyte presented a brownish yellow colour after oxidation in alkaline conditions (0.1 M KOH) at a potential of 1.8 V vs RHE. This was attributed to carbon dissolution. For activated carbon electrodes herein studied, no apparent change in colour was detected in the experiments performed in the presence of 0.1 M NaOH. However, the long duration to which the electrodes were exposed to alkaline conditions may have affected the electrode microporous structure by the action of an etching effect by NaOH. Several studies pertaining to the activation of carbon materials have used NaOH to develop the material porosity [90]–[94] and have found that the development of mesopores (i.e., pores between 2 and 50 nm) is favoured as the NaOH to raw material ratio (w/w) is increased. In the study by Ding et al., (2013) [92], the increase in NaOH ratio had a negative effect on the material surface area and capacitance. Moreover, as the NaOH ratio increased, elemental analysis showed a decrease in oxygen content (%wt.). During the experiments conducted at a pH value of 13, large NaOH to active material ratios conditions were met (i.e., 1 M NaOH in a 100 mL compartment with electrodes containing approx. 4.2 mg of active material). Hence, it is possible that during the 500 min the electrodes were subject to this condition, the coalescence of micropores reduced the electrode surface area thus decreasing the electrode capacitance. This reaction seems to have happened slowly at early cycling stages, but its effect became apparent after the 10th cycle. The relatively slower change in the electrode E_{PZC} (see

Figure 3.28) might be indicative of the evolution of mesoporosity occurring at faster rate than surface oxidation, hence explaining the discrepancy between the loss of capacitance and electrode E_{PZC}. Therefore, the loss of electrode capacitance presented in Figure 3.27 could be reflecting the combined effect of carbon oxidation and the decrease in surface area (i.e., reduction in available active sites) caused by carbon dissolution which affected the electrode porous structure. Further experiments could be performed with milder alkaline conditions to study and minimize the effect of etching. Furthermore, it would be valuable to assess changes in the electrode surface area and porosity by means of mercury porosimetry or helium pycnometry analysis.

On the other hand, a substantial improvement in capacitance retention was observed while cycling under acidic conditions. After 50 cycles, approx. 30% of the initial capacitance was lost. In comparison, at the same cycling time, at least an 80% loss was observed for the other cases studied. As was mentioned previously, under acidic conditions, the formation of surface oxides and CO_2 is favoured. Moreover, if the catalytic effect of H^+ proposed by Yi et al. (2017) [89] for glassy carbon were to hold true for amorphous carbons, it would be possible to suggest that, in accordance to the study by Kinoshita & Bett (1973) [76], Maass et al. (2008) [35] and Macauley et al. (2018) [38], the formation of a passivating oxide layer will slow down the kinetics of carbon corrosion. In addition, the smaller voltage difference being applied when compared to that available when starting with a neutral electrolyte can be translated into a reduced rate of carbon oxidation. In combination, these two could explain the increased retention of capacitance and lower E_{PZC} shift of the tests performed at pH of 1. The effect of this protective layer became apparent when performing experiments with increased half cycle times (i.e., increased potentiostatic holds).

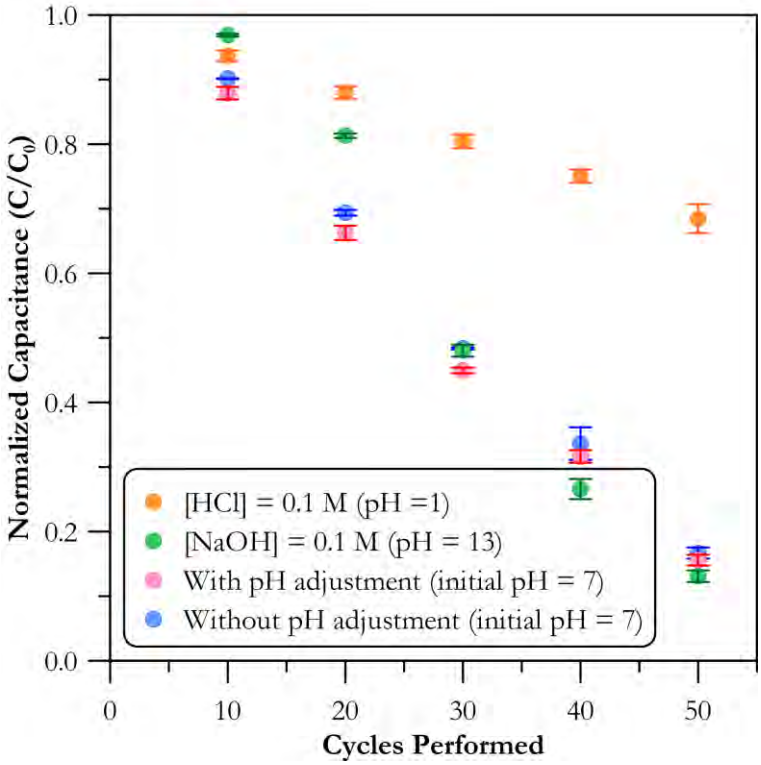

Figure 3.27 Normalized capacitance as a function of the number of cycles performed under O_2 saturation with a half cycle time of 5 min, at room temperature and different electrolyte pH conditions. The working electrode potential for the experiments conducted at a pH of 1 and with and without pH adjustment was 1.2 V vs RHE. On the other hand, the working electrode potential for experiments conducted at a pH of 13 was 0.49 V vs RHE. In all cases, the discharge potential was equal to the open circuit potential measured at the beginning of each set of cycles (see Appendix A). The initial electrolyte pH of the experiments with and without pH adjustment was 7. Error bars represent the range between two replicates

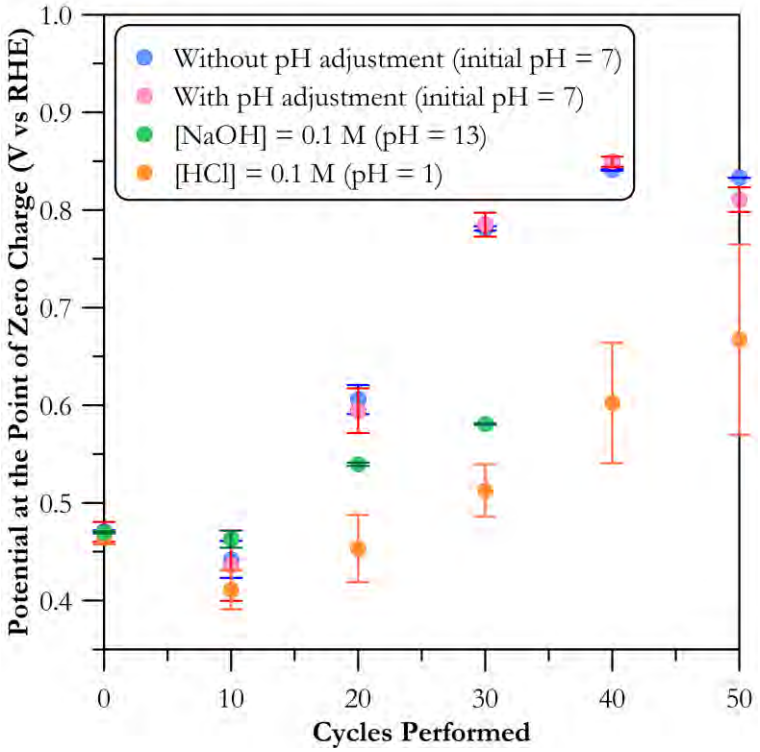

Figure 3.28 E_{PZC} profiles as a function of the number of cycles performed under O_2 saturation with a half cycle time 5 min, at room temperature, an electrolyte concentration of 1 M (NaCl) and different electrolyte pH conditions. The working electrode potential for the experiments conducted at a pH of 1 and with and without pH adjustment was 1.2 V vs RHE. On the other hand, the working electrode potential for experiments conducted at a pH of 13 was 0.49 V vs RHE. In all cases, the discharge potential was equal to the open circuit potential measured at the beginning of each set of cycles (see Appendix A). The initial electrolyte pH of the experiments with and without pH adjustment was 7. Error bars represent the range between two replicates

The influence of HCT on the loss of capacitance and relocation of the E_{PZC} is shown in Figures 3.29 and 3.30, respectively. In contrast to the previously discussed results, these parameters are presented as a function of the time the electrode was held at a potential of 1.2 V vs RHE. As mentioned in section 2.3.1, the selection of different half cycle times was based on using multipliers of the 5 min HCT, with the objective to normalize the x-axis of Figures 3.29 and

3.30 to the amount of time the working electrode was held at a potential of 1.2 V vs RHE. Following this idea, after 2 cycles with a half cycle time of 50 min, the time the electrode was held at the charging potential of 1.2 V vs RHE is equal to the case were cycling consisted of 4 cycles with a half cycle time of 25 minutes. Observed variations in the loss of capacitance suggested that HCT had an impact on the stability of the electrode. Overall, as HCT decreased from 250 to 25 min, so did the retention of capacitance. Nonetheless, the 1 and 5 min HCT did not follow this trend. Specifically, after electrodes were held for 250 min at a potential of 1.2 V vs RHE, capacitance was retained around 25%, 17%, 32%, 42% and 95% for HCTs of 1, 5, 25, 50 and 250 min, respectively. Moreover, after the second and third cycles were performed with an HCT of 250 min (see Appendix A.1), capacitance retention was 58% and 23%, respectively. The latter was observed to be close to the capacitance retention of electrodes cycled with HCTs of 5 and 1 min. On the other hand, the differences in E_{PZC} shift were not as clear, especially between the 1 & 5 min and the 25 & 50 min HCT. However, more rapid relocations were observed for the 1 & 5 min when compared to the 25 & 50 min HCT, hence suggesting a higher degree of surface oxidation for the electrodes cycled with an HCT of 1 and 5 min. In addition, the E_{PZC} of the electrodes tested with an HCT of 250 min remained at the same value as that for the BOL state (i.e., ~ 460 mV vs RHE) after the first cycle, but increased rapidly after the second (i.e., ~700 mV vs RHE at a C/C_0 ~ 0.58) and third (~ 770 mV vs RHE at a C/C_0 ~ 0.23) cycle with an HCT of 250 min.

The increased capacitance retention and reduced E_{PZC} shift as the HCT increased could be explained by the formation of a passivating oxide layer, as described in section 3.2 and shown in Figure 3.11. Kinoshita & Bett (1973) [76] observed that as the potentiostatic hold increases, the oxide layer will cover more surface area and will increase in thickness (see Figure 3.31). At the

same time, CO_2 will be released from the electrode surface. The increase in layer thickness will increase the time required for the reactant to diffuse through the layer and reach available active sites located deeper in the electrode, thus delaying the change in the electrode capacitance and E_{PZC}. As was previously mentioned, CO_2 release will become the main Faradaic reaction as cycling time progresses. This causes a loss of carbon mass and through the coalesence of micropores, an additional reduction of available surface area is reflected in the loss of capacitance.

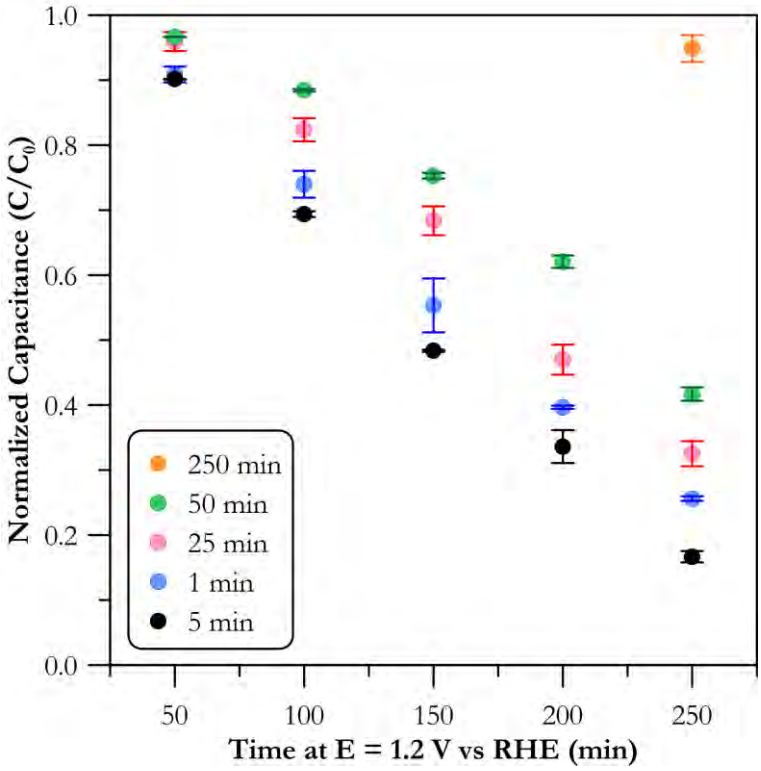

Figure 3.29 Normalized capacitance as a function of time the working electrode was held at a potential of 1.2 V vs RHE for different half cycle times. Cycles performed under O_2 saturation, an electrolyte concentration of 1 M (NaCl) and at room temperature. Error bars represent the range between two replicates

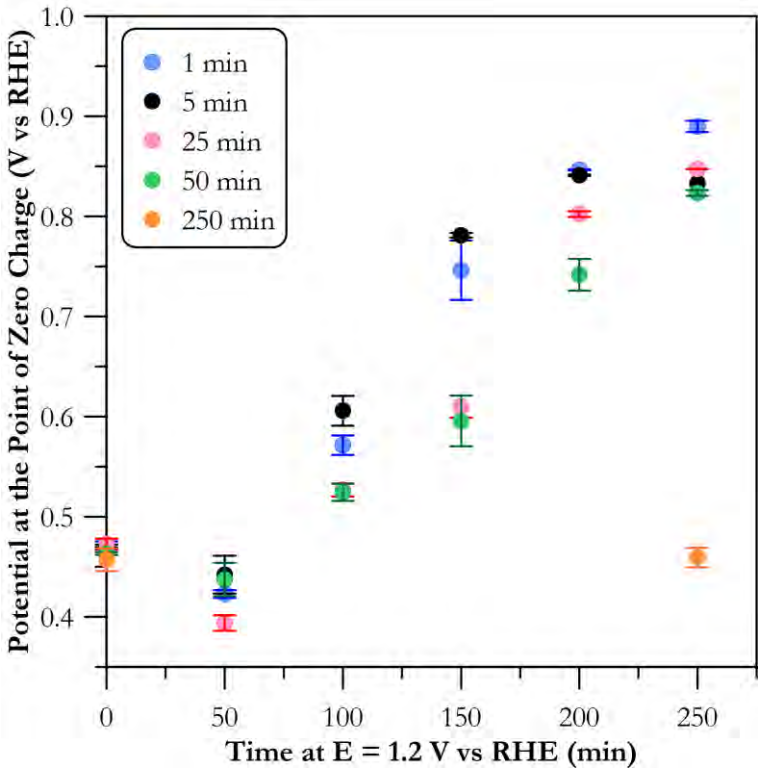

Figure 3.30 E_{PZC} profile as a function of time at a working electrode potential of 1.2 V vs RHE for different half cycle times. Cycles performed under O_2 saturation, an electrolyte concentration of 1 M (NaCl) and at room temperature. Error bars represent the range between two replicates

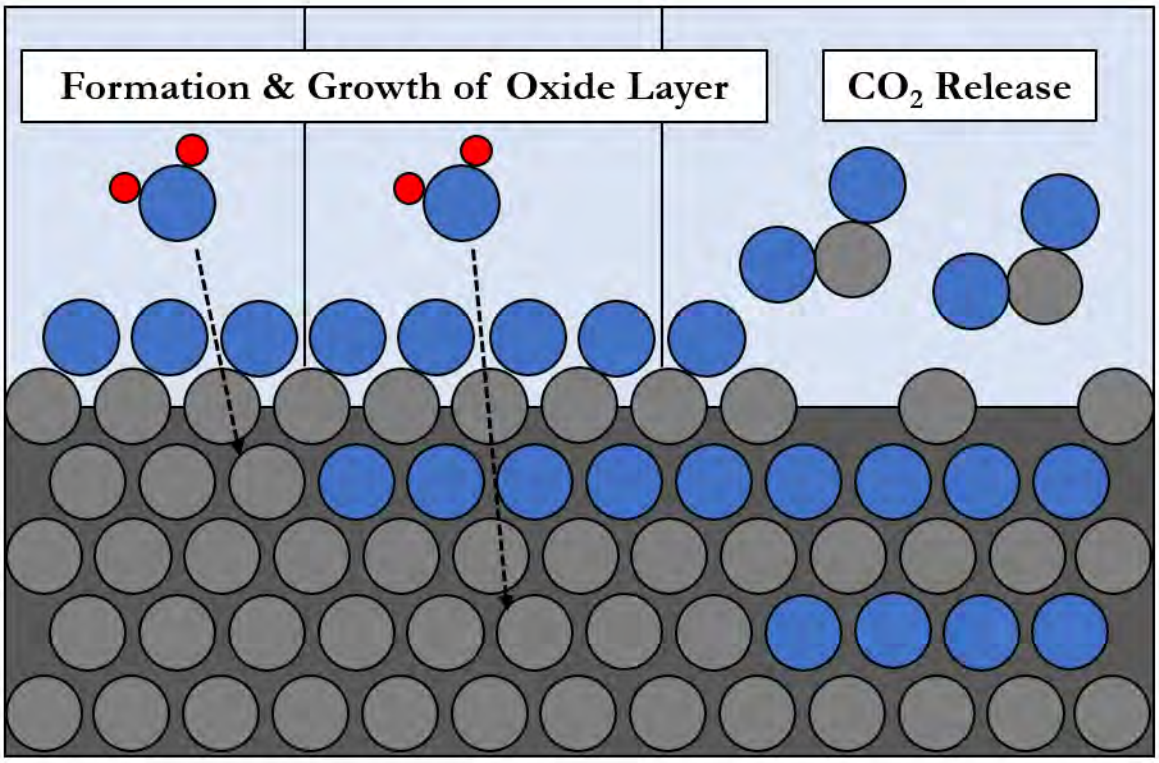

Figure 3.31 Schematic of the development of the oxide layer as a result of the carbon corrosion process. Evolution of CO_2 occurs simultaneously and over time becomes the main Faradaic reaction. The formation of an oxide layer reduces the amount of available active sites and the evolution of CO_2 reduces the electrode surface area

The results observed for the 1 and 5 min HCT are challenging to justify. However, they might be explained by the electrolyte pH values recorded at the end of each experiment. The pH results are presented in Figure 3.32. It is important to consider that every set of cycles started with fresh, unbuffered electrolyte with a pH of 7.04 ± 0.06, and that the observed increase in pH as cycling progressed is a result of a reduced impact from oxidation processes, as discussed earlier. When comparing the data sets for the 1 and 5 min HCT, it was observed that the final pH value is consistently less acidic for the 5 min HCT tests. The differences became more apparent when the final concentration of H^+ is considered. Previously shown results indicated that capacitance

retention was improved when the electrode was cycled under constant acidic conditions (i.e., pH = 1). However, the difference in pH or H^+ observed for the 1 and 5 min HCT trials, was not that substantial and suggested that further experiments with increasing pH increments could provide useful insights to explain these results. Regardless of the results observed at 1 and 5 min of HCT, it has been demonstrated that the selection of cycling time for long-term stability testing is a parameter that will affect the long-term stability of the electrode and requires special attention. Ideally, the duration of the HCT should be determined by a study of the electrode electrosorption performance at different applied potentials. The HCT should not exceed the time required for the electrode to be saturated at a particular applied potential. Extending the determined HCT serves no practical purpose as no further desalination can be achieved and charge will be consumed driving secondary processes. Nonetheless, a strategy might be developed in such a way that the holding time is increased to delay electrode degradation and additional banks of electrodes are phased in to continue with the desalination step.

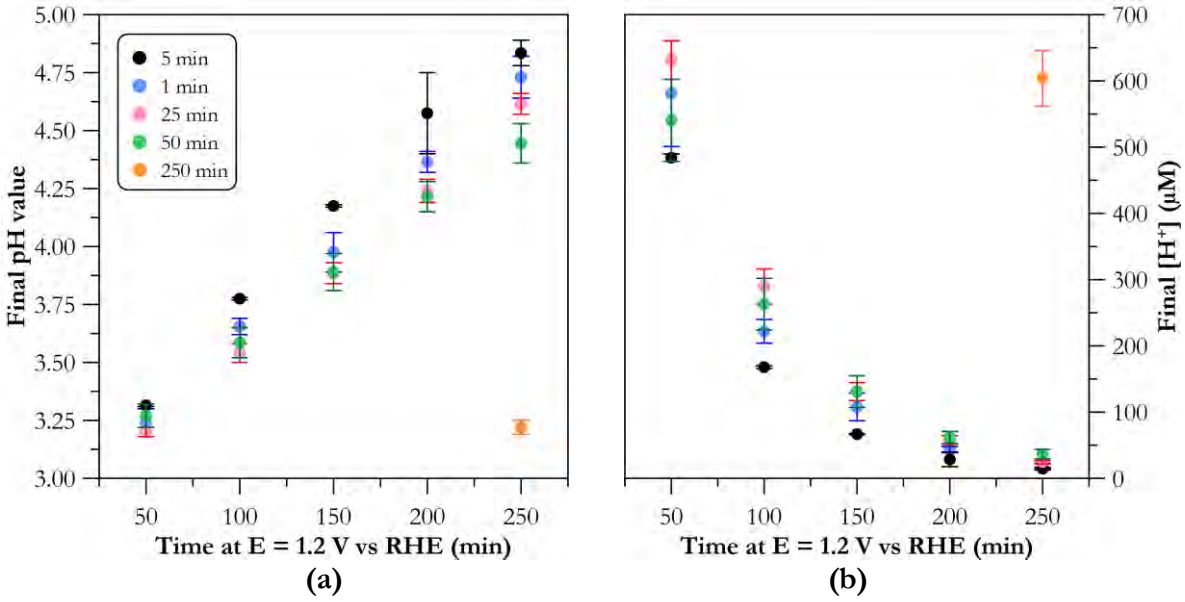

Figure 3.32 (a) Final pH and (b) final H^+ concentration at the end of every set of cycles performed with a working electrode potential of 1.2 V vs RHE for different half cycle times. Cycles performed under O_2 saturation, an electrolyte concentration of 1 M (NaCl) and at room temperature. Error bars represent the range between two replicates

3.5 Electrode Stability using a Two-Electrode Flow Cell

The use of two-electrode cells is extensive in the CDI literature. They are particularly useful to obtain performance metrics such as salt adsorption capacity, charge efficiency and specific energy consumption under practical conditions. Although extremely practical, two-electrode CDI cells are not suited for fundamental studies. The main reason for this is the lack of control over the potential applied to each individual electrode. This is a critical aspect, as the potential at the electrode surface plays an important role in determining the feasibility of electron transfer reactions. Moreover, in CDI, the individual electrode potential and its corresponding E_{PZC} determine the driving force for electrosorption on a particular electrode. Another challenge with conventional two-electrode (i.e., without membrane) CDI cells is the possibility of reaction coupling between Faradaic reactions, such as carbon oxidation and oxygen reduction. In this case

for instance, the H^+ produced as a by-product of carbon corrosion at the anode (see reactions 1.3 and 1.4) is used at the cathode to reduce oxygen and produce hydrogen peroxide (see reaction 1.7). Moreover, the reduction of hydrogen peroxide will consume H^+ to produce water (see reaction 1.5). Another challenge is the redistribution of potential between the electrodes as a result of the disparity in kinetics of the processes happening at the anode and cathode to maximize the charge efficiency (see section 1.4.3.4).

A two-electrode cell setup (see Figure 2.2) was used to explore the difficulties of performing fundamental work, especially during long-term studies. The experiments performed, summarized in Table 2.3, were designed to demonstrate the effect of reaction coupling (i.e., effect of dissolved oxygen) and the importance of applied potential on electrode degradation. In addition to the electrode's electrochemical properties, the potential distribution to the anode and cathode was measured using a reference electrode to evaluate the relative drift of the electrode potentials to more thermodynamically adverse conditions. As mentioned in section 2.3.2, the changes occurring to the anode are of great interest. To measure the anode potential, a low-profile Ag/AgCl reference electrode was placed 3 mm away from its surface. The interelectrode gap was 1.6 cm. Thus, the potential measured for the counter electrode, could be affected by the Ohmic drop as a result of the 13 mm separation. Nonetheless, comparison of the cell potential being applied with the individual electrode potentials (i.e., $E_{anode} + E_{cathode}$) indicated a difference of a few millivolts, thus suggesting a negligible effect from the Ohmic drop on the measurement of the cathode potential. This being said, the primary goal of these measurements was to monitor the drift of the anodic potential.

The equivalent circuit schematic for the two-electrode cell setup is presented in Figure 3.33. Here, A and C refer to the anode and cathode, respectively; R_A and R_C correspond to the

electrode internal resistance, C_A and C_C correspond to the electrode capacitance, R_{FA} and R_{FC} correspond to the Faradaic resistance (i.e., current leakage due to parasitic processes) and R_S corresponds to the solution resistance.

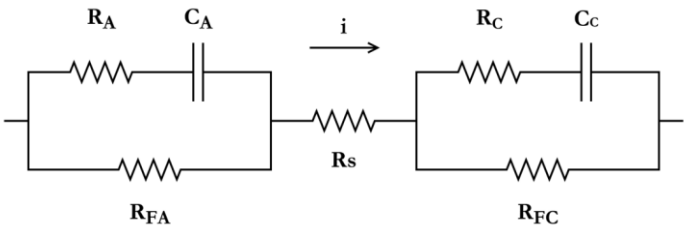

Figure 3.33 Equivalent circuit of the two-electrode cell setup

The capacitance and E_{PZC} profiles for anaerobic tests performed at cell potentials of 1.3 and 1.8 V are presented in Figure 3.34. The first 40 cycles shown, performed with a cell potential of 1.3 V, resulted in a retention of capacitance of around 92% and 89% for the cathode and anode, respectively. In addition, the E_{PZC} showed no positive shift, thus indicating a negligible functionalization of the electrode surface. Within this time frame, it was observed (see Figures 3.35 and 3.36) that the anode potential drifted from an initial value of 1.0 V to 1.1 V vs RHE at the 40th cycle. Given the minor degradation observed, further tests were performed with a cell potential of 1.8 V. Over the 35 cycles performed at this cell potential, the anode potential drifted from 1.1 to 1.8 V vs RHE. Surprisingly, during the first ten cycles, the anode capacitance was slightly affected (i.e., approx. 2% decrease). This could be explained by the range of potentials, at which the anode was subject to (see Figure 3.36), which varied from ~1.15 to ~1.27 V vs RHE. However, despite the small change in electrode capacitance, the E_{PZC} displayed a shift from 470 to 530 mV vs RHE, hence indicating the evolution of surface oxygen functionalities. From the 50th to 60th cycle, capacitance decreased significantly, on average, around 27% and the E_{PZC} changed significantly to a potential of 770 mV. Over these ten cycles, the potential attributed to the anode ranged between ~1.27 to ~1.50 V vs RHE. In particular, it was possible to see that the

potential attributed to the anode was fairly constant (~1.27 V vs RHE) between the 51st and 55th cycle (i.e., between the 11th and 15th cycle at a cell potential of 1.8 V), and then, gradually increased to up to ~1.50 V vs RHE, thus accelerating the process of carbon corrosion. In accordance to the steep decrease in capacitance observed over the last 5 cycles performed, Figure 3.36 shows that the anode was subject to potentials between 1.4 and 1.8 V vs RHE. Note, no sign of gas evolution was observed (even at the high anodic potentials noted) and roughly, 10% of the cathodic capacitance was lost and its E_{PZC} remained practically unchanged over the 65 cycles performed.

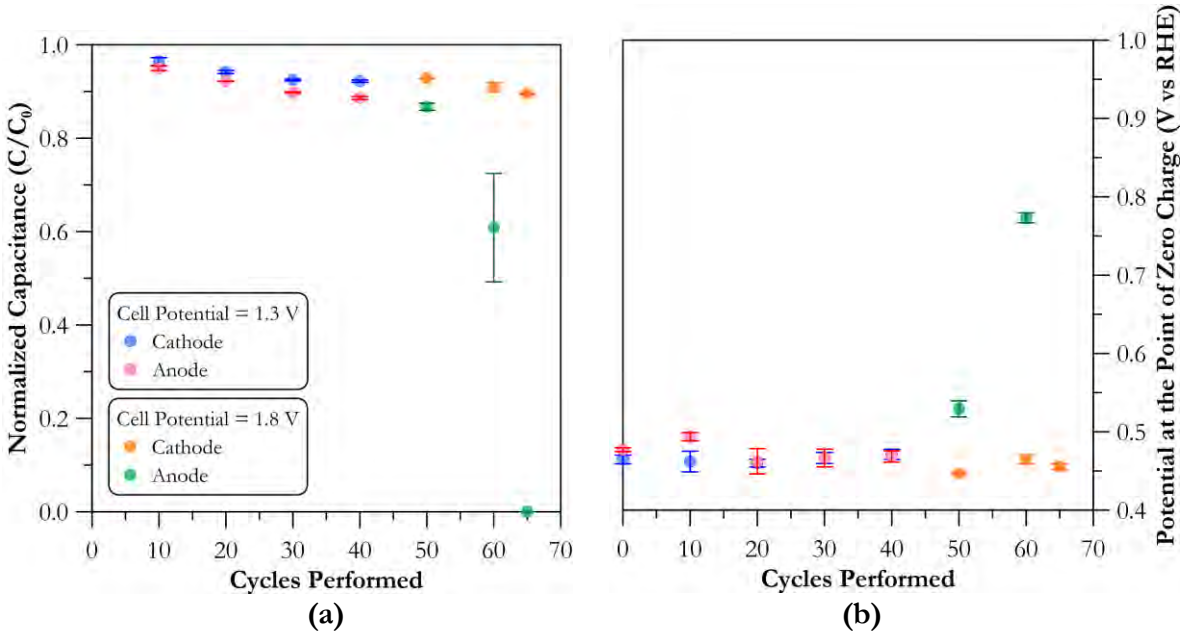

Figure 3.34 (a) Normalized capacitance, and (b) E_{PZC} profiles as functions of the number of cycles performed under N_2 saturation at a cell potential of 1.3 V and 1.8 V with a half cycle time of 5 min, an electrolyte concentration of 17.1 mM (1000 mg NaCl L^{-1}) and at room temperature. The electrodes were discharged at zero voltage (i.e., V_{cell} = 0). Error bars represent the range between two replicates

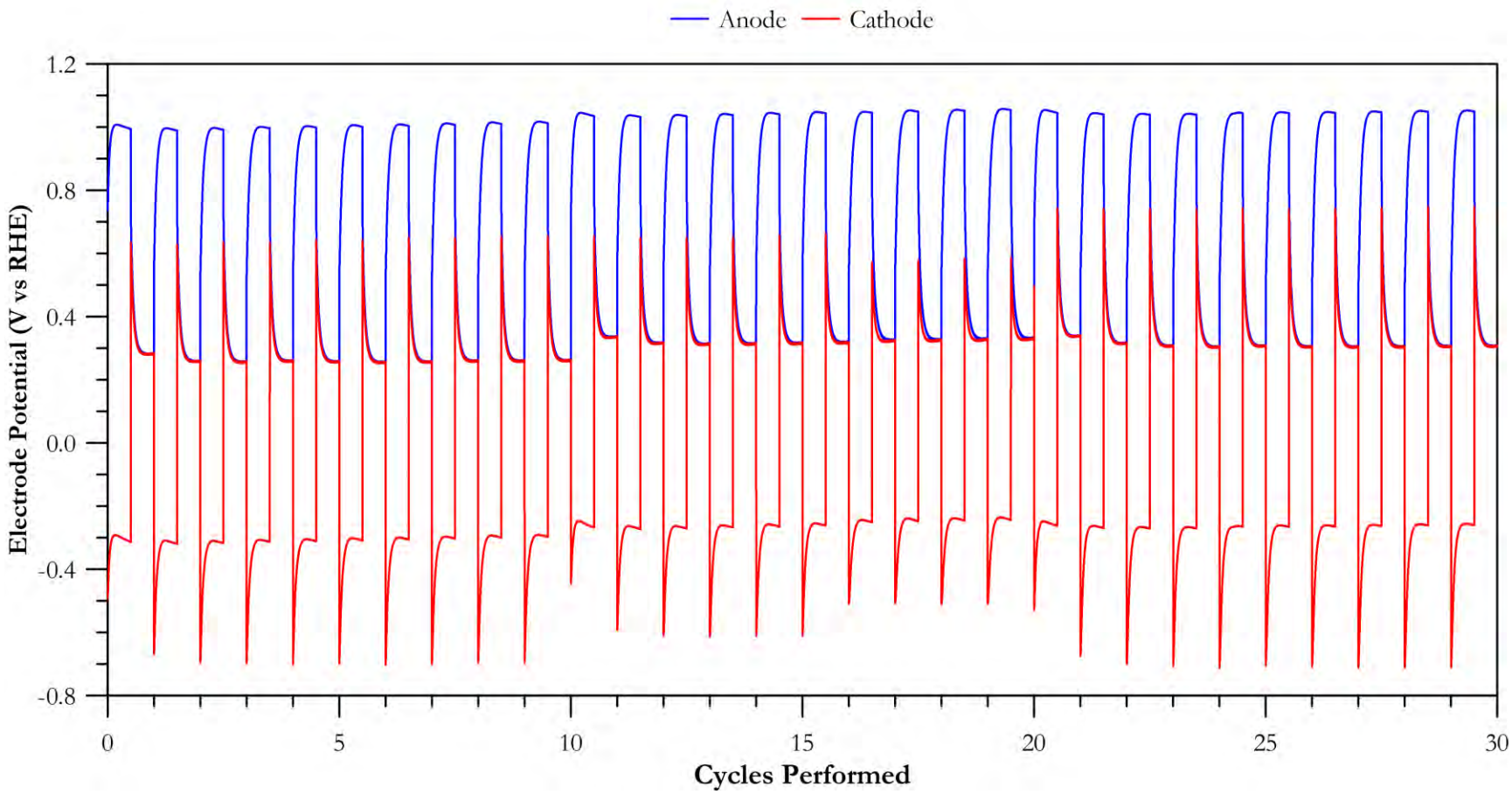

Figure 3.35 Electrode potential distribution throughout cycling (1st-30th cycle) with a cell potential of 1.3 V and a half cycle time of 5 min performed under N_2 saturation using an electrolyte concentration of 17.1 mM (1000 mg NaCl L^{-1}) at room temperature. The electrodes were discharged at zero voltage (i.e., $V_{cell} = 0$)

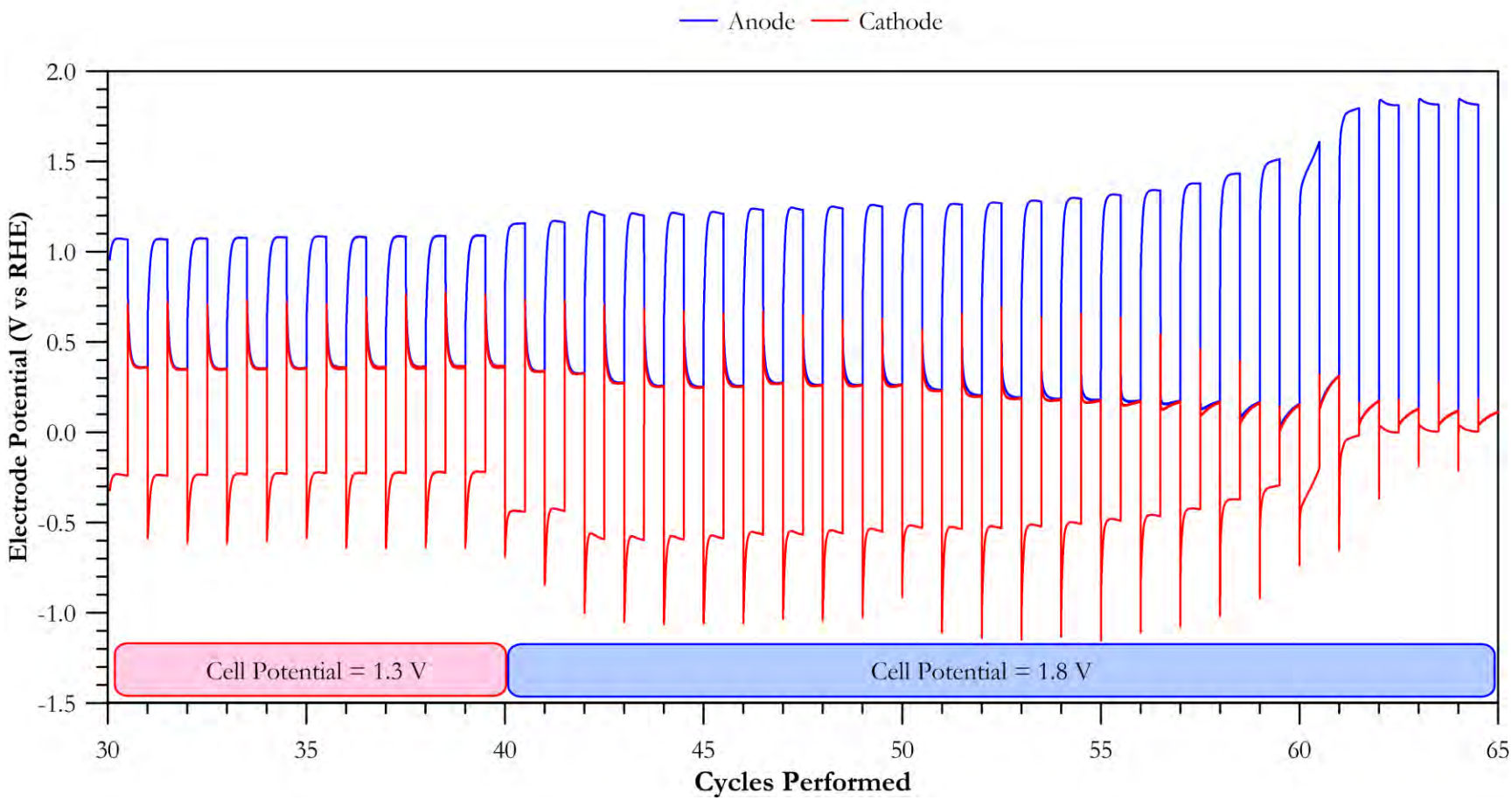

Figure 3.36 Electrode potential distribution throughout cycling (31st-65th cycle) with a cell potential of 1.3 V and 1.8 V and a half cycle time of 5 min performed under N_2 saturation using an electrolyte concentration of 17.1 mM (1000 mg NaCl L^{-1}) at room temperature. The electrodes were discharged at zero voltage (i.e., $V_{cell} = 0$)

Figure 3.37 shows the profiles of capacitance loss and E_{PZC} relocation for electrodes cycled under aerobic conditions with a cell potential of 1.3 V. Over the first 20 cycles, approx. 5% and 10% of the initial capacitance was lost and the E_{PZC} shifted approx. 15 and 25 mV for the cathode and anode, respectively. In a similar way, the relatively low degradation observed could be associated with the anodic potential over the first 20 cycles. From Figure 3.38, the anodic potential ranged between 1.10 and 1.25 V vs RHE. In fact, this range was very similar to the one observed over the first 40 cycles performed under anaerobic conditions. By the 30th cycle, 32% of the initial anodic capacitance was lost and the E_{PZC} moved to a potential of ~620 mV vs RHE (i.e., ~118 mV difference with the E_{PZC} at the 20th cycle). On the other hand, cathodic capacitance was only reduced an additional 2% and there was no significant change in its E_{PZC}. From Figure 3.39 it can be noted, in particular over the last five cycles, that the anode potential increased progressively, and by the 30th cycle, reached values close to 1.35 V vs RHE. The last ten cycles performed caused a steep decrease in capacitance and, by the 40th cycle, approx. 90% of the initial anodic capacitance had been lost. Over these cycles, the anode was subject to relatively high, adverse potentials. Specifically, the anode potential ranged between approx. 1.3 and 1.5 V vs RHE. Very similar results were observed for electrodes cycled under aerobic conditions and in presence of 0.2 mg Fe^{2+} L^{-1} (refer to Appendix A.3 for the capacitance, E_{PZC} and electrode potential distribution profiles). The only striking difference arose from the scaling nature of iron. Overall, capacitance was lost at a slightly faster rate and the E_{PZC} showed a negative shift by the end of the tenth cycle but, at the end of the 30th cycle it showed similar values as those observed for the aerobic baseline case. These observations were supported by the recorded potential distribution, which is shown to drift slightly faster than that of the aerobic baseline case.

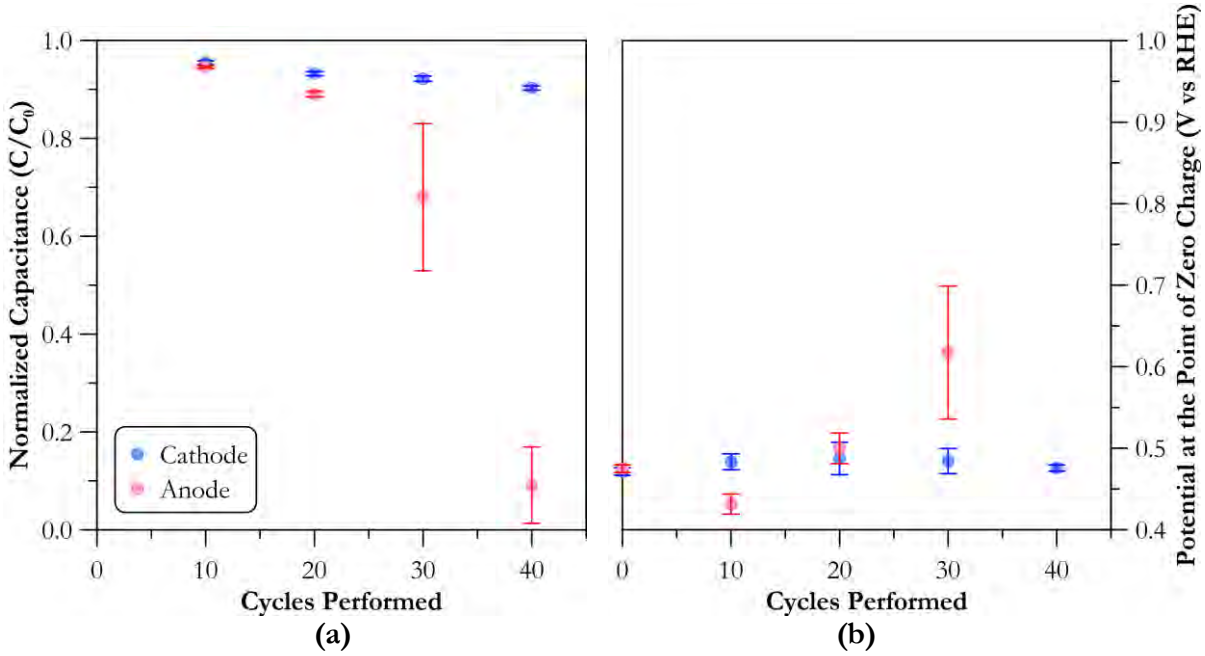

Figure 3.37 (a) Normalized capacitance, and (b) E_{PZC} profiles as a function of the number of cycles performed under O_2 saturation at a cell potential of 1.3 V with a half cycle time of 5 min, an electrolyte concentration of 17.1 mM (1000 mg NaCl L^{-1}) and at room temperature. The electrodes were discharged at zero voltage (i.e., V_{cell} = 0). Error bars represent the range between two replicates

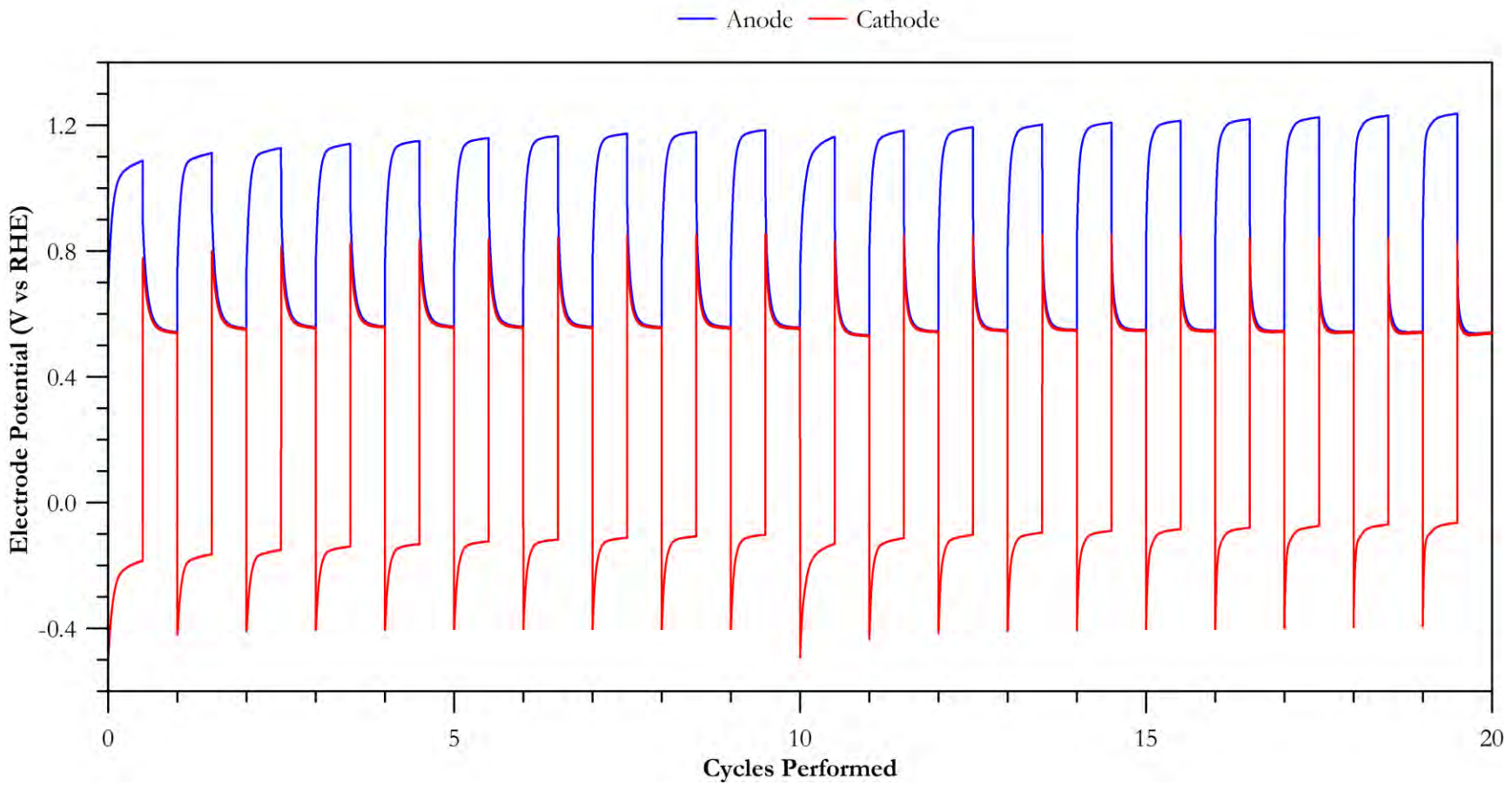

Figure 3.38 Electrode potential distribution throughout cycling (1st-20th cycle) with a cell potential of 1.3 V with a half cycle time of 5 min performed under O_2 saturation using an electrolyte concentration of 17.1 mM (1000 mg NaCl L^{-1}) at room temperature. The electrodes were discharged at zero voltage (i.e., $V_{cell} = 0$)

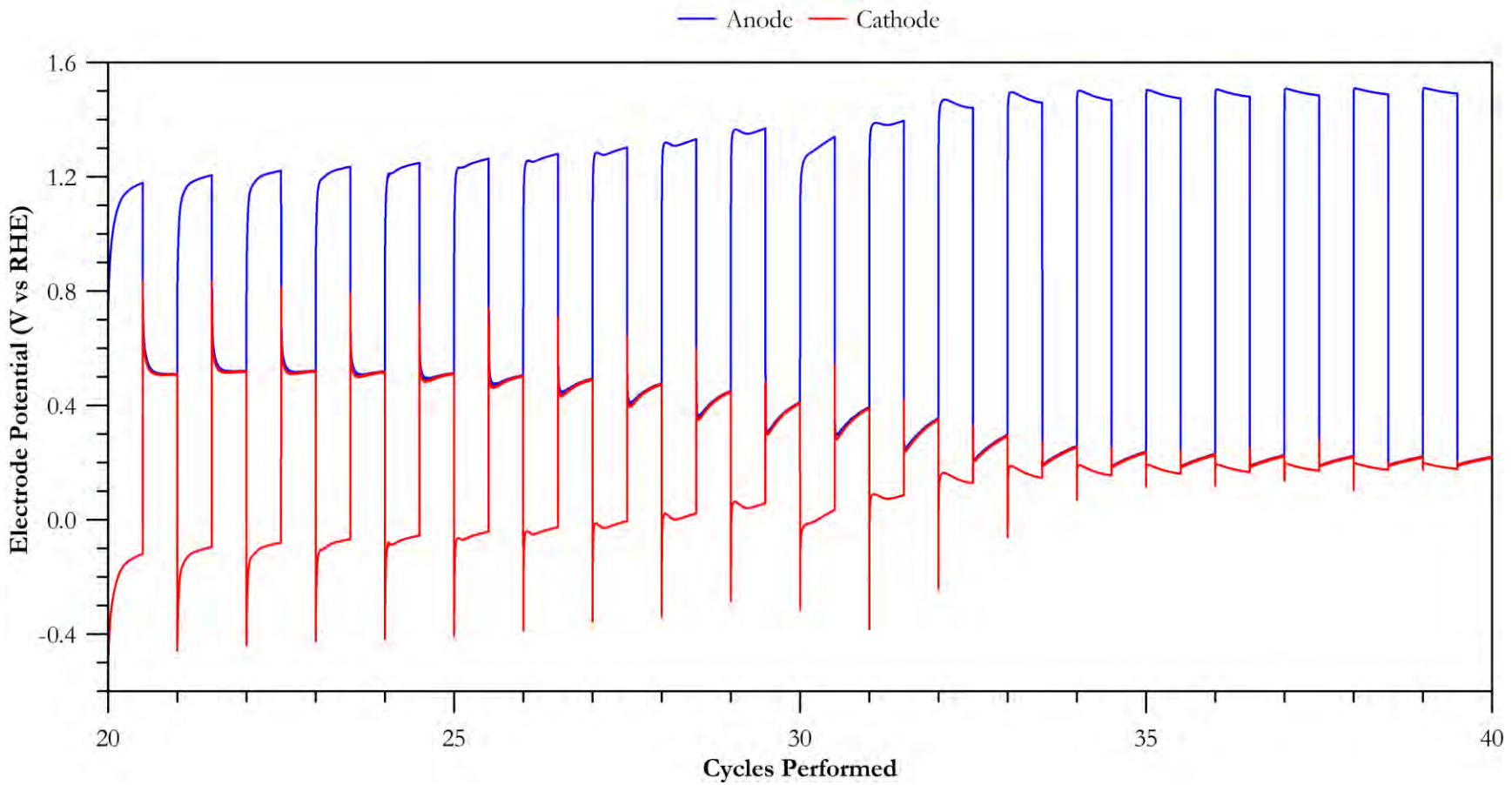

Figure 3.39 Electrode potential distribution throughout cycling (21st-40th cycle) with a cell potential of 1.3 V with a half cycle time of 5 min performed under O_2 saturation using an electrolyte concentration of 17.1 mM (1000 mg NaCl L^{-1}) at room temperature. The electrodes were discharged at zero voltage (i.e., $V_{cell} = 0$)

The role of dissolved oxygen was clear when comparing the anaerobic and aerobic results at a cell potential of 1.3 V. These results indicated that the formation of a reaction couple, between the processes of carbon oxidation and oxygen reduction, was likely. This is, the consumption of the H^+ generated at the anode, as a result of carbon oxidation, to drive the reduction of oxygen and hydrogen peroxide at the cathode. Moreover, a consequence of carbon oxidation is the increase in electrode resistivity [8], [9] (RA in Figure 3.33). As a result, as cycling proceeds, the potential attributed to the anode will increase progressively, hence exacerbating the corrosion process.

However, the detrimental effect of this coupling can be mitigated to an extent, in conventional CDI, by operating the cell at lower potentials at the cost of desalination performance. To show this, cycling experiments were performed under aerobic conditions with a cell potential of 1.0 V. Figure 3.40 shows the gradual loss of capacitance and E_{PZC} induced by the cycling conditions. Over one hundred cycles, around 12% and 22% of the initial capacitance was lost by the cathode and anode, respectively. Moreover, the E_{PZC} of the anode shifted ~50 mV and the E_{PZC} of the cathode remained practically unchanged. Relative to the RHE, the cell potential slowly moved to more positive values. In fact, Figures 3.41 and 3.42 show that the potential difference between the 1st and the 100th was 10 mV only, respectively. In addition, over the one hundred cycles performed, the anodic potential never surpassed 1.1 V vs RHE. Finally, although no further cycles were performed to observe the full capacitance decay curve, it is possible to hypothesize that capacitance will decay rapidly (perhaps precipitously) as the anodic potential progressively increases to higher values, hence increasing the driving force for carbon oxidation.

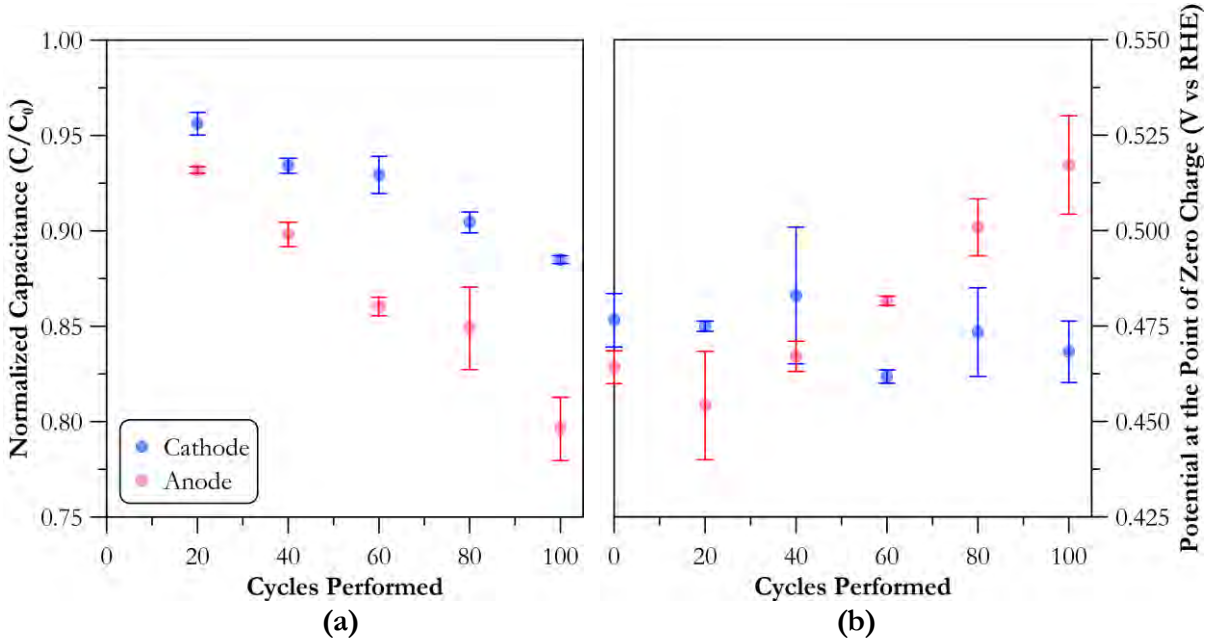

Figure 3.40 (a) Normalized capacitance and (b) E_{PZC} profiles as functions of the number of cycles performed under O_2 saturation at a cell potential of 1.0 V with a half cycle time of 5 min, an electrolyte concentration of 17.1 mM (1000 mg NaCl L^{-1}) and at room temperature. The electrodes were discharged at zero voltage (i.e., V_{cell} = 0). Error bars represent the range between two replicates

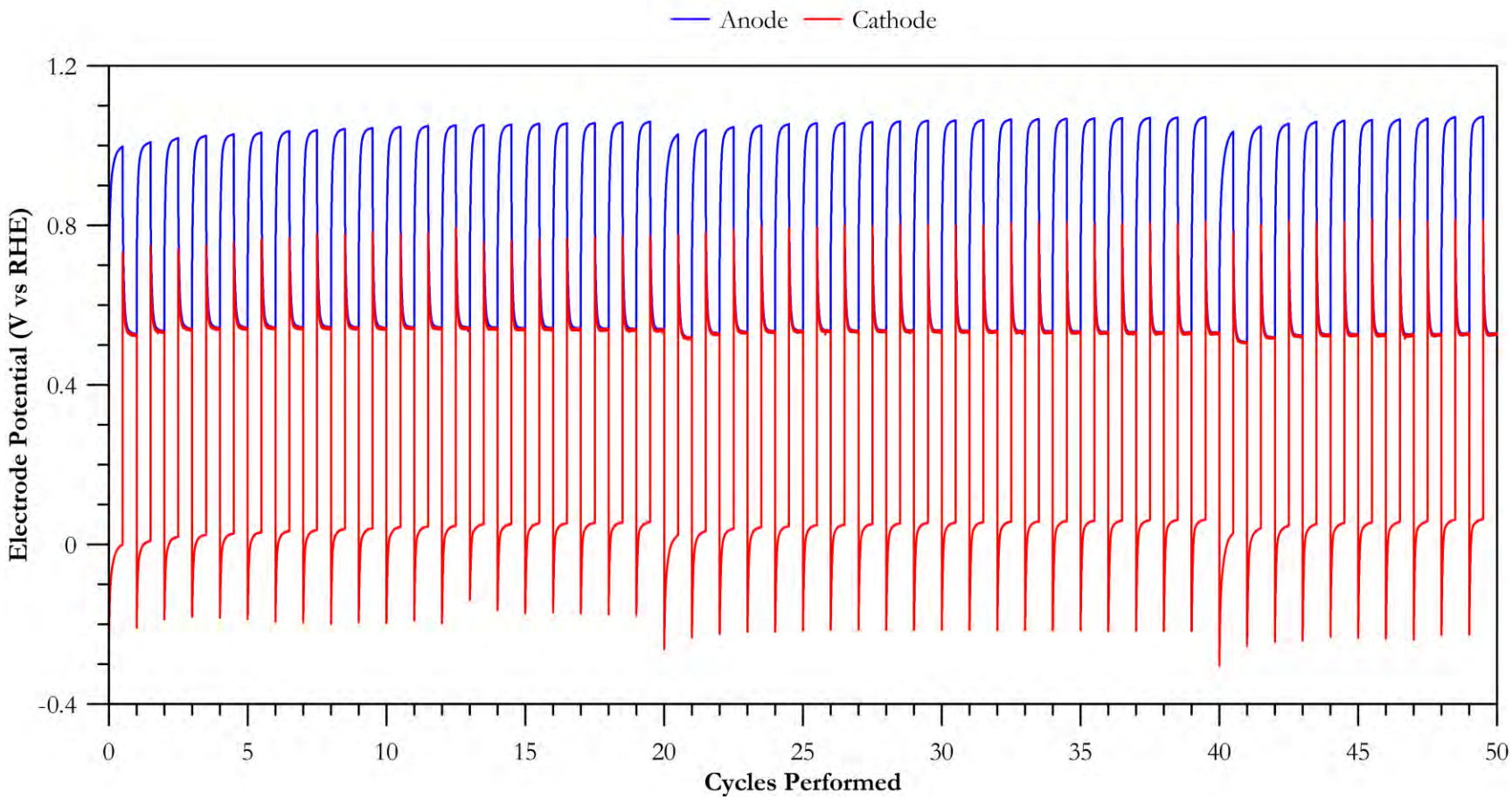

Figure 3.41 Electrode potential distribution throughout cycling (1st-50th cycle) with a cell potential of 1.0 V with a half cycle time of 5 min performed under O_2 saturation using an electrolyte concentration of 17.1 mM (1000 mg NaCl L^{-1}) at room temperature. The electrodes were discharged at zero voltage (i.e., $V_{cell} = 0$)

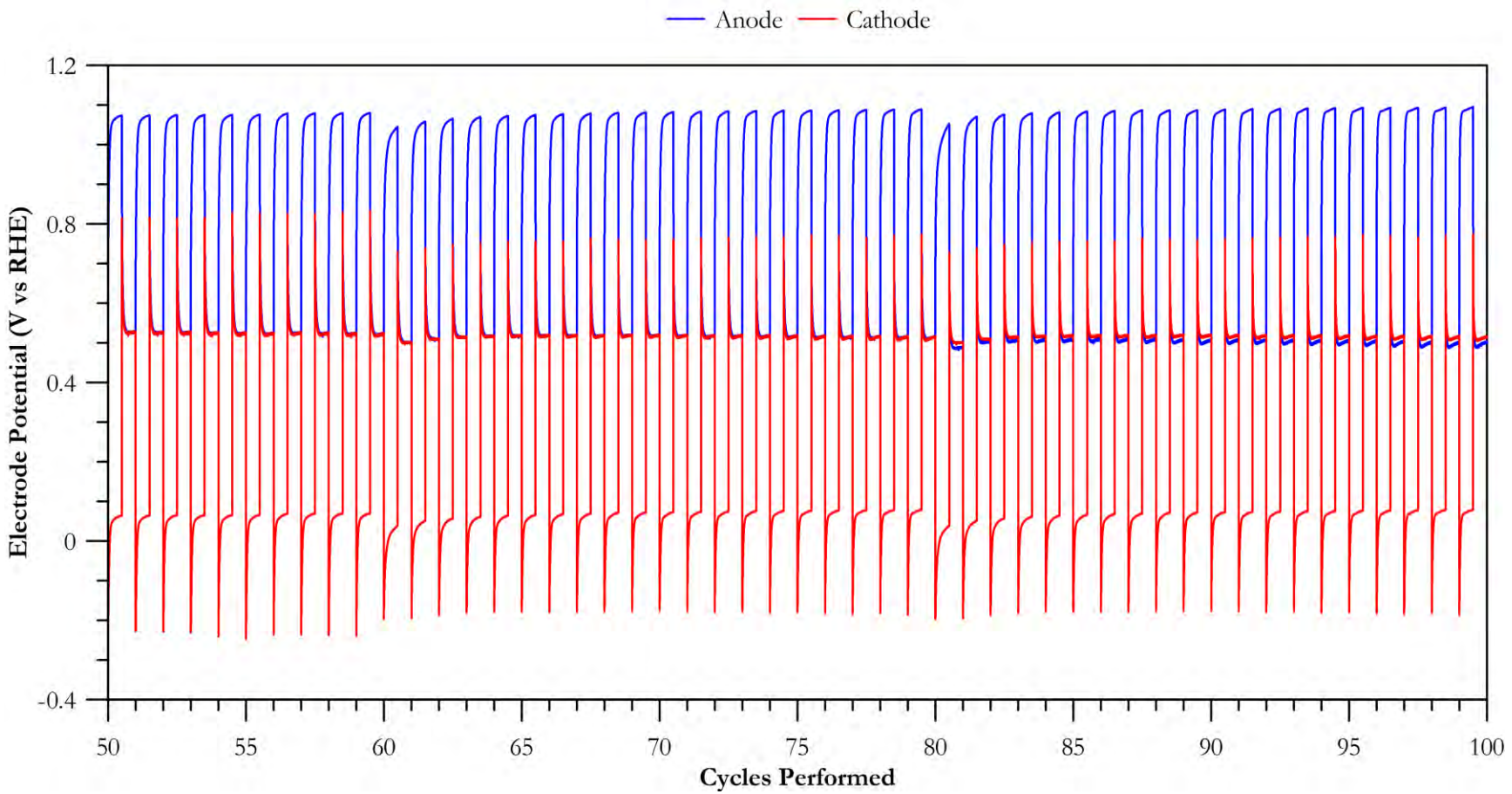

Figure 3.42 Electrode potential distribution throughout cycling (51st-100th cycle) with a cell potential of 1.0 V with a half cycle time of 5 min performed under O_2 saturation using an electrolyte concentration of 17.1 mM (1000 mg NaCl L^{-1}) at room temperature. The electrodes were discharged at zero voltage (i.e., $V_{cell} = 0$)

3.6 Conclusions

The degradation of activated carbon electrodes was studied under an ideal electrolyte composition (i.e., only NaCl), and in solutions with supplemental iron (II) and Suwannee River NOM. Changes in electrochemical properties such as capacitance and E_{PZC} were monitored and complemented by tracking the formation of oxygen containing surface groups, the elemental composition, bulk porosity and wettability.

Experiments conducted in the presence of SRNOM, showed that this organic carbon surrogate has a negligible fouling potential, even at a relatively high concentration of 40 mg L^{-1}. Conversely, the scaling potential of iron was noted at concentrations as low as 0.2 mg Fe^{2+} L^{-1} (3.58 μM $FeCl_2$ L^{-1}). In all cases, electrodes cycled in the presence of iron experienced an accelerated loss of capacitance when compared to that observed for the baseline. Approximately 90% of the initial capacitance was lost after 225 min of operation at 1.2 V vs RHE and 5 min of HCT. In comparison, electrodes cycled under baseline conditions and SRNOM, reached this value after 300 min of operation. Regarding the solutes effect on the E_{PZC} relocation, when compared to the shift observed under baseline conditions, no substantial effect was induced by the presence of SRNOM. In contrast, iron-based deposits such as Fe_2O_3 and $Fe(OH)_3$ appear to balance out the effect of surface oxides by slowing down the E_{PZC} relocation.

Elemental analysis revealed that, for all cases tested, most oxygen incorporation took place during the first 15 to 20 cycles performed. Specifically, the O/C ratio increased by a factor of four over this time frame and then remained stable up and until the end of the electrode life. In addition, an increase in wettability was observed over the early stages of cycling as the contact angle decreased from an initial value of ~130° to ~34°, on average. Due to the qualitative nature of FTIR and the coverage by the oxide layer of the most top layer of the electrode, no changes

were observed with cycling time with respect to the absorption bands associated with oxygen containing functionalities such as C = O, C – O and O – H.

Experiments conducted with different half cycle times demonstrated the importance of this parameter on electrode stability. It was observed that an increasing HCT resulted in an increased capacitance retention. For instance, after the electrodes were held at a potential of 1.2 V vs RHE, around 75%, 83%, 68%, 58% and 5% of the initial capacitance was lost for HCTs of 1, 5, 25, 50 and 250 min, respectively. This effect is likely to be caused by the passivating effect of the oxide layer that results from carbon oxidation. As a result, the rate of carbon corrosion decreased over extended periods of potentiostatic hold (i.e., increased half cycle time). The formation of this layer can be catalyzed by H^+, thus explaining the substantial improvement (approx. 3.75 times) in capacitance retention observed for electrodes cycled in acidic (pH = 1) electrolytes.

By comparing the results obtained from two and three-electrode cells it has been shown that dissolved oxygen is detrimental to the stability of a conventional CDI cell. Its effect arises from the formation of a reaction couple between carbon corrosion and oxygen reduction. In fact, water acts as the oxygen donor for the carbon oxidation process. A consequence of the coupling between these two secondary processes, in a two-electrode cell, the relative electrode potential against a reference electrode will progressively move to higher values, hence increasing the driving force for the corrosion process. However, this process can be alleviated by operating the cell at lower potentials, at the expense of reducing the salt adsorption capacity of the cell. All in all, the ever-changing anodic potential demonstrates the limitations of two-electrode cells to study, from a fundamental point of view, the process of electrode stability in CDI. Nonetheless, two-electrode

cells complement fundamental studies by providing more practical insights on the operation of CDI.

Overall, the results presented in this chapter underline the complexity of selecting experimental conditions for electrode stability studies such as potential and cycling time. Consequently, claims of stability found in the literature need more critical scrutiny, and to avoid bias, a protocol to evaluate the long-term performance of the continuously growing available materials for CDI applications is required.

Chapter 4: Electrochemical Regeneration

Chapter 3 presented the effect of carbon oxidation on the electrode stability and its dependence on the applied potential, half cycle time and cell configuration. Moreover, the effect of fouling and scaling solutes on the loss of performance was investigated. It was demonstrated that through the oxidation of the electrode surface and the evolution of CO_2, the electrode loses its ability to store charge due to unavailability of active sites and the reduction in surface area. In chapter 4, the effect of applying reductive potentials on the recovery of the electrode capacitance and potential at the point of zero charge (E_{PZC}) is presented. The electrochemical reduction of the surface oxides generated during cycling could be a strategy to mitigate the detrimental effect of carbon oxidation on the electrode lifetime. Upon electrochemical regeneration, changes in the electrode electrochemical properties are complemented by the corresponding assessment of the electrode's elemental composition and wettability.

First and foremost, the response surface for the recovery of capacitance and E_{PZC} are surveyed as functions of applied potential and holding time. A 3^2-factorial design of experiments was designed and generated the different treatment combinations to map the responses. Cyclic voltammograms and impedance Nyquist plots are presented to show the changes induced in key aspects of the electrochemical response of the electrode after the application of the different potential-time treatments using a three-electrode setup. Subsequently, the response surface is investigated over the potential domain to further the understanding of capacitance recovery and to find a point of maximum recovery. Finally, the long-term retention of capacitance is studied by the inclusion of a reductive step in the cycling protocol.

4.1 Investigating the Recovery of Capacitance and E_{PZC} Regression

A factorial design of experiments was used to investigate the effect of applied potential and holding time on the recovery of capacitance and regression of the E_{PZC}. The levels for each one of the independent variables are shown in Table 2.4. The selection of the lowest potential level was made in accordance with preliminary tests performed to evaluate the instrument's (i.e., potentiostat) current limitation. This is also linked to the dimensions of the electrochemical cell and electrolyte strength used in the experiments. Conversely, the highest potential was selected by calculating the corresponding thermodynamic potential for the hydrogen evolution reaction (HER) (i.e., using $E = E^0 - 0.059 \cdot pH$) while considering the observed average initial pH (i.e., pH = 7.04 ± 0.06) of the electrolyte. Regarding holding time, on the other hand, the cyclic nature of CDI was considered. If successful, a regeneration step implemented as a step of the cycling protocol should have the smallest influence on the production of freshwater. Therefore, holding times shorter than the half cycle time (HCT) used (i.e., under five minutes) were selected. A schematic showing the potential profiles of the cycling and the electrochemical regeneration protocol is presented in Figure 4.1.

The other point to be considered was the time in the electrode's lifetime when the regenerative step should be applied. To select this, it was presumed that in order to successfully recover the electrode electrochemical properties and extend its stability, one should reduce oxygen functionalities shortly after they are formed to prevent extensive surface coverage. In addition, at least 18 cycled electrodes had to be generated (i.e., all at comparable values of C/C_0) to perform two full replicates of the experimental matrix. Taking these two factors into account, a target C/C_0 value of 0.85 was selected.

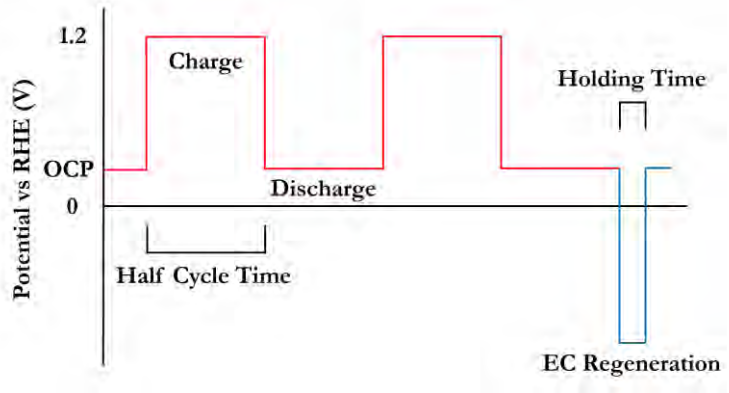

Figure 4.1 Schematic showing the potential profile of the cycling and electrochemical regeneration protocol. The electrode was degraded at a potential of 1.2 V vs RHE with a half cycle time of 5 min until a value of $C/C_0 \approx 0.85$. The electrochemical regeneration consisted of a reductive potential, between -0.4 and -2.1 V vs RHE for holding times of 10, 50 and 90 s under baseline conditions (1 M NaCl, O_2 saturated). Electrode discharge was conducted with a working electrode potential equal to the open circuit potential measured at the beginning of the experiment[8] which was, on average, 0.560 ± 0.001 V vs RHE

The percent capacitance recovery presented in this chapter is based on how much of the capacitance, that was lost during the degradation of the electrode to a value of C/C_0 of 0.85, was recovered after application of different potential-holding time treatments (see equation 2.2 in section 2.4). The recovery of capacitance is a response to an increase of the available surface area or reduction of surface oxygen functionalities, or both. These two increase the number of active sites where ions can be electrosorbed. Then, in cases where capacitance recovery exceeded 100%, either more available surface area or less surface oxygen functionalities, or both, existed when compared to the ones of the electrode at the beginning-of-life. The outcome of applying the different potential-holding time treatments on capacitance and E_{PZC} recovery are presented in Figures 4.2 and 4.3, respectively. Capacitance was successfully recovered to varying degrees under

[8] The potential values at which the electrodes were discharged are presented in Appendix B

all conditions tested. In contrast, all treatments failed to regress the E_{PZC}. Inspection of Figure 4.2 indicated a clear, rapid increase in capacitance recovery as the potential decreased from -0.4 to -1.25 V vs RHE. In addition, holding time had no particular effect when the applied potential was -0.4 V vs RHE, but had a contrasting effect at potentials of -1.25 and -2.1 V vs RHE.

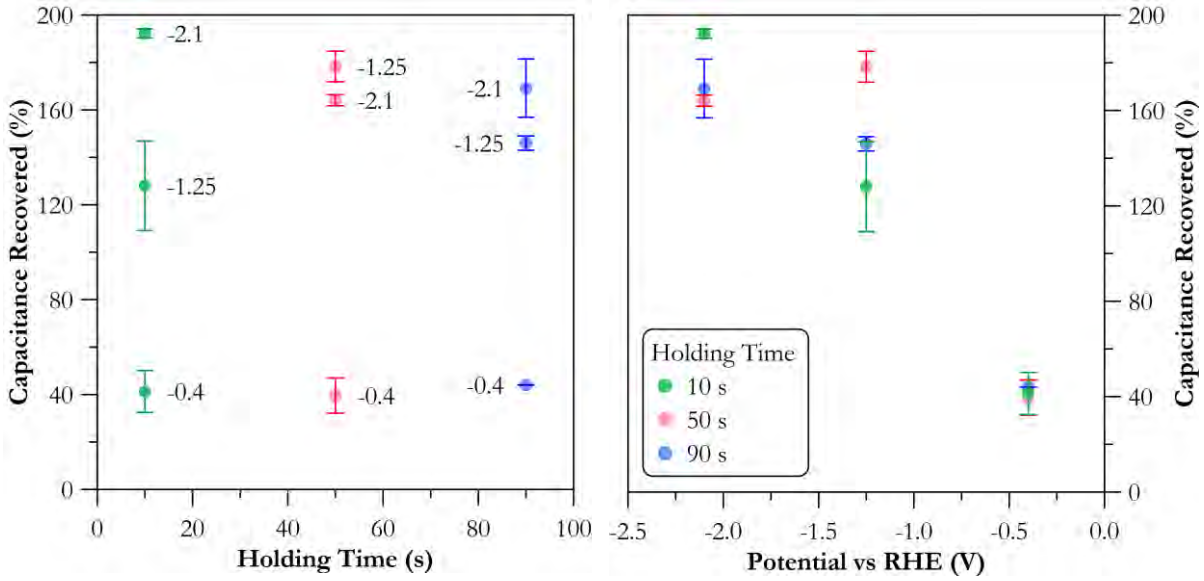

Figure 4.2 Capacitance recovered as a function of holding time and applied potential. Error bars indicate the range between two replicates

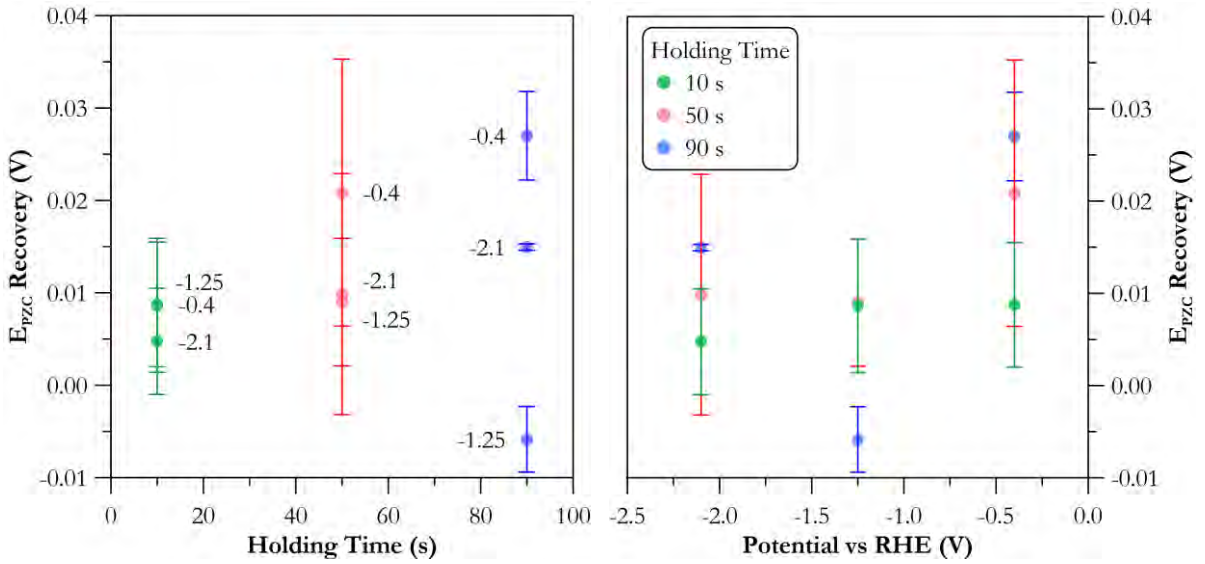

Figure 4.3 E_{PZC} recovery as a function of holding time and applied potential. Error bars indicate the range between two replicates

The hypothesis supporting the selection of the factors used in the factorial design of experiments was that lower potentials and longer holding times were going to be able to recover more capacitance and regress, to a greater extent, the electrode E_{PZC}. Given the negligible regression in the electrode E_{PZC}, the statistical analysis was only performed to the effect of the two tested factors on the recovery of capacitance. To provide a statistical confirmation of the behaviour observed in the 2-dimensional plots presented in Figure 4.2, Analysis of Variance (ANOVA) was performed at a 95% confidence level (i.e., $\alpha = 0.05$) to test the statistical significance of each factor and interaction on the recovery of capacitance. The results are summarized in Table 4.1. At a 95% confidence level, it was concluded that applied potential and the two-way interaction contributed significantly (i.e., p-value < 0.05) to the recovery of capacitance. Moreover, there was insufficient evidence (i.e., p-value > 0.05) to conclude that holding time had a statistically significant contribution to the recovery of the electrode capacitance.

Table 4.1 ANOVA results summary for the recovery of capacitance after the application of potential-holding time treatments

Source	df	Adj SS	Adj MS	F-value	p-value
Model	8	64201.0	8025.1	51.57	0.000
Linear	4	60890.8	15222.7	97.83	0.000
Applied Potential	2	60681.3	30340.6	194.99	0.000
Holding Time	2	209.6	104.8	0.67	0.534
Two-Way Interactions	4	3310.1	827.5	5.32	0.018
Applied Potential·Holding Time	4	3310.1	827.5	5.32	0.018
Error	9	1400.4	155.6		
Total	17				

Figures 4.4 and 4.5 show representative changes in the features of cyclic voltammograms and Nyquist plots (refer to Appendix B.1 for the figures corresponding to the remaining treatments). After degradation, the voltammograms exhibited a reduction of the shaded area, which translated into a reduction of capacitance, and a relocation of the E_{PZC}, which in turn demonstrated surface oxidation. As previously discussed, an increase in resistivity might be responsible for the slanted nature of the reverse scan of the voltammogram. Evidence for the increase in resistivity was also observed when comparing the beginning-of-life (BOL) and degraded complex impedance plane plots. Specifically, an increase in the depressed semicircle diameter was noted, which has been attributed by Frackowiak et al. (2016) [80] to the formation of surface oxygen functionalities as a by-product of carbon corrosion and by Wang et al. (2020) [19] to ion accumulation at the electrode-electrolyte interface. In addition, a linear feature appeared to the right of the semicircle following an angle of 22.5°. Shitanda et al. (2015) [95] and Sharma (2019) [96] correlated the length of this feature with an enhancement in mesopore area as a result of increasing pore depth. On the other hand, Suss et al. (2013) [97] associated the lengthen of this feature to an increase in micropore resistance.

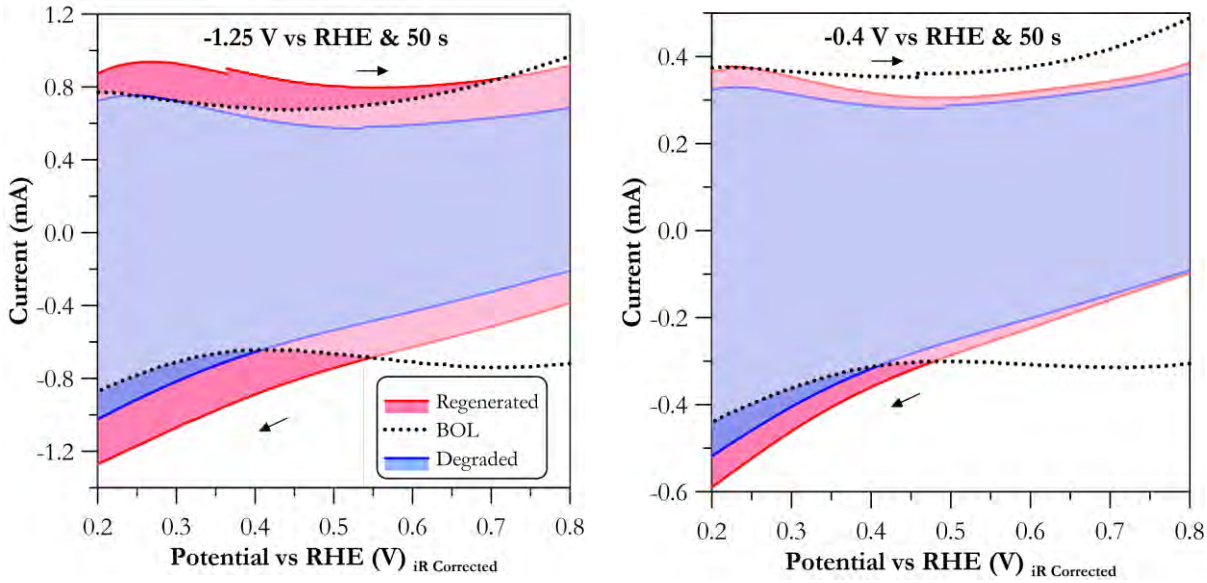

Figure 4.4 Cyclic voltammograms obtained in deaerated 17.1 mM NaCl at room temperature and 1 mV s^{-1} for the pristine (BOL), cycled (degraded to $C/C_0 \approx 0.85$) and regenerated electrodes under selected potential-holding time treatments. Diagrams are enlarged to exhibit the change in the capacitive response and shift of the E_{PZC}

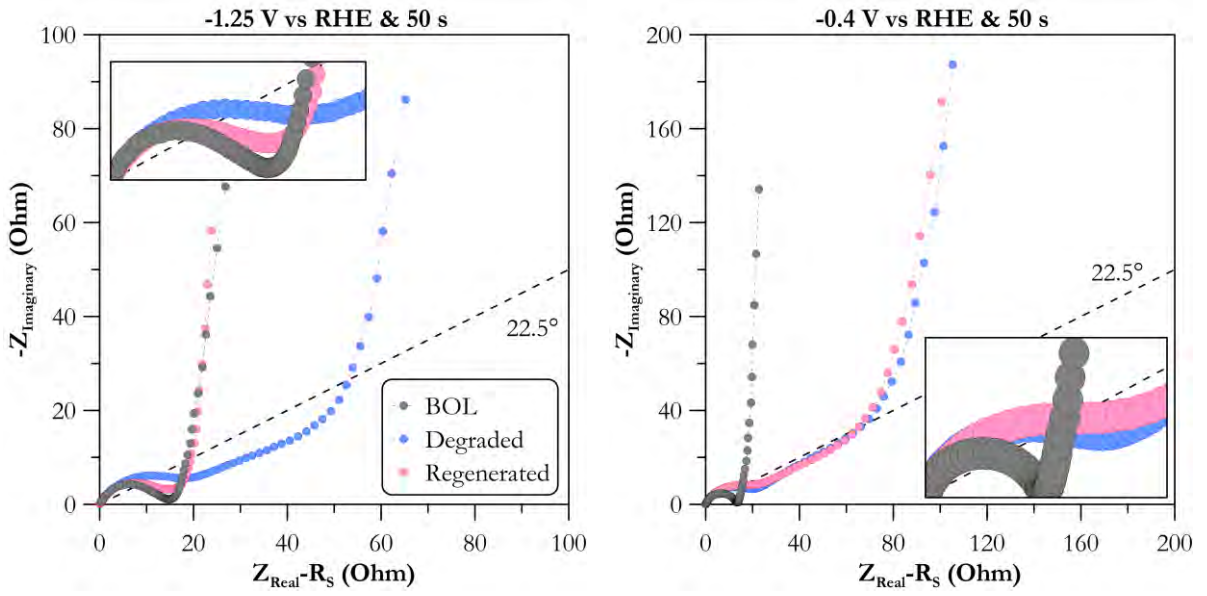

Figure 4.5 Complex impedance plane plots obtained at 0.5 V vs RHE between 350 kHz – 5 mHz in 17.1 mM deaerated NaCl at room temperature with a sine amplitude of 5 mV (3.54 mV_{RMS}) for the pristine (BOL), cycled (degraded to $C/C_0 \approx 0.85$) and regenerated electrodes under selected potential-holding time treatments

After regeneration, voltammograms displayed different extents of enhancement of the area under the I-E curve for all tested treatments. Interestingly, the resistive behaviour observed for the reverse scan was not restored. Nonetheless, the contributions to the increase in capacitance were observed at both anodic and cathodic portions of the voltammograms. The increase in capacitance was also observed in the complex impedance plane plots and could be attributed to an increase of the available surface area. This was correlated to the observed reduction in the impedance modulus (i.e., $|Z|$) at the lowest frequency (i.e., 5 mHz). The observed increase in capacitance and changes in the features exhibited by the Nyquist plots, could be explained by the evolution of H_2 as a result of the negative potentials applied, in particular at -1.25 and -2.1 V vs RHE. The nucleation of bubbles can break up the electrode surface, thus exposing new active sites (i.e., more surface area) which enhanced the electrode capacitance. Analysis of the Nyquist plots suggested no improvement of the semicircle diameter, hence implying no modification in the surface oxygen functionalities formed during degradation. This was supported by the marginal reduction of the oxygen to carbon ratios, presented in Table 4.2. Qualitatively, no change was observed in the absorption bands for the different oxygen functionalities (i.e., C = O, C – O and O – H) evolved during cycling to a C/C_0 value of ≈ 0.85. Refer to Appendix B.3 for the raw FTIR and normalized spectra. In this analysis, the reference spectrum was that of an electrode cycled to a C/C_0 value of ≈ 0.85. In the normalized and background corrected spectrum, a negative change in transmittance change can be correlated with an increase in absorption with respect to the reference spectrum. As shown in Figures 4.6 and 4.7, subtle changes in transmittance were observed, in the background corrected spectrum, for electrodes regenerated at potentials of -0.4 V and -2.1 V vs RHE with holding times of 10 and 90 s. Furthermore, the complex plane plots for treatments performed at potentials of -2.1 and -1.25 V vs RHE, showed varying degrees of

regression of the linear portion following an angle of 22.5° (refer to Appendix B.1 for the figures corresponding to the remaining treatments). Consequently, this influenced the position of the vertical asymptote to which the impedance response aligns as frequency decreases. Suss et al. (2013) [97] attributed this behaviour to the evolution of microporosity after studying the effect of thermal activation processes for the development of hierarchical carbon electrodes.

Table 4.2 Oxygen to carbon ratios of electrodes regenerated under different potential-holding time treatments after degradation at a working electrode potential of 1.2 V vs RHE and a half cycle time of 5 min under baseline conditions (1 M NaCl, O_2 saturated) until a C/C_0 value ≈ 0.85. Uncertainty represents the propagation of error attributed to the averages and standard deviations obtained from three EDS elemental composition analyses

Applied Potential (V vs RHE)	Holding Time (s)			Pristine	Cycled to $C/C_0 \approx 0.85$
	10	50	90		
	O/C x 10^2			O/C x 10^2	O/C x 10^2
-0.4	20.1 ± 0.73	20.1 ± 2.27	19.7 ± 0.62		
-1.25	19.9 ± 0.57	17.5 ± 0.21	17.9 ± 0.16	5.22 ± 1.70	20.5 ± 0.70
-2.1	17.8 ± 0.18	18.5 ± 0.67	17.3 ± 0.33		

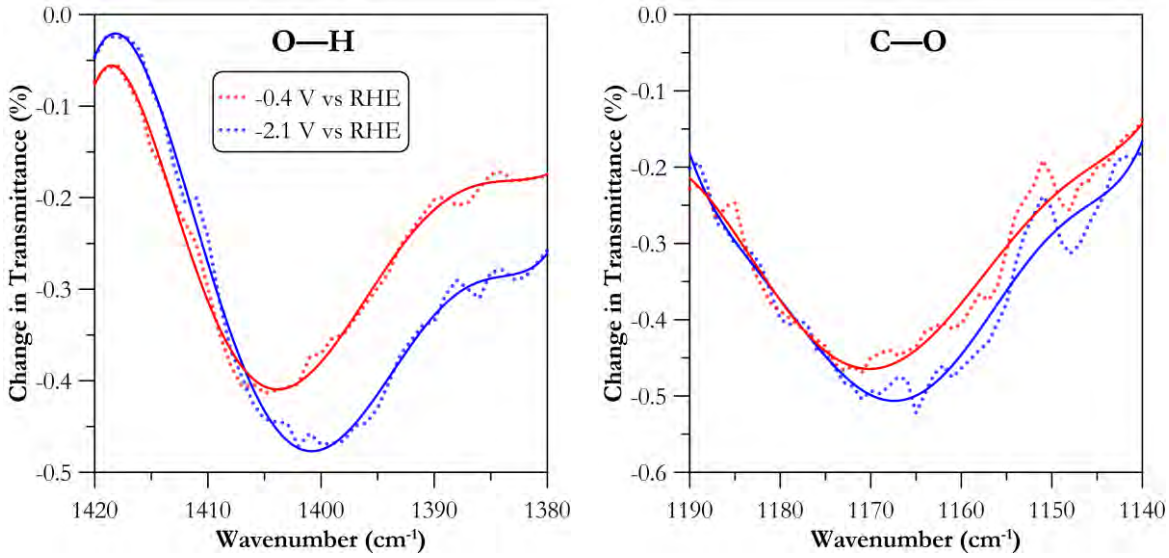

Figure 4.6 Change in transmittance of for the O – H and C – O absorption bands for electrodes regenerated at -2.1 and -0.4 V vs RHE and a holding time of 10 s relative to that exhibited by a degraded electrode to a C/C_0 value ≈ 0.85. The dotted lines represent the actual change in transmittance. The solid lines are given to facilitate the visualization of the trend of the data

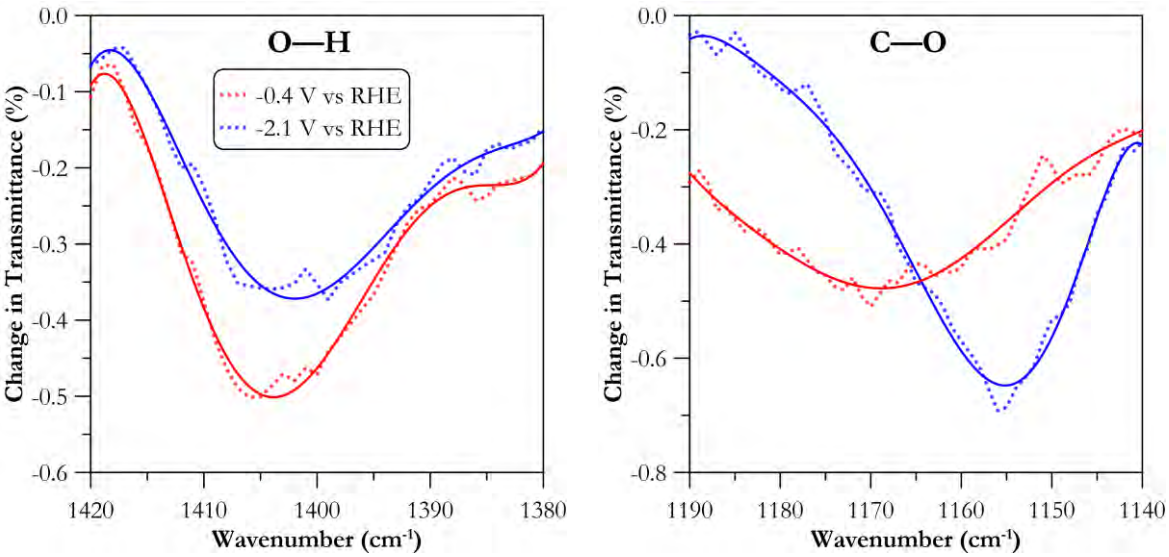

Figure 4.7 Change in transmittance of for the O – H and C – O absorption bands for electrodes regenerated at -2.1 and -0.4 V vs RHE and a holding time of 90 s relative to that exhibited by a degraded electrode to a C/C_0 value ≈ 0.85. The dotted lines represent the actual change in transmittance. The solid lines are given to facilitate the visualization of the trend of the data

4.2 Further Probing along the Potential Domain

Additional regeneration experiments were performed along the potential domain with a holding time of 50 s. These were done with the objective to further understand the recovery of capacitance and to identify whether a zone of maximum recovery existed. The resulting capacitance and E_{PZC} recovered after the potential treatments, presented in section 2.4.2, are displayed in Figure 4.8. In agreement with the results presented earlier, the E_{PZC} of the cycled electrodes showed an inconsequential change after the regeneration tests. On the other hand, capacitance recovery showed a steep increase as the applied potential decreased from -0.61 to -0.83 V vs RHE. Examination of the potentials between -1.46 and -1.89 V vs RHE resulted in a stable capacitance recovery of approximately 175%. Figure 4.9 shows the cyclic voltammograms and complex plane plots of an electrode that displayed the largest capacitance recovery (i.e., at a potential of -1.68 V vs RHE). Refer to Appendix B.2 for the figures corresponding to the other additional points. Specifically, the voltammogram of the regenerated electrode exhibited an increase of the area under the I-E curve (as previously mentioned) when compared to that of the degraded electrode (i.e., to a value of $C/C_0 \approx 0.85$) and at the beginning-of-life (BOL). Conversely, the Nyquist plot showed that the linear segment (to the right of the semicircle) following a 22.5° angle and the impedance imaginary component at the lowest frequency (i.e., 5 mHz) were completely regressed after regeneration. The recession of these features increased between -0.61 and -0.83 V vs RHE and was completely regressed for the remaining of the applied potentials. Refer to Appendix B.2 for the figures corresponding to the other additional points. Moreover, the semicircle diameter attributed to the presence of surface oxides remained virtually the same after regeneration. The latter was consistent with the lack of morphological and compositional changes consistently observed for this and the rest of potential-holding time treatments. Moreover, for the

electrode that showed the largest capacitance recovery, image analysis of cross-sectional portions indicated the bulk porosity was not affected by the evolution of bubbles. Specifically, the cycled (i.e., $C/C_0 \approx 0.85$) and regenerated electrodes showed bulk porosities of 44.0% ± 3.8% and 46.7% ± 0.9%, respectively.

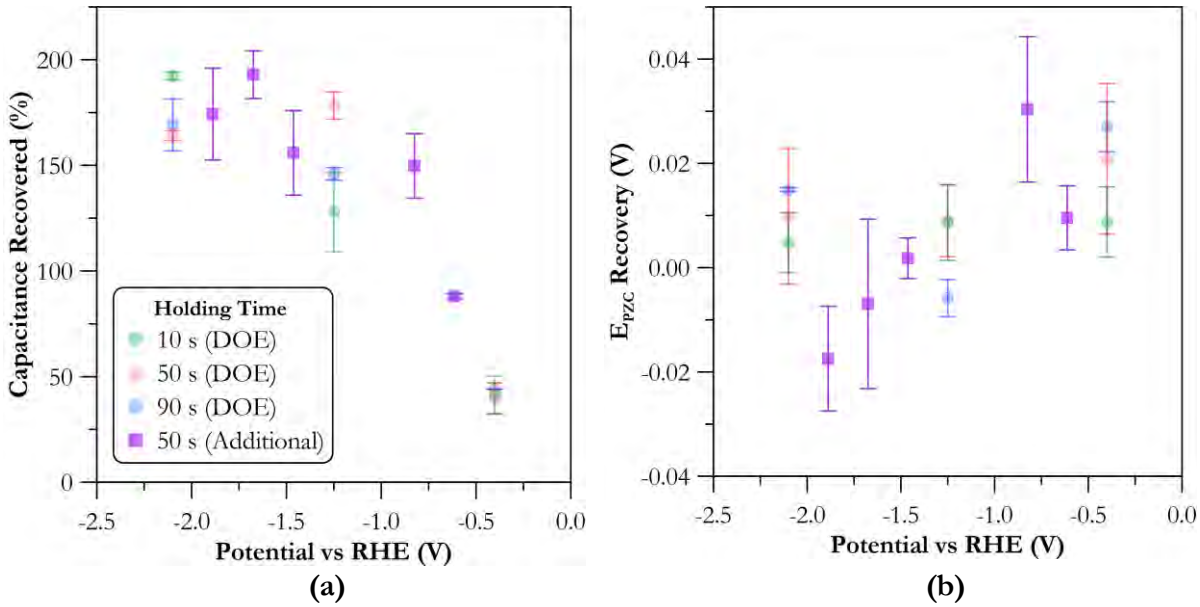

Figure 4.8 (a) Capacitance and (b) E_{PZC} recovered as a function of applied potential for different potential-holding time treatments. Additional 50 s holding time points along the potential domain. Results from the 3^2-factorial DOE provided as reference as a way of contrast. The electrodes were degraded at a potential of 1.2 V vs RHE with a half cycle time of 5 min under baseline conditions (1 M NaCl, O_2 saturated) until a value of $C/C_0 \approx 0.85$. Error bars indicate the range between two replicates

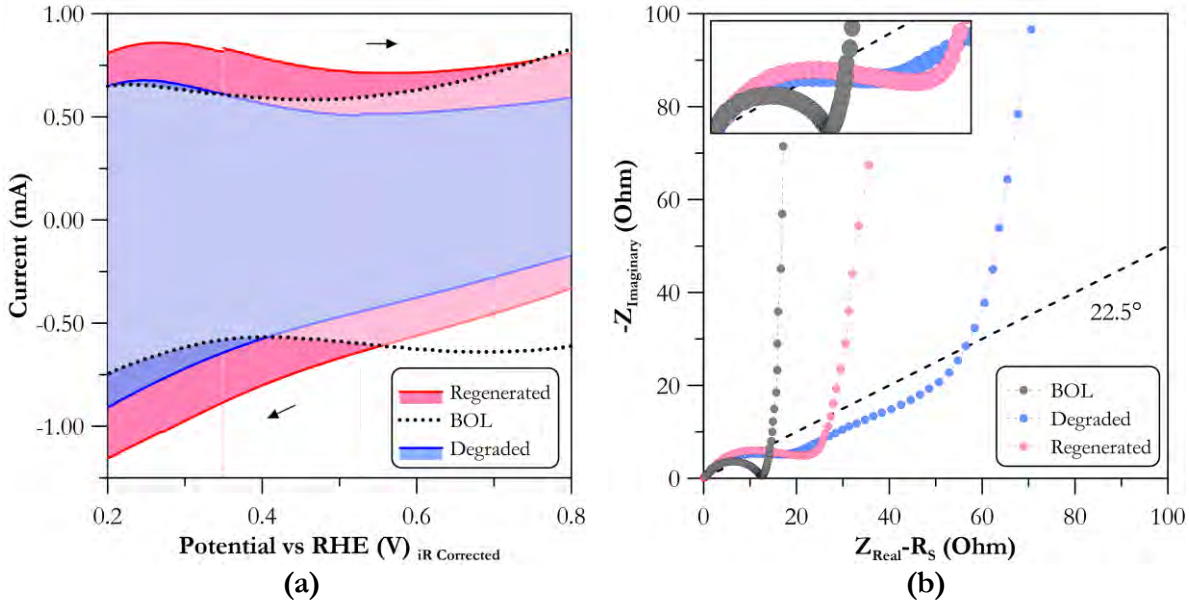

Figure 4.9 (a) Cyclic voltammograms obtained in deaerated 17.1 mM NaCl at room temperature and 1 mV s^{-1} for the pristine (BOL), cycled (degraded to $C/C_0 \approx 0.85$) and regenerated electrodes cycled under an applied potential of -1.68 V vs RHE and 50 s of holding time under baseline conditions (1 M NaCl, O_2 saturated) and (b) Complex impedance plane plots obtained at 0.5 V vs RHE between 350 kHz – 5 mHz in 17.1 mM deaerated NaCl at room temperature with a sine amplitude of 5 mV (3.54 mV_{RMS}) for the pristine (BOL), cycled (degraded to $C/C_0 \approx 0.85$) and regenerated electrodes under an applied potential of -1.68 V vs RHE and 50 s of holding time under baseline conditions (1 M NaCl, O_2 saturated)

4.3 Influence on Electrode Stability

Despite the negligible E_{PZC} recovery, the effect of a regenerative step on the electrode cyclability was tested. It consisted of an applied potential of -1.68 V vs RHE and a holding time of 10 s. The applied potential of -1.68 V vs RHE was selected as it showed the greatest capacitance recovery and the 10 s holding time was chosen as it represented a desirable duration from a practical standpoint, for an additional step (i.e., not a step involving desalination) within the cycling protocol. As summarized in section 2.4.3, this assessment was performed under baseline aerobic conditions (i.e., NaCl alone) and in the presence of 20 mg SRNOM L^{-1} and 0.2 mg Fe^{2+} L^{-1}.

The normalized capacitance and E_{PZC} profiles obtained, under these different conditions, are presented from Figure 4.10 up to Figure 4.15. As expected, the regenerative step was not successful at regressing the electrode E_{PZC}. Nonetheless, for all cases after the 20th cycle, a difference in the E_{PZC} of approx. 50 mV was observed between the degraded and regenerated electrodes. It is noteworthy that towards the latter stages of cycling, this difference increased to around 100 mV for the test in the presence of SRNOM. Capacitance, on the other hand, was recovered to nearly the same degree up until the 25th cycle for the baseline and iron containing experiments and over the first 20 cycles for the test with SRNOM. From these cycle points and onwards, capacitance was no longer recovered. For this reason, the aforementioned recovery in the E_{PZC} (i.e., recovery of operational potential window) after the 20th cycle will have a progressively smaller effect as the electrode continuously losses capacitance. In addition, the normalized capacitance profiles indicated that, although this property was being recovered, it was being lost at a faster rate when compared to that of cycling experiments without a regenerative step. This observation is in agreement with that made by Theodoridou et al. (1981) [25] where an accelerated oxidation of carbon fibres was reported after a reductive treatment. This behaviour was hypothesized to be caused by a large number of defects, resulting from the incomplete reduction reaction, thereby leading to a surface vulnerable to oxidation. All in all, the application of a regenerative step had no positive impact on the overall retention of capacitance.

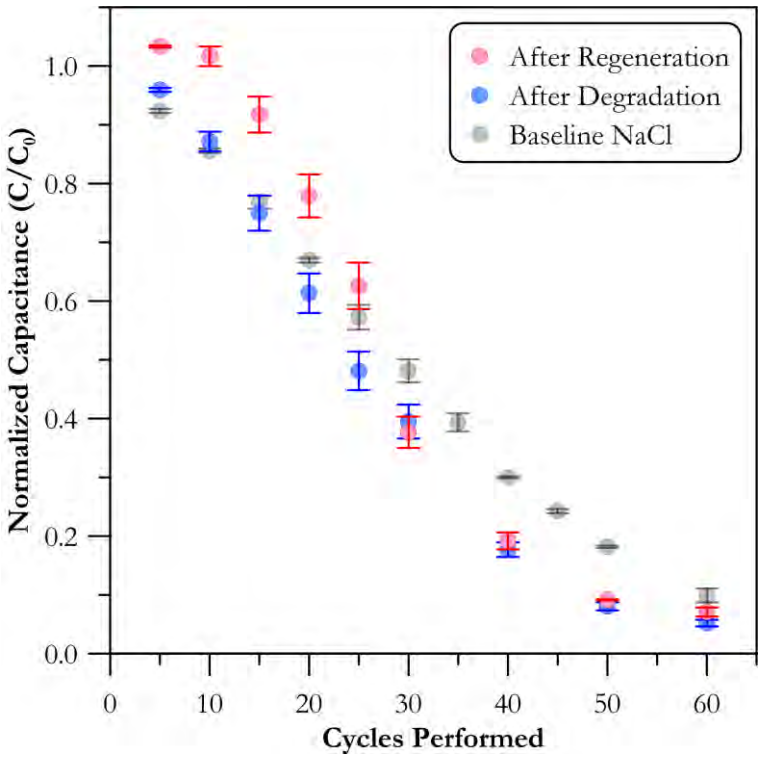

Figure 4.10 Normalized capacitance as a function of the number of cycles performed after degradation at a working electrode potential of 1.2 V vs RHE under baseline conditions (1 M NaCl, O_2 saturated) with a half cycle time of 5 min and after a regeneration step at a working electrode potential of -1.68 V vs RHE and 10 s of holding time under baseline conditions (1 M NaCl, O_2 saturated). Results are contrasted against cycling experiments without the use of a regeneration step. Error bars represent the range between two replicates

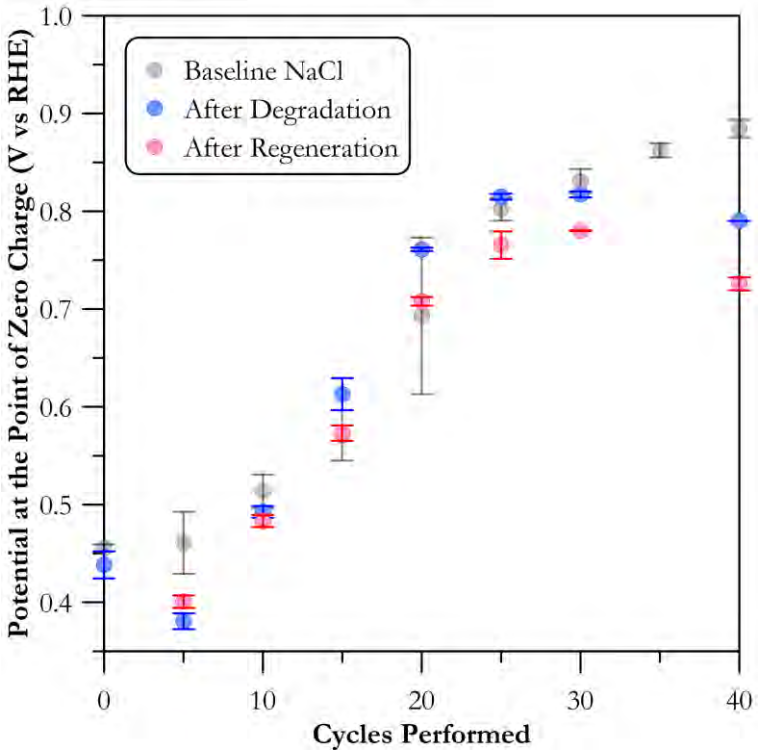

Figure 4.11 E_{PZC} profile as a function of the number of cycles performed after degradation at a working electrode potential of 1.2 V vs RHE under baseline conditions (1 M NaCl, O_2 saturated) with a half cycle time of 5 min and after a regeneration step at a working electrode potential of -1.68 V vs RHE and 10 s of holding time under baseline conditions (1 M NaCl, O_2 saturated). Results are contrasted against cycling experiments without the use of a regeneration step. Error bars represent the range between two replicates

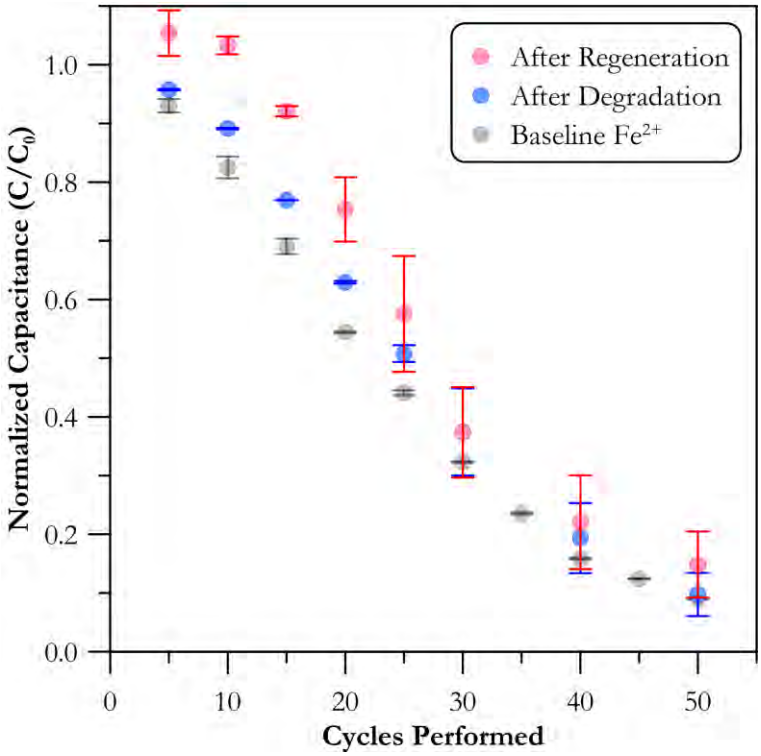

Figure 4.12 Normalized capacitance as a function of the number of cycles performed after degradation at a working electrode potential of 1.2 V vs RHE under presence of 0.2 mg Fe^{2+} L^{-1} (1 M NaCl, O_2 saturated) with a half cycle time of 5 min and after a regeneration step at a working electrode potential of -1.68 V vs RHE and 10 s of holding time under baseline conditions (1 M NaCl, O_2 saturated). Results are contrasted against cycling experiments without the use of a regeneration step. Error bars represent the range between two replicates

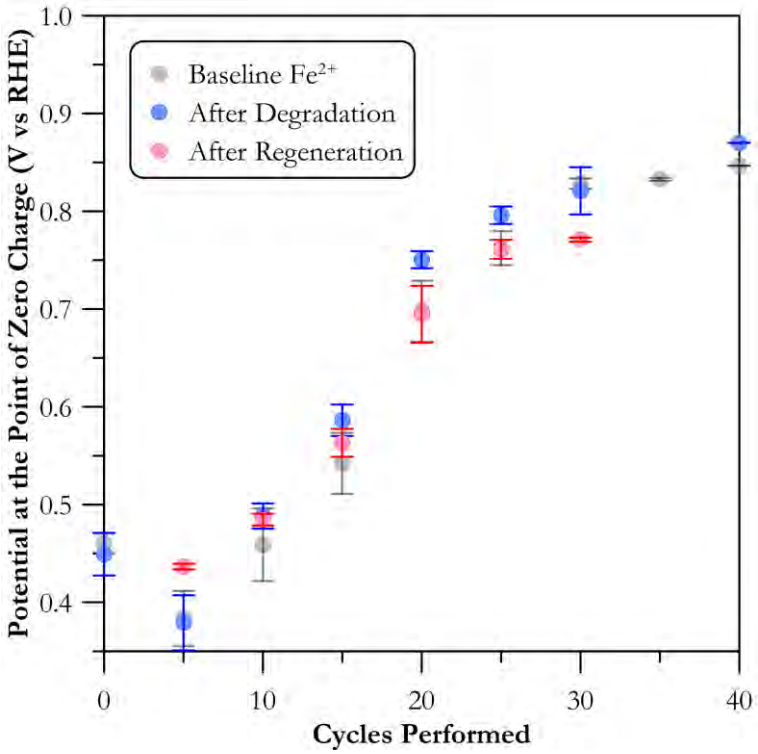

Figure 4.13 E_{PZC} profile as a function of the number of cycles performed after degradation at a working electrode potential of 1.2 V vs RHE under baseline conditions under presence of 0.2 mg Fe^{2+} L^{-1} (1 M NaCl, O_2 saturated) with a half cycle time of 5 min and after a regeneration step at a working electrode potential of -1.68 V vs RHE and 10 s of holding time under baseline conditions (1 M NaCl, O_2 saturated). Results are contrasted against cycling experiments without the use of a regeneration step. Error bars represent the range between two replicates

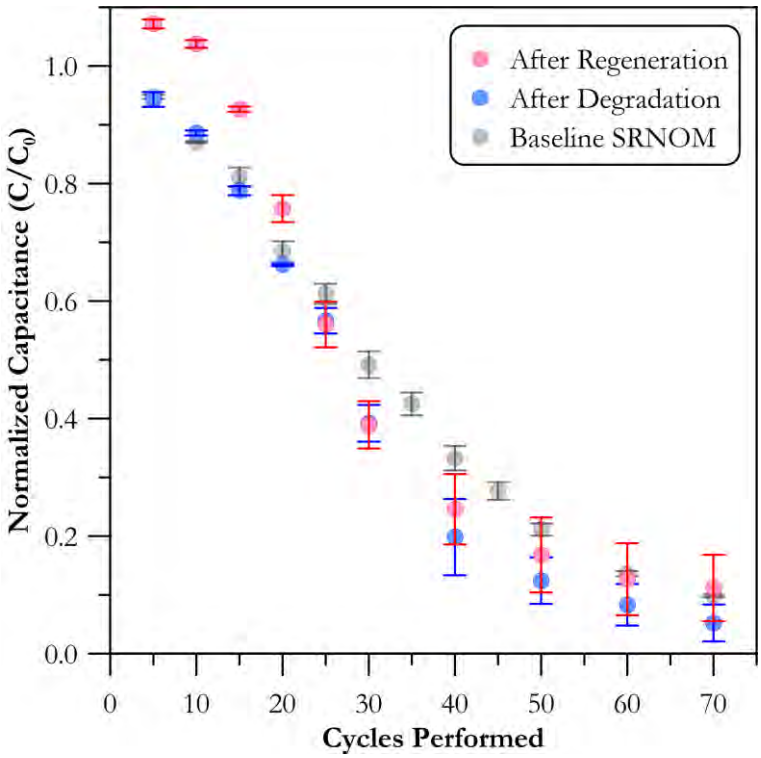

Figure 4.14 Normalized capacitance as a function of the number of cycles performed after degradation at a working electrode potential of 1.2 V vs RHE under presence of 20 mg SRNOM L^{-1} (1 M NaCl, O_2 saturated) with a half cycle time of 5 min and after a regeneration step at a working electrode potential of -1.68 V vs RHE and 10 s of holding time under baseline conditions (1 M NaCl, O_2 saturated). Results are contrasted against cycling experiments without the use of a regeneration step. Error bars represent the range between two replicates

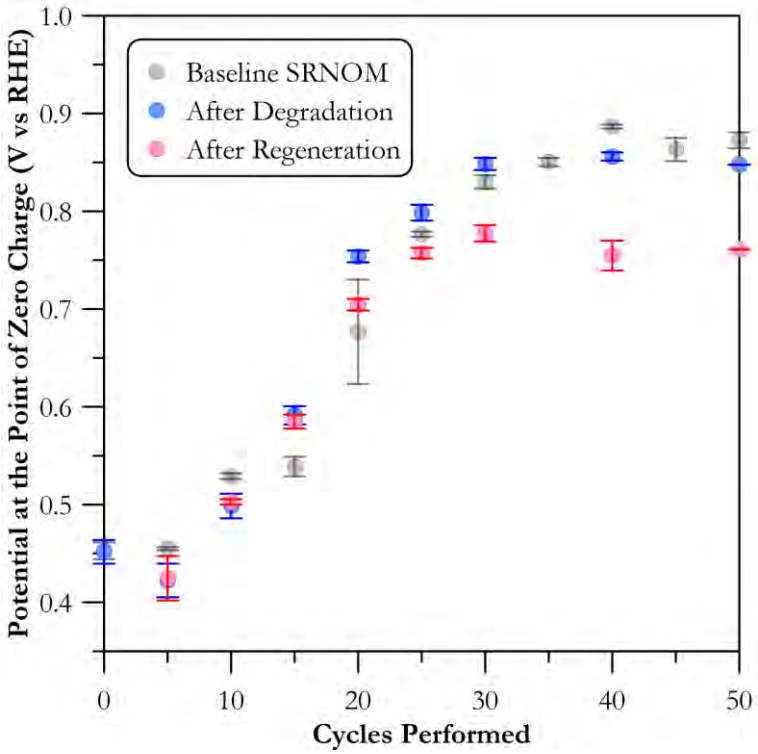

Figure 4.15 E_{PZC} profile as a function of the number of cycles performed after degradation at a working electrode potential of 1.2 V vs RHE under presence of 20 mg SRNOM L^{-1} (1 M NaCl, O_2 saturated) with a half cycle time of 5 min and after a regeneration step at a working electrode potential of -1.68 V vs RHE and 10 s of holding time under baseline conditions (1 M NaCl, O_2 saturated). Results are contrasted against cycling experiments without the use of a regeneration step. Error bars represent the range between two replicates

Inspection of the Nyquist plots, presented in Figures 4.16, 4.17 and 4.18, displayed the progressive evolution and regression of features as a result of consecutive degradation and regeneration steps. For instance, it was observed that the length of the linear portion following a 22.5° angle feature associated with increase in pore length and micropore resistance increased substantially after the second degradation, and then it was reduced after the second regeneration. Moreover, the impedance modulus (i.e., |Z|) at the lowest frequency (i.e., 5 mHz) was seen to relocate between relatively higher and lower values after each degradation and regeneration step,

respectively. This can be correlated to the loss and generation of new active sites (i.e., reduction and recovery of surface area) arising from consecutive degradation and regeneration steps. Upon the third degradation and onwards (data not shown), the depressed semicircle did not appear nor was it recovered after the regeneration step.

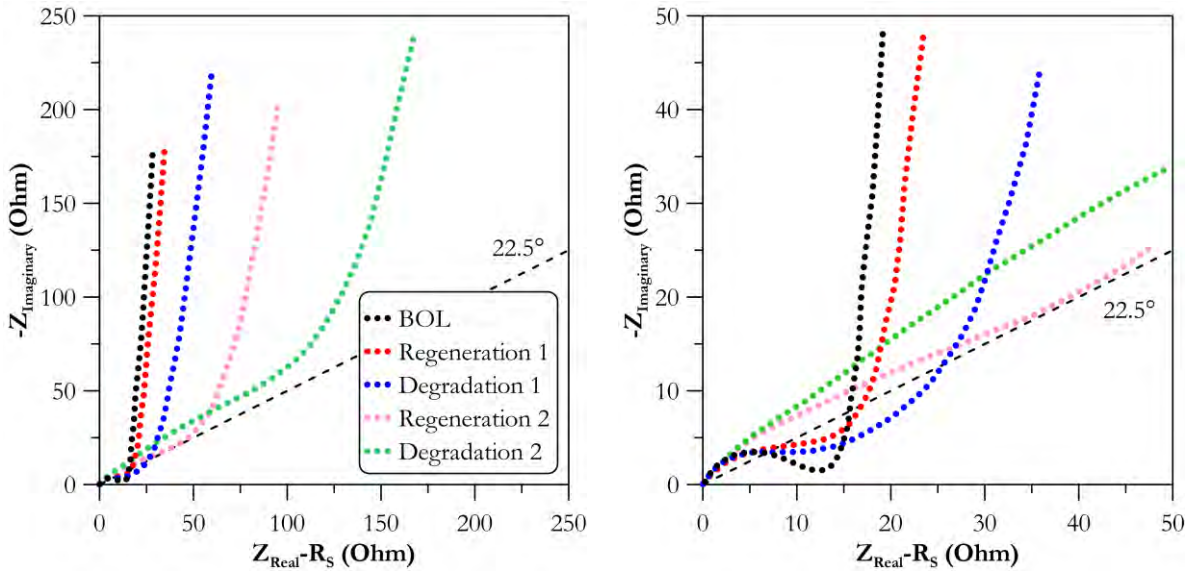

Figure 4.16 Complex impedance plane plots obtained at 0.5 V vs RHE between 350 kHz – 5 mHz in 17.1 mM deaerated NaCl at room temperature with a sine amplitude of 5 mV (3.54 mV_{RMS}) for consecutive degradation and regeneration steps. The electrode was degraded under baseline conditions (1 M NaCl, O_2 saturated) at a working electrode potential of 1.2 V vs RHE with a 5 min half cycle time and regenerated at a working electrode potential of -1.68 V vs RHE and 10 s of holding time under baseline conditions (1 M NaCl, O_2 saturated)

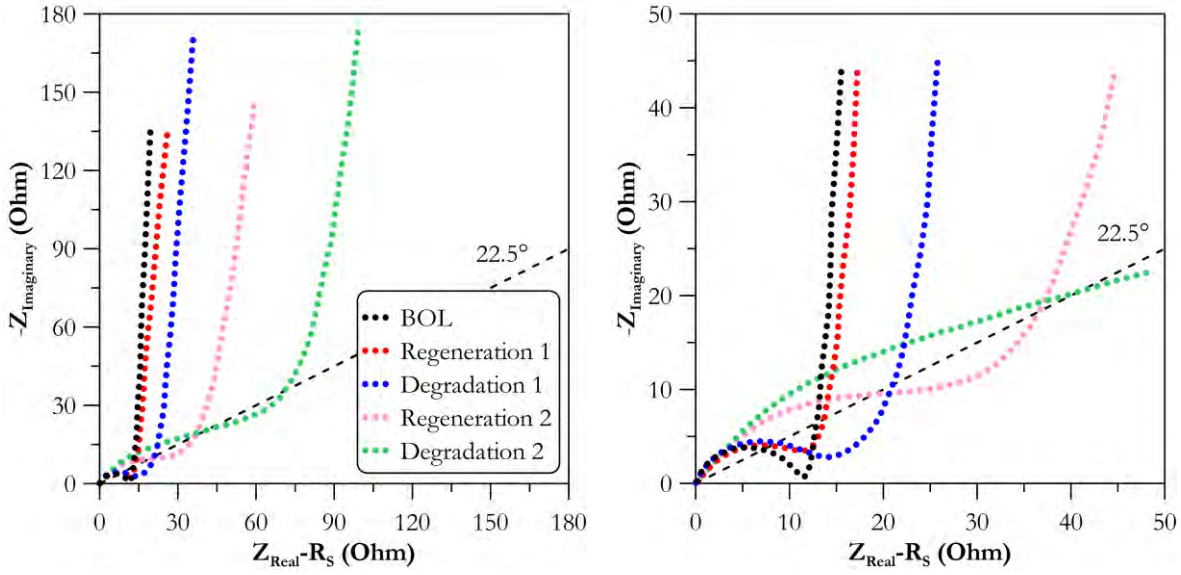

Figure 4.17 Complex impedance plane plots obtained at 0.5 V vs RHE between 350 kHz – 5 mHz in 17.1 mM deaerated NaCl at room temperature with a sine amplitude of 5 mV (3.54 mV_{RMS}) for consecutive degradation and regeneration steps. The electrode was degraded under presence of 20 mg SRNOM L^{-1} (1 M NaCl, O_2 saturated) at a working electrode potential of 1.2 V vs RHE with a 5 min half cycle time and regenerated at a working electrode potential of -1.68 V vs RHE and 10 s of holding time under baseline conditions (1 M NaCl, O_2 saturated)

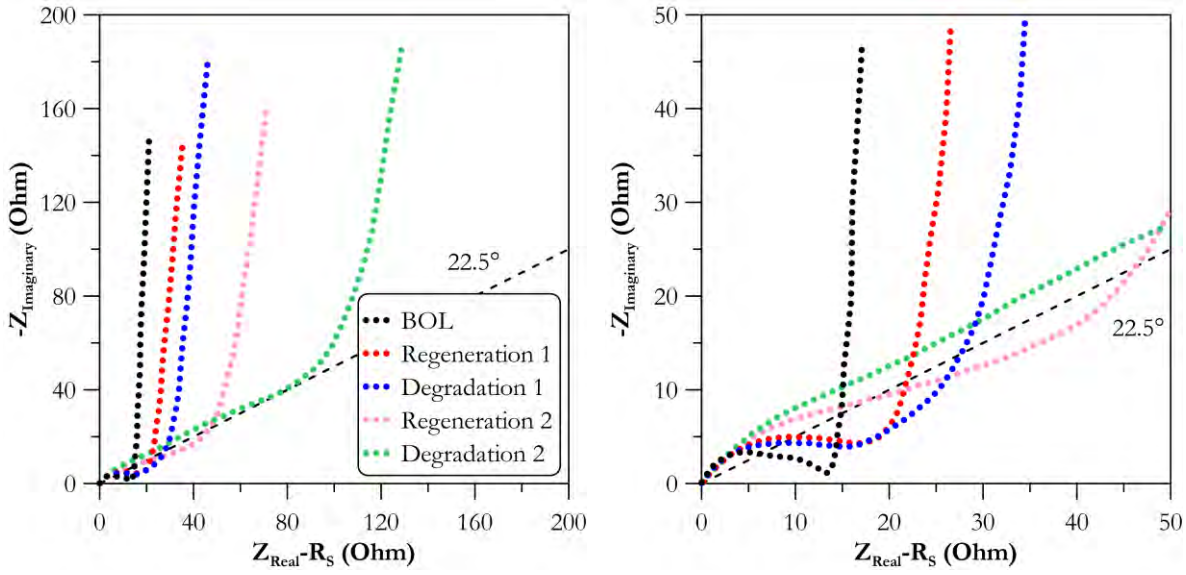

Figure 4.18 Complex impedance plane plots obtained at 0.5 V vs RHE between 350 kHz – 5 mHz in 17.1 mM deaerated NaCl at room temperature with a sine amplitude of 5 mV (3.54 mV_{RMS}) for consecutive degradation and regeneration steps. The electrode was degraded under presence of 0.2 mg Fe^{2+} L^{-1} (1 M NaCl, O_2 saturated) at a working electrode potential of 1.2 V vs RHE with a 5 min half cycle time and regenerated at a working electrode potential of -1.68 V vs RHE and 10 s of holding time under baseline conditions (1 M NaCl, O_2 saturated)

The oxygen to carbon ratios and contact angle measurements at the end-of-life, are presented in Table 4.3 and compared against those observed for electrodes cycled without a regeneration stage. A contradictory behaviour is observed when comparing these two parameters. One would expect an increase in the O/C ratio to be accompanied by an increase in wettability (i.e., decrease in contact angle). However, this was not the case for the electrodes cycled with a regeneration step, where despite showing relatively larger contact angles, the O/C ratios showed slightly higher values than those calculated for electrodes cycled without a regeneration step. Finally, qualitative analysis of the raw and normalized FTIR spectrum (refer to Appendix B.3) of electrodes at end-of-life conditions indicated, as expected per previous results, no difference in the evolved absorption bands (i.e., C = O, C – O and O – H). In this case, the FTIR spectrum

was normalized relative to the corresponding spectrum at EOL condition without a regeneration step and was background corrected. Figure 4.19 shows the slight changes observed for the C – O and O – H absorption bands.

Table 4.3 Comparison of the oxygen to carbon ratios and contact angle of electrodes at the end-of-life (EOL), cycled with and without an electrochemical regeneration step. The electrode was cycled at a working electrode potential of 1.2 V vs RHE with a 5 min half cycle time under baseline conditions (1 M NaCl, O_2 saturated) and under presence of 20 mg SRNOM L^{-1} (1 M NaCl, O_2 saturated) or 0.2 mg Fe^{2+} L^{-1} (1 M NaCl, O_2 saturated). The electrode was regenerated at a working electrode potential of -1.68 V vs RHE and 10 s of holding time under baseline conditions (1 M NaCl, O_2 saturated)

Electrolyte Composition	O/C[9] x 10^2		Contact Angle (degrees)[10]	
	Without Regeneration	With Regeneration	Without Regeneration	With Regeneration
Baseline	17.8 ± 1.66	19.2 ± 0.69	39 ± 3.5	86 ± 5.6
20 mg SRNOM L^{-1}	15.3 ± 3.36	20.5 ± 1.85	28 ± 0.9	55 ± 9.8
0.2 mg Fe^{2+} L^{-1}	13.9 ± 5.16	20.2 ± 2.00	63 ± 3.7	100 ± 7.1
BOL	5.22 ± 1.70		131± 2.4	

[9] Uncertainty of the O/C represents the propagation of error attributed to the averages and standard deviations obtained from three EDS elemental composition analyses

[10] Error bars represent the standard error of the measurements

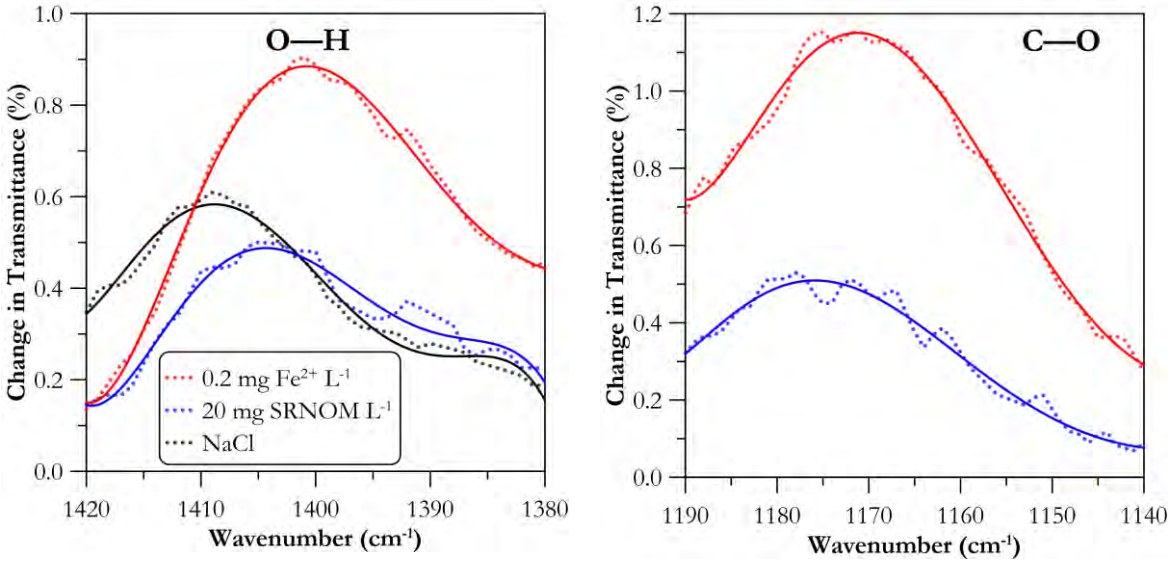

Figure 4.19 Change in transmittance of for the O – H and C – O absorption bands for electrodes at EOL conditions cycled with a working electrode potential of 1.2 V vs RHE and a half cycle time of 5 min with a regeneration step at -1.68 V vs RHE and a holding time of 50 s relative to that exhibited by the corresponding electrode at EOL conditions cycled with a working electrode potential of 1.2 V vs RHE and a half cycle time of 5 min without a regeneration step. The dotted lines represent the actual change in transmittance. The solid lines are given to facilitate the visualization of the trend of the data

4.4 Conclusions

The application of reductive potentials for the recovery of capacitance and E_{PZC} was investigated. Ex-situ analysis, such as EDS, FTIR spectroscopy and contact angle measurements, were performed to evaluate the changes in morphology, composition and wettability.

The capacitance and E_{PZC} recovery surface response were first mapped with the aid of a 3^2-factorial design of experiments. The different recovery treatments consisted of combinations of applied potentials of -0.4, -1.25 and -2.1 V vs RHE and holding times of 10, 50 and 90 s. With the aid of ANOVA, performed at a confidence level of 95% ($\alpha = 0.05$), it was found that the applied potential has a statistically significant contribution towards capacitance recovery. Capacitance was recovered, to some level after all applied potential-holding time treatments.

Further evidence supporting the regenerative effect of the treatments was obtained from impedance spectroscopy. Features such as the linear portion following a 22.5° and the impedance modulus (|Z|) were observed to evolve and regress, to different degrees, after every treatment. On the other hand, no substantial changes were noted in the diameter of the semicircle at high frequencies. In accordance with the latter, the E_{PZC} of the electrodes showed no sign of recovery, indicating that the surface remained functionalized.

Further exploration of the capacitance recovery surface response was done by performing experiments along the potential domain with a holding time of 50 s. These experiments demonstrated that capacitance recovery increases sharply between potentials of -0.4 and -0.83 V vs RHE and it appears to stabilize at a value of 175% between -1.25 and -2.1 V vs RHE.

Even though the electrode E_{PZC} was not regressed, a reductive step was included as part of the cycling protocol to study its effect on the long-term retention of capacitance. This step, at a potential of -1.68 V vs RHE and a holding time of 10 s, was tested for electrodes cycled under baseline aerobic conditions (i.e., only NaCl) and in presence of SRNOM or iron (II). For all cases, a constant capacitance recovery was observed during the first 20 to 25 cycles. After this point, capacitance was no longer recovered. Despite the recovery observed, this did not translate to an extended retention of capacitance. In fact, capacitance was lost at a faster rate during the first 20 to 25 cycles.

Altogether, under the experimental conditions that were tested herein, the use of electrochemical regeneration approaches was not an effective method to mitigate the effect of carbon corrosion and thus, prolong the electrode cyclability. However, other cycling protocols (i.e., applied potential and half cycle time) out of the scope of this study, may impact the electrode

oxidation process in such a way that electrochemical regeneration approaches are an effective way to mitigate the effect of carbon corrosion.

Chapter 5: Conclusions and Recommendations for Future Work

5.1 Conclusions

This study investigated the long-term stability and electrochemical regeneration of activated carbon electrodes used in CDI applications. First, the influence of iron and dissolved organic matter on the electrode electrochemical and morphological properties over its lifetime was studied. Experiments were conducted using a 3-electrode cell setup, at a working electrode potential of 1.2 V vs RHE and a half cycle time of 5 min with electrolytes (1 M NaCl) containing different concentrations of iron or dissolved organic matter. From these series of experiments, the main findings are as follows:

- The presence of iron, at concentrations as low as 0.2 mg Fe^{2+} L^{-1} was shown to contribute to the loss of electrode capacitance and delayed the change in the electrode potential at the point of zero charge. The effect increased with Fe^{2+} concentration, but no differences were noted between iron concentrations of 2 and 20 mg Fe^{2+} L^{-1}. The scaling behaviour of iron arises from the formation of insoluble Fe^{3+} deposits on the electrode surface, which can reduce the availability of active sites as a result of pore blockage. Therefore, a pre-treatment stage (e.g., Greensand filtration) is required to minimize the contribution of scaling to the reduction of electrode life.
- Suwannee River NOM used as a surrogate for dissolved organic carbon had no contribution to the loss of electrode capacitance and change in the electrode potential at the point of zero charge even at concentrations as high as 40 mg SRNOM L^{-1}. Nonetheless, it should be noted that dissolved organic matter has been reported to decrease salt adsorption performance, due to competition for active sites and

enmeshment with the electrode porous network. Therefore, further studies are required to elucidate and explain the results observed in this research (see section 5.2).

- Elemental analysis through EDS and contact angle measurements indicated a substantial incorporation of oxygen during the first 20 cycles performed. A limitation of the contact angle measurement is that this technique is only capturing the changes in hydrophobicity at the top layer of carbon. As per the discussion of the oxidation mechanism, an oxide layer develops over time. Then, it could be possible that over the first 20 cycles, the oxide layer covered most of the electrode top layer and, as a result, minor changes were observed at different points in the electrode lifetime (i.e., C/C_0) between the 20^{th} cycle and EOL conditions. Despite this limitation, complementary elemental analysis through EDS indicated, in agreement with the observed changes in contact angle, a 4-fold increase in oxygen content over the first 20 cycles performed.
- Analysis of the bulk porosity showed slight changes between BOL and EOL conditions. Specifically, an increase in bulk porosity was noted for electrodes cycled in the presence of 20 mg SRNOM L^{-1} and a decrease was observed for electrodes cycled at 20 mg Fe^{2+} L^{-1}. It is important to note that this parameter was estimated from image analysis of cross-sectional SEM images. The grayscale nature of the images made difficult to differentiate between carbon particles and the epoxy filler, especially for particles that were located towards the far end of the cross-sectional image.
- FTIR analysis revealed the evolution of oxygen containing functionalities with cycling. However, due to the qualitative nature of the analysis and the quick formation of an oxide layer on the top layers of the electrode, no changes were observed during the electrode life. A more quantitative analysis could be helpful to elucidate which

functionalities dominate the electrode surface and whether they change over the electrode life. To do this, XPS could be used. Unfortunately, the possibilities did not exist to perform this analysis (and other techniques suggested in section 5.2) locally and due to COVID-19. Thus, FTIR was chosen as a complementary ex-situ analysis technique. However, analysis of FTIR spectra of activated carbon is challenging because of the curved baseline and scattering.

Second, the effect of pH and half cycle time on the electrode electrochemical properties was explored. Experiments were conducted using a 3-electrode cell setup, at a working electrode potential of 1.2 V vs RHE with electrolytes containing only sodium chloride (1 M NaCl). From these series of experiments, the following conclusions were obtained:

- An increase in half cycle time reduced the loss of electrode capacitance and slowed the change in the electrode potential at the point of zero charge. Increased potentiostatic holds exhibited lower degradation rates as a result of the passivating effect induced by the oxide layer. This reveals that in addition to the applied potential, half cycle time is an extremely important parameter and should be subject to standardization to enable a fair comparison between different electrode materials. In practice, extending the holding time beyond the time required for the electrode surface to be saturated with ions results in energy losses. However, it could be possible to prolong the electrode lifetime by cycling with extended half cycle times and still achieve the required desalination by phasing in unsaturated electrode stacks.
- At a pH value of 1, the electrodes showed reduced loss of capacitance and change in the electrode potential at the point of zero charge. The process of carbon corrosion is catalyzed by H^+. However, the quick formation of the oxide layer passivates the

electrode surface and the electrochemical properties are lost at a slower rate than those of electrodes cycled with near neutral electrolytes. On the other hand, electrodes cycled at a pH value of 13, showed a similar capacitance loss profile to that of electrodes cycled with near neutral electrolytes. However, the change in the electrode potential at the point of zero charge suggested that the loss of capacitance was not dominated by carbon corrosion. It is likely that the exposure of the electrode to NaOH etched its carbon surface affecting its porous structure resulting in a reduction in surface area.

Third, the electrode stability was studied using a more practical two-electrode setup to understand the role of applied potential and dissolved oxygen during long-term operation. Experiments were conducted at cell potentials of 1.0, 1.3 and 1.8 V with electrolytes saturated with N_2 or O_2 and containing only sodium chloride (17.1 mM NaCl). The main findings from these series of experiments are:

- In comparison with the experiments using a three-electrode setup, the presence of dissolved oxygen accelerated the loss of capacitance and change in the potential at the point of zero charge of the anode when cycling at a cell potential of 1.3 V. In the absence of oxygen, the anode showed only a slight change in these electrochemical properties. Nonetheless, at a cell potential of 1.8 V, it was possible to fully degrade the electrode in just 20 cycles. These results confirmed the reaction coupling occurring between the processes of carbon oxidation and oxygen reduction.
- The effect of this reaction coupling on the electrode stability can be alleviated by operating the CDI cell at lower cell potentials at the cost of desalination performance or by using membranes. Moreover, the CDI cell could be operated in an alternating

polarization mode, in the sense that the electrodes can act as the anode or cathode every other cycle.

- From a practical standpoint, the potential attributed to the anode can be monitored (with the aid of an external reference electrode) and used as an additional metric for cell performance as it will be an indirect measure of the anode oxidation state.
- From a fundamental point-of-view, the use of two-electrode cells to investigate the stability of materials for CDI applications, which is common in CDI literature, is an inadequate approach as the attributed potential to the anode increases as it becomes more oxidized.

Fourth, the application of electrochemical regeneration approaches with the aim to mitigate the effect of carbon oxidation by reduction of the surface oxides was investigated. The recovery of the electrode capacitance and its potential at the point of zero charge were used as measures of the treatment efficacy. The effect of the different regeneration treatments on the electrode morphological properties was also analyzed. Finally, the contribution of a regenerative step towards the long-term electrode cyclability was investigated. Experiments were conducted using a 3-electrode cell setup, at working electrode potentials ranging from -2.1 to -0.4 V vs RHE and holding times between 10 and 90 s. From these series of experiments, it was found that

- Electrochemical regeneration treatments recovered, to different extents, the electrode capacitance but were unable to regress the change in the potential of zero charge caused by the carbon oxidation process. Of the two variables that were hypothesized to affect the recovery, only the applied potential was found to be statistically significant (at an alpha value of 0.05). Capacitance recovery increased with a decreased in potential between -0.4 and -0.83 V vs RHE to then plateau between -0.83 and -2.1 V vs RHE.

The evolution of bubbles, as a result of the evolution of hydrogen may have disrupted the electrode porous structure, thus making available new active sites and a corresponding increase in surface area. Electrochemical impedance provided evidence of change in features associated with increase in surface area and reduction in micropore resistance. Moreover, in agreement with the negligible change in the electrode potential at the point of zero charge, the elemental analysis of regenerated electrodes showed no reduction in oxygen content.

- When implemented as part of the cycling protocol, capacitance was recovered almost at the same degree up to the 25th cycle. Beyond this point, capacitance was not recovered. It was noted that the regenerated capacitance was quickly lost in the subsequent set of cycles. Overall, the electrode cyclability was not positively influenced by the application of an electrochemical regeneration step.
- An important point to consider is the cycling regime used to degrade the electrodes. The investigation herein presented has demonstrated that applied potential and cycling time influence the rate and extent of electrode degradation. It is then relevant to hypothesized that, under a different cycling regime the use of electrochemical regeneration might show improved results in both electrochemical properties.

5.2 Recommendations for future work

The stability of activated carbon electrodes for CDI applications was investigated. Special attention was given to understanding the changes that gradually occur to key electrochemical properties such as capacitance and E_{PZC}. Additionally, the effects of elemental composition, porosity and wettability were monitored. The influences of dissolved oxygen, iron and organic matter were explored and contrasted with experiments performed under anaerobic and ideal

electrolyte composition. The system behaviour, observed throughout these tests, motivated the study of the effect of other parameters such as half cycle time (HCT) and electrolyte pH. Finally, for the purpose of comparison with the more rigorous 3-electrode cell setup, selected experimental conditions were investigated using a conventional two-electrode cell. With the results and insights obtained from this study, the following research inquiries can be recommended for future research:

1. In iron containing groundwaters, the occurrence of manganese is likely. As with iron, several insoluble components, such as MnO_2 or Mn_2O_3 could be formed depending on the applied potential and electrolyte pH conditions. Therefore, it would be interesting to conduct tests with electrolytes containing manganese or a mixture of iron and manganese.
2. The negligible impact of the organic carbon surrogate used in this study (SRNOM) is unusual. Therefore, experiments with other natural organic matter standard isolates would be important to reveal whether they have an effect on the decay of electrochemical properties.
3. The potential dependence of carbon corrosion can be further explored by performing degradation experiments with potentials below 1.2 V vs RHE where carbon corrosion is minimal, using a three-electrode cell. In parallel, two-electrode cell experiments can be performed to track the progressive increase in the anodic potential at different cell potentials. Results from these tests can provide useful kinetic information that can be used to tune the cycling conditions.
4. Since local pH values cannot be neglected, studying the effect of cycling time using flow cell (two and three-electrode) might provide relevant information to verify the results seen while using a three-electrode cell.

5. From a fundamental point of view, additional experiments with increasing pH values from 1.0 to 4.0 could provide a deeper understanding of the observed hindering effect of this parameter on electrode degradation.
6. There is a vast amount of off-the-shelve carbon materials that have been developed for electrical double layer capacitor applications (EDLCs). It would be valuable to perform a comparison of a few such materials that possess similar surface area, electrical conductivity and porosity using the same applied potential and half cycle time.
7. The survey of literature and the contrast observed between the two and three-electrode tests underscores the need for a state-of-the-art reference material and a standardized protocol, in the CDI field, to evaluate and compare newly developed materials.
8. The electrodes utilized in this work used PVDF as a binder, which is hydrophobic by nature. To the best of the author's knowledge, the effect of binder on electrode stability, if any, has not been investigated. In this sense, it is possible to use polyvinyl alcohol and a cross linking agent (e.g., citric, fumaric or glutaric acid) to generate a hydrophilic electrode. Other common binders include carboxymethylcellulose and polytetrafluoroethylene.
9. The use of complementary ex-situ analysis techniques such as mercury porosimetry and helium pycnometry to determine changes in electrode porosity; XPS, time-of-flight secondary ion mass spectrometry (ToF-SIMS) and thermogravimetric analysis (TGA) to elucidate changes in the surface functionalities at the electrode surface; Raman spectroscopy to determine the speciation of the iron deposits that scale the electrode surface; and transmission electron microscopy (TEM) will provide important details on the modifications occurring to the electrode surface functionalities, porous network and morphology as degradation progresses and it is attempted to be recovered through electrochemical regeneration methods.

The use of electrochemical regeneration approaches was explored. Mapping of the capacitance and E_{PZC} recovery response surfaces was done by means of a 3^2-factorial design of experiments. The former was examined in detail by performing additional tests along the potential domain. Lastly, the effect of a regenerative step on the electrode stability was investigated. Given the outcomes and recognizing the exploratory nature of this work, the following research questions could deserve further efforts:

1. From a mechanistic point of view, investigating the role of pH might provide valuable insights regarding the feasibility of this approach in aqueous electrolytes.
2. In this work, a single potentiostatic step approach was used. Nonetheless, one can apply potential as a series of pulses or different waveforms. In addition, a galvanostatic approach could also be implemented.
3. In a similar way, other types of EDLCs developed carbons might have a different response to the different potential-holding time treatments presented is this work.

Bibliography

[1] N. Voutchkov, *Desalination Engineering: Planning and Design*. McGraw-Hill, 2013.

[2] J. Kucera, "Introduction to Desalination," *Desalination: Water from Water*, John Wiley & Sons, Inc., Hoboken, NJ, USA, pp. 1–37, Jan. 31, 2014.

[3] National Ground Water Association, "NGWA Information Brief: Brackish Groundwater," 2010.http://www.ngwa.org/mediacenter/briefs/documents/brackish_water_info_brief_2010.pdf (accessed Oct. 06, 2016).

[4] "Total Dissolved Solids (TDS)," 1991. http://health.canada.ca/publications/healthy-living-vie-saine/water-dissolved-solids-matieres-dissoutes-eau/alt/water-dissolved-solids-matieres-dissoutes-eau-eng.pdf (accessed Aug. 24, 2019).

[5] M. A. Anderson, A. L. Cudero, and J. Palma, "Capacitive deionization as an electrochemical means of saving energy and delivering clean water. Comparison to present desalination practices: Will it compete?," *Electrochim. Acta*, vol. 55, no. 12, pp. 3845–3856, Apr. 2010, doi: 10.1016/j.electacta.2010.02.012.

[6] F. A. AlMarzooqi, A. A. Al Ghaferi, I. Saadat, and N. Hilal, "Application of Capacitive Deionisation in water desalination: A review," *Desalination*, vol. 342, pp. 3–15, Jun. 2014, doi: 10.1016/j.desal.2014.02.031.

[7] A. J. Bard and L. R. Faulkner, *Electrochemical Methods: Fundamentals and Applications*, Second. New York: Wiley, 2001.

[8] I. Cohen, E. Avraham, Y. Bouhadana, A. Soffer, and D. Aurbach, "Long term stability of capacitive de-ionization processes for water desalination: The challenge of positive electrodes corrosion," *Electrochim. Acta*, vol. 106, pp. 91–100, Sep. 2013, doi: 10.1016/j.electacta.2013.05.029.

[9] I. Cohen, E. Avraham, Y. Bouhadana, A. Soffer, and D. Aurbach, "The effect of the flow-regime, reversal of polarization, and oxygen on the long term stability in capacitive de-ionization processes," *Electrochim. Acta*, vol. 153, pp. 106–114, 2015, doi: 10.1016/j.electacta.2014.12.007.

[10] X. Gao, A. Omosebi, J. Landon, and K. Liu, "Dependence of the Capacitive Deionization Performance on Potential of Zero Charge Shifting of Carbon Xerogel Electrodes during Long-Term Operation," *J. Electrochem. Soc.*, vol. 161, no. 12, pp. E159–E166, Aug. 2014, doi: 10.1149/2.0561412jes.

[11] F. Duan, X. Du, Y. Li, H. Cao, and Y. Zhang, "Desalination stability of capacitive deionization using ordered mesoporous carbon: Effect of oxygen-containing surface groups and pore propertiesDesalination stability of capacitive deionization using ordered mesoporous carbon: Effect of oxygen-containing," *Desalination*, vol. 376, pp. 17–24, 2015, doi: 10.1016/j.desal.2015.08.009.

[12] E. Avraham, M. Noked, Y. Bouhadana, A. Soffer, and D. Aurbach, "Limitations of charge efficiency in capacitive deionization processes III: The behavior of surface oxidized activated carbon electrodes," *Electrochim. Acta*, vol. 56, no. 1, pp. 441–447, 2010, doi: 10.1016/j.electacta.2010.08.056.

[13] E. Avraham, M. Noked, I. Cohen, A. Soffer, and D. Aurbach, "The Dependence of the Desalination Performance in Capacitive Deionization Processes on the Electrodes PZC," *J. Electrochem. Soc.*, vol. 158, no. 12, pp. P168–P173, 2011, doi: 10.1149/2.078112jes.

[14] Y. Bouhadana, M. Ben-Tzion, A. Soffer, and D. Aurbach, "A control system for operating and investigating reactors: The demonstration of parasitic reactions in the water desalination by capacitive de-ionization," *Desalination*, vol. 268, no. 1, pp. 253–261, 2011, doi: 10.1016/j.desal.2010.10.037.

[15] M. Mossad and L. Zou, "Study of fouling and scaling in capacitive deionisation by using dissolved organic and inorganic salts," *J. Hazard. Mater.*, vol. 244–245, pp. 387–393, Jan. 2013, doi: 10.1016/j.jhazmat.2012.11.062.

[16] M. Mossad, W. Zhang, and L. Zou, "Using capacitive deionisation for inland brackish groundwater desalination in a remote location," *Desalination*, vol. 308, pp. 154–160, Jan. 2013, doi: 10.1016/j.desal.2012.05.021.

[17] M. Haro, G. Rasines, C. MacIas, and C. O. Ania, "Stability of a carbon gel electrode when used for the electro-assisted removal of ions from brackish water," *Carbon N. Y.*, vol. 49, no. 12, pp. 3723–3730, 2011, doi: 10.1016/j.carbon.2011.05.001.

[18] G. Newcombe and M. Drikas, "Adsorption of NOM onto activated carbon: Electrostatic and non-electrostatic effects," *Carbon N. Y.*, vol. 35, no. 9, pp. 1239–1250, 1997, doi: 10.1016/S0008-6223(97)00078-X.

[19] T. Wang, C. Zhang, L. Bai, B. Xie, Z. Gan, J. Xing, G. Li, and H. Liang, "Scaling behavior of iron in capacitive deionization (CDI) system," *Water Res.*, vol. 171, p. 115370, Mar. 2020, doi: 10.1016/j.watres.2019.115370.

[20] W. Zhang, M. Mossad, and L. Zou, "A study of the long-term operation of capacitive deionisation in inland brackish water desalination," *Desalination*, vol. 320, pp. 80–85, Jul. 2013, doi: 10.1016/j.desal.2013.04.010.

[21] C. Wang, H. Song, Q. Zhang, B. Wang, and A. Li, "Parameter optimization based on capacitive deionization for highly efficient desalination of domestic wastewater biotreated effluent and the fouled electrode regeneration," *Desalination*, vol. 365, pp. 407–415, Jun. 2015, doi: 10.1016/j.desal.2015.03.025.

[22] Y. Yang and Z. G. Lin, "In situ FTIR characterization of the electrooxidation of glassy carbon electrodes," *J. Appl. Electrochem.*, vol. 25, no. 3, pp. 259–266, Mar. 1995, doi: 10.1007/BF00262965.

[23] A. D. Jannakoudakis, P. D. Jannakoudakis, E. Theodoridou, and J. O. Besenhard, "Electrochemical oxidation of carbon fibres in aqueous solutions and analysis of the surface oxides," *J. Appl. Electrochem.*, vol. 20, no. 4, pp. 619–624, Jul. 1990, doi: 10.1007/BF01008872.

[24] H. Binder, A. Köhling, K. Richter, and G. Sandstede, "Über die anodische oxydation von aktivkohlen in wässrigen elektrolyten," *Electrochim. Acta*, vol. 9, no. 3, pp. 255–274, Mar. 1964, doi: 10.1016/0013-4686(64)80015-3.

[25] E. Theodoridou, J. O. Besenhard, and H. P. Fritz, "Chemically modified carbon fibre electrodes. Part I. Bulk-functionalized carbon fibres," *J. Electroanal. Chem.*, vol. 122, no. C, pp. 67–71, May 1981, doi: 10.1016/S0022-0728(81)80141-6.

[26] S. Porada, R. Zhao, A. Van Der Wal, V. Presser, and P. M. Biesheuvel, "Review on the science and technology of water desalination by capacitive deionization," *Prog. Mater. Sci.*, vol. 58, no. 8, pp. 1388–1442, 2013, doi: 10.1016/j.pmatsci.2013.03.005.

[27] M. Suss, S. Porada, X. Sun, M. Biesheuvel, J. Yoon, and V. Presser, "Water desalination via capacitive deionization: what is it and what can we expect from it?," *Energy Environ. Sci.*, vol. 8, no. Cdi, pp. 2296–2319, 2015, doi: 10.1039/C5EE00519A.

[28] K. Kinoshita, *Carbon: Electrochemical and Physicochemical Properties*, First. New York: Wiley, 1988.

[29] J. Willsau and J. Heitbaum, "The inluence of Pt-activation on the corrosion of carbon in gas diffusion electrodes - a DEMS study," *J. Electroanal. Chem.*, vol. 161, pp. 93–101, 1984, doi: 10.1108/17579861211281227.

[30] S. D. Knights, K. M. Colbow, J. St-Pierre, and D. P. Wilkinson, "Aging mechanisms and lifetime of PEFC and DMFC," in *Journal of Power Sources*, Mar. 2004, vol. 127, no. 1–2, pp. 127–134, doi: 10.1016/j.jpowsour.2003.09.033.

[31] K. H. Kangasniemi, D. A. Condit, and T. D. Jarvi, "Characterization of Vulcan Electrochemically Oxidized under Simulated PEM Fuel Cell Conditions," *J. Electrochem. Soc.*, vol. 151, no. 4, p. E125, Apr. 2004, doi: 10.1149/1.1649756.

[32] L. M. Roen, C. H. Paik, and T. D. Jarvi, "Electrocatalytic Corrosion of Carbon Support in PEMFC Cathodes," *Electrochem. Solid-State Lett.*, vol. 7, no. 1, p. A19, 2004, doi: 10.1149/1.1630412.

[33] M. Cai, M. S. Ruthkosky, B. Merzougui, S. Swathirajan, M. P. Balogh, and S. H. Oh, "Investigation of thermal and electrochemical degradation of fuel cell catalysts," *J. Power Sources*, vol. 160, no. 2 SPEC. ISS., pp. 977–986, Oct. 2006, doi: 10.1016/j.jpowsour.2006.03.033.

[34] Y. Shao, G. Yin, and Y. Gao, "Understanding and approaches for the durability issues of Pt-based catalysts for PEM fuel cell," *Journal of Power Sources*, vol. 171, no. 2. Elsevier, pp. 558–566, Sep. 27, 2007, doi: 10.1016/j.jpowsour.2007.07.004.

[35] S. Maass, F. Finsterwalder, G. Frank, R. Hartmann, and C. Merten, "Carbon support oxidation in PEM fuel cell cathodes," *J. Power Sources*, vol. 176, no. 2, pp. 444–451, Feb. 2008, doi: 10.1016/j.jpowsour.2007.08.053.

[36] B. Avasarala, R. Moore, and P. Haldar, "Surface oxidation of carbon supports due to potential cycling under PEM fuel cell conditions," *Electrochim. Acta*, vol. 55, no. 16, pp. 4765–4771, Jun. 2010, doi: 10.1016/j.electacta.2010.03.056.

[37] Y. Yu, Z. Tu, H. Zhang, Z. Zhan, and M. Pan, "Comparison of degradation behaviors for open-ended and closed proton exchange membrane fuel cells during startup and shutdown cycles," *J. Power Sources*, vol. 196, no. 11, pp. 5077–5083, Jun. 2011, doi: 10.1016/j.jpowsour.2011.01.075.

[38] N. Macauley, D. D. Papadias, J. Fairweather, D. Spernjak, D. Langlois, R. Ahluwalia, K. L. More, R. Mukundan, and R. L. Borup, "Carbon Corrosion in PEM Fuel Cells and the Development of Accelerated Stress Tests," *J. Electrochem. Soc.*, vol. 165, no. 6, pp. F3148–F3160, Mar. 2018, doi: 10.1149/2.0061806jes.

[39] M. He, K. Fic, E. Frackowiak, P. Novák, and E. J. Berg, "Ageing phenomena in high-voltage aqueous supercapacitors investigated by in situ gas analysis," *Energy Environ. Sci.*, vol. 9, no. 2, pp. 623–633, 2016, doi: 10.1039/c5ee02875b.

[40] W. Tang, D. He, C. Zhang, P. Kovalsky, and T. D. Waite, "Comparison of Faradaic reactions in capacitive deionization (CDI) and membrane capacitive deionization (MCDI) water treatment processes," *Water Res.*, vol. 120, pp. 229–237, 2017, doi: 10.1016/j.watres.2017.05.009.

[41] D. He, C. E. Wong, W. Tang, P. Kovalsky, and T. David Waite, "Faradaic Reactions in Water Desalination by Batch-Mode Capacitive Deionization," *Environ. Sci. Technol. Lett.*, vol. 3, no. 5, pp. 222–226, May 2016, doi: 10.1021/acs.estlett.6b00124.

[42] C. Zhang, D. He, J. Ma, W. Tang, and T. D. Waite, "Faradaic reactions in capacitive deionization (CDI) - problems and possibilities: A review," *Water Research*, vol. 128. Pergamon, pp. 314–330, Jan. 01, 2018, doi: 10.1016/j.watres.2017.10.024.

[43] X. Gao, A. Omosebi, N. Holubowitch, A. Liu, K. Ruh, J. Landon, and K. Liu, "Polymer-coated composite anodes for efficient and stable capacitive deionization," *Desalination*, vol. 399, pp. 16–20, 2016, doi: 10.1016/j.desal.2016.08.006.

[44] X. Gao, A. Omosebi, J. Landon, and K. Liu, "Surface charge enhanced carbon electrodes for stable and efficient capacitive deionization using inverted adsorption–desorption behavior," *Energy Environ. Sci.*, vol. 8, no. Cx, p. 897, 2015, doi: 10.1039/c4ee03172e.

[45] D. Lu, W. Cai, and Y. Wang, "Optimization of the voltage window for long-term capacitive deionization stability," *Desalination*, vol. 424, pp. 53–61, Dec. 2017, doi: 10.1016/j.desal.2017.09.026.

[46] J.-H. Lee, W.-S. Bae, and J.-H. Choi, "Electrode reactions and adsorption/desorption performance related to the applied potential in a capacitive deionization process," *Desalination*, vol. 258, no. 1–3, pp. 159–163, Aug. 2010, doi: 10.1016/j.desal.2010.03.020.

[47] Y. Liu, C. Nie, X. Liu, X. Xu, Z. Sun, L. Pan, S. J. Kim, S. H. Ko, K. H. Kang, J. Han, M. Elimelech, W. A. Phillip, T. Humplik, J. Lee, S. O'Hern, B. Fellman, M. Baig, S. Hassan, M. Atieh, *et al.*, "Review on carbon-based composite materials for capacitive deionization," *RSC Adv.*, vol. 5, no. 20, pp. 15205–15225, 2015, doi: 10.1039/C4RA14447C.

[48] J. J. Lado, R. E. Pérez-Roa, J. J. Wouters, M. I. Tejedor-Tejedor, C. Federspill, and M. A. Anderson, "Continuous cycling of an asymmetric capacitive deionization system: An evaluation of the electrode performance and stability," *J. Environ. Chem. Eng.*, vol. 3, no. 4, pp. 2358–2367, Dec. 2015, doi: 10.1016/j.jece.2015.08.025.

[49] Y. Bouhadana, E. Avraham, M. Noked, M. Ben-Tzion, A. Soffer, and D. Aurbach, "Capacitive deionization of NaCl solutions at non-steady-state conditions: Inversion functionality of the carbon electrodes," *J. Phys. Chem. C*, vol. 115, no. 33, pp. 16567–16573, Aug. 2011, doi: 10.1021/jp2047486.

[50] Y. Bouhadana, E. Avraham, A. Soffer, and D. Aurbach, "Several basic and practical aspects related to electrochemical deionization of water," *AIChE J.*, vol. 56, no. 3, pp. 779–789, 2009, doi: 10.1002/aic.12005.

[51] P. Srimuk, M. Zeiger, N. Jäckel, A. Tolosa, B. Krüner, S. Fleischmann, I. Grobelsek, M. Aslan, B. Shvartsev, M. E. Suss, and V. Presser, "Enhanced performance stability of carbon/titania hybrid electrodes during capacitive deionization of oxygen saturated saline water," *Electrochim. Acta*, vol. 224, pp. 314–328, Jan. 2017, doi: 10.1016/j.electacta.2016.12.060.

[52] E. Avraham, M. Noked, A. Soffer, and D. Aurbach, "The feasibility of boron removal from water by capacitive deionization," *Electrochim. Acta*, vol. 56, no. 18, pp. 6312–6317, 2011, doi: 10.1016/j.electacta.2011.05.037.

[53] H. Tobias and A. Soffer, "The immersion potential of high surface electrodes," *J. Electroanal. Chem. Interfacial Electrochem.*, vol. 148, no. 2, pp. 221–232, 1983, doi: 10.1016/S0022-0728(83)80398-2.

[54] B. Pillay and J. Newman, "The Influence of Side Reactions on the Performance of Electrochemical Double-Layer Capacitors," *J. Electrochem. Soc.*, vol. 143, no. 6, pp. 1806–1814, 1996, doi: 10.1149/1.1836908.

[55] C. J. Gabelich, T. D. Tran, and I. H. "Mel" Suffet, "Electrosorption of Inorganic Salts from Aqueous Solution Using Carbon Aerogels," *Environ. Sci. Technol.*, vol. 36, no. 13, pp. 3010–3019, Jul. 2002, doi: 10.1021/es0112745.

[56] M. Pourbaix, *Atlas of electrochemical equilibria in aqueous solutions*, 2nd ed., vol. 13, no. 4. Houston. TX: National Association of Corrosion Engineers, 1967.

[57] H. A. Moreno-Casillas, D. L. Cocke, J. A. G. Gomes, P. Morkovsky, J. R. Parga, and E. Peterson, "Electrocoagulation mechanism for COD removal," *Sep. Purif. Technol.*, vol. 56, no. 2, pp. 204–211, Aug. 2007, doi: 10.1016/J.SEPPUR.2007.01.031.

[58] R. M. Cornell and U. Schwertmann, *The Iron Oxides: Structure, Properties, Reactions, Occurences and Uses*, 2nd ed. Wiley, 2003.

[59] J. D. Hem and W. H. Cropper, "Survey of ferrous-ferric chemical equilibria and redox potentials," in *Chemistry of Iron in Natural Water*, U.S. G.P.O., 1959.

[60] Z. Ogumi, Z. Takehara, and S. Yoshizawa, "Gas Permeation in SPE Method I . Oxygen Permeation Through Nafion and NEOSEPTA," *J. Electrochem. Soc.*, vol. 131, no. 4, pp. 769–773, Apr. 1984, doi: 10.1149/1.2115696.

[61] A. Omosebi, X. Gao, J. Landon, and K. Liu, "Asymmetric Electrode Configuration for Enhanced Membrane Capacitive Deionization," *ACS Appl. Mater. Interfaces*, vol. 6, no. 15, pp. 12640–12649, Aug. 2014, doi: 10.1021/am5026209.

[62] A. G. El-Deen, N. A. M. Barakat, and H. Y. Kim, "Graphene wrapped MnO2-nanostructures as effective and stable electrode materials for capacitive deionization desalination technology," *Desalination*, vol. 344, pp. 289–298, Jul. 2014, doi: 10.1016/j.desal.2014.03.028.

[63] A. G. El-Deen, N. A. M. Barakat, K. A. Khalil, M. Motlak, and H. Yong Kim, "Graphene/SnO2nanocomposite as an effective electrode material for saline water desalination using capacitive deionization," *Ceram. Int.*, vol. 40, no. 9 PART B, pp. 14627–14634, Nov. 2014, doi: 10.1016/j.ceramint.2014.06.049.

[64] A. G. El-Deen, J. H. Choi, C. S. Kim, K. A. Khalil, A. A. Almajid, and N. A. M. Barakat, "TiO2 nanorod-intercalated reduced graphene oxide as high performance electrode material for membrane capacitive deionization," *Desalination*, vol. 361, pp. 53–64, Apr. 2015, doi: 10.1016/j.desal.2015.01.033.

[65] J. O. Besenhard and T. E., "Electrochemical applications of grafite intercalation compunds," *Synt. Mater.*, vol. 4, pp. 211–223, 1982, Accessed: Mar. 19, 2019. [Online].

[66] P.-I. Liu, L.-C. Chung, C.-H. Ho, H. Shao, T.-M. Liang, M.-C. Chang, C.-C. M. Ma, and R.-Y. Horng, "Comparative insight into the capacitive deionization behavior of the activated carbon electrodes by two electrochemical techniques," *Desalination*, vol. 379, pp. 34–41, 2016, doi: 10.1016/j.desal.2015.10.008.

[67] X. Gao, J. Landon, J. K. Neathery, and K. Liu, "Modification of Carbon Xerogel Electrodes for More Efficient Asymmetric Capacitive Deionization," *J. Electrochem. Soc.*, vol. 160, no. 9, pp. E106–E112, Jul. 2013, doi: 10.1149/2.111309jes.

[68] X. Gao, A. Omosebi, J. Landon, and K. Liu, "Enhancement of charge efficiency for a capacitive deionization cell using carbon xerogel with modified potential of zero charge," *Electrochem. commun.*, vol. 39, pp. 22–25, 2014, doi: 10.1016/j.elecom.2013.12.004.

[69] X. Gao, A. Omosebi, J. Landon, and K. Liu, "Enhanced Salt Removal in an Inverted Capacitive Deionization Cell Using Amine Modified Microporous Carbon Cathodes," 2015.

[70] X. Gao, A. Omosebi, N. Holubowitch, J. Landon, and K. Liu, "Capacitive Deionization Using Alternating Polarization: Effect of Surface Charge on Salt Removal," *Electrochim. Acta*, vol. 233, pp. 249–255, Apr. 2017, doi: 10.1016/j.electacta.2017.03.021.

[71] J. McMurray, *Organic Chemistry*, 6th ed. Belmont, CA: Thomson-Brooks/Cole, 2004.

[72] J. Coates, "Interpretation of Infrared Spectra, A Practical Approach," in *Encyclopedia of Analytical Chemistry*, Chichester, UK: John Wiley & Sons, Ltd, 2006.

[73] Z. Lukács, "The numerical evaluation of the distortion of EIS data due to the distribution of parameters," *J. Electroanal. Chem.*, vol. 432, no. 1–2, pp. 79–83, Jul. 1997, doi: 10.1016/S0022-0728(97)00217-9.

[74] M. E. Orazem and B. Tribollet, *Electrochemical impedance spectroscopy*. Wiley, 2008.

[75] E. Barsoukov and J. R. Macdonald, Eds., *Impedance spectroscopy : theory, experiment, and applications.*, 3rd ed. Hoboken, NJ: Wiley.

[76] K. Kinoshita and J. Bett, "Electrochemical oxidation of carbon black in concentrated phosphoric acid at 135°C," *Carbon N. Y.*, vol. 11, no. 3, pp. 237–247, Jun. 1973, doi: 10.1016/0008-6223(73)90026-2.

[77] P. D. More, P. R. Jadhav, A. A. Ghanwat, I. A. Dhole, Y. H. Navale, and V. B. Patil, "Spray synthesized hydrophobic α-Fe2O3 thin film electrodes for supercapacitor application," *J. Mater. Sci. Mater. Electron.*, vol. 28, no. 23, pp. 17839–17848, Dec. 2017, doi: 10.1007/s10854-017-7725-5.

[78] T. Li, H. Yu, L. Zhi, W. Zhang, L. Dang, Z. Liu, and Z. Lei, "Facile Electrochemical Fabrication of Porous Fe2O3 Nanosheets for Flexible Asymmetric Supercapacitors," *J. Phys. Chem. C*, vol. 121, no. 35, pp. 18982–18991, Sep. 2017, doi: 10.1021/acs.jpcc.7b04330.

[79] Y. Xiang, Z. Yang, S. Wang, M. S. A. Hossain, J. Yu, N. A. Kumar, and Y. Yamauchi, "Pseudocapacitive behavior of the Fe2O3 anode and its contribution to high reversible capacity in lithium ion batteries," *Nanoscale*, vol. 10, no. 37, pp. 18010–18018, Sep. 2018, doi: 10.1039/c8nr04871a.

[80] E. Frackowiak, P. Ratajczak, and F. Béguin, "Electrochemical Capacitors Based on Carbon Electrodes in Aqueous Electrolytes," in *Advances in Electrochemical Science and Engineering*, vol. 16, John Wiley & Sons, Ltd, 2016, pp. 285–312.

[81] M. M. Bazri and M. Mohseni, "Impact of natural organic matter properties on the kinetics of suspended ion exchange process," *Water Res.*, vol. 91, pp. 147–155, Mar. 2016, doi: 10.1016/j.watres.2015.12.036.

[82] F. Dixit, B. Barbeau, and M. Mohseni, "Characteristics of competitive uptake between Microcystin-LR and natural organic matter (NOM) fractions using strongly basic anion exchange resins," *Water Res.*, vol. 139, pp. 74–82, Aug. 2018, doi: 10.1016/j.watres.2018.03.074.

[83] H. Särkkä, M. Vepsäläinen, and M. Sillanpää, "Natural organic matter (NOM) removal by electrochemical methods - A review," *Journal of Electroanalytical Chemistry*, vol. 755. Elsevier, pp. 100–108, Oct. 15, 2015, doi: 10.1016/j.jelechem.2015.07.029.

[84] B. Wallén and G. Wranglén, "Influence of pH and sulphate content of the solution on the corrosion of graphite anodes in alkali chloride electrolysis," *Electrochim. Acta*, vol. 10, no. 1, pp. 43–48, Jan. 1965, doi: 10.1016/0013-4686(65)87005-0.

[85] M. M. Jakšić, "The effect of pH on graphite wear in a chlorate cell process," *J. Appl. Electrochem.*, vol. 3, no. 3, pp. 219–225, Aug. 1973, doi: 10.1007/BF00619164.

[86] M. A. Rabah, A. A. Abdul Azim, and A. Ismail, "Wear of graphite anodes during electrolysis of add sulphate solutions," *J. Appl. Electrochem.*, vol. 11, no. 1, pp. 41–47, Jan. 1981, doi: 10.1007/BF00615320.

[87] M. A. Rabah, N. Nassif, and A. A. A. Azim, "Electrochemical wear of graphite anodes during electrolysis of brine," *Carbon N. Y.*, vol. 29, no. 2, pp. 165–171, Jan. 1991, doi: 10.1016/0008-6223(91)90066-R.

[88] M. Rueffer, D. Bejan, and N. J. Bunce, "Graphite: An active or an inactive anode?," *Electrochim. Acta*, vol. 56, no. 5, pp. 2246–2253, Feb. 2011, doi: 10.1016/j.electacta.2010.11.071.

[89] Y. Yi, G. Weinberg, M. Prenzel, M. Greiner, S. Heumann, S. Becker, and R. Schlögl, "Electrochemical corrosion of a glassy carbon electrode," *Catal. Today*, vol. 295, pp. 32–40, Oct. 2017, doi: 10.1016/j.cattod.2017.07.013.

[90] R. L. Tseng, "Mesopore control of high surface area NaOH-activated carbon," *J. Colloid Interface Sci.*, vol. 303, no. 2, pp. 494–502, Nov. 2006, doi: 10.1016/j.jcis.2006.08.024.

[91] A. L. Cazetta, A. M. M. Vargas, E. M. Nogami, M. H. Kunita, M. R. Guilherme, A. C. Martins, T. L. Silva, J. C. G. Moraes, and V. C. Almeida, "NaOH-activated carbon of high surface area produced from coconut shell: Kinetics and equilibrium studies from the methylene blue adsorption," *Chem. Eng. J.*, vol. 174, no. 1, pp. 117–125, Oct. 2011, doi: 10.1016/j.cej.2011.08.058.

[92] L. Ding, B. Zou, Y. Li, H. Liu, Z. Wang, C. Zhao, Y. Su, and Y. Guo, "The production of hydrochar-based hierarchical porous carbons for use as electrochemical supercapacitor electrode materials," *Colloids Surfaces A Physicochem. Eng. Asp.*, vol. 423, pp. 104–111, Apr. 2013, doi: 10.1016/j.colsurfa.2013.02.003.

[93] M. A. Islam, I. A. W. Tan, A. Benhouria, M. Asif, and B. H. Hameed, "Mesoporous and adsorptive properties of palm date seed activated carbon prepared via sequential hydrothermal carbonization and sodium hydroxide activation," *Chem. Eng. J.*, vol. 270, pp. 187–195, Jun. 2015, doi: 10.1016/j.cej.2015.01.058.

[94] M. A. Islam, M. J. Ahmed, W. A. Khanday, M. Asif, and B. H. Hameed, "Mesoporous activated carbon prepared from NaOH activation of rattan (Lacosperma secundiflorum) hydrochar for methylene blue removal," *Ecotoxicol. Environ. Saf.*, vol. 138, pp. 279–285, Apr. 2017, doi: 10.1016/j.ecoenv.2017.01.010.

[95] I. Shitanda, S. Tsujimura, H. Yanai, Y. Hoshi, and M. Itagaki, "Electrochemical Impedance Simulation of Branch Structure Porous Carbon Electrode Using Transmission Line Model," *Electrochemistry*, vol. 83, no. 5, pp. 335–338, 2015, doi: https://doi.org/10.5796/electrochemistry.83.335.

[96] T. Sharma, "Impedance characterization of porous carbon electrodes with controlled pore size distribution : experimental verification," University of British Columbia, 2019.

[97] M. E. Suss, T. F. Baumann, M. A. Worsley, K. A. Rose, T. F. Jaramillo, M. Stadermann, and J. G. Santiago, "Impedance-based study of capacitive porous carbon electrodes with hierarchical and bimodal porosity," *J. Power Sources*, vol. 241, pp. 266–273, Nov. 2013, doi: 10.1016/j.jpowsour.2013.03.178.

Appendices

Appendix A

A.1 Degradation in Presence of Scaling and Fouling Solutes

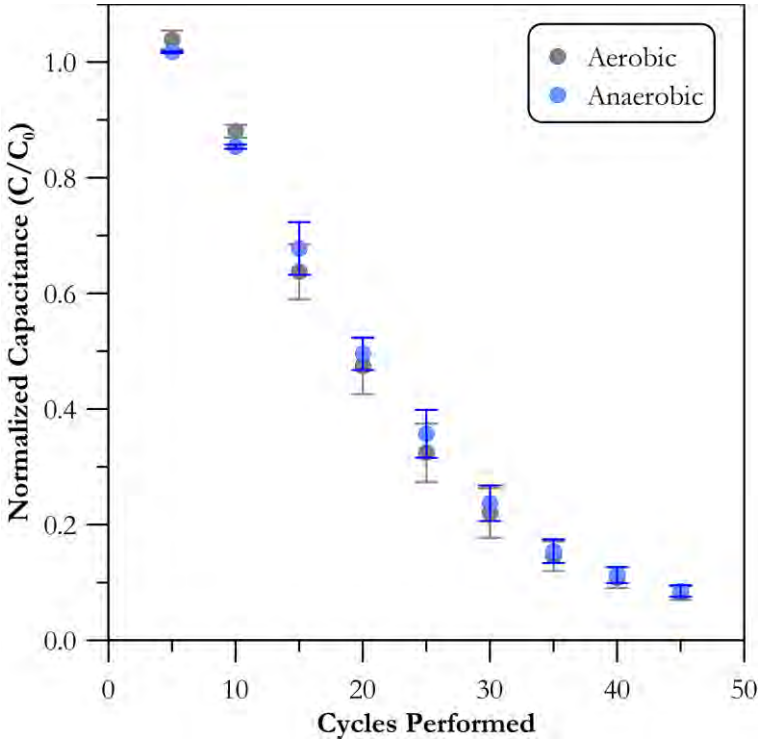

Figure A.1 Normalized capacitance as a function of the number of cycles performed under N_2 or O_2 saturation at a working electrode potential of 1.2 V vs RHE, a half cycle time of 5 min and 20 mg Fe^{2+} L^{-1}. Gray markers provided as a reference for aerobic results. Error bars represent the range between two replicates

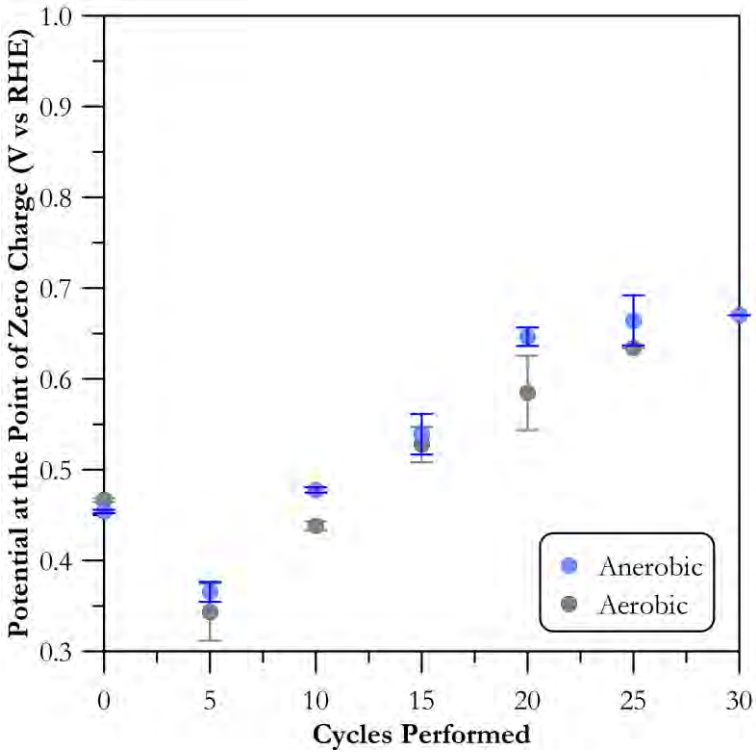

Figure A.2 E_{PZC} profiles as a function of the number of cycles performed under N_2 or O_2 saturation at a working electrode potential of 1.2 V vs RHE, a half cycle time of 5 min and 20 mg Fe^{2+} L^{-1}. Gray markers provided as a reference for aerobic results. Error bars represent the range between two replicates

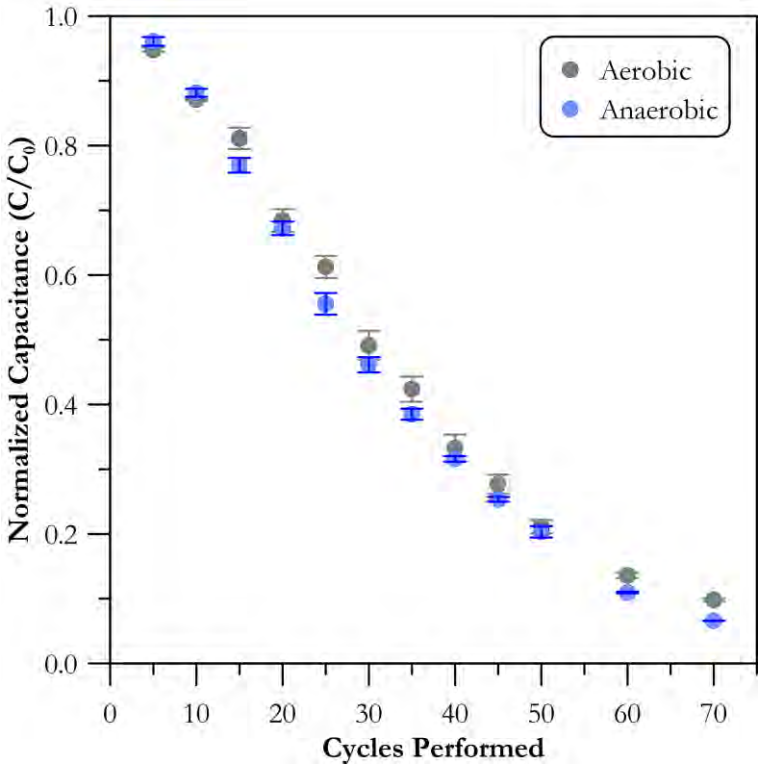

Figure A.3 Normalized capacitance as a function of the number of cycles performed under N_2 or O_2 saturation at a working electrode potential of 1.2 V vs RHE, a half cycle time of 5 min and 20 mg SRNOM L^{-1}. Error bars represent the range between two replicates

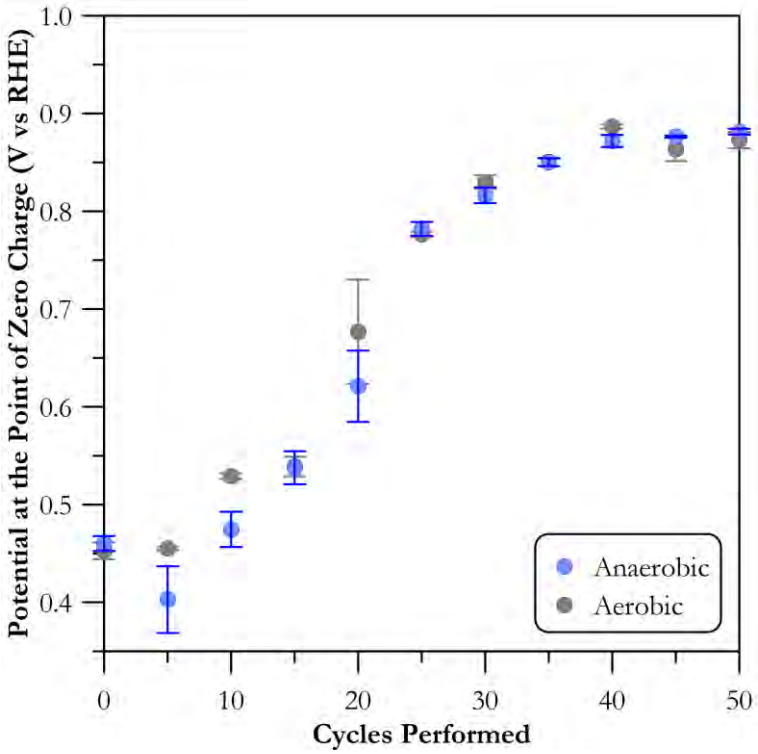

Figure A.4 E_{PZC} profiles as a function of the number of cycles performed under N_2 or O_2 saturation at a working electrode potential of 1.2 V vs RHE, a half cycle time of 5 min and 20 mg SRNOM L^{-1}. Error bars represent the range between two replicates

A.2 Effect of Cycling Time and Solution pH

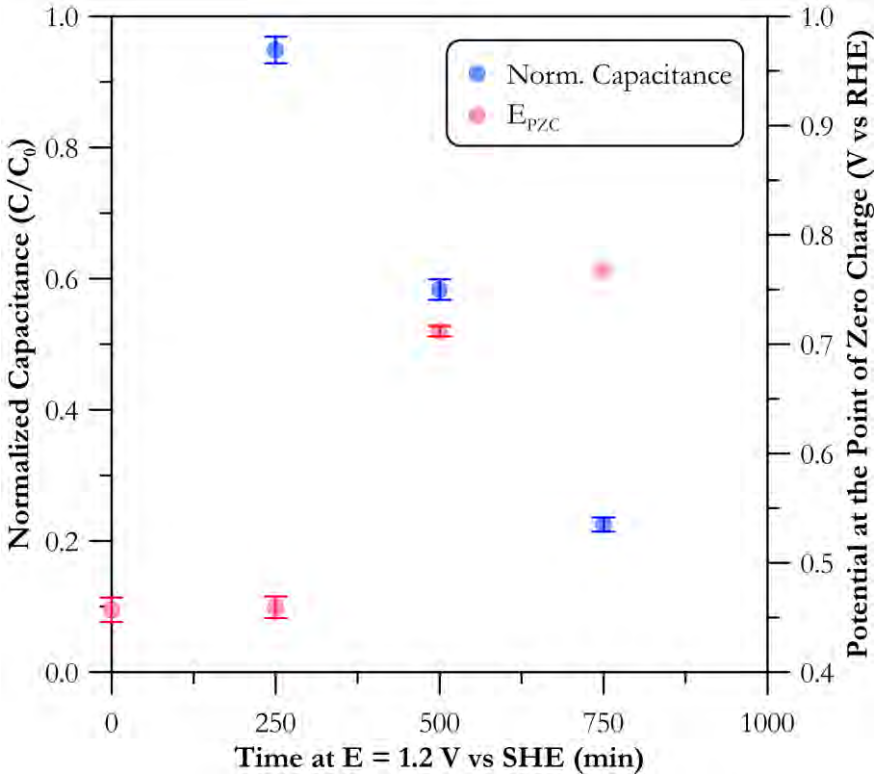

Figure A.5 Normalized capacitance and E_{PZC} as functions of time at a working electrode potential of 1.2 V vs RHE for a half cycle time of 250 min. Cycles performed under O_2 saturation and an electrolyte strength of 1 M (NaCl). Error bars represent the range between two replicates

A.3 Electrode Stability using a Two-Electrode Flow Cell

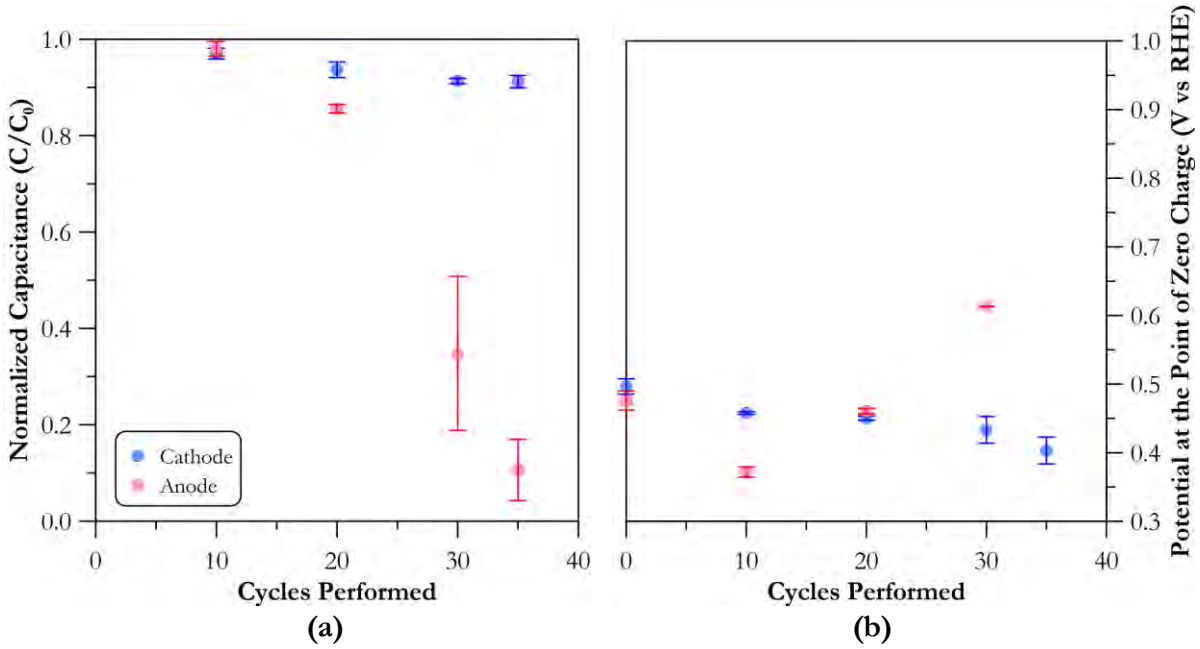

Figure A.6 (a) Normalized capacitance and (b) E_{PZC} profiles as functions of the number of cycles performed under O_2 saturation and 0.2 mg Fe^{2+} L^{-1} at a cell potential of 1.3 V and a half cycle time of 5 min. Error bars represent the range between two replicates

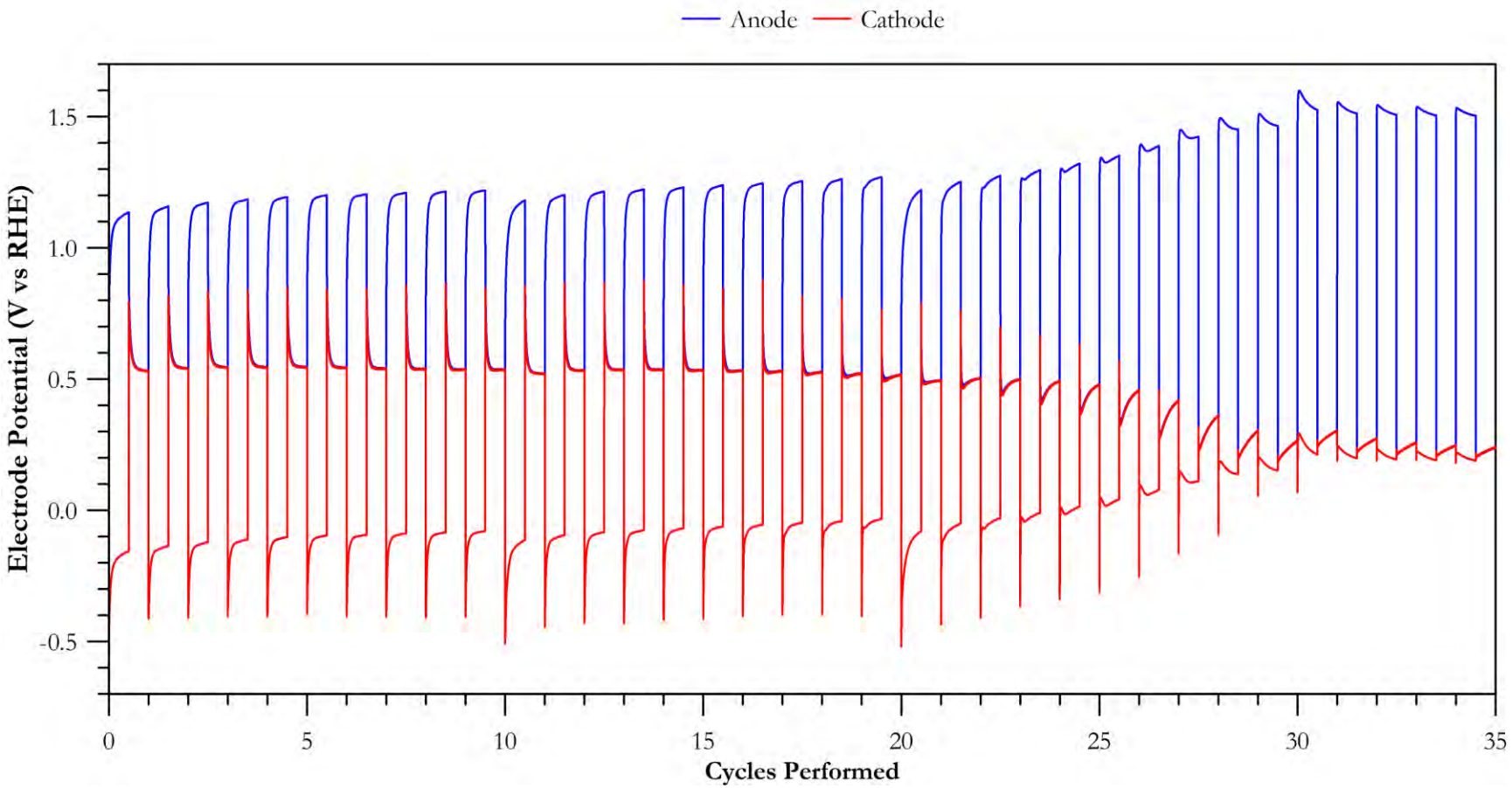

Figure A.7 Electrode potential distribution throughout cycling (1st-35th cycle) with a cell potential of 1.3 V and a half cycle time of 5 min performed under O_2 saturation and 0.2 mg Fe^{2+} L^{-1} using an electrolyte concentration of 17.1 mM (1000 mg NaCl L^{-1}) at room temperature. The electrodes were discharged at zero voltage (i.e., $V_{cell} = 0$)

A.4 Raw and Normalized FTIR Spectra

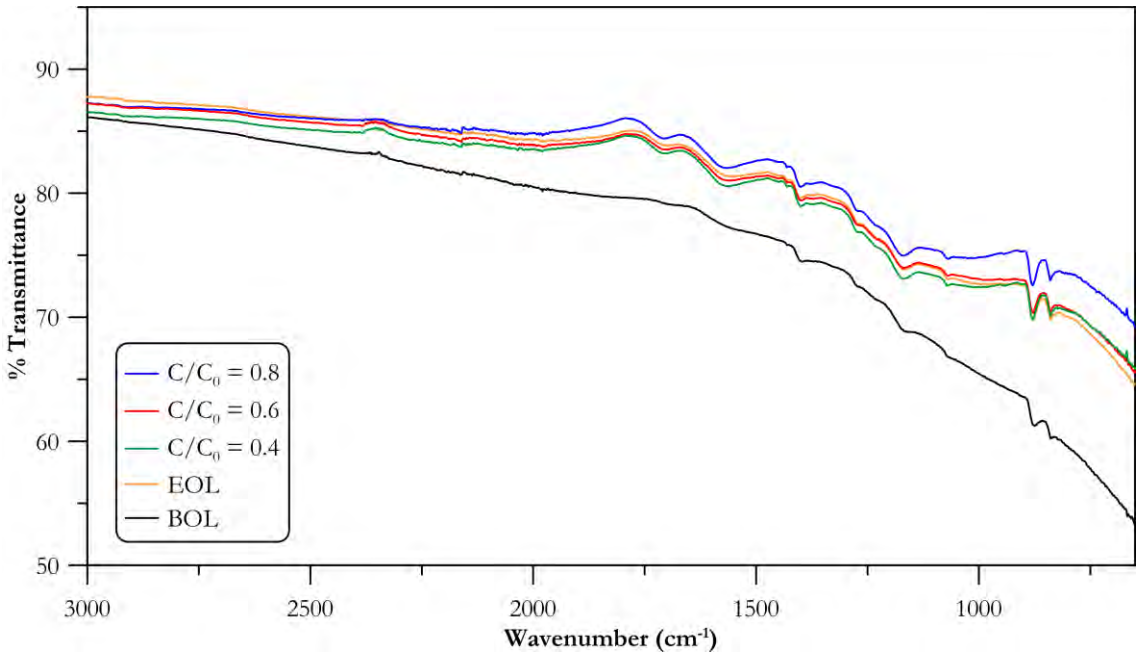

Figure A.8 FTIR spectra of electrodes at different degradation stages after cycling under anaerobic conditions at a working electrode potential of 1.2 V vs RHE and a half cycle time of 5 min

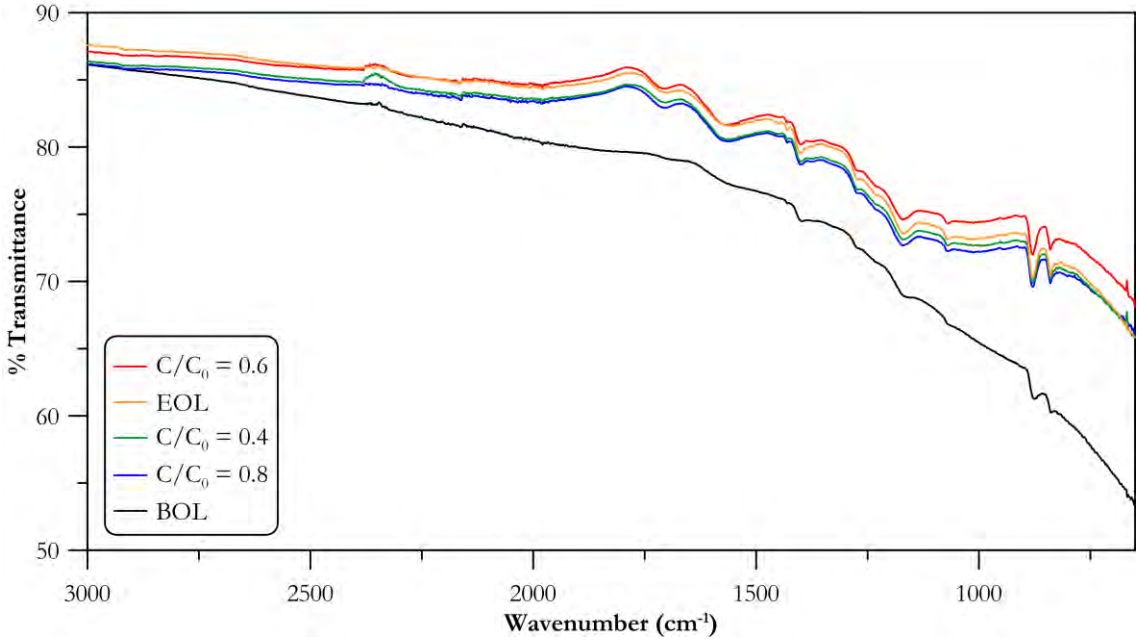

Figure A.9 FTIR spectra of electrodes at different degradation stages after cycling under aerobic conditions at a working electrode potential of 1.2 V vs RHE and a half cycle time of 5 min

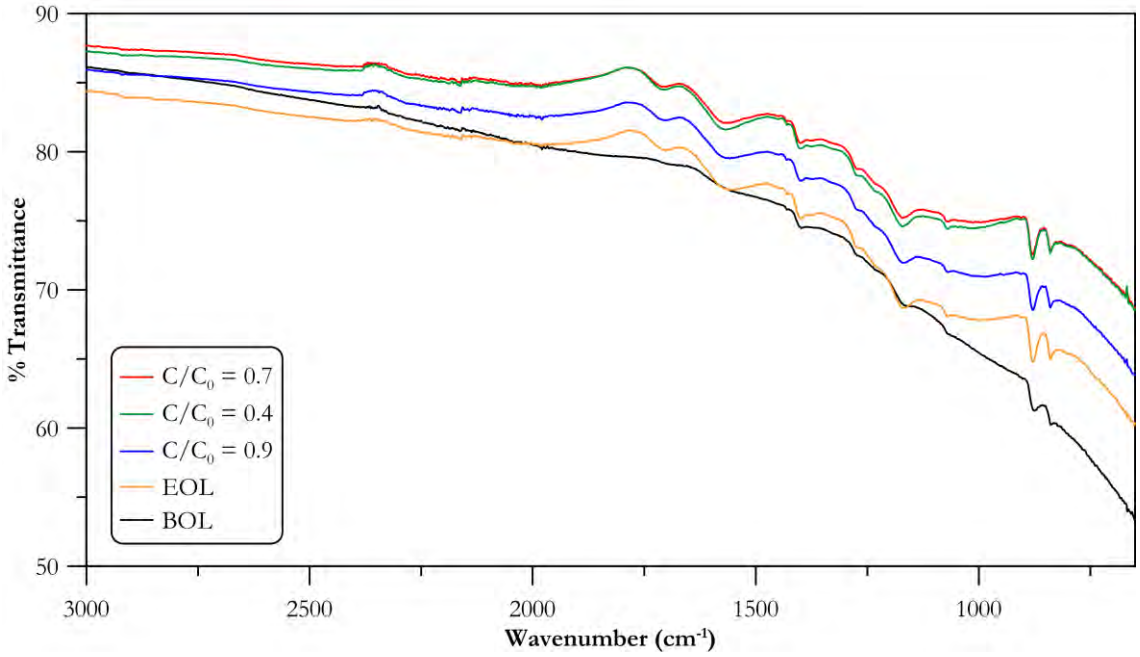

Figure A.10 FTIR spectra of electrodes at different degradation stages after cycling under aerobic conditions and 0.2 mg Fe^{2+} L^{-1} at a working electrode potential of 1.2 V vs RHE and a half cycle time of 5 min

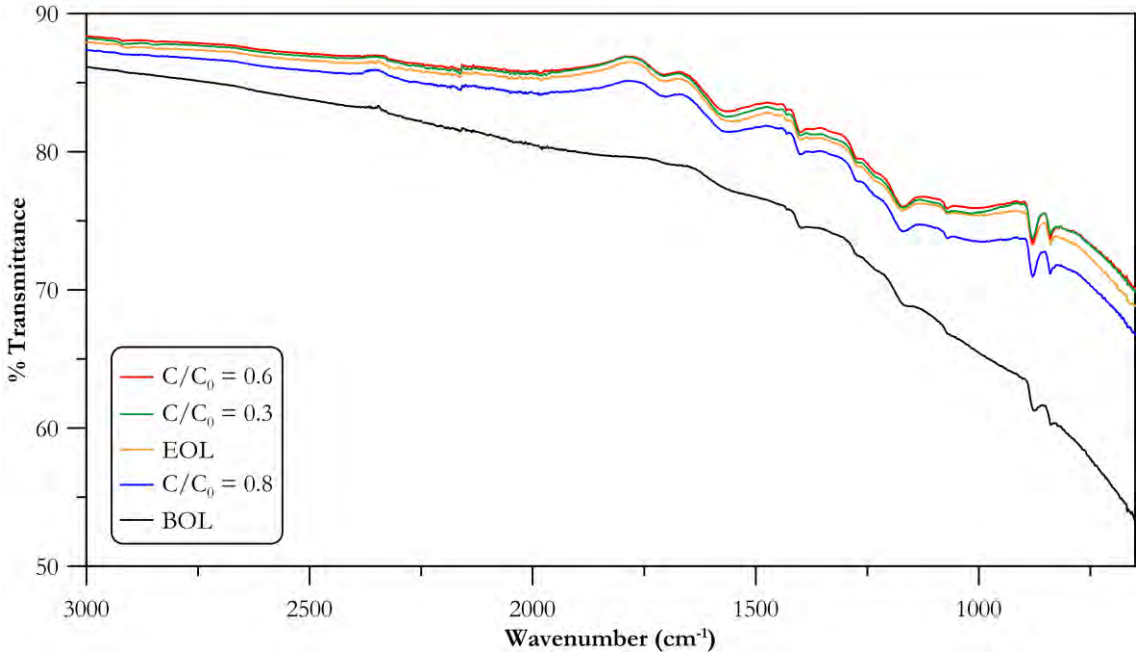

Figure A.11 FTIR spectra of electrodes at different degradation stages after cycling under aerobic conditions and 2.0 mg Fe^{2+} L^{-1} at a working electrode potential of 1.2 V vs RHE and a half cycle time of 5 min

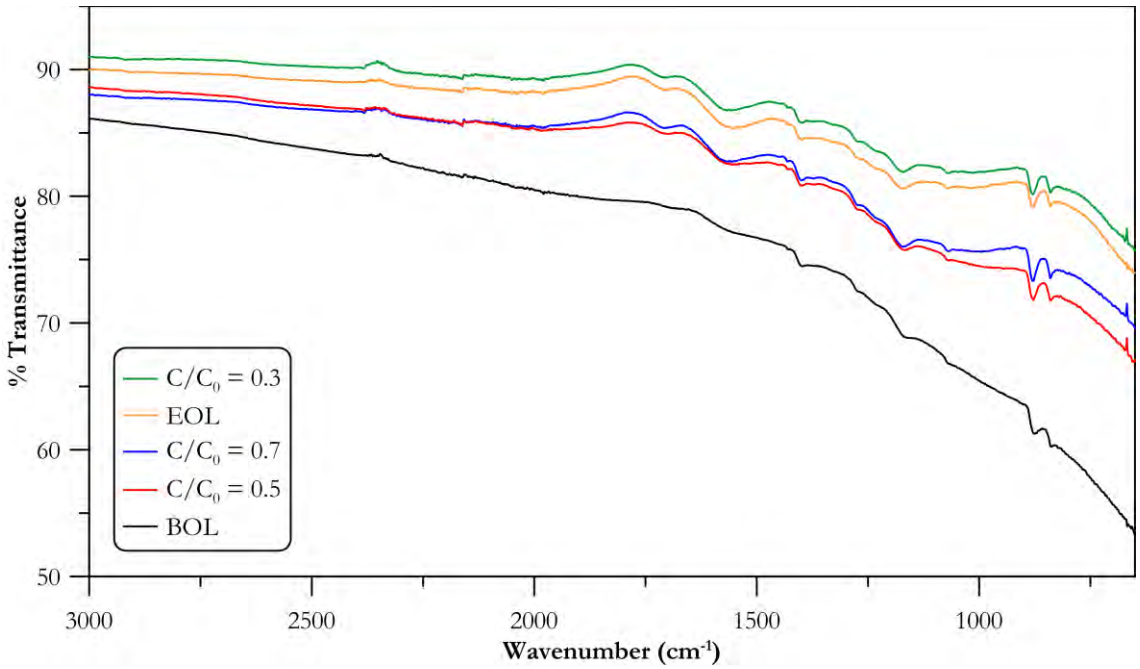

Figure A.12 FTIR spectra of electrodes at different degradation stages after cycling under aerobic conditions and 20 mg Fe^{2+} L^{-1} at a working electrode potential of 1.2 V vs RHE and a half cycle time of 5 min

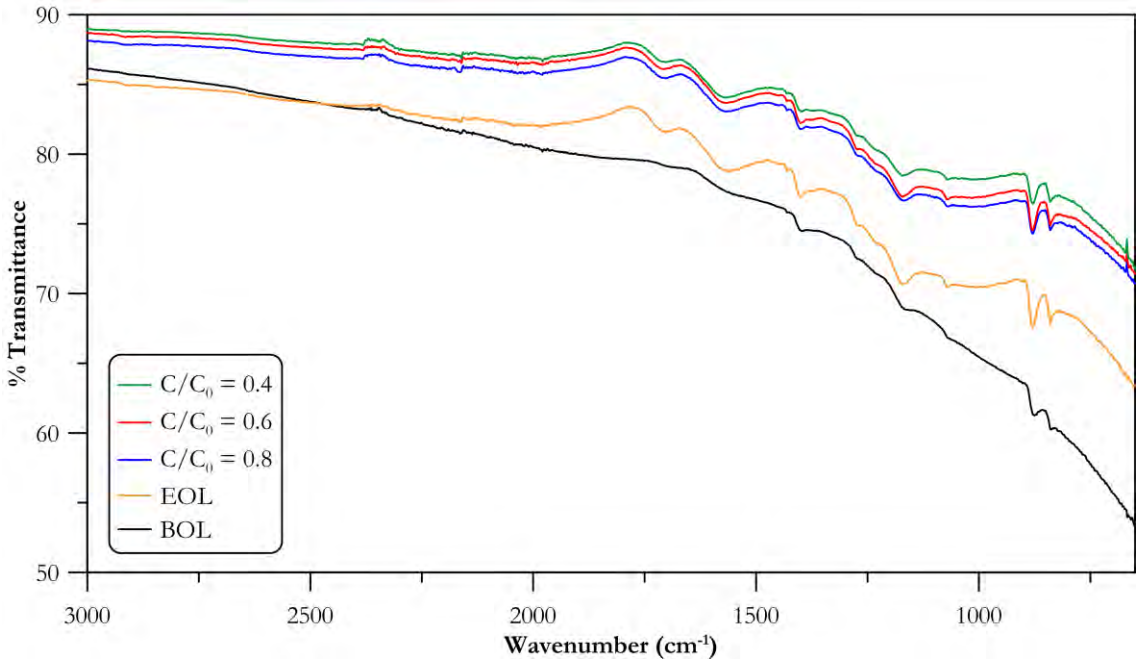

Figure A.13 FTIR spectra of electrodes at different degradation stages after cycling under aerobic conditions and 20 mg SRNOM L^{-1} at a working electrode potential of 1.2 V vs RHE and a half cycle time of 5 min

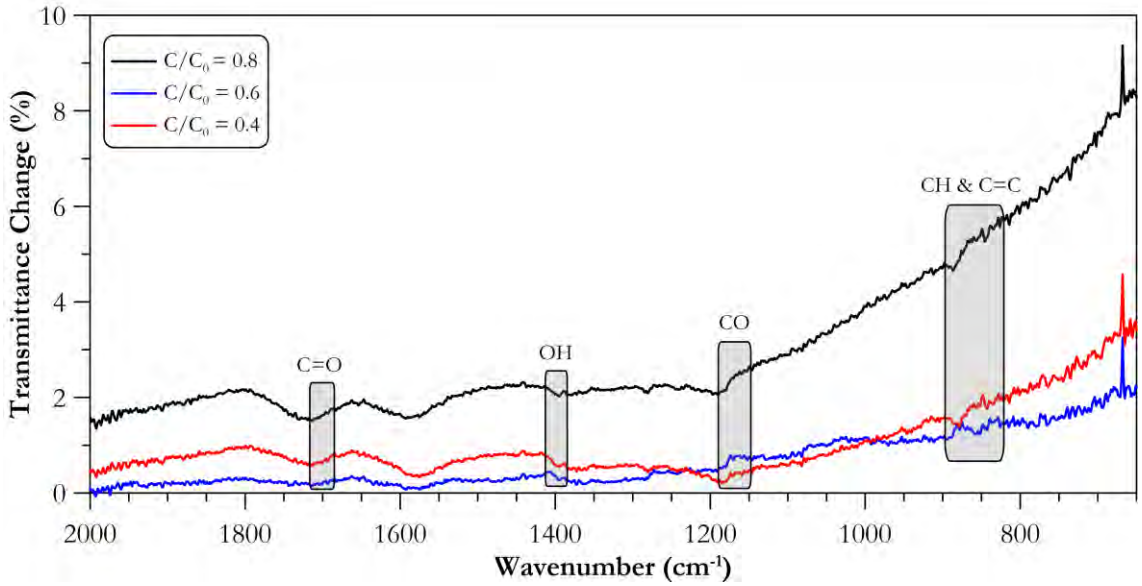

Figure A.14 Normalized FTIR spectra of electrodes at different degradation stages after cycling under anaerobic conditions at a working electrode potential of 1.2 V vs RHE and a half cycle time of 5 min. Electrode at end-of-life used as the reference for normalization

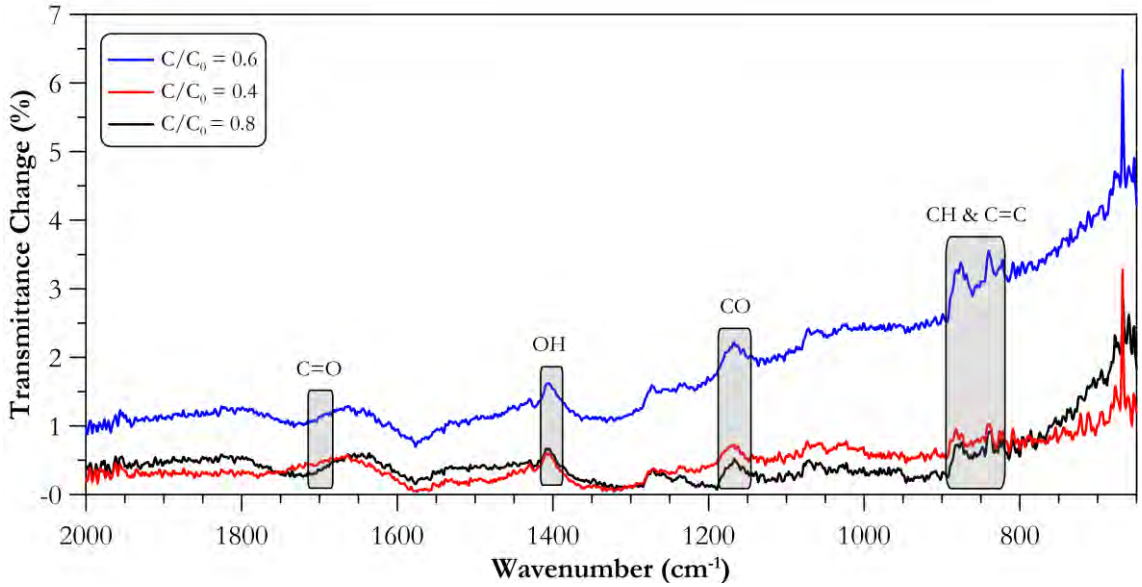

Figure A.15 Normalized FTIR spectra of electrodes at different degradation stages after cycling under aerobic conditions at a working electrode potential of 1.2 V vs RHE and a half cycle time of 5 min. Electrode at end-of-life used as the reference for normalization

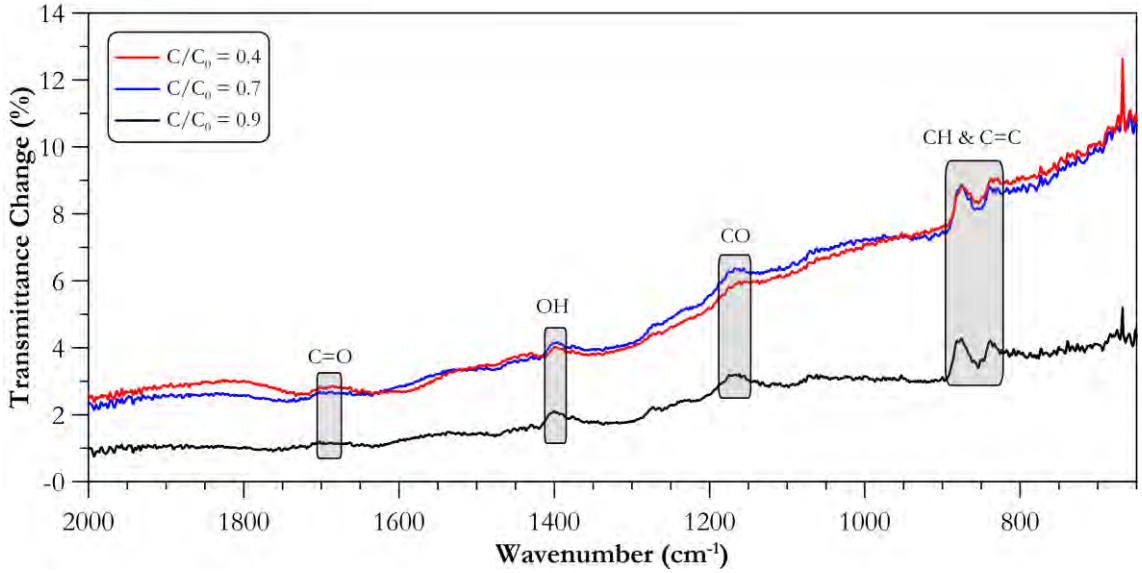

Figure A.16 Normalized FTIR spectra of electrodes at different degradation stages after cycling under aerobic conditions and 0.2 mg Fe^{2+} L^{-1} at a working electrode potential of 1.2 V vs RHE and a half cycle time of 5 min. Electrode at end-of-life used as the reference for normalization

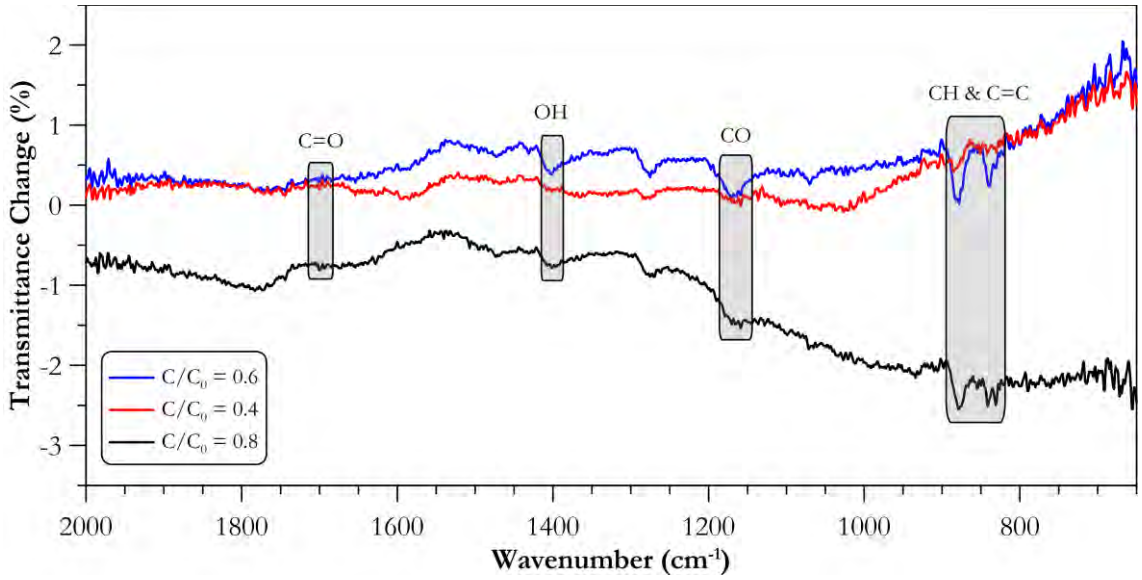

Figure A.17 Normalized FTIR spectra of electrodes at different degradation stages after cycling under aerobic conditions and 2.0 mg Fe^{2+} L^{-1} at a working electrode potential of 1.2 V vs RHE and a half cycle time of 5 min. Electrode at end-of-life used as the reference for normalization

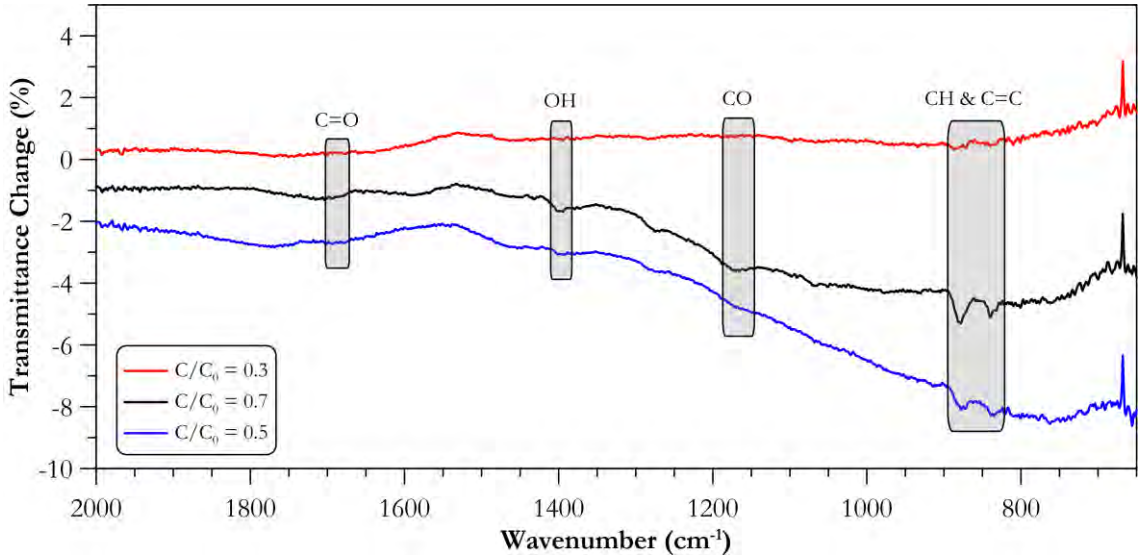

Figure A.18 Normalized FTIR spectra of electrodes at different degradation stages after cycling under aerobic conditions and 20 mg Fe^{2+} L^{-1} at a working electrode potential of 1.2 V vs RHE and a half cycle time of 5 min. Electrode at end-of-life used as the reference for normalization

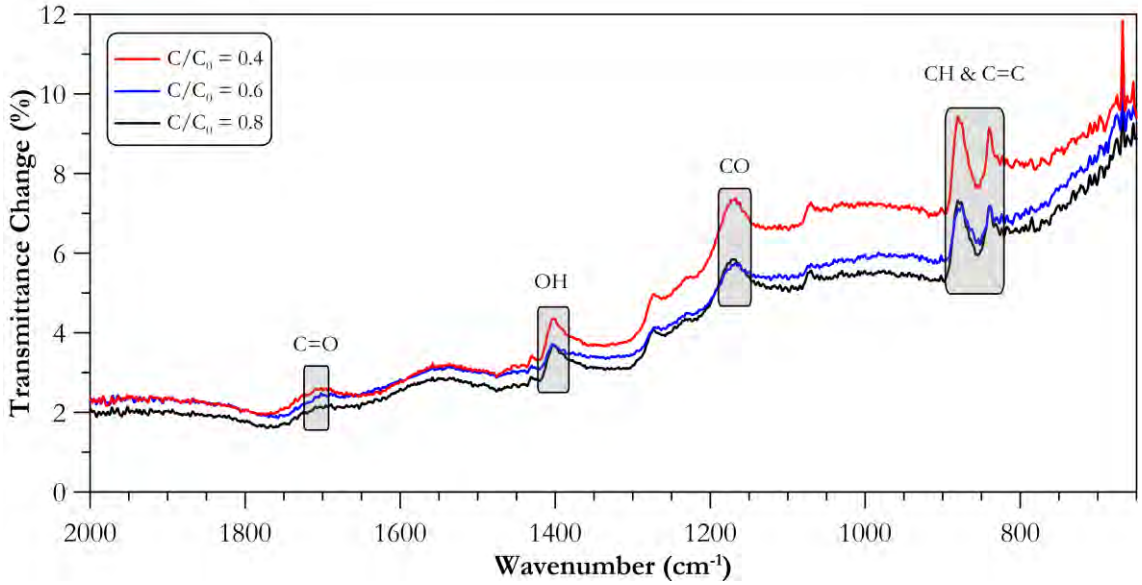

Figure A.19 Normalized FTIR spectra of electrodes at different degradation stages after cycling under aerobic conditions and 20 mg SRNOM L^{-1} at a working electrode potential of 1.2 V vs RHE and a half cycle time of 5 min. Electrode at end-of-life used as the reference for normalization

A.5 Bulk Porosity Analysis

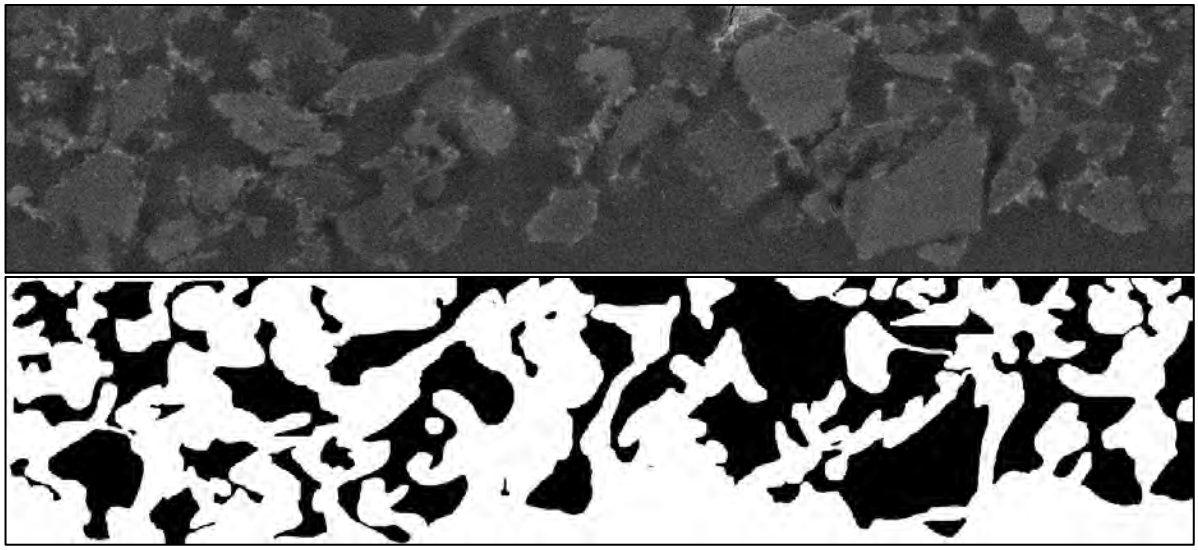

Figure A.20 Raw and processed images used to estimate the bulk porosity of a pristine electrode

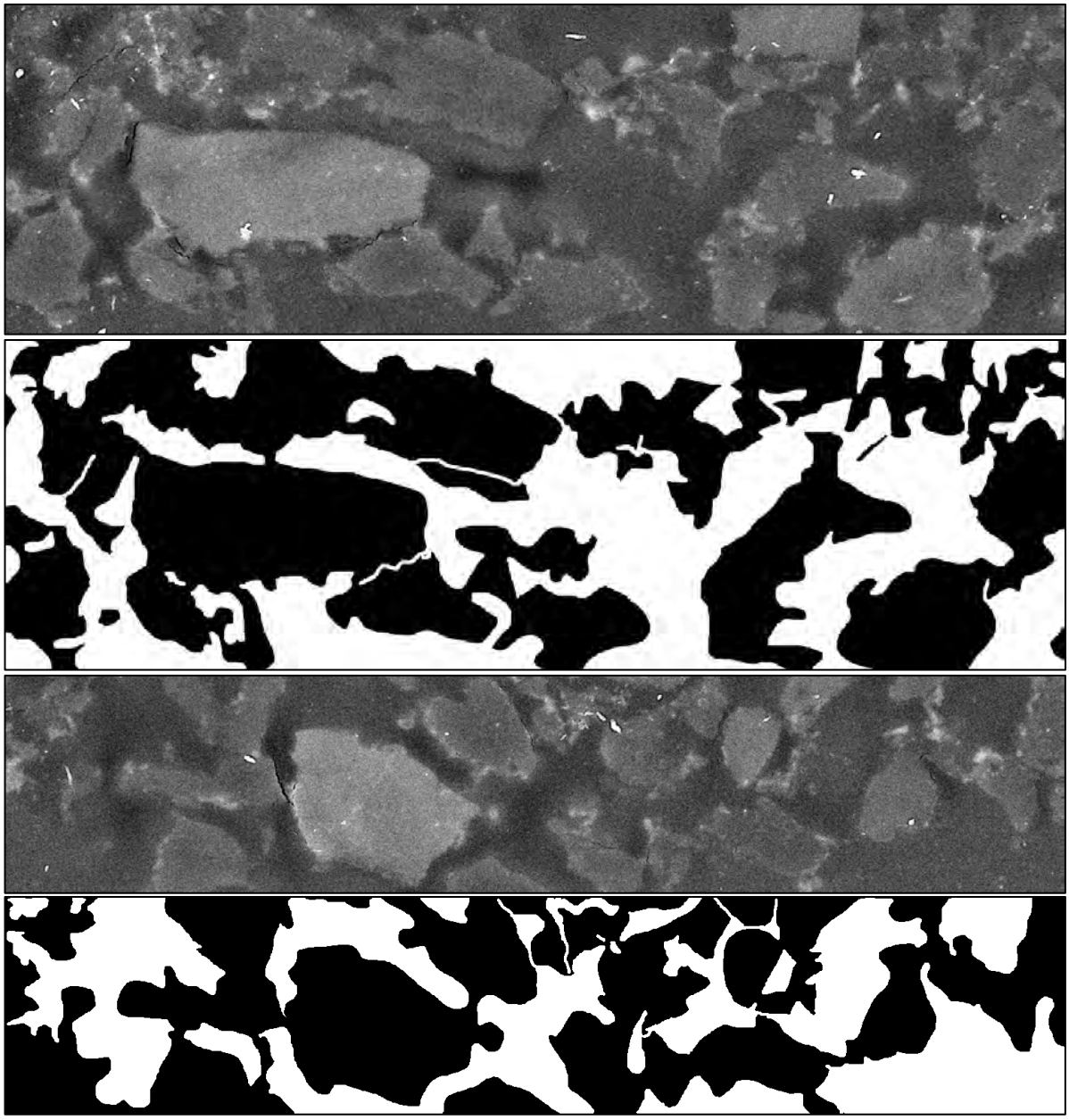

Figure A.20 (Continued) Raw and processed images used to estimate the bulk porosity of a pristine electrode

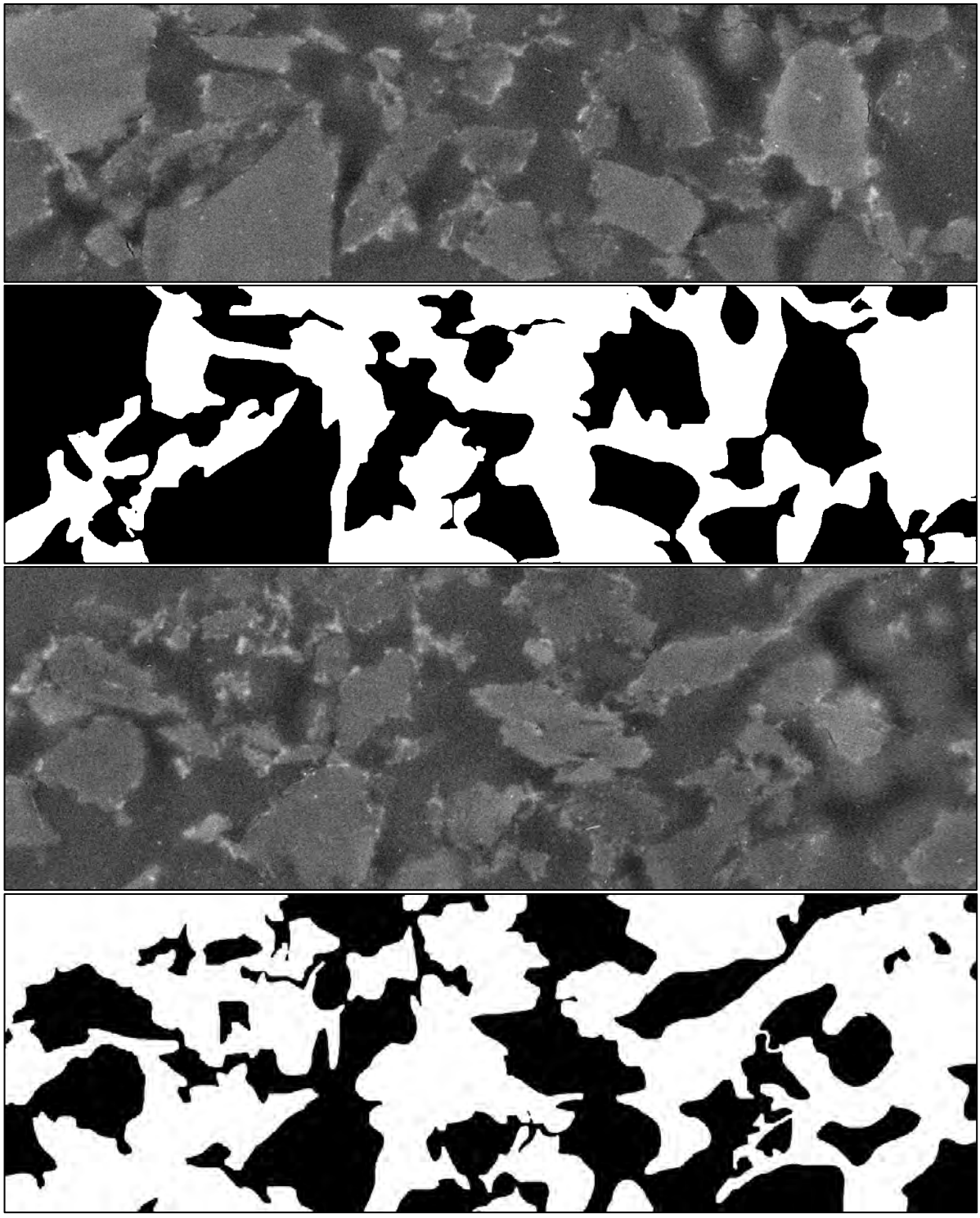

Figure A.20 (Continued) Raw and processed images used to estimate the bulk porosity of a pristine electrode

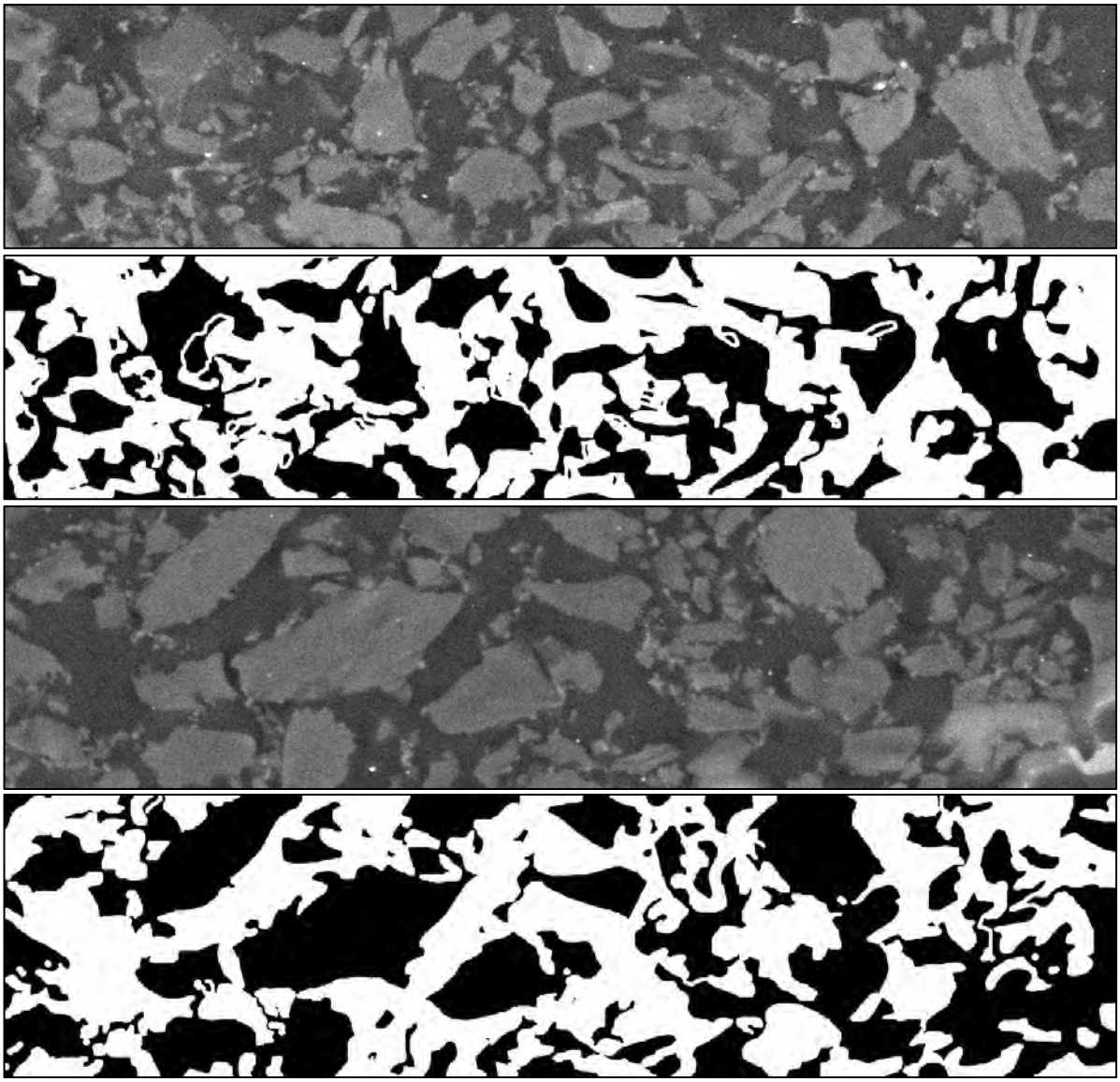

Figure A.21 Raw and processed images used to estimate the bulk porosity of an electrode at EOL conditions after cycling under aerobic conditions with a working electrode potential of 1.2 V vs RHE and a half cycle time of 5 min

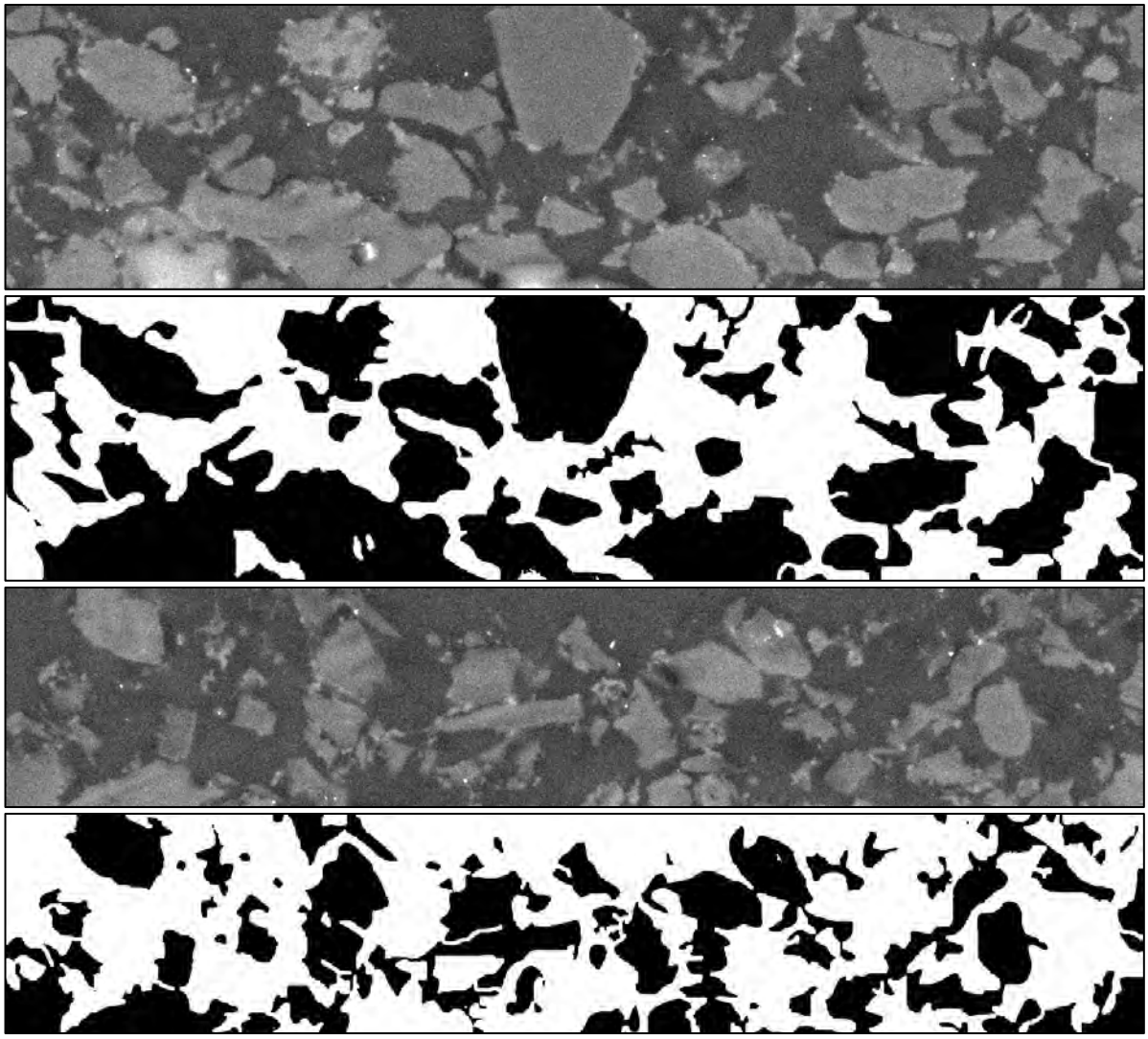

Figure A.21 (Continued) Raw and processed images used to estimate the bulk porosity of an electrode at EOL conditions after cycling under aerobic conditions with a working electrode potential of 1.2 V vs RHE and a half cycle time of 5 min

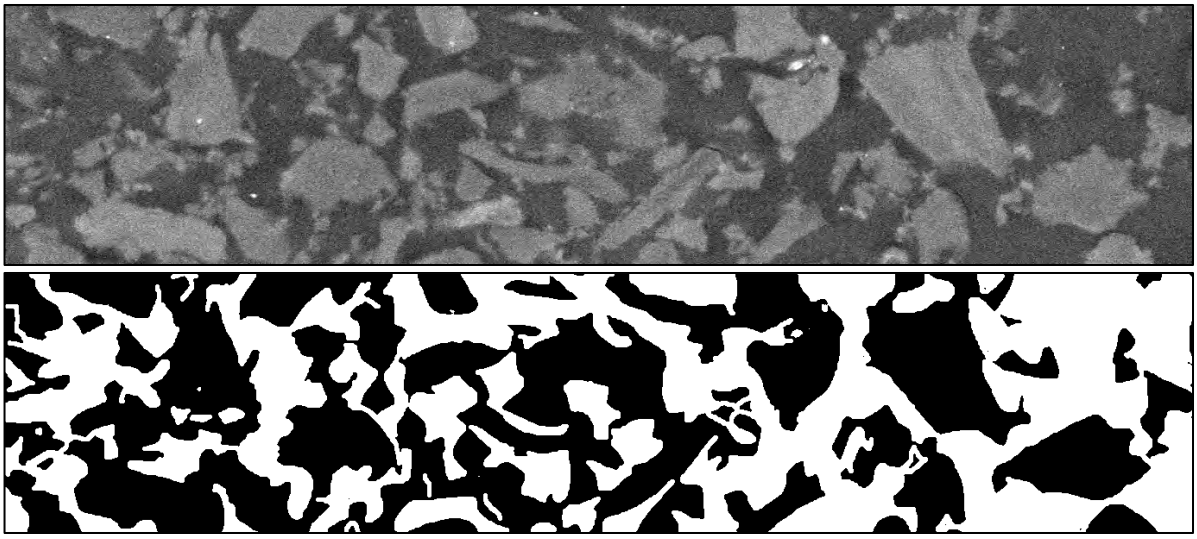

Figure A.21 (Continued) Raw and processed images used to estimate the bulk porosity of an electrode at EOL conditions after cycling under aerobic conditions with a working electrode potential of 1.2 V vs RHE and a half cycle time of 5 min

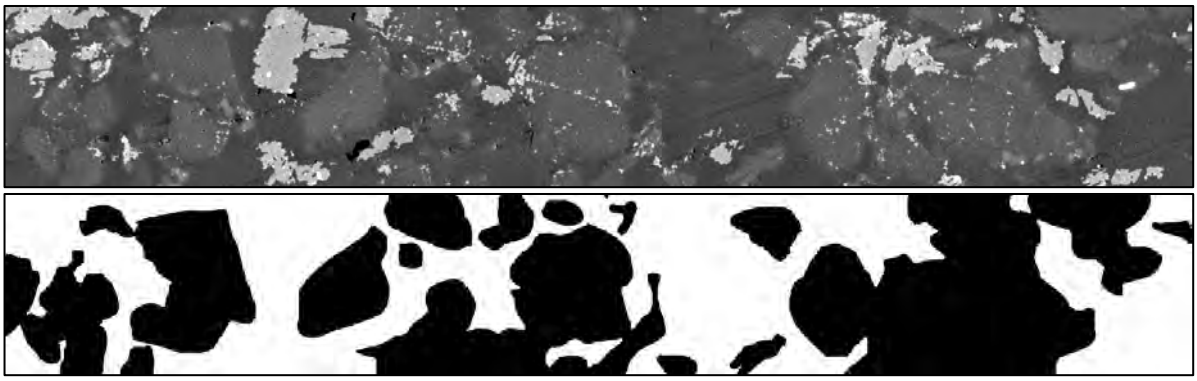

Figure A.22 Raw and processed images used to estimate the bulk porosity of an electrode at EOL conditions after cycling under aerobic conditions and 0.2 mg Fe^{2+} L^{-1} with a working electrode potential of 1.2 V vs RHE and a half cycle time of 5 min

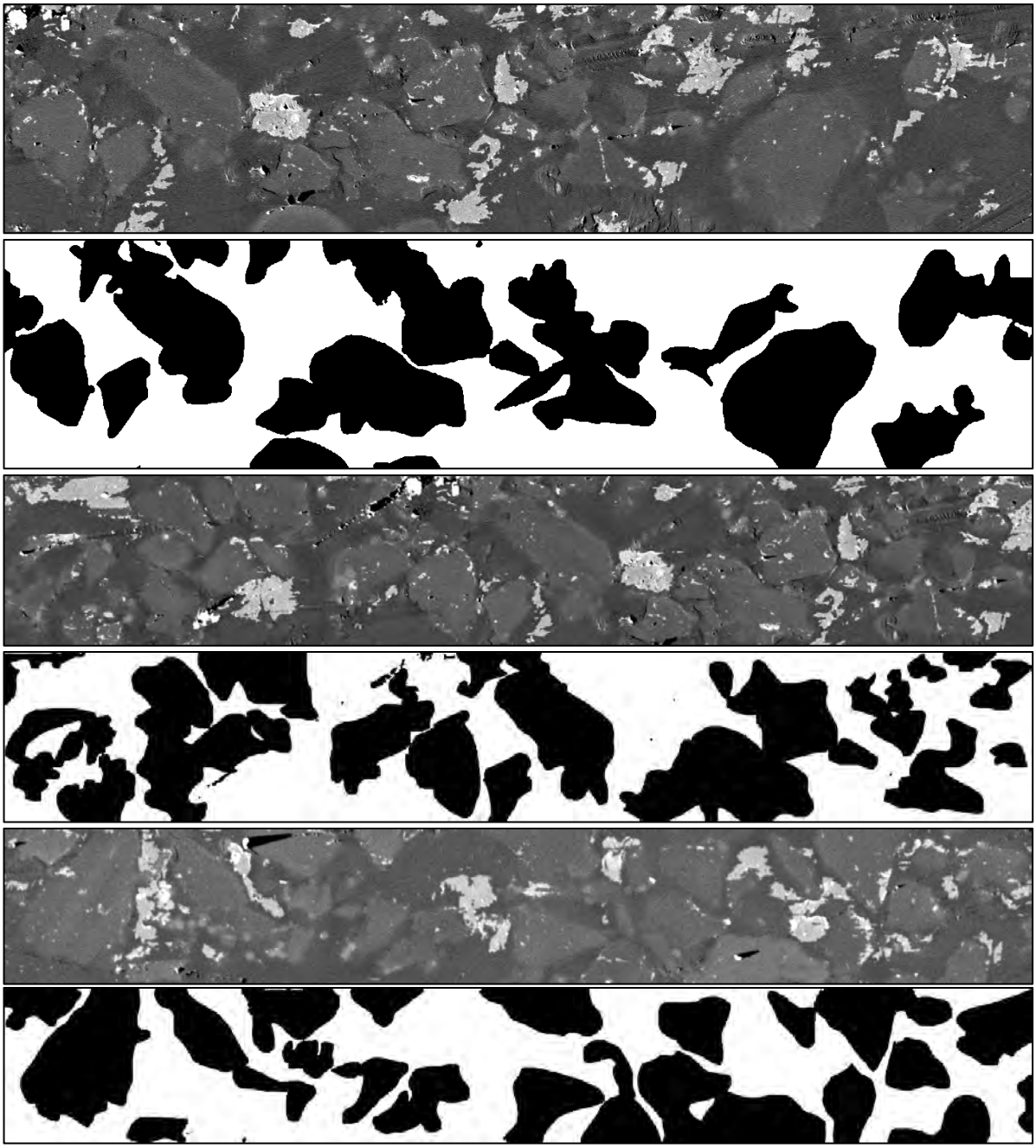

Figure A.22 (Continued) Raw and processed images used to estimate the bulk porosity of an electrode at EOL conditions after cycling under aerobic conditions and 0.2 mg Fe^{2+} L^{-1} with a working electrode potential of 1.2 V vs RHE and a half cycle time of 5 min

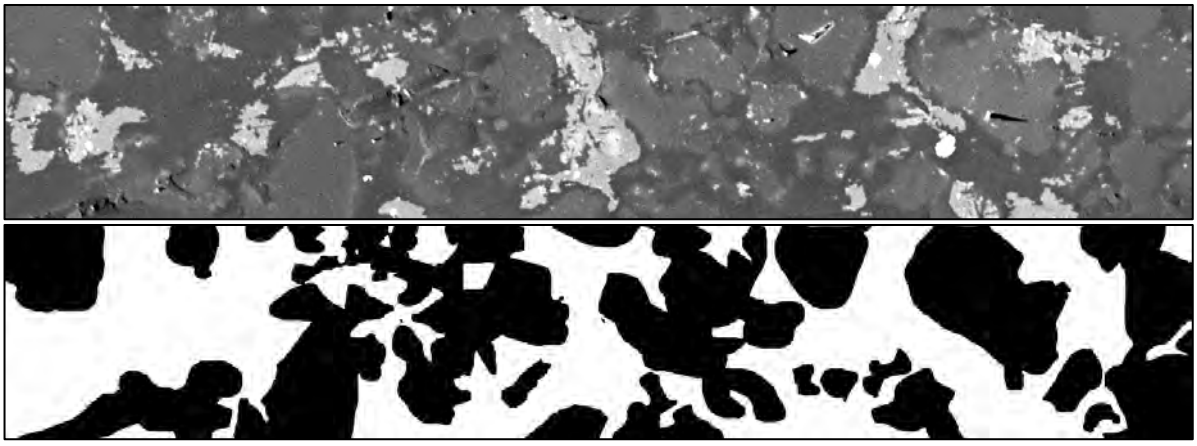

Figure A.22 (Continued) Raw and processed images used to estimate the bulk porosity of an electrode at EOL conditions after cycling under aerobic conditions and 0.2 mg Fe^{2+} L^{-1} with a working electrode potential of 1.2 V vs RHE and a half cycle time of 5 min

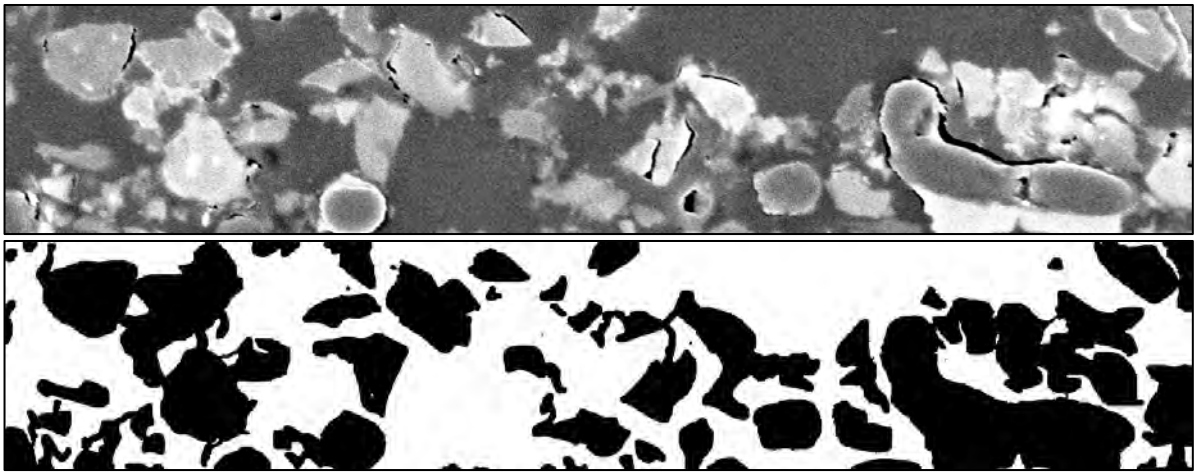

Figure A.23 Raw and processed images used to estimate the bulk porosity of an electrode at EOL conditions after cycling under aerobic conditions and 20 mg Fe^{2+} L^{-1} with a working electrode potential of 1.2 V vs RHE and a half cycle time of 5 min

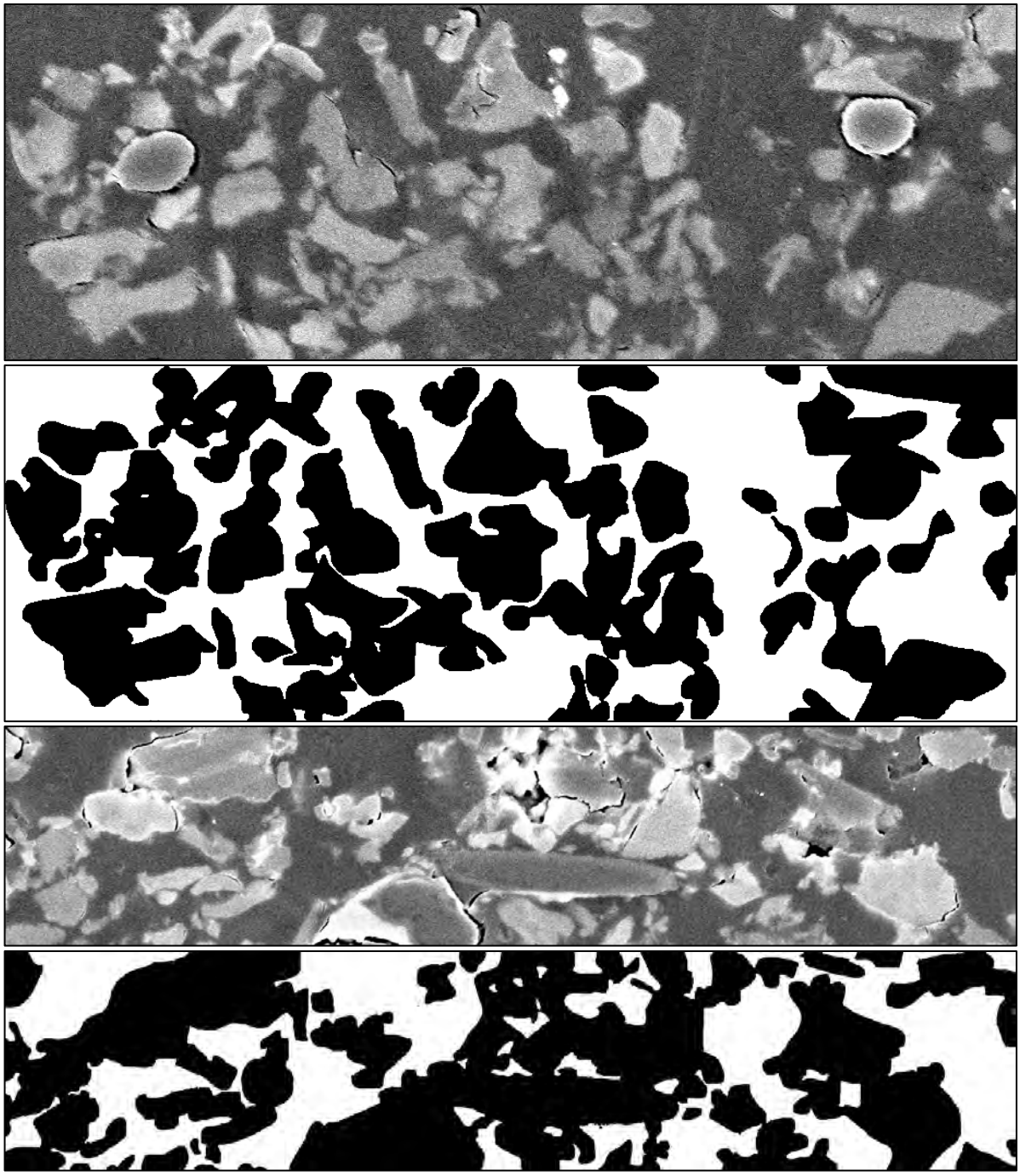

Figure A.23 (Continued) Raw and processed images used to estimate the bulk porosity of an electrode at EOL conditions after cycling under aerobic conditions and 20 mg Fe^{2+} L^{-1} with a working electrode potential of 1.2 V vs RHE and a half cycle time of 5 min

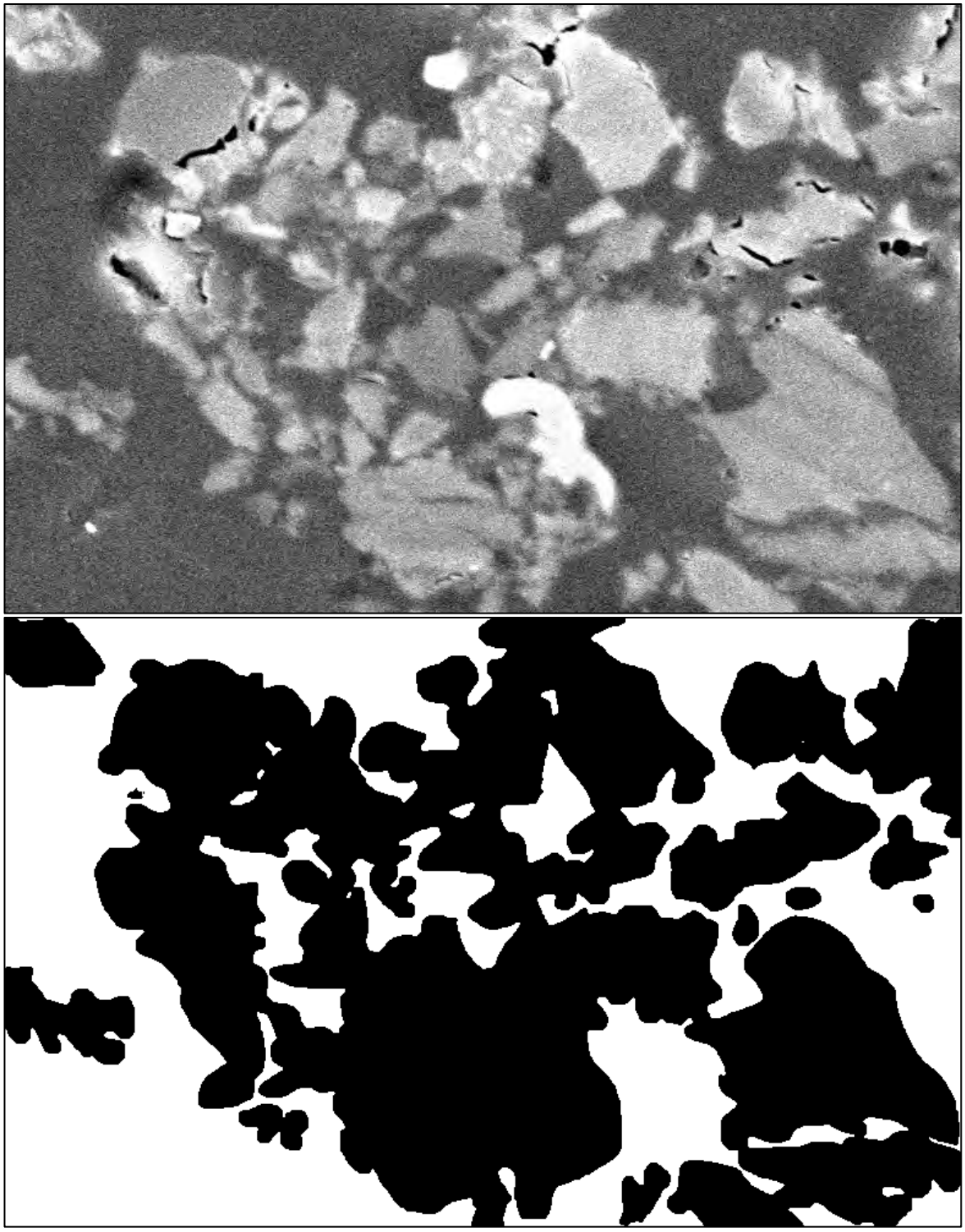

Figure A.23 (Continued) Raw and processed images used to estimate the bulk porosity of an electrode at EOL conditions after cycling under aerobic conditions and 20 mg Fe^{2+} L^{-1} with a working electrode potential of 1.2 V vs RHE and a half cycle time of 5 min

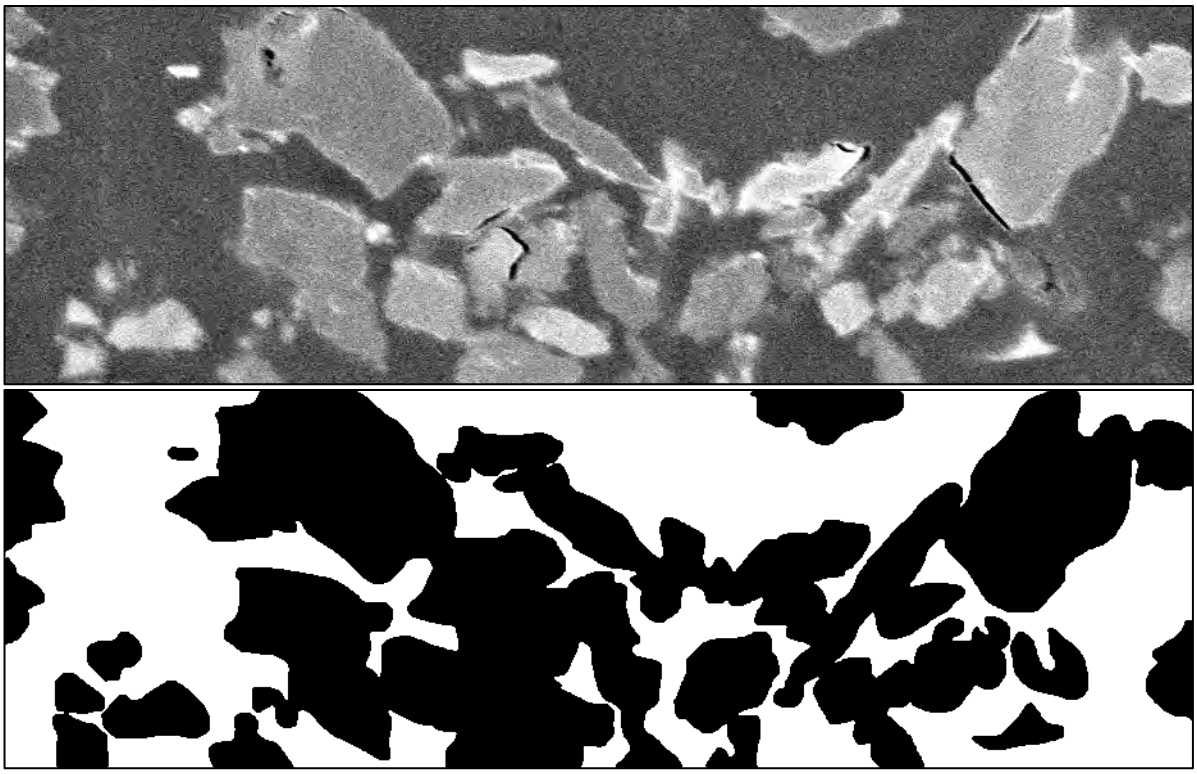

Figure A.23 (Continued) Raw and processed images used to estimate the bulk porosity of an electrode at EOL conditions after cycling under aerobic conditions and 20 mg Fe^{2+} L^{-1} with a working electrode potential of 1.2 V vs RHE and a half cycle time of 5 min

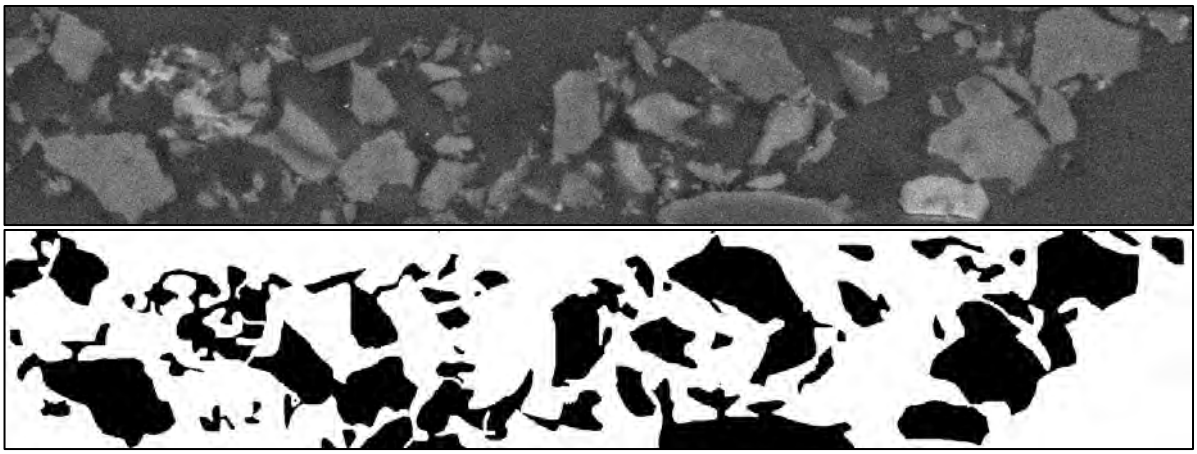

Figure A.24 Raw and processed images used to estimate the bulk porosity of an electrode at EOL conditions after cycling under aerobic conditions and 20 mg SRNOM L^{-1} with a working electrode potential of 1.2 V vs RHE and a half cycle time of 5 min

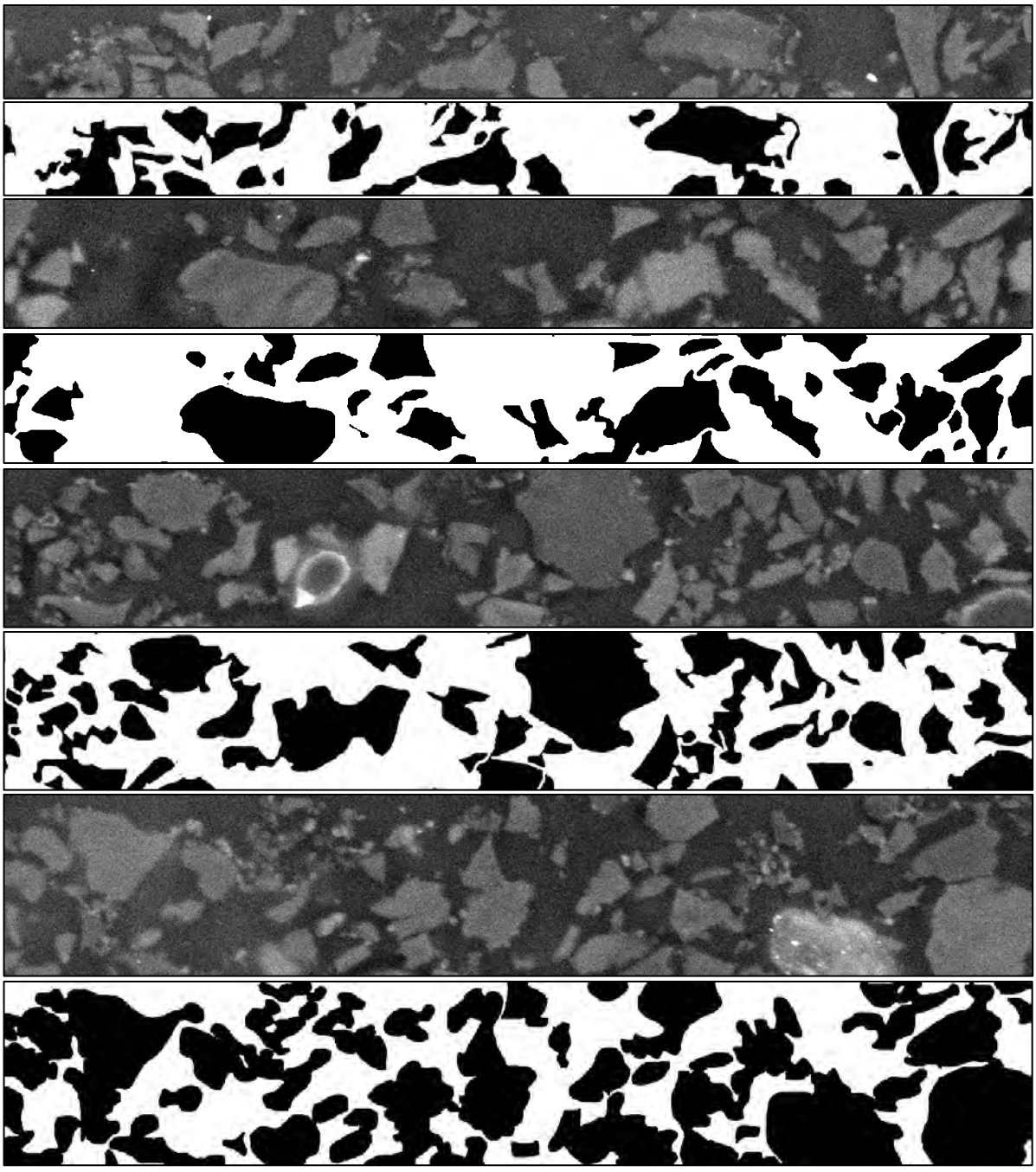

Figure A.24 (Continued) Raw and processed images used to estimate the bulk porosity of an electrode at EOL conditions after cycling under aerobic conditions and 20 mg SRNOM L^{-1} with a working electrode potential of 1.2 V vs RHE and a half cycle time of 5 min

A.6 Discharging Potentials of Degradation Experiments

Table A.1 Discharging potential (V vs RHE) for experiments conducted under N_2 or O_2 saturation with a working electrode potential of 1.2 V vs RHE and a half cycle time of 5 min. The discharge potential equals the open circuit potential measured at the beginning of each set of cycles

Experiment	Baseline – Anaerobic		Baseline – Aerobic	
Cycles performed	Replicate 1 (V vs RHE)	Replicate 2 (V vs RHE)	Replicate 1 (V vs RHE)	Replicate 2 (V vs RHE)
1-5	0.507	0.500	0.500	0.497
6-10	0.533	0.541	0.537	0.573
11-15	0.548	0.550	0.551	0.561
16-20	0.550	0.550	0.551	0.556
21-25	0.561	0.562	0.563	0.548
26-30	0.551	0.549	0.553	0.550
31-35	0.519	0.550	0.555	0.558
36-40	0.451	0.546	0.519	0.562
41-45	0.384	0.504	0.452	0.548
46-50	0.391	0.458	0.412	0.565
51-60	0.559	0.560	0.558	0.562
61-70	0.544	0.374	0.526	0.561

Table A.2 Discharging potential (V vs RHE) for experiments conducted under O_2 saturation with a working electrode potential of 1.2 V vs RHE and a half cycle time of 5 min in presence of 0.2 and 2.0 mg Fe^{2+} L^{-1}. The discharge potential equals the open circuit potential measured at the beginning of each set of cycles

Experiment	0.2 mg Fe^{2+} L^{-1}		2.0 mg Fe^{2+} L^{-1}	
Cycles performed	Replicate 1 (V vs RHE)	Replicate 2 (V vs RHE)	Replicate 1 (V vs RHE)	Replicate 2 (V vs RHE)
1-5	0.513	0.515	0.510	0.514
6-10	0.553	0.552	0.548	0.546
11-15	0.556	0.554	0.545	0.549
16-20	0.559	0.558	0.538	0.551
21-25	0.559	0.556	0.535	0.553
26-30	0.563	0.561	0.546	0.553
31-35	0.562	0.562	0.544	0.552
36-40	0.564	0.565	0.550	0.551
41-45	0.562	0.561	0.537	0.556
46-50	0.556	0.556	-	-

Table A.3 Discharging potential (V vs RHE) for experiments conducted under N_2 or O_2 saturation with a working electrode potential of 1.2 V vs RHE and a half cycle time of 5 min in presence of 20 mg Fe^{2+} L^{-1}. The discharge potential equals the open circuit potential measured at the beginning of each set of cycles

Experiment	20 mg Fe^{2+} L^{-1} – Anaerobic		20 mg Fe^{2+} L^{-1} – Aerobic	
Cycles performed	Replicate 1 (V vs RHE)	Replicate 2 (V vs RHE)	Replicate 1 (V vs RHE)	Replicate 2 (V vs RHE)
1-5	0.500	0.652	0.515	0.511
6-10	0.527	0.496	0.483	0.482
11-15	0.525	0.502	0.484	0.477
16-20	0.514	0.513	0.505	0.511
21-25	0.516	0.503	0.482	0.499
26-30	0.489	0.517	0.501	0.511
31-35	0.518	0.508	0.492	0.484
36-40	0.518	0.514	0.506	0.517
41-45	0.521	0.509	0.497	0.502

Table A.4 Discharging potential (V vs RHE) for experiments conducted under N_2 or O_2 saturation with a working electrode potential of 1.2 V vs RHE and a half cycle time of 5 min in presence of 20 and 40 mg SRNOM L^{-1}. The discharge potential equals the open circuit potential measured at the beginning of each set of cycles

Experiment	20 mg SRNOM L^{-1} Anaerobic		20 mg SRNOM L^{-1} Aerobic		40 mg SRNOM L^{-1} Aerobic	
Cycles performed	Replicate 1 (V vs RHE)	Replicate 2 (V vs RHE)	Replicate 1 (V vs RHE)	Replicate 2 (V vs RHE)	Replicate 1 (V vs RHE)	Replicate 2 (V vs RHE)
1-5	0.504	0.513	0.517	0.512	0.534	0.529
6-10	0.568	0.575	0.562	0.559	0.570	0.568
11-15	0.558	0.560	0.566	0.564	0.572	0.575
16-20	0.548	0.553	0.563	0.562	0.573	0.571
21-25	0.540	0.549	0.564	0.563	0.570	0.568
26-30	0.548	0.551	0.567	0.567	0.578	0.576
31-35	0.556	0.560	0.568	0.568	0.576	0.572
36-40	0.561	0.561	0.570	0.569	0.575	0.576
41-45	0.536	0.540	0.569	0.569	0.570	0.570
46-50	0.565	0.562	0.569	0.567	0.561	0.568
51-60	0.568	0.568	0.570	0.567	0.571	0.571
61-70	0.566	0.566	0.567	0.563	0.565	0.567

Table A.5 Discharging potential (V vs RHE) for experiments conducted under O_2 saturation with a half cycle time of 5 min under acidic (pH = 1) and alkaline (pH = 13) conditions. The working electrode potential for the experiments conducted at a pH of 1 was 1.2 V vs RHE. On the other hand, the working electrode potential for experiments conducted at a pH of 13 was 0.49 V vs RHE. The discharge potential equals the open circuit potential measured at the beginning of each cycle

Experiment	Acidic (pH = 1)		Alkaline (pH = 13)	
Cycles number	Replicate 1 (V vs RHE)	Replicate 2	Replicate 1 (V vs RHE)	Replicate 2
1	0.659	0.663	0.124	0.114
2	0.706	0.709	0.128	0.128
3	0.741	0.745	0.134	0.135
4	0.778	0.784	0.136	0.138
5	0.808	0.811	0.136	0.137
6	0.814	0.816	0.135	0.133
7	0.837	0.839	0.135	0.139
8	0.859	0.859	0.137	0.141
9	0.876	0.878	0.135	0.141
10	0.895	0.897	0.139	0.142
11	0.743	0.750	0.087	0.089
12	0.776	0.781	0.105	0.106
13	0.805	0.809	0.114	0.116
14	0.832	0.835	0.115	0.121
15	0.859	0.860	0.116	0.123
16	0.877	0.876	0.124	0.127
17	0.894	0.891	0.125	0.130
18	0.911	0.906	0.127	0.131
19	0.927	0.920	0.128	0.133
20	0.939	0.930	0.130	0.135
21	0.712	0.713	0.085	0.083
22	0.750	0.748	0.096	0.098
23	0.789	0.785	0.107	0.107
24	0.823	0.817	0.112	0.114
25	0.854	0.843	0.117	0.118
26	0.884	0.869	0.111	0.115
27	0.915	0.895	0.117	0.120
28	0.941	0.914	0.122	0.124
29	0.962	0.931	0.132	0.131
30	0.982	0.946	0.135	0.134
31	0.757	0.759	0.077	0.083
32	0.798	0.787	0.100	0.104
33	0.836	0.821	0.109	0.115

Table A.5 (Continued) Discharging potential (V vs RHE) for experiments conducted under O_2 saturation with a half cycle time of 5 min under acidic (pH = 1) and alkaline (pH = 13) conditions. The working electrode potential for the experiments conducted at a pH of 1 was 1.2 V vs RHE. On the other hand, the working electrode potential for experiments conducted at a pH of 13 was 0.49 V vs RHE. The discharge potential equals the open circuit potential measured at the beginning of each cycle

Experiment	Acidic (pH = 1)		Alkaline (pH = 13)	
Cycles number	Replicate 1 (V vs RHE)	Replicate 2	Replicate 1 (V vs RHE)	Replicate 2
34	0.877	0.851	0.117	0.122
35	0.917	0.878	0.123	0.127
36	0.952	0.904	0.133	0.135
37	0.981	0.923	0.149	0.149
38	1.006	0.944	0.163	0.162
39	1.021	0.960	0.174	0.170
40	1.030	0.976	0.187	0.183
41	0.742	0.745	0.077	0.085
42	0.796	0.785	0.101	0.106
43	0.849	0.821	0.119	0.120
44	0.904	0.854	0.137	0.138
45	0.954	0.885	0.157	0.156
46	0.992	0.917	0.175	0.171
47	1.015	0.944	0.193	0.191
48	1.027	0.967	0.201	0.191
49	1.034	0.988	0.209	0.210
50	1.035	1.000	0.206	0.213

Table A.6 Discharging potential (V vs RHE) for experiments conducted under O_2 saturation with a working electrode potential of 1.2 V vs RHE, a half cycle time of 5 min with and without pH adjustment after every cycle. The discharge potential equals the open circuit potential measured at the beginning of each cycle

Experiment	No Adjustment		With Adjustment	
Cycles number	Replicate 1 (V vs RHE)	Replicate 2	Replicate 1 (V vs RHE)	Replicate 2
1	0.489	0.509	0.483	0.484
2	0.578	0.590	0.541	0.540
3	0.628	0.642	0.577	0.607
4	0.672	0.689	0.607	0.629
5	0.699	0.721	0.629	0.647
6	0.723	0.725	0.644	0.661
7	0.740	0.745	0.656	0.672
8	0.755	0.765	0.666	0.681

Table A.6 (Continued) Discharging potential (V vs RHE) for experiments conducted under O_2 saturation with a working electrode potential of 1.2 V vs RHE, a half cycle time of 5 min with and without pH adjustment after every cycle. The discharge potential equals the open circuit potential measured at the beginning of each cycle

Experiment	No Adjustment		With Adjustment	
Cycles number	Replicate 1 (V vs RHE)	Replicate 2	Replicate 1 (V vs RHE)	Replicate 2
9	0.769	0.782	0.674	0.688
10	0.778	0.798	0.682	0.577
11	0.545	0.589	0.533	0.537
12	0.574	0.609	0.558	0.564
13	0.602	0.631	0.580	0.587
14	0.629	0.654	0.599	0.610
15	0.655	0.679	0.618	0.633
16	0.669	0.703	0.625	0.647
17	0.647	0.728	0.645	0.670
18	0.726	0.757	0.669	0.697
19	0.756	0.786	0.690	0.725
20	0.791	0.819	0.718	0.758
21	0.553	0.523	0.542	0.550
22	0.592	0.559	0.584	0.596
23	0.640	0.604	0.634	0.651
24	0.705	0.657	0.691	0.715
25	0.767	0.716	0.744	0.771
26	0.818	0.776	0.788	0.810
27	0.847	0.821	0.814	0.832
28	0.852	0.850	0.819	0.836
29	0.861	0.859	0.830	0.850
30	0.859	0.872	0.828	0.844
31	0.579	0.565	0.571	0.573
32	0.668	0.665	0.658	0.678
33	0.751	0.758	0.737	0.767
34	0.799	0.815	0.779	0.810
35	0.828	0.845	0.806	0.835
36	0.836	0.854	0.818	0.844
37	0.745	0.867	0.826	0.852
38	0.849	0.867	0.829	0.855
39	0.845	0.866	0.824	0.848
40	0.848	0.868	0.825	0.852
41	0.564	0.563	0.562	0.562
42	0.677	0.676	0.668	0.678
43	0.748	0.756	0.740	0.752
44	0.777	0.796	0.767	0.784

Table A.6 (Continued) Discharging potential (V vs RHE) for experiments conducted under O_2 saturation with a working electrode potential of 1.2 V vs RHE, a half cycle time of 5 min with and without pH adjustment after every cycle. The discharge potential equals the open circuit potential measured at the beginning of each cycle

Experiment	No Adjustment		With Adjustment	
Cycles number	Replicate 1 (V vs RHE)	Replicate 2	Replicate 1 (V vs RHE)	Replicate 2
45	0.799	0.817	0.789	0.809
46	0.814	0.824	0.803	0.826
47	0.820	0.833	0.808	0.827
48	0.818	0.837	0.804	0.822
49	0.820	0.835	0.803	0.822
50	0.819	0.834	0.802	0.821

Appendix B

B.1 Investigating the Recovery of Capacitance and E_{PZC} regression

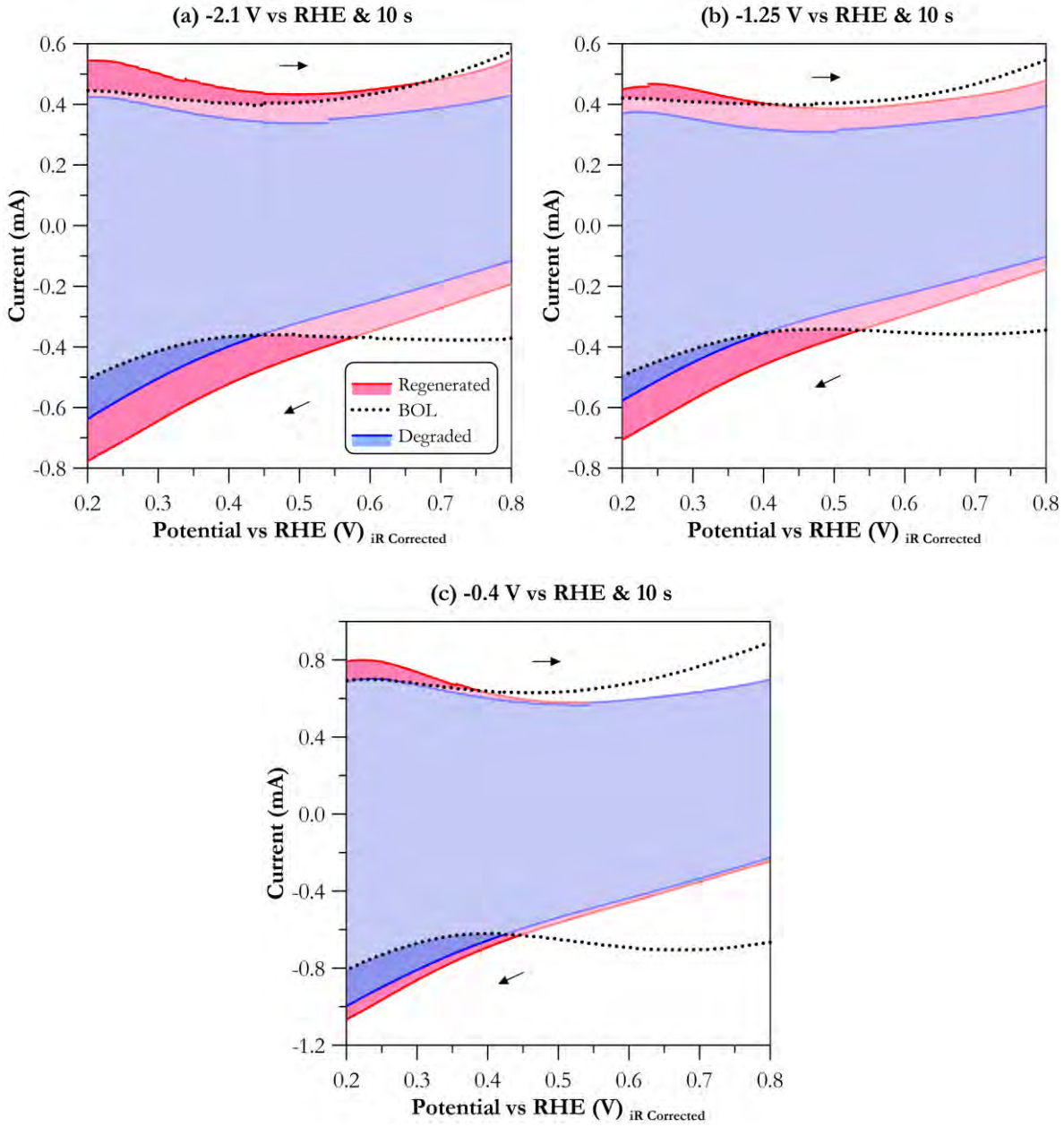

Figure B.1 Cyclic voltammograms obtained in deaerated 17.1 mM NaCl at room temperature and 1 mV s^{-1} for the pristine (BOL), cycled (degraded to $C/C_0 \approx 0.85$) and regenerated electrodes under different potential-holding time treatments. Diagrams are enlarged to exhibit the change in the capacitive response and shift of the E_{PZC}

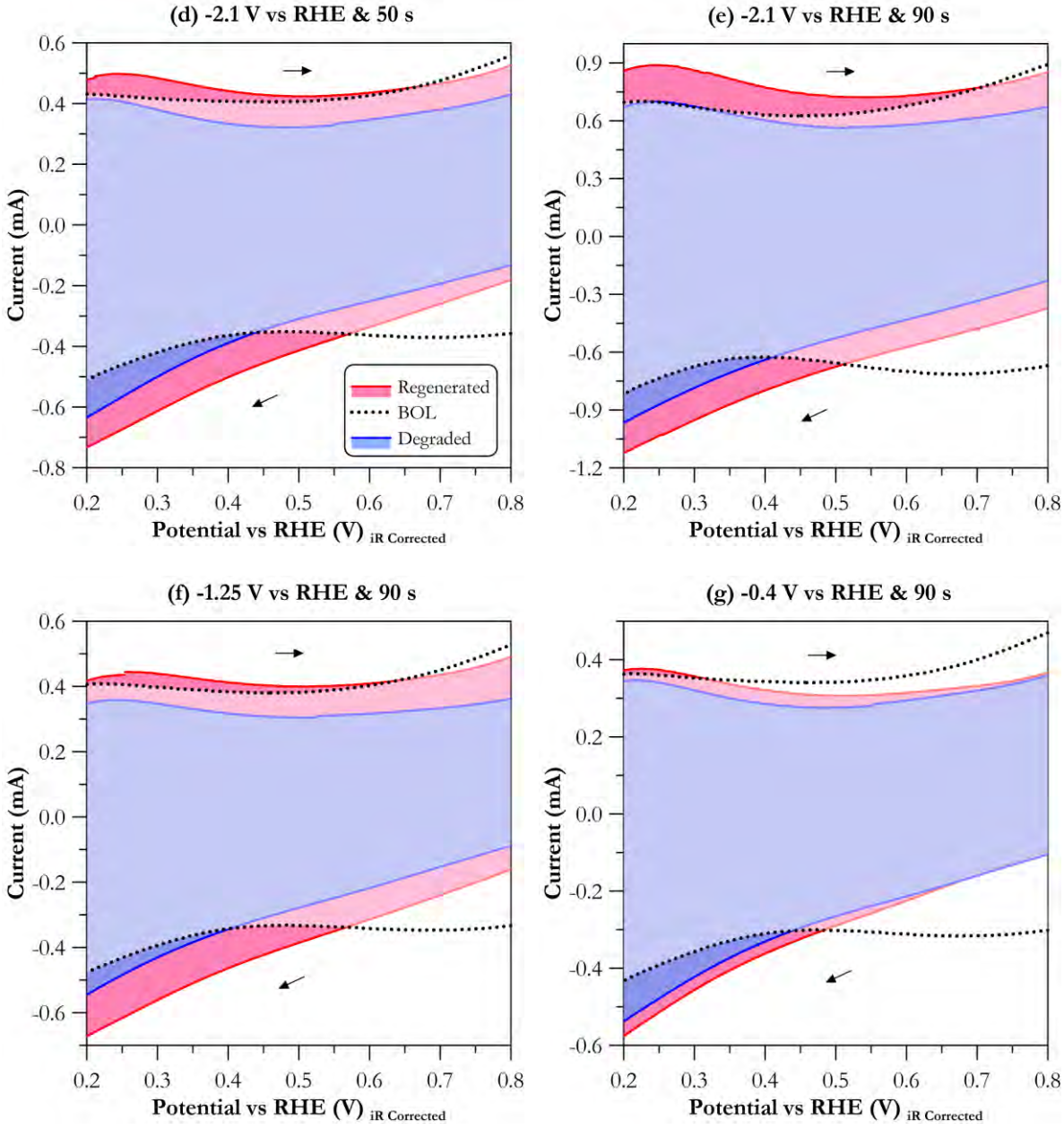

Figure B.1 (Continued) Cyclic voltammograms obtained in deaerated 17.1 mM NaCl at room temperature and 1 mV s^{-1} for the pristine (BOL), cycled (degraded to $C/C_0 \approx 0.85$) and regenerated electrodes under different potential-holding time treatments. Diagrams are enlarged to exhibit the change in the capacitive response and shift of the E_{PZC}

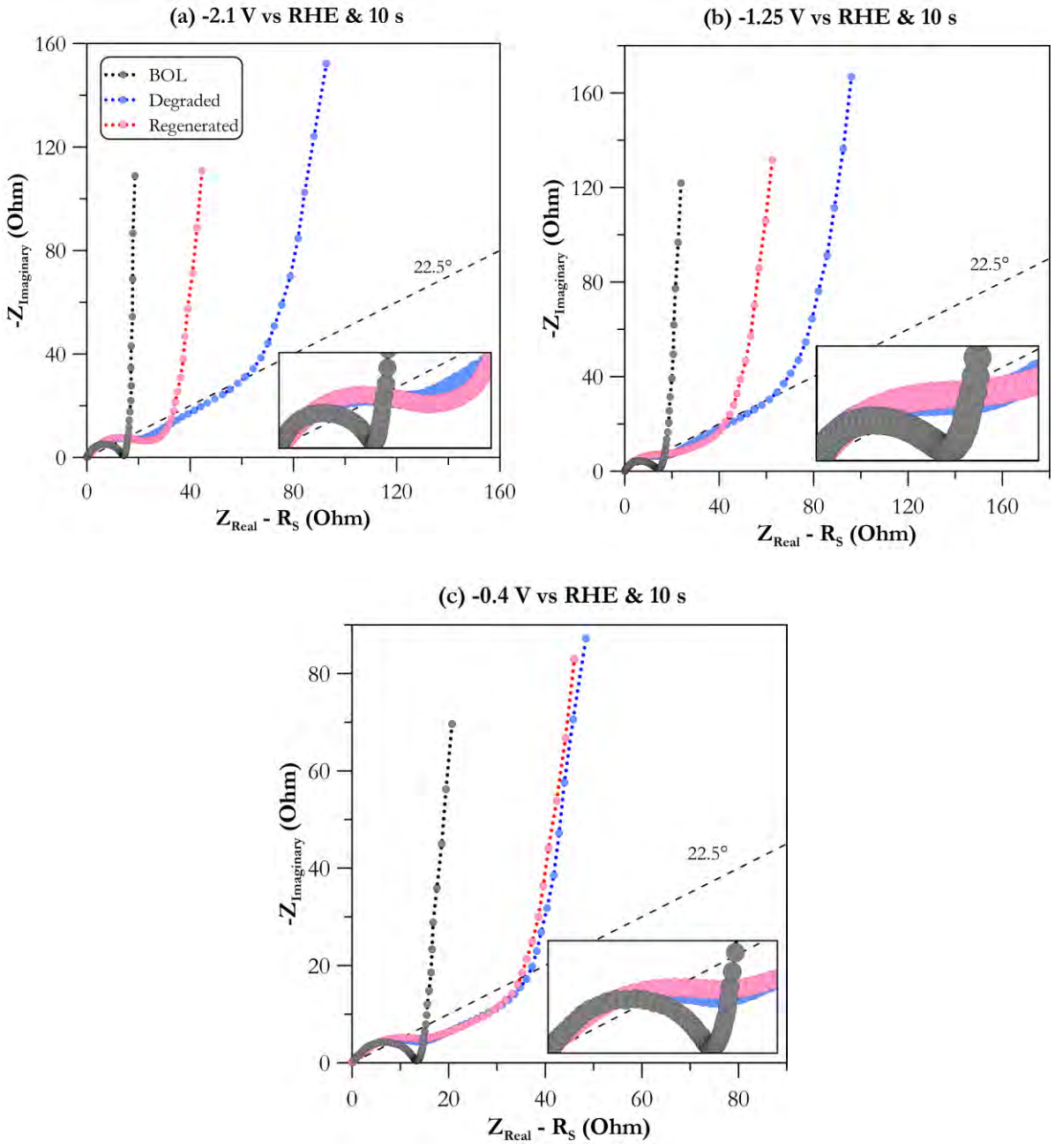

Figure B.2 Complex impedance plane plots obtained at 0.5 V vs RHE between 350 kHz – 5 mHz in 17.1 mM deaerated NaCl at room temperature with a sine amplitude of 5 mV (3.54 mV_{RMS}) for the pristine (BOL), cycled (degraded to $C/C_0 \approx 0.85$) and regenerated electrodes under different potential-holding time treatments

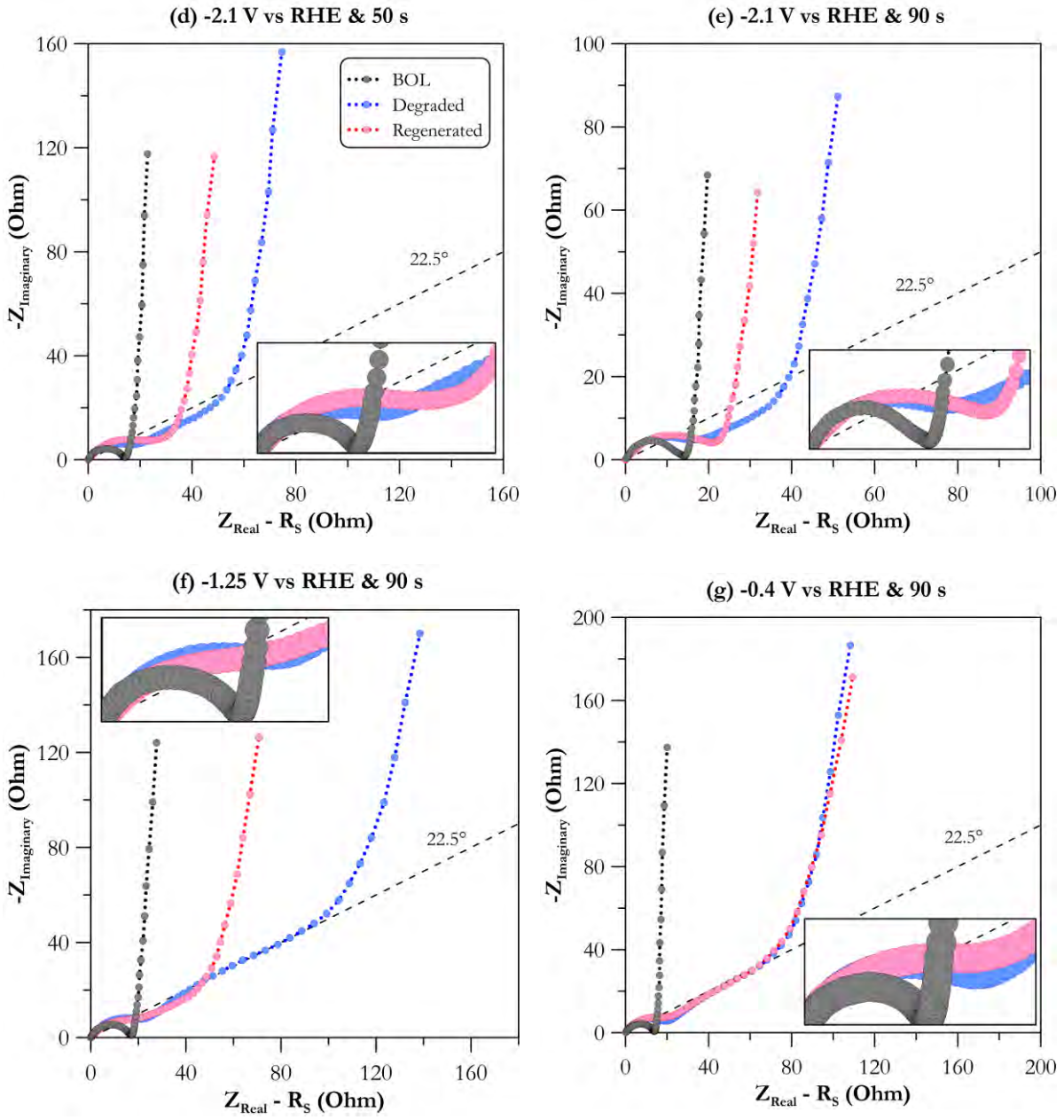

Figure B.2 (Continued) Complex impedance plane plots obtained at 0.5 V vs RHE between 350 kHz – 5 mHz in 17.1 mM deaerated NaCl at room temperature with a sine amplitude of 5 mV (3.54 mV_{RMS}) for the pristine (BOL), cycled (degraded to $C/C_0 \approx 0.85$) and regenerated electrodes under different potential-holding time treatments

B.2 Further Probing along the Potential Domain

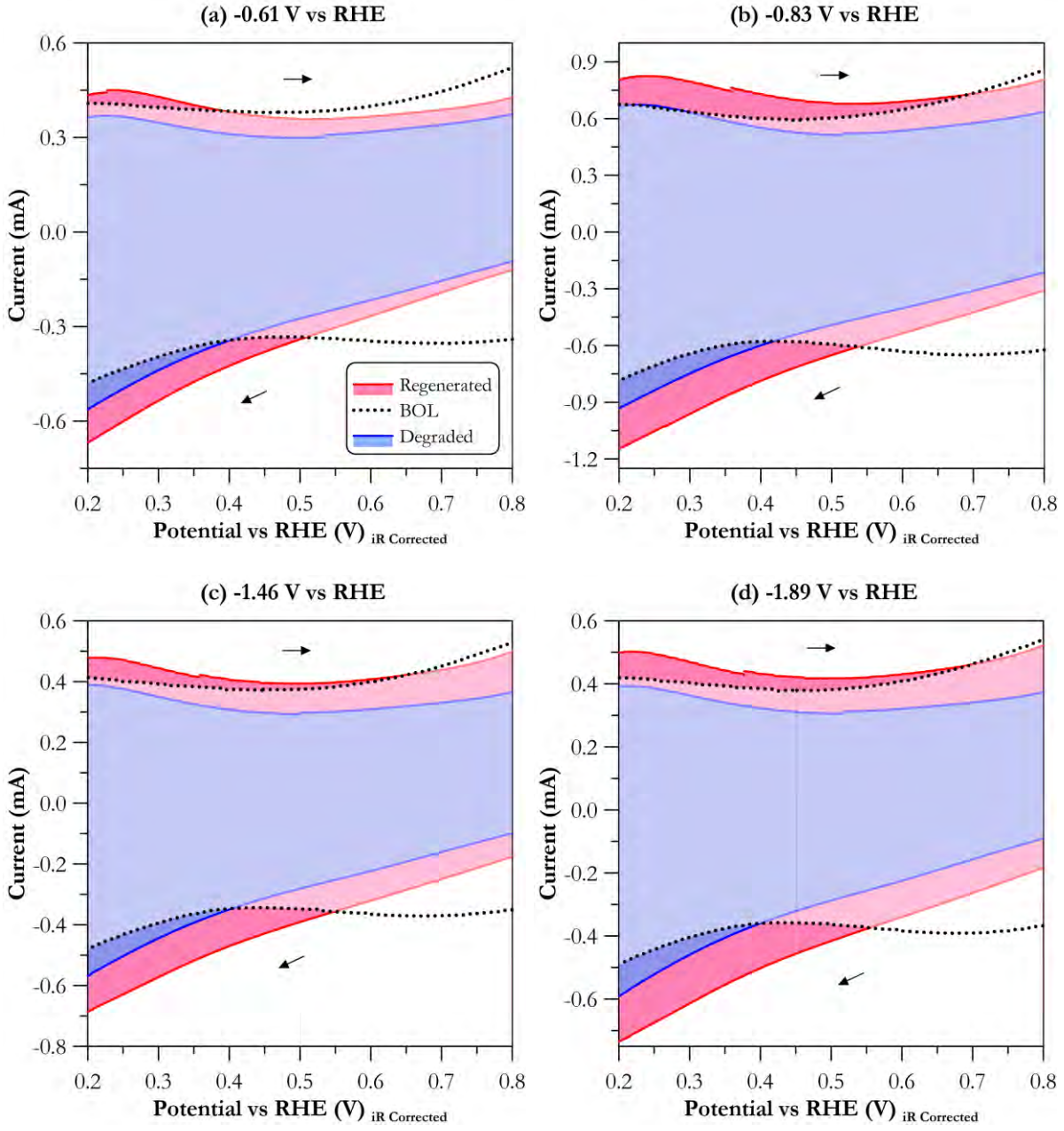

Figure B.3 Cyclic voltammograms obtained in deaerated 17.1 mM NaCl at room temperature and 1 mV s^{-1} for the pristine (BOL), cycled (degraded to $C/C_0 \approx 0.85$) and regenerated electrodes under different reductive potentials and a holding time of 50 s. Diagrams are enlarged to exhibit the change in the capacitive response and shift of the E_{PZC}

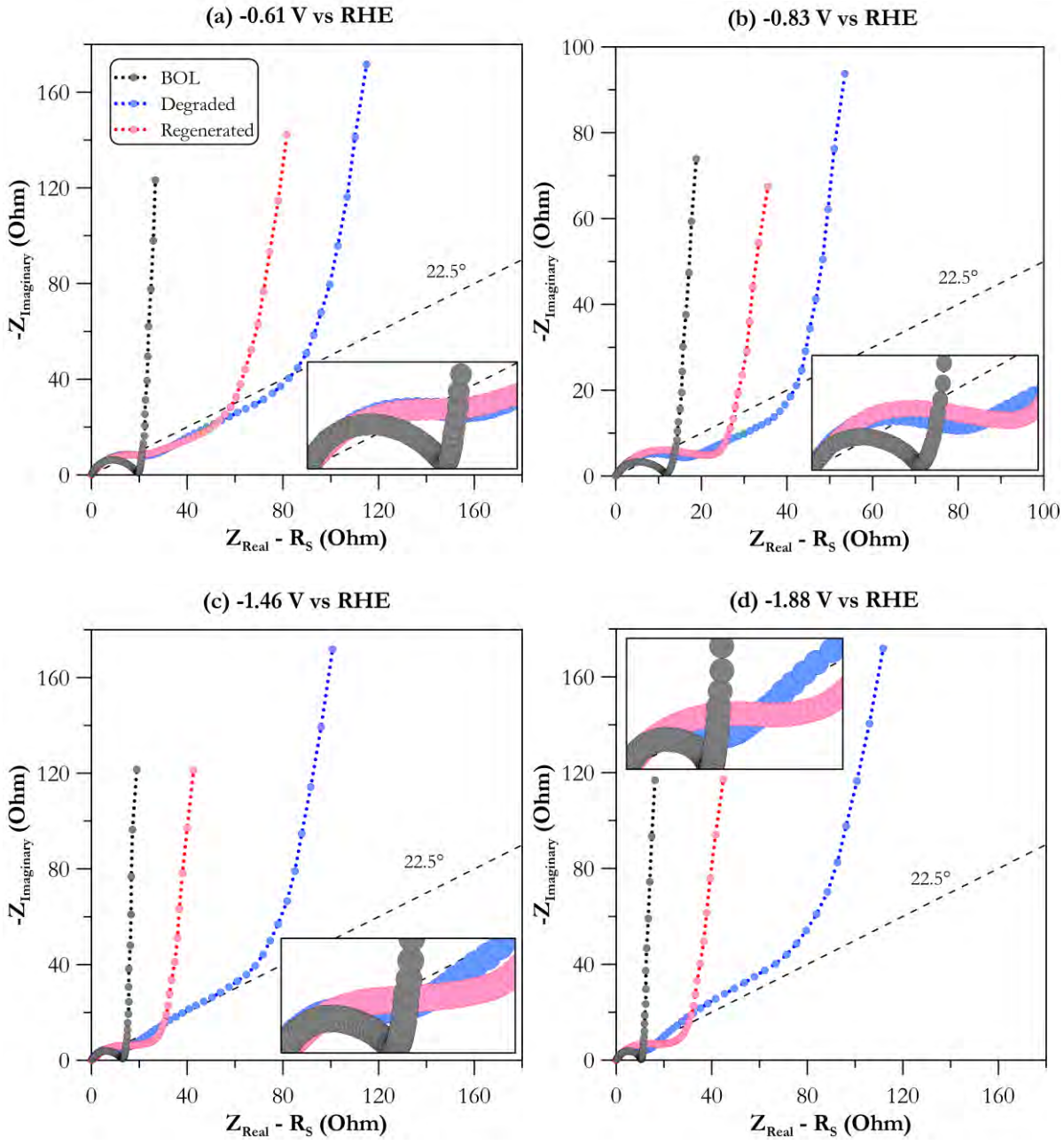

Figure B.4 Complex impedance plane plots obtained at 0.5 V vs RHE between 350 kHz – 5 mHz in 17.1 mM deaerated NaCl at room temperature with a sine amplitude of 5 mV (3.54 mV_{RMS}) for the pristine (BOL), cycled (degraded to $C/C_0 \approx 0.85$) and regenerated electrodes under different reductive potentials and a holding time of 50 s

B.3 Raw and Normalized FTIR Spectra

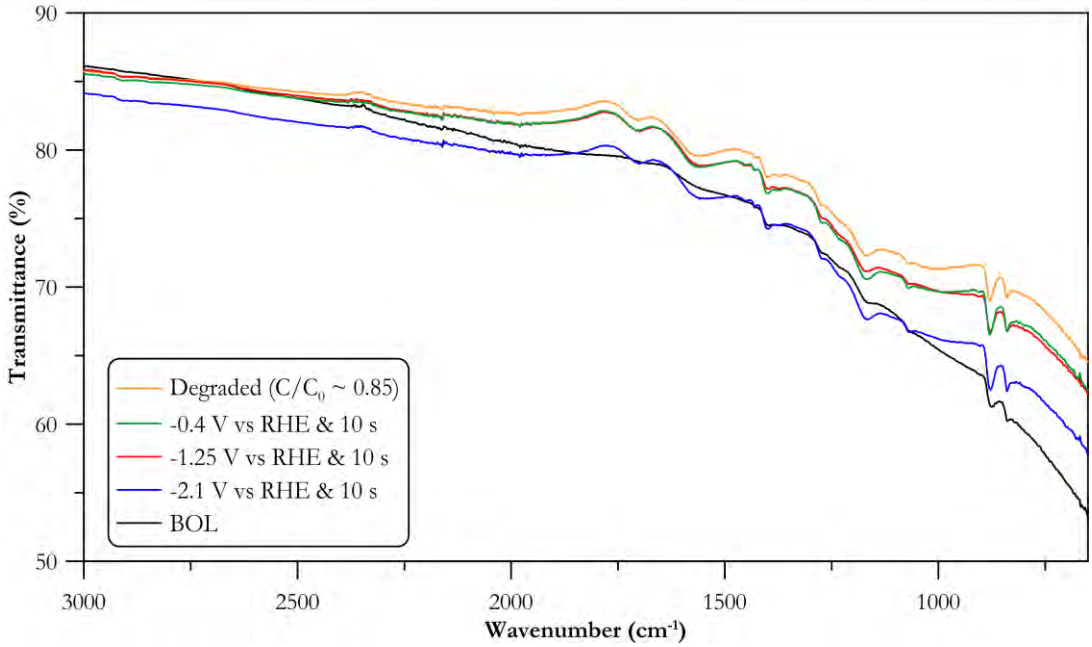

Figure B.5 FTIR spectra of electrodes regenerated at -2.1, -1.25 and -0.4 V vs RHE and a holding time of 10 s after cycling at a working electrode potential of 1.2 V vs RHE and a half cycle time of 5 min

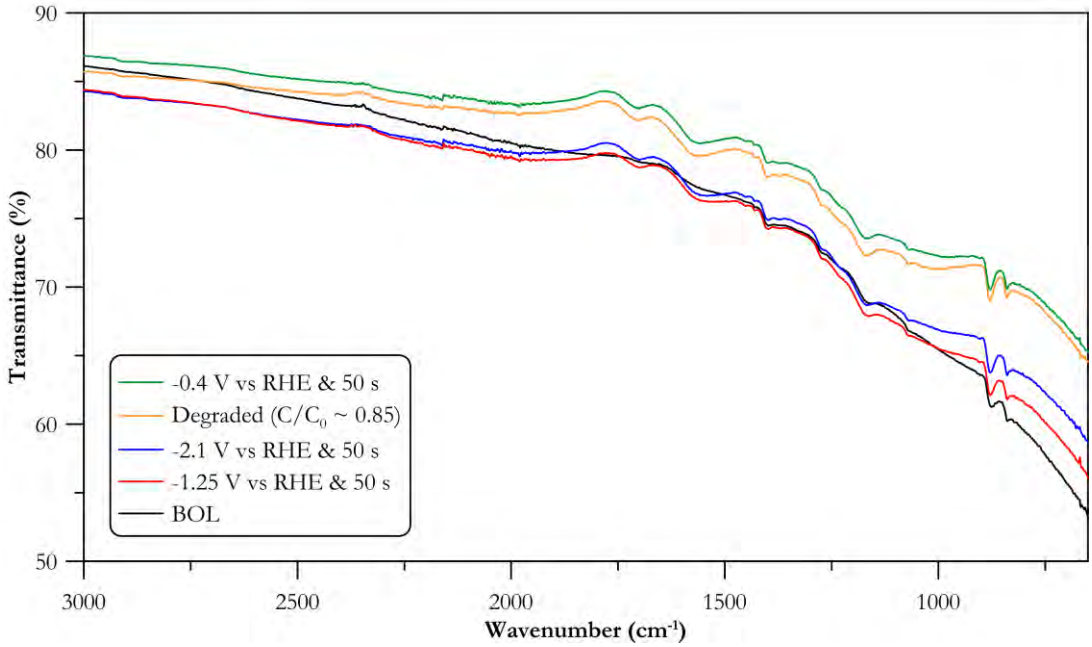

Figure B.6 FTIR spectra of electrodes regenerated at -2.1, -1.25 and -0.4 V vs RHE and a holding time of 50 s after cycling at a working electrode potential of 1.2 V vs RHE and a half cycle time of 5 min

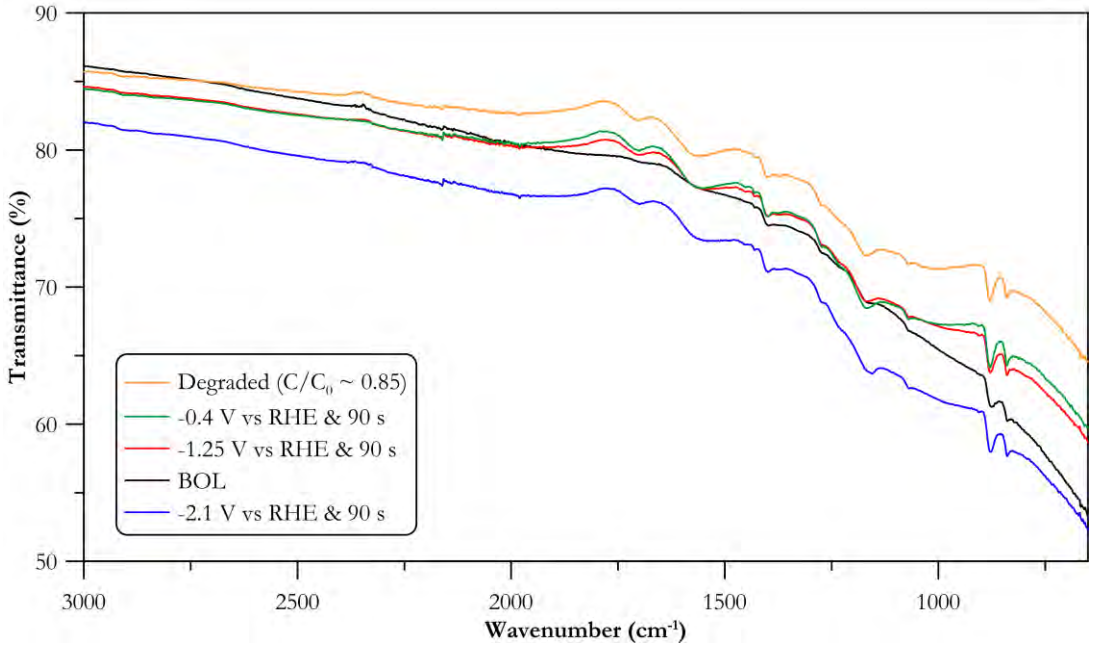

Figure B.7 FTIR spectra of electrodes regenerated at -2.1, -1.25 and -0.4 V vs RHE and a holding time of 90 s after cycling at a working electrode potential of 1.2 V vs RHE and a half cycle time of 5 min

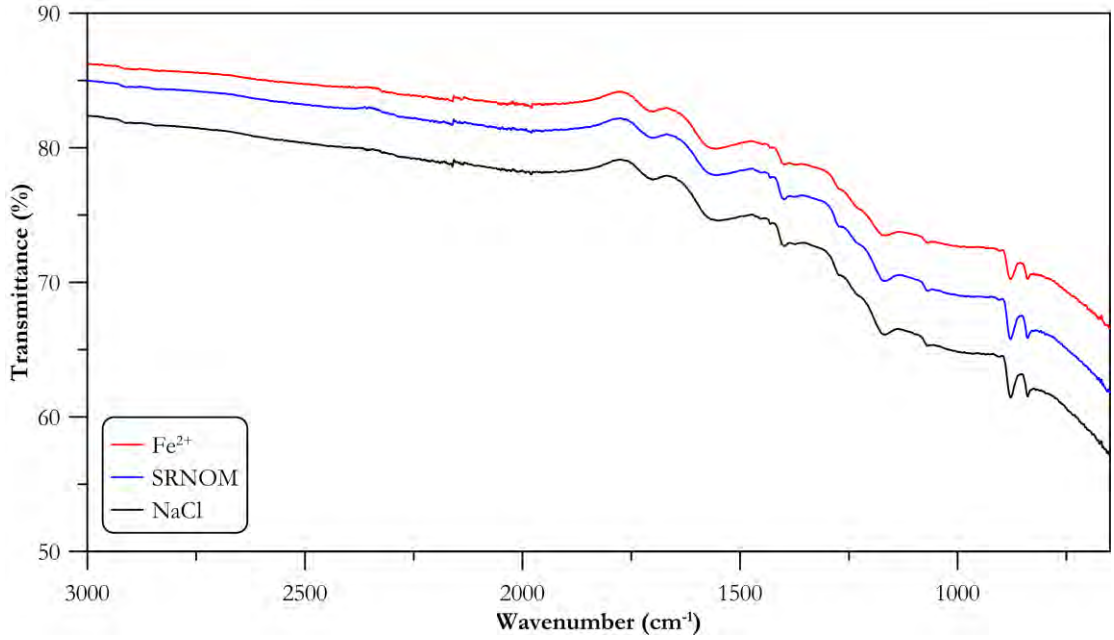

Figure B.8 FTIR spectra at the end-of-life of electrodes cycled with a working electrode potential of 1.2 V vs RHE and a half cycle time of 5 min and an added regenerative step with working electrode potential of -1.68 V vs RHE and a holding time of 10 s

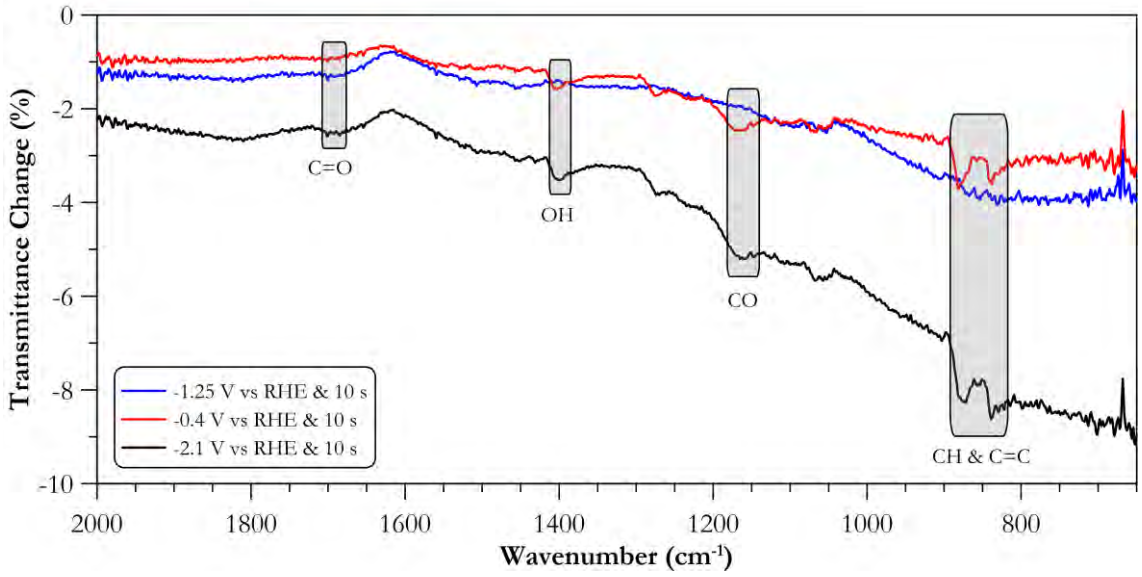

Figure B.9 Normalized FTIR spectra of regenerated electrodes with different reductive potentials and a holding time of 10 s after cycling to a C/C_0 value ≈ 0.85 at a working electrode potential of 1.2 V vs RHE and a half cycle time of 5 min. Electrode at a C/C_0 value ≈ 0.85 used as the reference for normalization

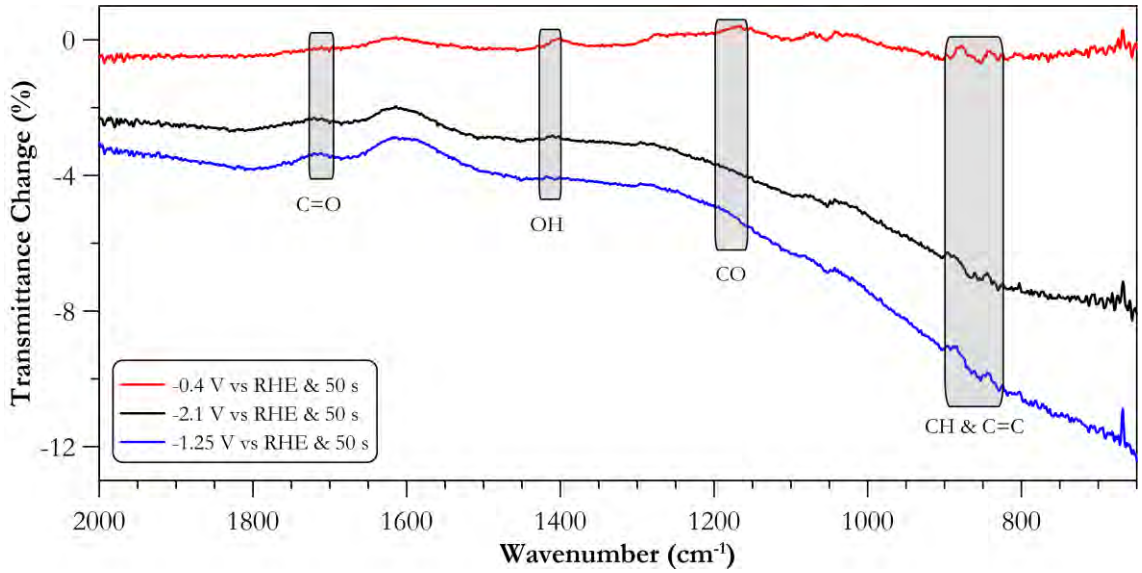

Figure B.10 Normalized FTIR spectra of regenerated electrodes with different reductive potentials and a holding time of 50 s after cycling to a C/C_0 value ≈ 0.85 at a working electrode potential of 1.2 V vs RHE and a half cycle time of 5 min. Electrode at a C/C_0 value ≈ 0.85 used as the reference for normalization

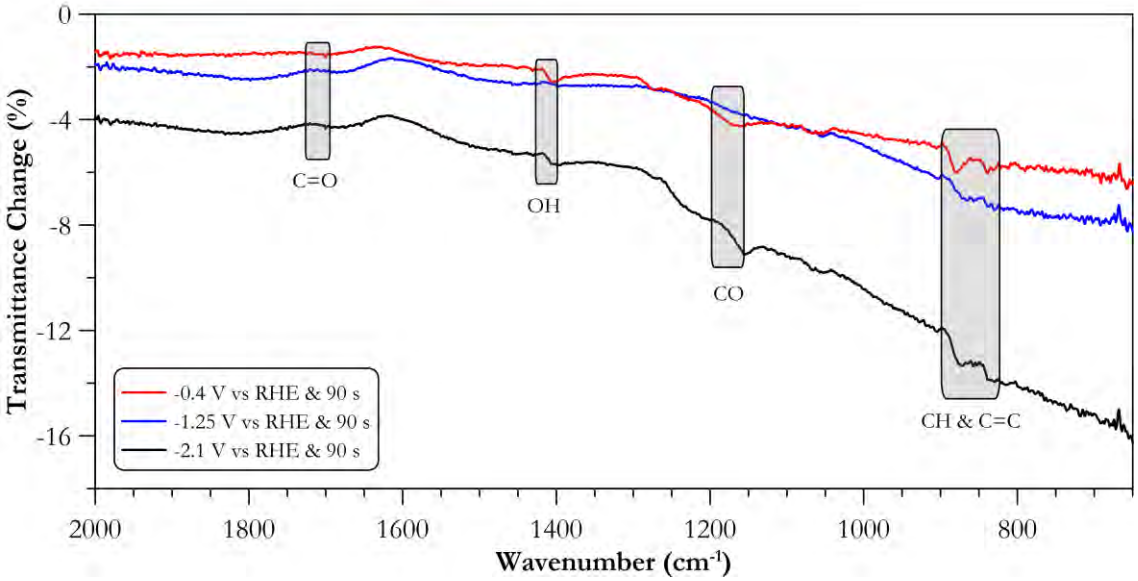

Figure B.11 Normalized FTIR spectra of regenerated electrodes with different reductive potentials and a holding time of 90 s after cycling to a C/C_0 value ≈ 0.85 at a working electrode potential of 1.2 V vs RHE and a half cycle time of 5 min. Electrode at a C/C_0 value ≈ 0.85 used as the reference for normalization

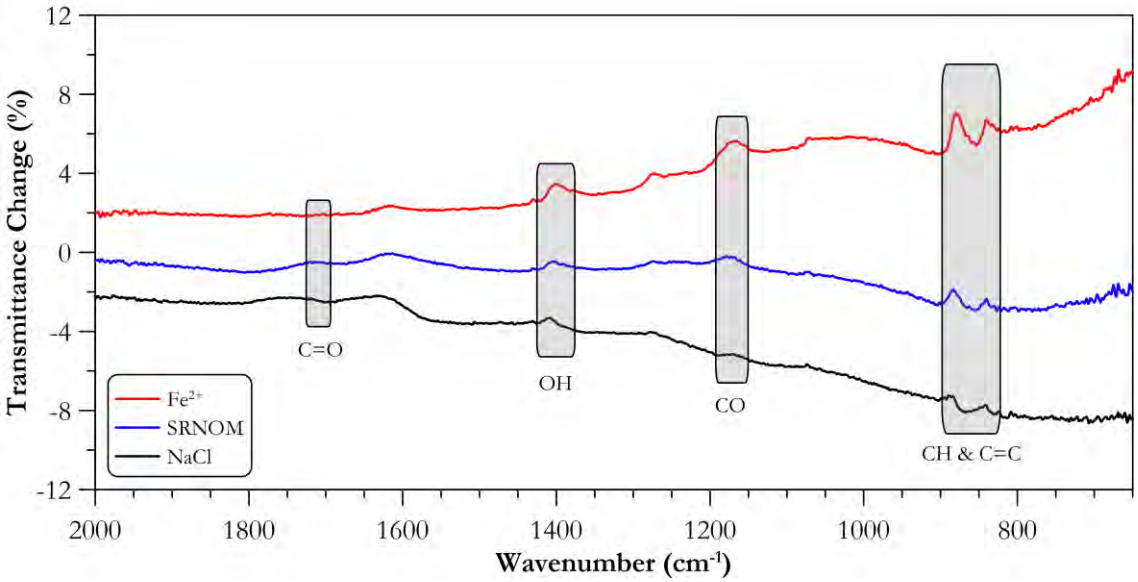

Figure B.12 Normalized FTIR spectra of electrodes at the end-of-life of electrodes cycled with a working electrode potential of 1.2 V vs RHE and a half cycle time of 5 min with a regeneration step at -1.68 V vs RHE and a holding time of 50 s Electrode at the end-of-life cycled with a working electrode potential of 1.2 V vs RHE and a half cycle time of 5 min used as the reference for normalization

B.4 Porosity Analysis

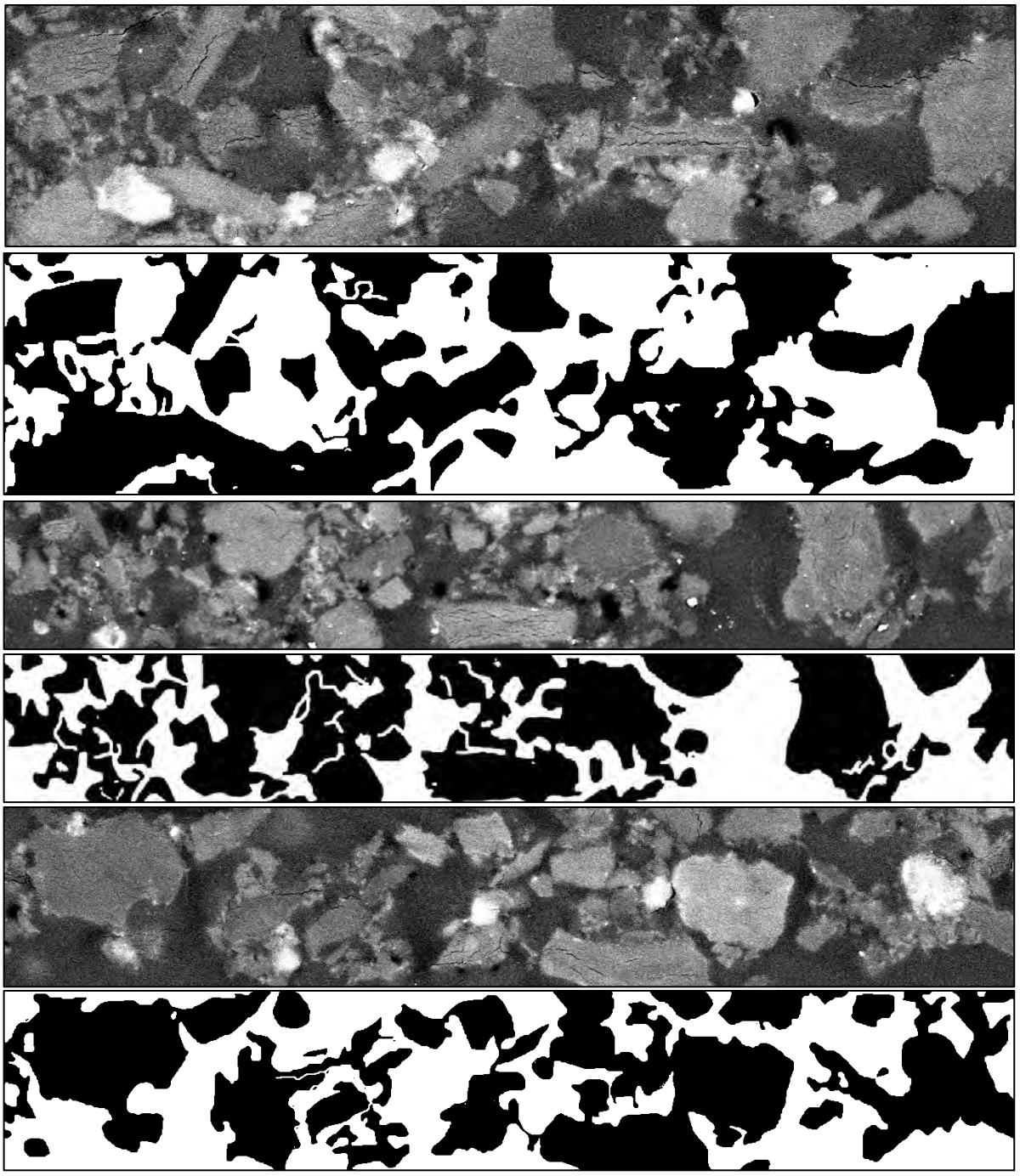

Figure B.13 Raw and processed images used to estimate the bulk porosity of an electrode degraded to a C/C_0 value ≈ 0.85

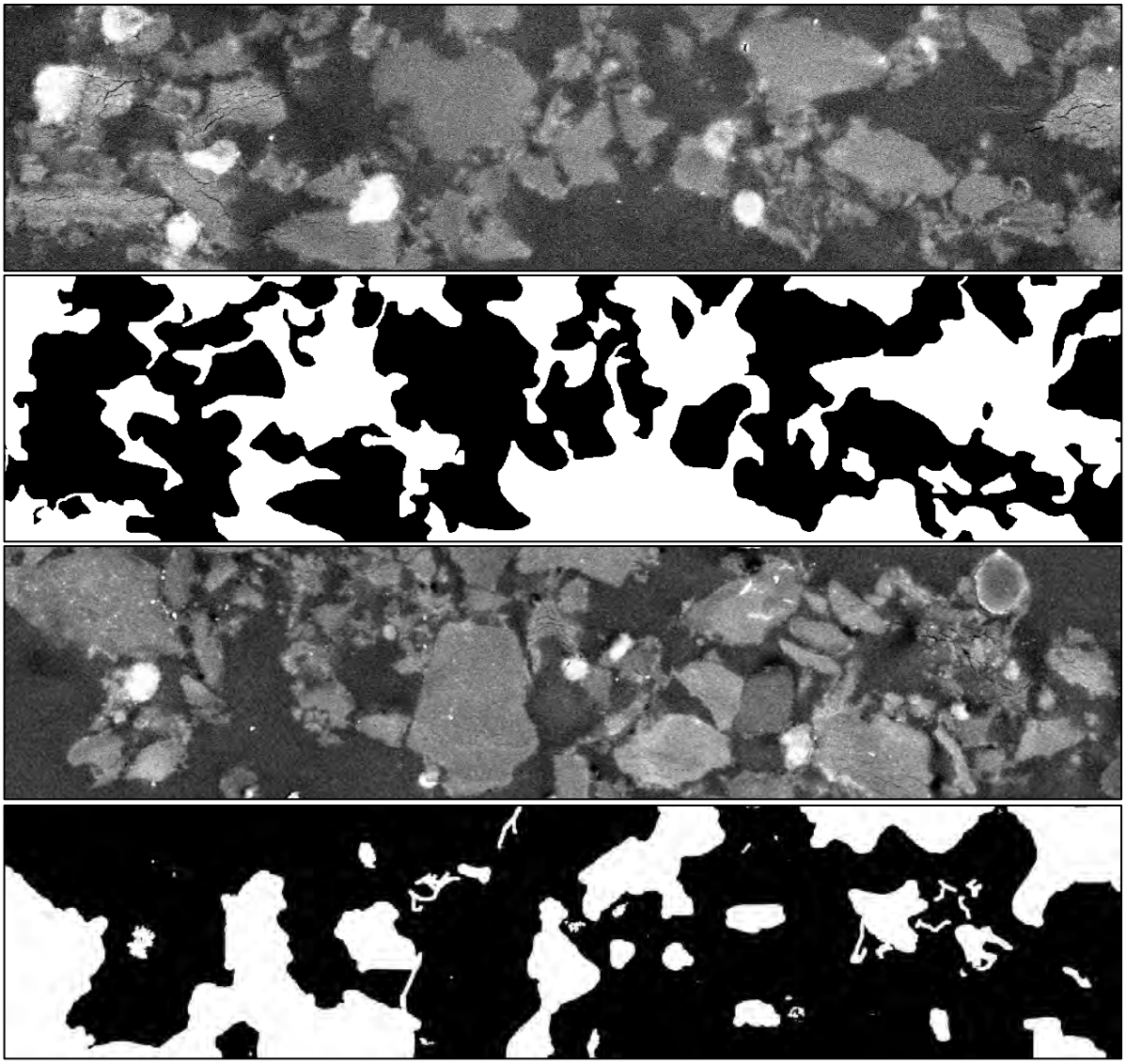

Figure B.13 (Continued) Raw and processed images used to estimate the bulk porosity of an electrode degraded to a C/C_0 value ≈ 0.85

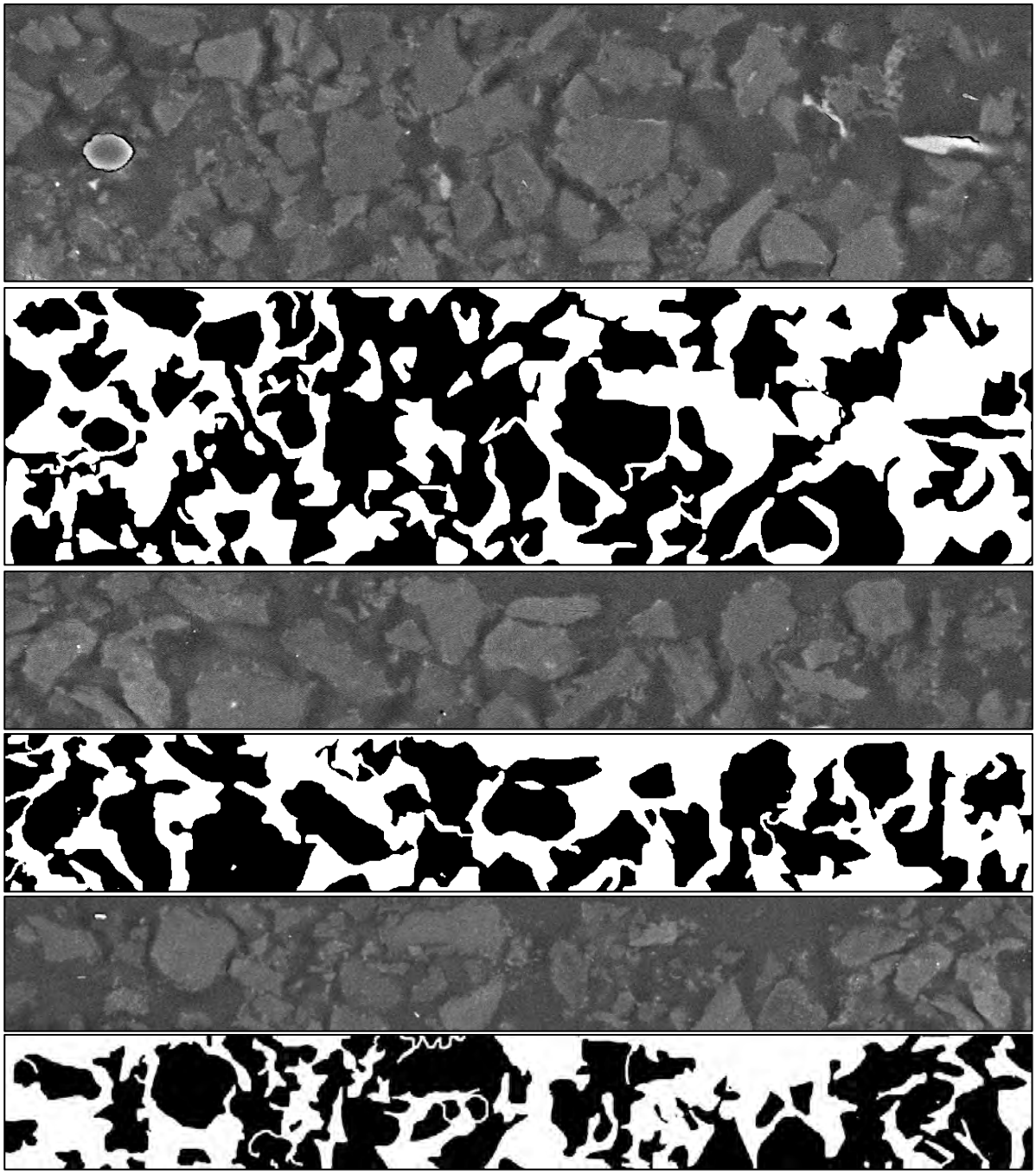

Figure B.14 Raw and processed images used to estimate the bulk porosity of an electrode regenerated at a potential of -1.68 V vs RHE and a holding time of 50 s after cycling under aerobic conditions with a working electrode potential of 1.2 V vs RHE and a half cycle time of 5 min until a C/C_0 value ≈ 0.85

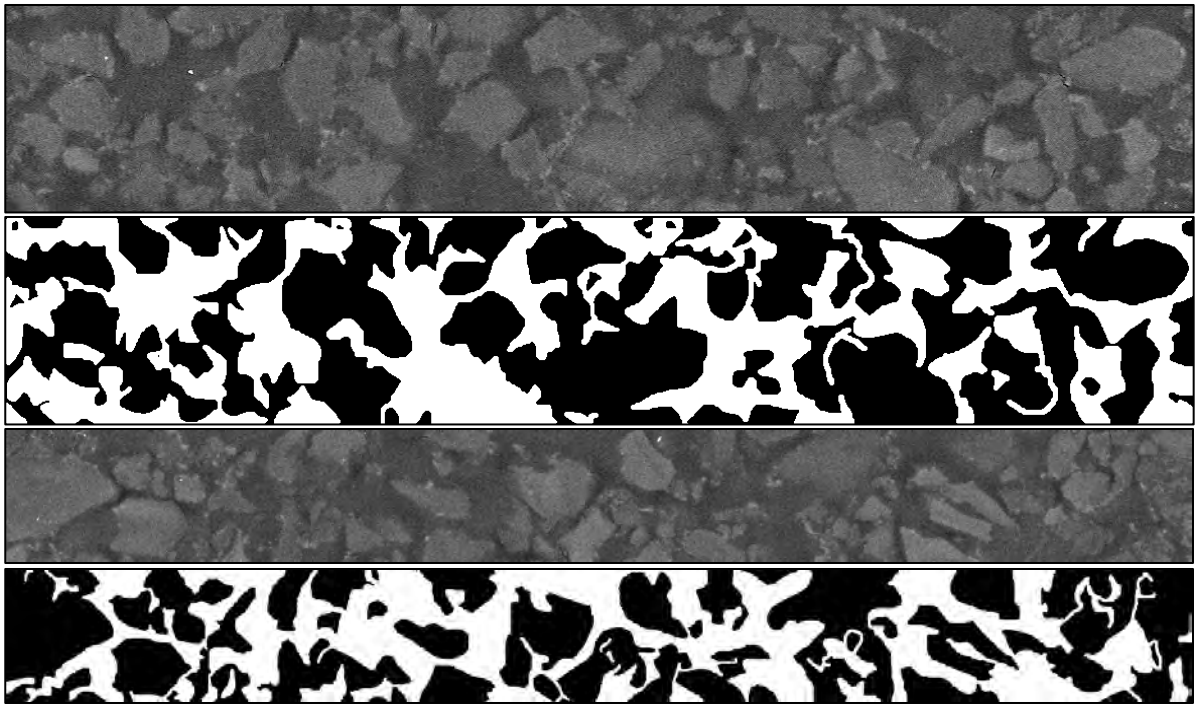

Figure B.14 (Continued) Raw and processed images used to estimate the bulk porosity of an electrode regenerated at a potential of -1.68 V vs RHE and a holding time of 50 s after cycling under aerobic conditions with a working electrode potential of 1.2 V vs RHE and a half cycle time of 5 min until a C/C_0 value ≈ 0.85

B.5 Discharging Potentials of Regeneration Experiments

Table B.1 Discharging potential (V vs RHE) for regeneration experiments of the 3^2-factorial design of experiments conducted under O_2 saturation and 1 M NaCl with different working electrode potentials and holding times. The discharge potential equals the open circuit potential measured at the beginning of each experiment

Experiment		Replicate 1	Replicate 2
Applied Potential (V vs RHE)	Holding Time (s)	(V vs RHE)	
-0.4		0.564	0.570
-1.25	10	0.567	0.571
-2.1		0.564	0.555
-0.4		0.559	0.566
-1.25	50	0.559	0.576
-2.1		0.559	0.567
-0.4		0.561	0.554
-1.25	90	0.566	0.571
-2.1		0.553	0.551

Table B.2 Discharging potential (V vs RHE) for regeneration experiments conducted along the potential domain conducted under O_2 saturation and 1 M NaCl with a holding time of 50 s. The discharge potential equals the open circuit potential measured at the beginning of each experiment

Experiment		Replicate 1	Replicate 2
Applied Potential (V vs RHE)	Holding Time (s)	(V vs RHE)	
-0.61		0.572	0.566
-0.83		0.549	0.560
-1.46	50	0.555	0.547
-1.68		0.552	0.553
-1.89		0.556	0.555

Table B.3 Discharging potential (V vs RHE) for degradation experiments performed with a working electrode potential of 1.2 V and a half cycle time of 5 min under O_2 saturation and regeneration experiments performed with a working electrode potential of -1.68 V vs RHE and a holding time of 10 s. The electrolyte concentration was 1 M NaCl. The discharge potential equals the open circuit potential measured at the beginning of each experiment

Experiment	Degradation			Regeneration	
Cycles performed	Replicate 1 (V vs RHE)	Replicate 2	Test	Replicate 1 (V vs RHE)	Replicate 2
1-5	0.513	0.513	1	0.555	0.546
6-10	0.546	0.553	2	0.565	0.556
11-15	0.551	0.553	3	0.557	0.552
16-20	0.551	0.547	4	0.561	0.555
21-25	0.557	0.559	5	0.564	0.557
26-30	0.554	0.546	6	0.567	0.560
31-40	0.560	0.560	7	0.566	0.559
41-50	0.554	0.556	8	0.557	0.546
51-60	0.542	0.556	9	0.553	0.548

Table B.4 Discharging potential (V vs RHE) for degradation experiments performed with a working electrode potential of 1.2 V and a half cycle time of 5 min under O_2 saturation and 0.2 mg Fe^{2+} L^{-1} and regeneration experiments performed with a working electrode potential of -1.68 V vs RHE and a holding time of 10 s. The electrolyte concentration was 1 M NaCl. The discharge potential equals the open circuit potential measured at the beginning of each experiment

Experiment	Degradation			Regeneration	
Cycles performed	Replicate 1 (V vs RHE)	Replicate 2 (V vs RHE)	Test	Replicate 1 (V vs RHE)	Replicate 2 (V vs RHE)
1-5	0.512	0.514	1	0.550	0.564
6-10	0.557	0.545	2	0.559	0.564
11-15	0.549	0.550	3	0.546	0.570
16-20	0.545	0.547	4	0.551	0.568
21-25	0.555	0.556	5	0.555	0.565
26-30	0.544	0.555	6	0.201	0.552
31-40	0.553	0.560	7	0.561	0.557
41-50	0.554	0.516	8	0.559	0.551
51-60	0.536	0.546	9	0.554	0.539

Table B.5 Discharging potential (V vs RHE) for degradation experiments performed with a working electrode potential of 1.2 V and a half cycle time of 5 min under O_2 saturation and 20 mg SRNOM L^{-1} and regeneration experiments performed with a working electrode potential of -1.68 V vs RHE and a holding time of 10 s. The electrolyte concentration was 1 M NaCl. The discharge potential equals the open circuit potential measured at the beginning of each experiment

Experiment	Degradation			Regeneration	
Cycles performed	Replicate 1 (V vs RHE)	Replicate 2 (V vs RHE)	Test	Replicate 1 (V vs RHE)	Replicate 2 (V vs RHE)
1-5	0.524	0.519	1	0.556	0.553
6-10	0.552	0.546	2	0.562	0.562
11-15	0.554	0.551	3	0.560	0.562
16-20	0.559	0.557	4	0.563	0.563
21-25	0.566	0.559	5	0.561	0.561
26-30	0.564	0.558	6	0.564	0.564
31-40	0.555	0.533	7	0.563	0.558
41-50	0.515	0.536	8	0.554	0.563
51-60	0.538	0.533	9	0.544	0.557
61-70	0.550	0.536	10	0.537	0.553

Appendix C

C.1 Technical Drawings of the Electrochemical Cell

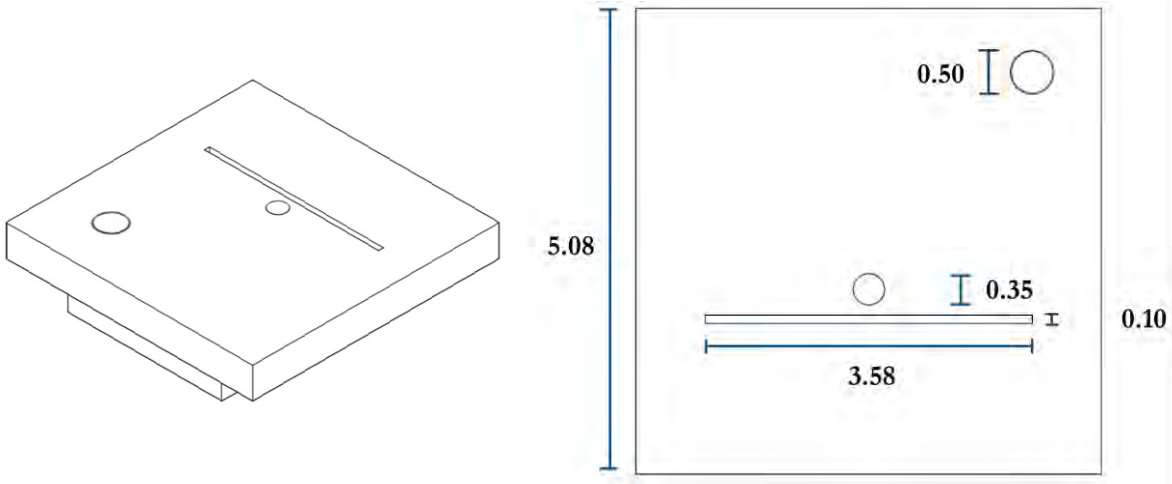

Figure C.1 Isometric view and dimensions in centimeters (top view) of the lid of the working electrode side of the electrochemical cell

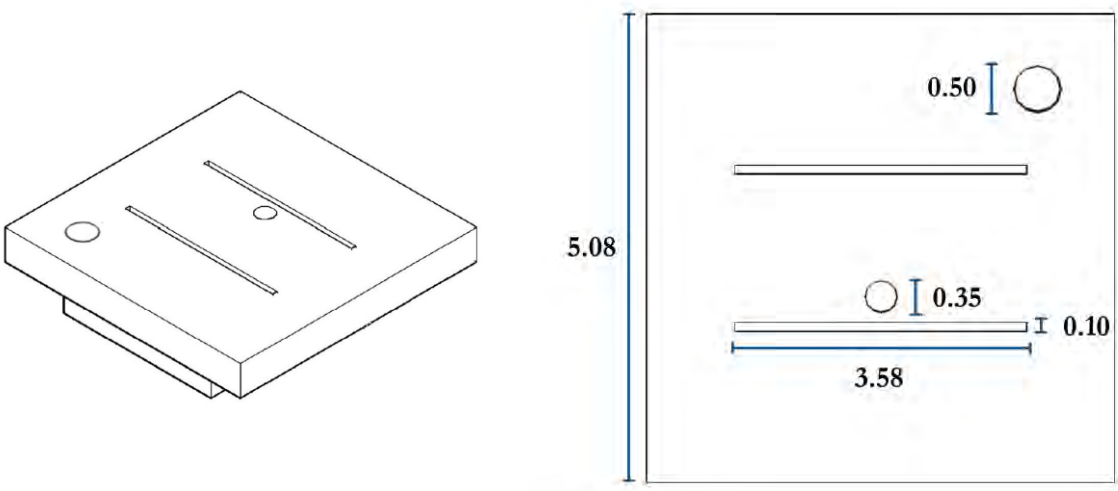

Figure C.2 Isometric view and dimensions in centimeters (top view) of the lid of the two-electrode flow-cell

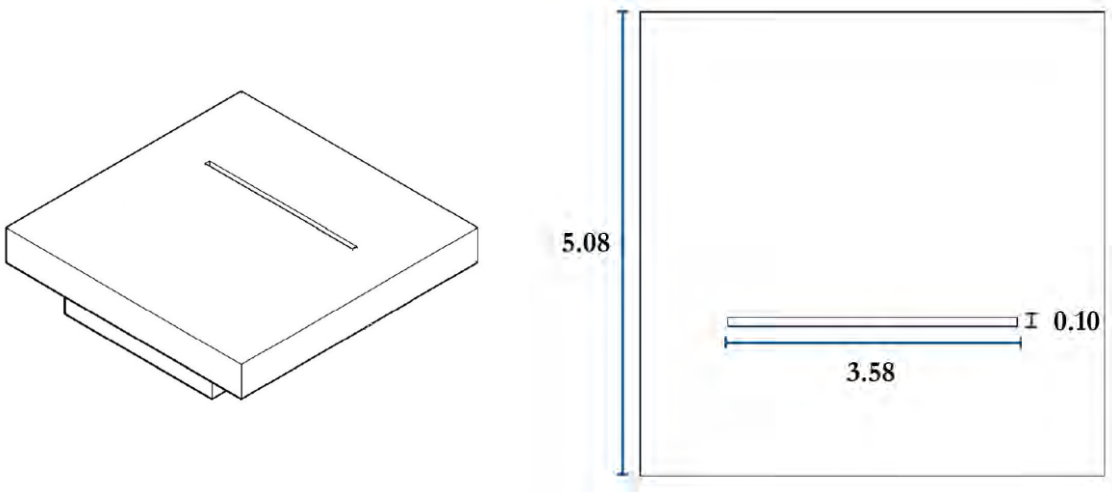

Figure C.3 Isometric view and dimensions in centimeters (top view) of the lid of the counter electrode side of the electrochemical cell

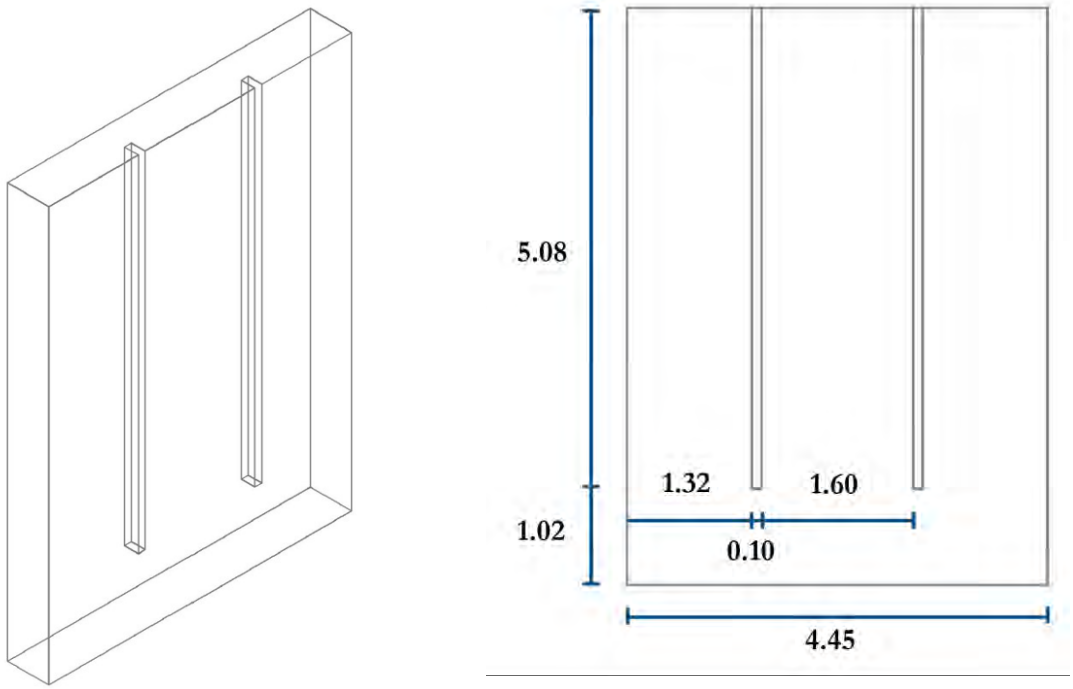

Figure C.4 Isometric view and dimensions in centimeters (top view) of the electrode holder

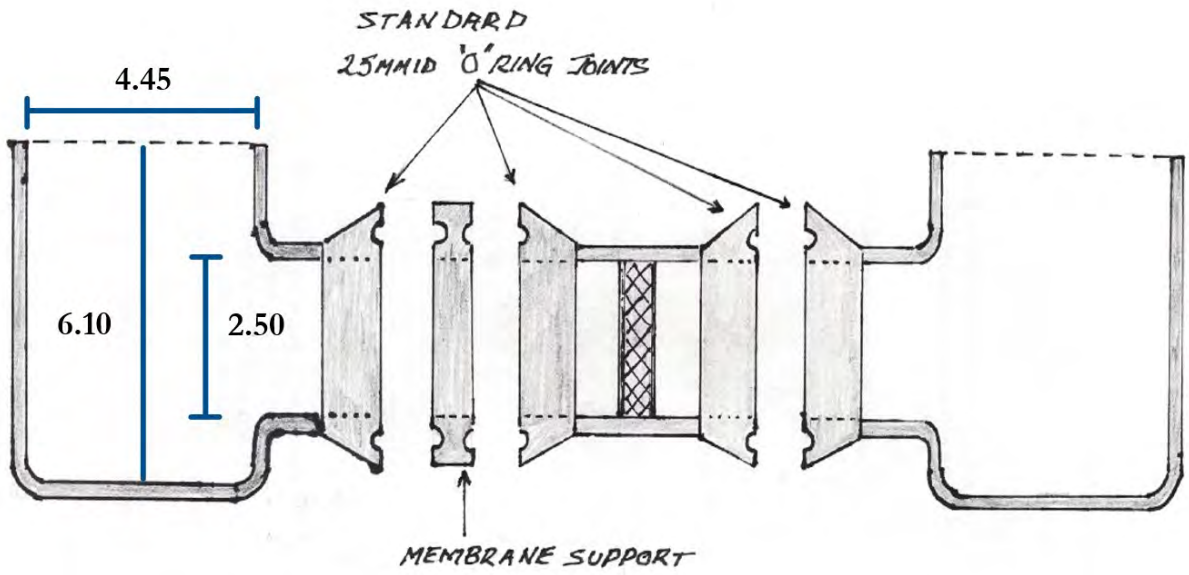

Figure C.5 Schematic and dimensions in centimeters of the compartments of the electrochemical cell